MECHANICAL BEHAVIOUR OF DOPED AND UNDOPED ZnO THIN FILMS

Ph.D. THESIS

by

VIPUL BHARDWAJ

DEPARTMENT OF METALLURGICAL AND MATERIALS ENGINEERING
INDIAN INSTITUTE OF TECHNOLOGY ROORKEE
ROORKEE – 247667 (INDIA)
JUNE, 2018

MECHANICAL BEHAVIOUR OF DOPED AND UNDOPED ZnO THIN FILMS

A THESIS

Submitted in partial fulfilment of the
requirements for the award of the degree

of

DOCTOR OF PHILOSOPHY

in

METALLURGICAL AND MATERIALS ENGINEERING

by

VIPUL BHARDWAJ

DEPARTMENT OF METALLURGICAL AND MATERIALS ENGINEERING
INDIAN INSTITUTE OF TECHNOLOGY ROORKEE
ROORKEE – 247667 (INDIA)
JUNE, 2018

INDIAN INSTITUTE OF TECHNOLOGY ROORKEE ROORKEE

CANDIDATE'S DECLARATION

I hereby certify that the work which is being presented in this thesis entitled **"MECHANICAL BEHAVIOUR OF DOPED AND UNDOPED ZnO THIN FILMS"** in partial fulfilment of the requirements for the award of the Degree of Doctor of Philosophy and submitted in the Department of Metallurgical and Materials Engineering of the Indian Institute of Technology Roorkee, Roorkee is an authentic record of my own work carried out during a period from August, 2013 to June, 2018 under the supervision of Dr. R. Jayaganthan, Professor, Department of Metallurgical and Materials Engineering and Dr. Rajib Chowdhury, Assistant Professor, Department of Civil Engineering, Indian Institute of Technology Roorkee, Roorkee.

The matter presented in the thesis has not been submitted by me for the award of any other degree of this or any other Institution.

(VIPUL BHARDWAJ)

This is to certify that the above statement made by the candidate is correct to the best of our knowledge.

(Rajib Chowdhury)
Supervisor

(R. Jayaganthan)
Supervisor

Date: June 2018

ABSTRACT

Fabrication of nanostructured thin films for numerous functional applications has been emerging rapidly in recent times due to their excellent mechanical, optical, and magnetic properties. Nanostructured thin films are rigorously explored in various disciplines such as material science, engineering applications, physical, chemical and biological fields owing to their multi-functional properties. Multi-functionality and diverse properties of ZnO thin films have led to continuous development and renewed interests among researchers. ZnO exhibits wide direct band gap, high exciton binding energy, high piezoelectric coefficient, easy to fabricate nanostructure, etc. However, nanostructure of ZnO offers remarkable stability and easily optimized by tailoring microstructure, defect morphology and crystallinity using synthesis route and thermal treatments. These properties of ZnO can be exploited for fabrication of piezoelectronics devices, UV-photo detectors, gas sensors, and dye sensitized solar cells etc. Also, incorporation of different dopants in ZnO thin films could manipulate its microstructure and crystalline properties, used to tailor the optical, gas sensing and piezoelectric properties. Commercialization of ZnO based nanostructured devices is heavily dependent on its structural integrity along with other functional properties.

This thesis is focused to investigate the mechanical and tribological properties of ZnO nanostructured thin films in a combined framework, using experimental and simulation techniques. Rare earth ions as the active constituents of ZnO, create distinct crystalline behavior after doping that could serve in many applications. ZnO thin films are doped with rare earth ions such as Yttrium and Praseodymium using direct current (DC) sputtering technique and their doping profile was studied by X-Ray photoelectron spectroscopy and Energy Dispersive X- Ray spectroscopy (EDS). The influence of deposition parameters on the structural and mechanical properties of thin films has been explained. The main objective of the present work is to, i) Synthesize pure ZnO thin films on glass substrate and fused quartz substrate using DC sputtering technique, and further to investigate the effect of sputtering process parameters on mechanical and tribological properties, ii) Study the effect of dopants e.g. (Yttrium, Praseodymium) on micro-structure and mechanical properties of ZnO thin films. iii) Develop a finite element model using nanoindentation parameters and to study the effect of friction, yield stress, substrate elastic-plastic properties on simulated load-displacement curve. The key results obtained are described as follows.

The nano-mechanical properties of pure ZnO thin films deposited at different substrate temperature such as (RT) 25^0C, 100^0C, 200^0C, and 300^0C using DC sputtering on glass substrate were investigated. The ZnO thin films are found to be predominately c-axis (002) oriented and sensitive to increasing substrate temperature, new crystal planes become visible at 300^0C as thin films become highly polycrystalline. The presence of (103) crystal plane is more pronounced with the increasing substrate temperature. High crystallinity and peak intensity ratio $I_{(002)}/I_{(103)}$ (counts) is highest for thin films deposited at 100^0C, attributed for high hardness and better adhesive properties observed for ZnO thin films. No major sudden burst of displacement 'pop-in' event in load-displacement curve of thin films was observed during indentation, indicating the films are dense with low defects and adhered strongly to the substrate.

Subsequently when underlying substrate has been changed from glass to fused quartz and ZnO thin films deposited at different sputtering deposition pressures (5, 10, 15, and 20 mTorr) using DC sputtering. The crystallinity and microstructure revealed a marked influence on the mechanical properties of ZnO thin films. The structural evolution of the thin films is in (002) crystal plane and influenced by deposition pressure variations. The intensity of (002) peak of the films rises initially and decreases with further increasing deposition pressure. The mechanical properties and coefficient of friction of ZnO thin films were measured using three-sided pyramidal Berkovich nanoindentation. The strength of thin films was measured by using scratch test under ramp up loading. Load–displacement profile of thin films at continuous indentation cycle was observed without any discontinuity revealed no fracture, cracking event, and defects, which is a consequence of dense microstructure and good adherence of films to the substrate.

The mechanical properties of Y (yttrium) doped ZnO (YZO) thin films deposited on glass substrates and fused quartz at different substrate temperature (Room temperature 25^0C, 100^0C) using DC sputtering were studied. It is observed that growth of crystalline nature and micro-structural features of thin films are sensitive to different substrate material and substrate temperature as indicated by X-Ray diffraction. YZO thin films have emerged in (002) diffraction plane and improves peak intensity with higher substrate temperature at glass substrate. The doping profile of Y (yttrium) in ZnO thin films and micro-structural features were characterized by X-Ray photoelectron spectroscopy (XPS), Atomic force microscopy (AFM) and Field effect scanning electron microscopy (FESEM). The scratch resistances in terms of lateral and normal force curve, hardness, Young’s modulus of the films were measured using Berkovich tip nanoindentation and nanoscratch. YZO thin films have shown better mechanical properties (hardness 5.06±0.70 GPa, Young’s modulus 166.81±16.39 GPa) on fused quartz substrate compared to glass substrate. XPS and EDS mapping of the films confirm Y^{3+} presence as well as uniform distributions throughout thin films. The mechanical properties of YZO thin films deposited at room temperature observed to be poor. It is due to the inadequate thermal energy at lower substrate temperature is not able to facilitate the formation of defect free and crystalline thin films. The denser microstructure and sharp morphology of the films observed at high substrate temperature have improved strength in terms of critical load 1210.6 µN of the films required for scratch resistance.

Furthermore, mechanical properties of Pr (Praseodymium) doped ZnO thin films deposited on glass substrates and fused quartz at different sputtering deposition pressure (5mTorr, 10mTorr) using DC sputtering were studied. Growth of crystalline phase in Pr doped ZnO thin films particularly in (002) diffraction plane is more pronounced and it improves with higher peak intensity at 10mTorr sputtering pressure as observed by X-Ray diffraction. However, the lower sputtering deposition pressure evoked deposition rates to the formation of poly-crystalline films emerged in several crystal planes. The presence of Pr ions incorporated ZnO host lattice as well as morphology was examined by XPS, AFM and FESEM. XPS spectroscopy revealed the presence of Pr^{3+}, Pr^{4+} at ZnO top surface layer and it was in tandem with EDS mapping. The thickness of thin films was found to be varying from 220 nm to 310 nm with dense morphology and uniform growth throughout on the deposited area. Nanoindentation prior to scratch testing (ramp up load condition) of Pr doped ZnO thin films was performed to understand its deformation characteristics. The three sided Berkovich indenter tip is used for the measurements and the films deposited on glass substrate have shown hardness (9.89±0.14 GPa), Young’s modulus (112.12±3.45 GPa) as compared to films deposited on fused quartz substrate, hardness (9.83±0.24 GPa), Young’s modulus 110.9±3.7 GPa), at similar synthesis conditions. The Nano-scratch tests yield lower critical load $Lc_{1,}$ 2250.5 µN for the crack initiation and upper critical load Lc_2, 2754.5 µN for the complete failure. The crack propagation resistance parameter (CPRS) of the films was evaluated using initial critical load Lc_1 and upper critical load Lc_2 for film failure. The better crack propagation resistance was observed for films deposited at 10mTorr sputtering pressure on both substrates, attributed to better crystalline nature of the films.

Finite element (FE) modeling and simulation of nano-mechanical behavior of ZnO thin films were performed. Experimental results obtained from nanoindentation, are used to develop the FE model. The FE calculation was performed as two dimensional model, assuming Berkovich tip as rigid material. FE analysis was used to elucidate the phenomenon of force-penetration depth by independently considering the variations in yield stress, friction coefficient and substrate effect of the crystalline ZnO thin films. The FE analysis was adopted in such a way to provide a best fit to experimental load displacement curve and investigated equivalency of force-indentation depth curves by Berkovich, conical or spherical tip with same radius. However, ZnO films are assumed as elastic-plastic material and perfectly bonded to substrate, so there is no slippage or delamination at the interface. The deformation in substrate depends on the difference in mechanical properties with coating and increase in penetration depth is observed when substrate yields before coating. FE simulation coupled with experimental process of indentation provides a better insight and optimization of the mechanical response for predicting the deformation behavior of ZnO thin films

ACKNOWLEDGEMENT

First and foremost, I would like to convey my sincerest appreciation and hearty thanks to my supervisors, Prof. R. Jayaganthan (Dept. of Metallurgical and Materials Engineering, IIT Roorkee) and Dr. Rajib Chowdhury, (Dept. of Civil Engineering, IIT Roorkee) for their valuable guidance and continuous mentoring throughout of research work. It was their understanding during the time of difficulties that stimulated strength and ideas through these years. I would also like to thank you for encouraging my research and motivation for future.

My special gratitude to the members of my research committee (SRC), Dr. G. P. Chaudhari (Chairman SRC, Dept. of Metallurgical and Materials Engineering, IIT Roorkee), Dr. P. Jeevanandam (External Expert SRC, Dept. of Chemistry, IIT Roorkee) and Prof. S. K. Nath (Internal Expert SRC, Dept. of Metallurgical and Materials Engineering, IIT Roorkee). The time and energy they spent on evaluating and reviewing research work is greatly appreciated.

I would like to thank Head of the Department, Prof. Anjan Sil, faculty members of the Dept. of Metallurgical & Materials engineering, IIT Roorkee for their support. I would like to thank MHRD and IIT Roorkee, India for doctoral fellowship and excellent facilities including Institute Instrumentation Center (IIC), Mahatma Gandhi Central Library, Institute Computer Center (ICC) and Information Superhighway Centre (ISC) made available for the accomplishment of research work.

I extend highest sense of gratitude to my teachers who taught me, from which my scientific interest is generated and multiplied with time. Therefore, I convey my special thanks to Prof. Ravi Kumar, Head of the Department CMSE, NIT Hamirpur (H.P.) and Prof. Ramesh Chandra, IIC, IIT Roorkee.

I am much obliged for the friendship of colleagues, including Dr. Ashwani Kumar, Mr. Arvind Kumar, Mr. Shiv Kumar, Dr. Vinay Tomar, Dr. Sunkulp Geol, Dr. Nikhil Kumar, Mr. Raviraj Verma, Dr. Sowjanya Montana, Mr. Rajkumar, Mr. Rahul Gupta, Mr. Guruprakash, Mr. Manoj Kumar and all of my Ph.D. batch mates (July, 2013). All your support constitutes the unforgettable memory of this period of life.

Last but not least, my lifetime gratitude for my Parents living in faraway hometown. Your prayers for me was what sustained me thus far. Many thanks goes to my wife, for her enormous amount of love, patience, with everlasting support.

Vipul Bhardwaj

LIST OF PUBLICATIONS

Refereed Journals

1. **Bhardwaj, V**., Chowdhury, R., & Jayaganthan, R. (2016). Nanomechanical and microstructural characterization of sputter deposited ZnO thin films. *Applied Surface Science*, *389*, 1023-1032.
2. **Bhardwaj, V**., Chowdhury, R., & Jayaganthan, R. (2017). Adhesion strength and nanomechanical characterization of ZnO thin films. *Journal of Materials Research*, *32*(8), 1432-1443
3. **Bhardwaj, V**., Chowdhury, R., & Jayaganthan, R. (2017). Effect of Post-Annealing Treatment on Mechanical Properties of ZnO Thin Films. *Int. J. Thin. Fil. Sci. Tec*, *6*(1), 37-44.
4. **Bhardwaj V**, Ashwani K, Chowdhury, R., & Jayaganthan R. (2018). Nanoindentation and Nanoscratch Behavior of ZnO:Pr Thin films Deposited by DC-Sputtering. *Journal of Materials Research* (Accepted).
5. **Bhardwaj V**, Ashwani K, Chowdhury, R., & Jayaganthan R. (2018). Nanomechanical and Tribological behavior of Y doped ZnO thin films deposited by DC sputtering. *Surface Engineering* (Submitted).
6. **Bhardwaj, V**., Chowdhury, R., & Jayaganthan, R. Finite element simulations of nano-indentation of ZnO thin films coated on quartz substrate *(To be communicated)*

International Conferences

1. **Bhardwaj, V**., Chowdhury, R., & Jayaganthan, R., Effect of sputtering deposition pressure on structural and mechanical properties of ZnO thin films. ICCT 2016, Poddar International College, Jaipur, March 26-27, 2016

CONTENTS

CHAPTER 5: FINITE ELEMENT ANALYSIS OF NANOINDENTATION ON ZnO THIN FILMS……………… 119

CHAPTER 6: CONCLUSION…………………………………. 133

REFERENCES…………………………………………………... 137

LIST OF FIGURES

Chapter 1

Chapter 2

Chapter 3

Chapter 4

Chapter 5

LIST OF TABLES

Table No. **Title** **Page**

Chapter 1

Chapter 2

Chapter 3

Chapter 4

Chapter 6

ABBREVIATIONS

PVD	Physical Vapor Deposition
CVD	Chemical Vapor Deposition
DC	Direct Current
RF	Radio Frequency
F-V	Frank-Vander Merwe Growth
V-W	Volmer-Weber Growth
S-K	Stranski-Krastanov Growth
Pr	Praseodymium
Y	Yttrium
HCP	Hexagonal Crystal Plane
TD	Threading Dislocation
Wt.	Weight
At.	Atomic
FE	Finite Element
XRD	X-Ray Diffraction
AFM	Atomic Force Microscopy
FE-SEM	Field Emission Scanning Electron Microscopy
XPS	X-Ray Photoelectron Spectroscopy
EDS	Energy Dispersive X-Ray Spectroscopy
YZO	Yttrium doped ZnO
ZnO:Pr	Praseodymium doped ZnO
RT	Room Temperature
RE	Rare Earth
BE	Binding Energy
CPRs	Crack Propagation Resistance Parameter
ZnO	Zinc Oxide
Sccm	Standard cubic centimeter per minute
GPa	Giga-pascal
PE-CVD	Plasma Enhanced Chemical Vapor Deposition
LP-CVD	Low Pressure Chemical Vapor Deposition

Chapter 1

INTRODUCTION AND LITERATURE REVIEW

This chapter provides background and scope for the research work presented in the thesis. Thin film deposition, literature review of the various properties in nanostructured ZnO thin films, more specifically the mechanical and tribological properties are discussed in this chapter. In subsequent section, Finite element based simulation dealing with nano-indentation is discussed.

Contents

1.1 BACKGROUND

Nano-science and nano-technology engineered materials utilized for up-gradation and enables to further develop innovative materials such as meta-materials, flexible electronic materials as compared to existing conventional materials [1]. Research in the field of nanostructured materials are essentially emphasize the improved performance with the benefits of miniaturization of devices. Objects in day-to-day life (e.g. computer, television, pots and cars) are surrounded by the miniaturized coated system. The widespread use of functional thin films in space applications, military applications (e.g. radars, satellites, solar systems and vehicles) has their own virtues to fulfill the requirements [2]. Also, biomaterial thin films used for blood contact to reduce the blood cell damages, could be beneficial for civil and military purposes [3]. Thin films growth and its applications is a major area which is explored in various disciplines e.g. material science, physics, chemistry and biology etc. [4].

Nanomaterials exhibit exceptional multi-functional properties compared to its bulk counterpart which could be utilized for new potential applications. The enhanced purity from contamination during the synthesis of nanomaterials preserve its inherent nano-phase properties. Nanomaterial synthesis from bottom-up approach is a reasonably favorable way for better purity and precise microstructure and doping. Several coating deposition techniques used high vacuum for film growth and maintained high purity without any contamination. The coatings have been in use from ancient times for the decorative and protective purposes; however, recent developments in functional applications of coatings have emerged due to new deposition techniques and characterization methods. With the emergence of more sophisticated tools for coating depositions ensuring to control their dimensions with manipulation of different microstructures pave a way to several new applications e.g. solar cell, transistors, biomedical coatings, corrosion resistant coatings etc. [5].

In the nanostructured thin films, the physical and chemical properties are altered due to size effect at nanoscale level, in which one of the dimensions is confined, leading to quantum confinement effects, substrate driven properties. The coatings performance and functionalities are likewise depending to a larger extent on underlying substrate properties, which is more pronounced when thickness of coating reduces to several nanometers only. The crystalline orientation of coatings is significantly affected by substrate conditions as well as synthesis parameters. Consequently, the nano-morphology of coating can be optimized to add several other functionalities in to existing properties.

1.2 NANOCRYSTALLINE THIN FILMS

In the surface engineering, thin films are considered when a material is applied onto a surface using the established techniques of deposition and afterwards growth of the film either in continuous or discontinuous microstructures take place throughout the substrate. Different design and manipulation of microstructure is promoted to achieve better properties i.e. optical properties, magnetic properties, electrical properties, mechanical properties and tribological properties. In the last decades of coatings development provide remarkable properties in the area as given below [6];

- Functional properties e.g. solar, optical, magnetic and electrical properties.
- Improved wear and corrosion properties.
- Hard coatings with enhanced fracture toughness.
- Thermal barrier coatings.

The surface of the material always possessing its significant importance in every application. Likewise, underlying substrate fairly influences the coating growth and interface and residual stress can be induced with different substrate materials [6]. The epitaxial coating growth on the substrate of same material or different material (i.e. Homoepitaxy or Heteroepitaxy) always possesses exceptional properties and technological importance due to its well-ordered microstructure and fewer defects as compared to its bulk counterpart [7]. The homo-epitaxy coating offers more access to control and re-engineered intrinsic properties compared to bulk properties, for instance silicon films deposited on silicon substrate for electronic chips. However, exciting properties can be achieved using heteroepitaxy where lattice misfit, residual stress in the films create diversity in lattice constants, crystal orientations, morphology of the thin films, eventually leads to different band gap and other functional properties [8].

1.2.1 Nucleation and Growth

The initial nucleation density, growth, re-crystallization during the coalescence stage determines the lateral grain size normal to the substrate. A mono-layer is formed depending upon the average separation of the initial nuclei, initial nucleation density and number of grains per unit area. In fact, thin film nucleation as a new phase on substrate is affected by presence of impurity, which leads to segregation, reconstruction of new abrupt, flat interface as well as crystal surface giving rise to different types of growth.

Likewise, film thickness determines the grain size grown normal to the substrate. For thicker films, incident species falls off at the tip of previously grown grains, and each column of grains grows multi-granularly with possible directions from normal growth depending upon the deposition conditions, the thermodynamic equilibrium of the deposited and the substrate surface. The general mechanism of thin film growth process is given below step by step as emerged from experimental as well as theoretical studies [7].

- The incident species impact and loses its normal component of velocity to substrate after striking so that it gets physically adsorbed at substrate surface.
- Initially, adsorbed species on substrate not in the equilibrium condition and these species units move randomly on surface to facilitate self-interaction forming a small size particles called nuclei.
- Nuclei still thermodynamically unstable state and depend on the deposition parameters in such a way that cluster collision with each other facilitate to grow in size and attaining a critical size called as nucleation barrier.
- Subsequently, microstructure forms with several phenomena throughout the substrate until a condition of super-saturation nucleation density is achieved.
- Energy of the impinging species, activation energies of adsorption, thermal diffusion, temperature, rate of impingement, nature of the substrate affect the nuclei size and density of microstructure.
- A nucleus growth and settlement take place either parallel or perpendicular to the substrate surface by diffusion under the influence of surface energy. Typically, it is observed that lateral growth is much higher.
- Film formation with the inclusion of small particles leads to formation islands, merging with each-other to shrink thereby reducing overall surface area. This process results in bigger islands, characterized as agglomeration and grows in size with higher mobility of the adsorbed species at the surface. Larger islands growth also leaves some channels and voids of uncovered substrate.
- The overall microstructure of the films from discontinuous island type to a continuous film throughout the substrate depends upon these aforementioned conditions.

Different types of growth modes observed discussed as follows;

1.2.1.1 Layer by layer growth or Frank-Vander Merwe (F-V)

Layer by layer growth are significantly observed in the materials having atoms that are more strongly bonded to substrate as compared to themselves. They first form the mono-layer over the substrate, which is most strongly attached to the substrate forming strong interface with uniform distribution, subsequently succeeding layers less tightly bounded to underlying substrate. This effect extends with thickness until bulk properties is achieved [9]. This kind of film growth process is favorable in adsorptions phenomenon and epitaxial growth shown in Fig. 1.1.

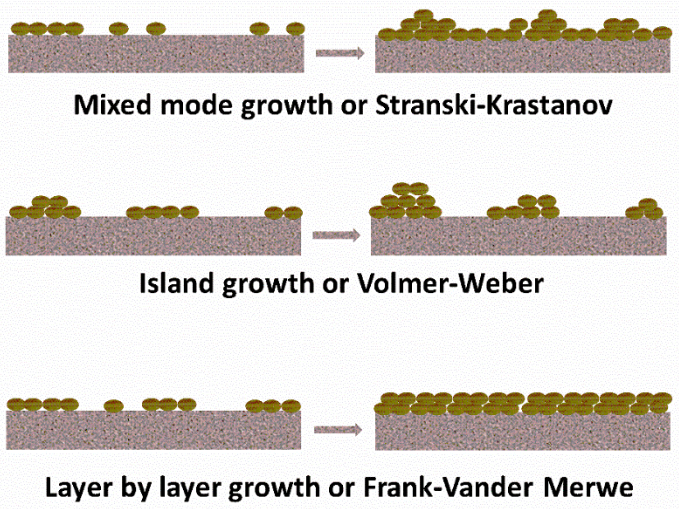

Figure 1.1. Different growth modes of thin films.

1.2.1.2 Island growth or Volmer-Weber (V-W)

Island growth is achieved when the incident species strike on substrate and preferably grow at the specific nucleation sites. Initial growth made up as the coalescence of atoms further constitutes as island kind of structure separated with distance referred as Volmer-Weber growth. The bonding between thin film molecules is much stronger as compared to substrate leading to such growth process. This kind of growth is observed in various metallic films, influenced by the stress state present in the films. The mechanism responsible for this growth depends upon deposition process as well as adatoms interaction for specific sites present at grain boundaries [10].

1.2.1.3 Mixed-Mode growth or Stranski-Krastanov (S-K)

Mixed mode growth is a micro-structural growth featured with dual kinds (e.g. F-V, V-W) of growth mechanism. In this growth process, the initial interaction of film materials is same as F-V growth mode and few layer of material cover up the substrate but substantial layer growth is hindered and formation of island is initiated. The growth of these islands depends upon the percolation thresholds. Depending upon the material specific properties, the percolation threshold lies in between nanometers to several microns.

The interfacial energy is relatively larger in island growth and discrete nuclei grows separately instead to filling-up a complete layer. In the mixed mode, interface energy is comparable to island formation energy that engages layer formation with island formation. However, interfacial energy is relatively less in layer by layer growth [10]. All the classical growth mechanism depends upon surface energy [9]. In addition, several other growth modes also considered including columnar growth, step flow, step bunching and screw island growth mode. These growth-modes depends upon the critical misfit which influence the deposit and substrate bonding behavior and accounted for deformability generally in oxide or iodide ions respectively [6].

Columnar growth is accompanied by V-W growth mode where the column as individual island forms continuous films throughout the substrates. However, presence of high density of defects is also associated with columnar growth as shown in the Fig. 1.2.

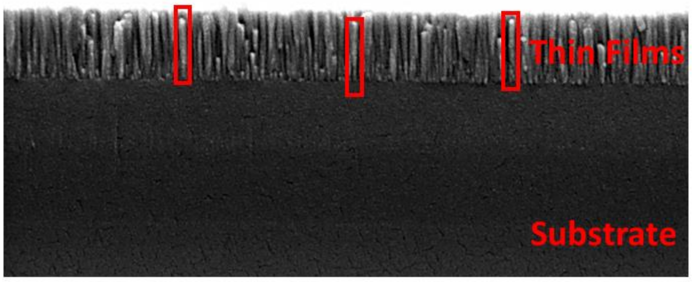

Figure 1.2. Columnar growth observed in cross sectional ZnO thin films.

Step-flow growth is diverse growth mode and induced when substrate mis-orientation (cut-off angle) is associated with crystal. This mis-cut provides atomic steps and incident species fall on these steps rather than forming surface islands. However, growth is attributed as change in the mobility of adatoms when surface terminates at layer from the substrate to the film [11].

Step-bunching growth is usually observed in heteroepitaxy to relieve the induced strain. When instability of growing crystals exists with large density of steps or terraces bunch together with significant step velocities over the growth surface, leads to step bunching growth. Macro steps forms when the higher steps and lower steps interact and exceed thickness of several mono-steps. The micro-steps exhibit individual growth rate and doping rates of impurities [12].

Screw island growth mode has high density of screw islands during initial growth depends upon mis-orientation of substrate; further coalescence of these islands may lead to screw dislocations with large burger vector responsible for screw-island growth mode. If continuous growth occurs, these islands form the columnar growth favored by high temperature and low super saturation [13]. Substrate of low misfit and low super-saturation leads to best structural perfection achieved by F-V growth mode.

1.2.2 Doping in thin films

Doping is induced in different concentrations for the variation in inherent properties of thin films. The various dopants can be incorporated in the thin films during the synthesis procedure and using precursor material. Likewise, different post deposition treatments e.g. thermal treatments (in vacuum and gas medium), implantation with different ions and chemical treatment also provide a different crystallinity and induced dopants in the host matrix. There is ongoing research on doping in thin films by analytical, computational and experimental analysis to achieve better performance and its real world industrial application. The tribological performance of several coatings has been improved after doping [14]. The external environment also causes to unwanted impurity, like oxide layer is deposited e.g. copper oxide are more prone to shearing than copper films [15]. There are several theoretical and simulations studies to understand the nano-physical changes after doping.

1.2.3 Defects in thin films

The crystallographic orientations and microstructure formation are entirely depending on the randomly distributed islands and an interface developed by grain boundaries. During growth and film formation process, defects gets incorporated in the microstructure, primarily induced by mismatch of unit cell geometrical configurations as well as crystallographic orientations of substrate-film. The grains distribution is randomly oriented in polycrystalline type of microstructure. Even if, the crystalline orientation pertaining to different grains might be same throughout, a single-crystal film could not be obtained and instead the formation of single-crystal grains oriented parallel to each other giving rise to low-angle grain boundaries. Likewise, when the grain size shrinks below a critical size (approximately less than 20 Å), it forms amorphous micro-structures accompanying enhanced disorder as compared to crystalline films [16]. Generally, thin films contain structural defects e.g. grain boundaries, twins and twin boundaries, dislocation, stacking fault and aggregate point defects etc. Defects e.g. twin boundaries or stacking faults are observed less frequently in polycrystalline films. However, major defects such as dislocations, grain boundaries and lattice misfit are significant in polycrystalline films. Primary mechanisms inducing dislocations in thin films depends upon lattice misfit, existing stresses in thin films and weaker adhesion at the interface.

Further, stress relaxation through dislocations movement by active slip system in thin films and buckling, chipping, delamination etc. could lead to the failure at the interface**.** The different types of defects are possible given in Fig. 1.3. The defect concentrations in the thin films also depends upon the thermal and post deposition treatment. The different thermal expansion coefficients of substrate and thin films can induce different strain depending upon the growth temperature.

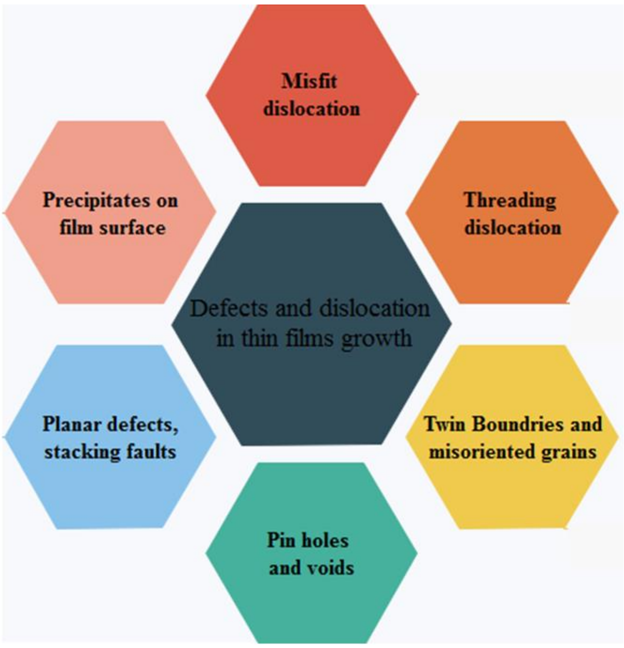

Figure 1.3. Schematic diagram showing defects induced in thin film during synthesis.

1.2.4 Roughness of the films

Roughness and topography of the films are affected by nucleation barrier as well as super-saturation; nucleation density is high while critical nucleus is small enough in initial stage of film formation. Number of nuclei formed depends upon nucleation barrier as well as the super saturation. High mobility enhances surface smoothness to fill concavities in the films. Also, roughness of the films is usually related to different modes of film growth e.g. F-V growth mode, provides the smooth surface compared to V-W growth mode. The topography including roughness, grain distributions and grain size can be investigated by atomic force microscopy. However, different temperature dependent strains generated due to thermal expansion mismatch between a film and substrate affects film microstructure and topography. Also, different crystal planes and their crystalline phases influences the planar density and changes the topography and microstructure of thin films [17].

1.2.5 Adhesion

Adhesion of thin film is the bonding force to the substrate, which is a significant factor for stable film structure, depends on chemical and physical state, surface energy minimization and microstructure of substrate material. This high adhesion is pre-requisite for the film formation and applications, which is achieved by optimizing the synthesis parameters and type of substrate used. Incident species falls off with specific kinetic energy and loses the velocity normal to substrate, and this kinetic energy is transformed as adsorption energy further to initiate nucleation process. However, impurity at the substrate deteriorates adhesion mechanism and homogeneous growth is not achieved. Also, pre-coated substrate with suitable materials to minimize the lattice mismatch as compared to bare substrate provides improved adhesion of a film. During deposition, vacuum and super saturation affects the density of films; poor vacuum generally deteriorates films quality with porous, contaminated microstructure. Different material of film and substrate induce internal stress and lattice misfit energy during growth [18].

1.2.6 Hardness in Nanocrystalline thin films

The hardness i.e. “the resistance of a material to plastic deformation” or materials ability to sustain under deformation through applied pressure. However, dislocation nucleation and propagation has an immense impact on mechanical properties of materials, and it is recognized that dislocation movements can be hindered, beneficial to gain high hardness by either grain refinement to enhance grain boundaries, or solid solution hardening. The mechanical strength increases with decrease in grain size by Hall-Petch relationship as given in Eq. (1.1) [19].

$$\sigma = \sigma_0 + \frac{k}{\sqrt{d}} \tag{1.1}$$

Where, σ is yield stress of the material, σ_0 is the intrinsic yield stress of the bulk material, k is the material constant and d is the grain diameter. It is evident from Fig. 1.4, that conventional bulk materials have the grain size variations beyond 100 nm to several micrometers. So, the influence of propagation of dislocations is not significant on the overall hardness. The mechanism responsible for hardness in bulk materials to have less number of grain boundaries impose as minor barrier to impede the movement of dislocations through the slip system. However, as the grain size reduces substantially below 100 nm, significant grain boundary volume fraction develops within the material. It can significantly obstruct movement of the dislocations at the grain boundary and increase the hardness as the materials competes against permanent deformations.

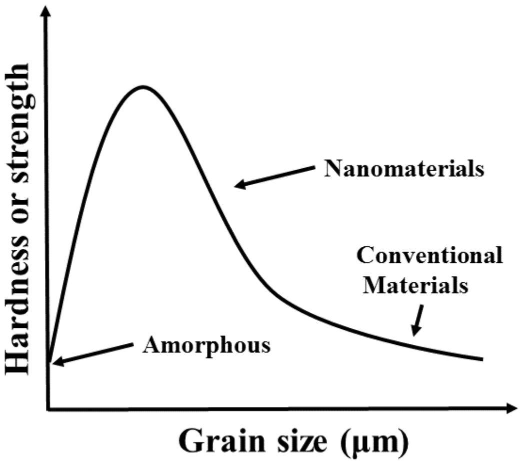

Figure 1.4. Schematics of hardness vs grain size variations in the material.

However, continuous reduction of grain size particularly less than 10 nm (critical grain size) has an adverse effect, which suddenly deteriorates hardness of the material due to grain boundary sliding effect. Grain boundaries cannot effectively impede the dislocation movement below critical grain size called inverse Hall-Petch effect. Coatings can be categorized on the basis of their intrinsic hardness as follows [20].

- Hard Coatings (H < 40 GPa)
- Super Hard Coatings (40 ≤ H ≤ 80 GPa)
- Ultra Hard Coatings (H > 80 GPa)

The hard coatings primarily used for tribological applications. Various physical and chemical synthesis methods are competing to achieve superior performance in actual engineering applications under dry or high speed machining conditions e.g. protective coatings for turbine blades, engine parts and cutting tools to improve their durability. The drawback of conventional hard coatings is higher thickness, which impose a risk of adhesion failure with the substrate. Also, the conventional hard coating are usually ceramics, however, nanocrystalline coatings can have better mechanical properties regardless of its bulk counterpart. Furthermore, Nano-crystalline coatings emerged with superior mechanical properties and considerable higher strength. The same Eq. (1.1) remains valid with grain size reduction in nanocrystalline coatings.

In the case of nanocrystalline coatings, increased hardness not only dependent on obstruction of movement of dislocation but the concentrations of defects can be reduced by manipulating the microstructure as well as type of substrate used.

However, there are considerable chances for reverse Hell-Petch effect which should be taken care. Generally, most metals have this critical grain size of ~10 nm. Analysis of critical grain size effect by several analytical models for the material behavior including dislocation/diffusion/grain boundary shearing/two phase models has been made in the literature. In addition, along with the improvement in hardness, ductility can be enhanced with reducing brittleness even in nano-crystalline ceramic coatings [21].

1.2.7 Toughness in Nanocrystalline thin films

Toughness represents a better combination of ductility and strength in the materials performance. Toughness broadly entitled to energy required for crack creation and propagation until fracture occur or, ability of material deformation to absorb energy up to fracture. High toughness in the coating has ability to pursue high resistance for cracks initiation under stress and also absorption of high energy deters crack propagation like chipping, flaking or catastrophic failure. In general, materials observed hard to cut at last has high toughness. In addition to super-hardness, high toughness of a coating is equally important, especially where to deal with high shear/normal forces. The protection needed in machining application as sliding contact may not be delivered by hardness alone. Sometimes, super-hardness is exhibited due to internal stresses developed within the films, and such conditions may deteriorate wear resistance and fatigue properties.

The high toughness in the coatings is achieved using ductile phase toughening, compressive stress toughening and phase transformation toughening, etc. However, recent studies confirmed that nanostructured and nano-composite coatings possess relatively high fracture toughness, increasing robust mechanical contact conditions that can drive materials with a combination of hardness and toughness [22]. For the sliding contact applications; high toughness is preferable as compared to high hardness. Nano-composite coatings can facilitate to combine higher hardness along with enhanced toughness for industrial applications [23]. Such coatings should exhibit low plastic deformation, better elastic, resilient properties. In the surface engineering, different design and microstructural engineering is promoted to achieve better properties i.e. mechanical properties and tribological.

1.2.8 Coatings application as Hard Coatings

Hard coatings are essential for protection of the component in any instrument due to wear or tear and robust use. Longer life spans along with ability to sustain high loads are few reasons for hard coatings. However, recent development of hard coatings depends not only upon their ingredient materials but also their thickness scale. Hard coatings generally are nitride based (e.g. titanium Nitride, chromium nitride, Zirconium Nitride, silicon nitride etc.), carbide based (e.g. silicon carbide, Tungsten carbide, Vanadium Carbide, boron carbide etc.) and several other multi-component [24], Furthermore, hard coatings is divided in two categories such as monolayer coatings and complex coatings. Monolayer coatings are metals, Al, Cr, Mo, or TiN, TiC, CrN etc. The complex coating consists of more than one material and extent of distribution is high Ti(C,N), (Ti, Al)N, (Ti, B)N, (Ti, Zr)N, (Ti, Nb)N, (Ti, Al, V)N etc [25]. Likewise, multiphase coatings in which one phase of material is dispersed in another phase (TiN-TiB_2) also give better results [26]. Apart from that, multi layered coatings is developed which provide good adhesion as well as better corrosion resistance forming like sandwich type structure [27]. Sandwich structures with different mechanical properties also provides better crack propagation resistance due to different interface and however crack nucleation and propagation is detrimental for monolayer coated system. The nano-composites hard coatings also provide improved hardness due to its nano-morphology. In hard coatings, fundamental properties are the followings.

- High hardness, toughness, high wear resistance properties
- Low friction coefficient
- Good adhesion
- Chemical inertness and smooth morphology
- Longevity

1.2.9 Functional Coatings applications

The application of functional coating includes electronics transistors at thermal application [28], piezoelectric device [29], sensors [30], tunable emission [31], biomedical applications [3], stem cell and tissue engineering applications [32], and corrosion resistant coatings [20] etc. As far as the actual performance of functional coating based device require the analysis of mechanical strength in rugged enviourment. Fabricated devices should ensure the service life as well as devices integrity and durability. The durability is primary concerned of semi-conducting coatings in electronic industries regarding the data storage manufacturing, optical devices and chip manufacturing [33]. The tangential and normal load bearing capacity should be high, because even minor scratch can deteriorate performance throughout the surface and lead to stress center where the failure/fracture is most probable to occur. Though functional applications of coatings are well known but the mechanical properties ought to be investigated. ZnO is also considered as a multi-functional material used in several applications.

1.3 GENERAL PROPERTIES OF ZnO

ZnO is renowned as wide band gap semiconductor considered as a key technological material and received huge attention due to pertaining multifold performance in electronics, sensing, solar cell as well as piezoelectric properties [34]. With the leading edge in advanced synthesis techniques and characterization methods not only provide the better understanding but also develop non silicon based miniaturized semiconducting devices. ZnO is white powder in color which is insoluble in water. It is widely used as an additive in materials preparation and production of many products such as ceramics, plastics, glass, cement, lubricants, ointments, adhesives, paints and pigments, batteries, ferrites, fire retardants, medicine and first aid tapes. ZnO naturally found in as traces of zinc blende and furthermore several techniques developed for extracting pure ZnO powder. ZnO corresponds to compound semiconductor belongs to II-VI semiconductor group possessing large band gap~3.4 eV.

In addition, ZnO is known for good transparency, high electron mobility and excellent luminescence at room temperature. The high electromechanical coupling and high exciton (electron-hole pair) energy ensure consequent use in actuators, piezoelectric devices as well as efficient excitonic emission even at room temperature [35]. Its optical properties are very much useful in emerging applications like transparent conducting oxide; electrodes used in liquid crystal display, energy applications, UV protections, used in thin film transistors etc. ZnO crystallizes predominantly in thermodynamically stable wurtzite polyhedral structure, with sp^3 covalent bonding, where each O^{2-} is surrounded by 4 Zn^{2+} and vice versa. Furthermore, bonding itself having substantial ionic character, resides in between covalent and ionic semiconductors [29]. The higher stability is determined by equilibrium cohesive energy using Hartree-Fock-LCAO theory and valued −5.658 eV for wurtzite, −5.606 eV for zinc-blende, and −5.416 eV for rocksalt phases. Furthermore, DFT- LDA analysis equilibrium cohesive energy, −9.769 eV for wurtzite, −9.754 eV for zinc-blende, and −9.611 eV rocksalt respectively [29]. Therefore, wurtzite phase energetically favorable in ambient conditions. Several models have been proposed for cohesive/lattice energy of nanostructures and often based on surface atoms binds with comparatively less number of chemical bonds, so there is less contribution to total energy than the bulk atoms. Also, with the decreasing size of nanoparticles, the ratio of surface atoms increases and therefore its cohesive energy also changes [36].

Recently, enormous attention is focused on ZnO nanostructures (particles, wires, thin films), preparation and characterization with and without doping in host ZnO. Several deposition techniques e.g. evaporation, pulse laser deposition and sputtering is used to deposit ZnO thin films [37]. However, solubility of transition metals in ZnO is found to be relatively low, exceeded the solubility limit leading to the precipitation of accompanying phases, or usually mixed oxides of zinc and transition metal, or ZnO phase may change either to rock-salt or spinel structure [36,38].

1.3.1 Crystal structure

Hexagonal ZnO wurtzite structure contain lattice parameter *a*, *c* along with '*c/a'* ratio ~1.60 belongs to the space group of C_{6v}^{4} or P6_3mc shown in Fig. 1.5. In ideal crystal of wurtzite, hexagonal close packed sub-lattices, relatively displaced to each other along the threefold *c*-axis by the amount of u =3/8 (*u*-length measures by which each atom get displaced along the next to the c axis)[35]. Each sub-lattice contains 4 atoms/unit cell and every group-II atom is surrounded by four group-VI atoms vice versa, coordinated at the edges of tetrahedron.

In actual ZnO crystal, its wurtzite structure deviates from the perfect arrangement, and varied '*c/a*' ratio or *u* parameter. It is essential to mention that a substantial correlation between the '*c/a*' ratio and *u* parameter exists, when '*c/a*' ratio reduces *u* parameter enhanced to stabilize four tetrahedral distances to approximately constant by distorting of tetrahedral angles depending on long-range polar interactions. Also, '*c/a'* ratio associated with relative difference of electro-negativities between two constituents affects the activated slip system and yield stress in the hexagonal crystal system [39].

In addition, ZnO exhibit pressure-induced phase transition i.e. rocksalt phase converted at approximately 10 GPa from wurtzite with an enormous volume reduction about 17% [40]. The reduction of the lattice parameters triggers interionic coulomb interaction to ionicity significant over the covalent character. ZnO in zinc-blende crystal structure is metastable, grown by hetero-epitaxy on cubic substrates provides a topological compatibility to inhibit the intrinsic tendency to grow a wurtzite phase [35]. All three structures possess no inversion symmetry and ZnO exhibits crystallographic polarity i.e. depend on the direction of the bonds along the *c* direction and sequential stacking of Zn^{2+} to O^{2-} referred either Zn^{2+} terminated surface or O^{2-} terminated surface which give rise to Zn or O polarity.

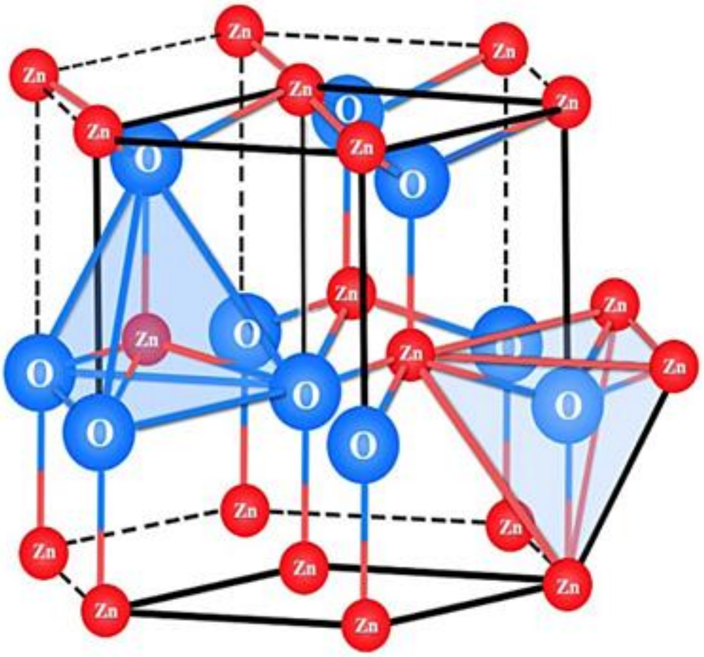

Figure 1.5. Crystal Structure of ZnO in the Wurtzite phase [41]**.**

Table 1.1. General Properties of ZnO.

ZnO Property	Scale
Lattice Parameter *'a'*	3.249 Å (at 300 K)
Lattice Parameter *'c'*	5.206 Å (at 300 K)
c/a	1.602 (<Ideal hcp)
Density	5.606 g cm^{-3}
Bond length	1.93 Å
Melting point	1975 ^{0}C
Thermal conductivity	0.6-1 W. cm^{-1} K^{-1}
Refractive index (Wurtzite)	2.008, 2.029
Energy gap	3.4 eV (direct)
Exciton binding energy	60 meV
Ionicity	0.616
Heat capacity (C*p*)	40.3 J. Mol^{-1} K^{-1}
Young's Modulus E (Bulk ZnO)	111.2±4.7 GPa
Bulk Hardness	5.0±0.1 GPa

Lattice parameters of semiconductor generally rely upon the factors including free-electron concentration, concentration of foreign atoms, defects as well as ionic radii difference with respect to each other matrix ion, and temperature, residual strains (induced by substrate). For wurtzite phase in ZnO, lattice constants are determined by experimental and theoretical analysis, typically varying from 3.247 to 3.250 Å for *a*-parameter and 5.204 to 5.207 Å for the *c*-parameter.

The '*c/a'* ratio and *u* parameter vary from 1.593 to 1.6035 (less than ideal) and from 0.383 to 0.3856, respectively. As indicated by Pauling scale, the ionic bond radii of Zn^{2+}, 0.074 nm and O^{2-}, 0.140 nm, individually [35]. The deviation from perfect wurtzite crystal is due to lattice stability and ionicity.

1.3.2 Thermal expansion coefficients

Thermal-expansion coefficients such as '$\Delta a/a$', and '$\Delta c/c$' are generally describing lattice deformations under the influence of temperature. Also, lattice deformations depend on stoichiometry, defects, and free carrier concentration. The dependence of lattice constants *a*, and *c* on temperature, and thermal-expansion coefficients of hexagonal ZnO determined by the capacitive method observed, α values at 300 K, $\alpha_c = 2.49 \times 10^{-6}\ K^{-1}$ and $\alpha_a = 4.31 \times 10^{-6}\ K^{-1}$ along *c*-axis and perpendicular to *c*-axis respectively [35]. Decrease in temperature reduces thermal expansion coefficients also, negative thermal coefficient from 20 K to 120 K typically found in tetrahedrally coordinated semiconductors.

1.3.3 Defects and Dislocations in ZnO

Native or intrinsic defects involve merely the constituent elements imperfections including vacancies (missing Zn^{2+}, or O^{2-} from lattice positions), interstitials (extra Zn^{2+}, or O^{2-} occupying position in the lattice) and antisites (Zn^{2+} lodging O^{2-} an lattice position or vice versa). Zinc oxide affected by point defect show variations in optical and electrical properties. Electronic states correspond to defects created in the band gap influences optical emission properties, minority carrier lifetime and luminescence efficiency. The concentrations of defects involved in the diffusion mechanisms which is associated with growth, processing as well as device failure. As grown ZnO observed to be *n*-type. In thermodynamic equilibrium, the defect–defect interactions are neglected, then the formation energies with electronic structure of intrinsic point defects in ZnO can be computed by first-principles [29]. A low formation energy suggests excessive equilibrium concentration of the defect and high formation energy found that defects unlikely to form. It has been demonstrated theoretically, zinc interstitial pursue high formation energies in *n*-type as compared to oxygen vacancy. There are two likely interstitial positions in the wurtzite ZnO i.e. tetrahedrally coordinated or octahedrally coordinated. Depending on partial pressure of Zn, common defects in ZnO likely to be oxygen and zinc vacancies. Specifically, oxygen vacancies having lower formation energy as compare to zinc interstitials.

Dislocation in ZnO led to relax strains produced by lattice misfit called as a misfit dislocation along with the film thickness, when misfit dislocations nucleated called the critical thickness. The strained, pseudomorphic thin film with and without the misfit dislocations to relaxed film shown in Fig. 1.6. Furthermore, apart from misfit dislocations, threading dislocation (TD) is also found in the thin films and they spread like thread into the film. The type of TD may be a perfect dislocation or a partial dislocation. Likewise, TDs may be edge, screw, or mixed dislocation relying on the Burgers vector and direction of dislocations. The misfit dislocation is normally the edge or the mixed dislocation. Here, it ought to be noticed that misfit dislocations exist at the interface while, the TDs are within the film as illustrated in Fig. 1.6. High density of TD in epitaxial ZnO thin films were observed using transmission electron microscopy on (0001) sapphire substrate and reduction of TD density is possible to use less mis-matched substrate [42,43]. However, misfit dislocation core structure in ZnO is found to be locally disrupting the interface to reduce the strain [44]. There are three sorts of perfect dislocations and three sorts of partial dislocations in the wurtzite structure. Depending upon the '*c/a*' ratio, ideally $(8/3)^{1/2}$, the relative energy of the dislocations is proportional to $|b|^2$ where b is called as Burger vector of dislocation while *a,* and *c* are the lattice parameters of hexagonal close packed (hcp) lattice.

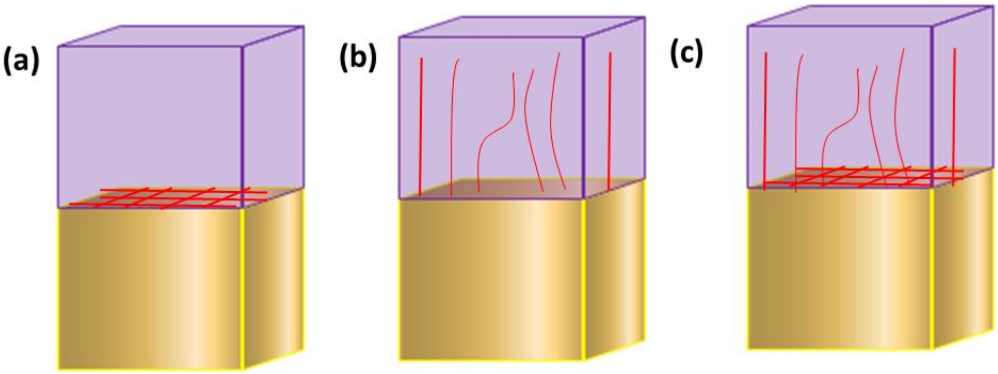

Figure 1.6. (a) misfit dislocations (b) threading dislocations (c) misfit and threading dislocations.

One out of three partial dislocations is Shockley partial, while remaining two are Frank partials. It is noted that types of dislocations is decided by the Burger vector and direction of the dislocation line [45]. The slip system in wurtzite structure ZnO and its deformation observed basal slip is significantly active as compared to prismatic slip at room temperature. Also, it is having light illumination dependence and less activity in the basal slip compared to prismatic slip under illumination of light indicates dislocation motion influenced by the thermally activated Peierls potentials [46]. The perfect dislocations in hcp unit cell with feasible Burger vectors and line direction is shown in the Fig. 1.7. Assuming, line direction in [0001], furthermore dislocations either edge, a screw, or a mixed type dislocations are decided by their Burgers vector. Peierls potential for screw dislocation is considerably lower compared to edge dislocation. Screw dislocations coupled with cross slip favors to follow a zigzag path on atomic scale in the directions of low Peierls potential, Peierls stress for edge dislocation is probable on high index planes and theoretically proportional to $\exp(2\pi a/b)$, where a, b are lattice spacing of the slip plane and strength of Burgers vector, respectively [47].

The basal slip in ZnO has larger critical resolved shear stress at elevated temperature compared to prismatic slip under the illumination of light. This ratio (3 at 250^0 C) increases with increasing temperature. However, numerous non-radiative defects are observed beneath indentation irrespective of crystal orientations. Different crystal planes, *a*-plane or *m*-plane triggers slip event along (0001) basal planes during nanoindentation in ZnO material, forming tensile strain along the basal planes as well as bands for defects. Furthermore, *c*-plane crystal induce tensile strain indented regions spreading away from indentation along the six-fold *a*-directions [48].

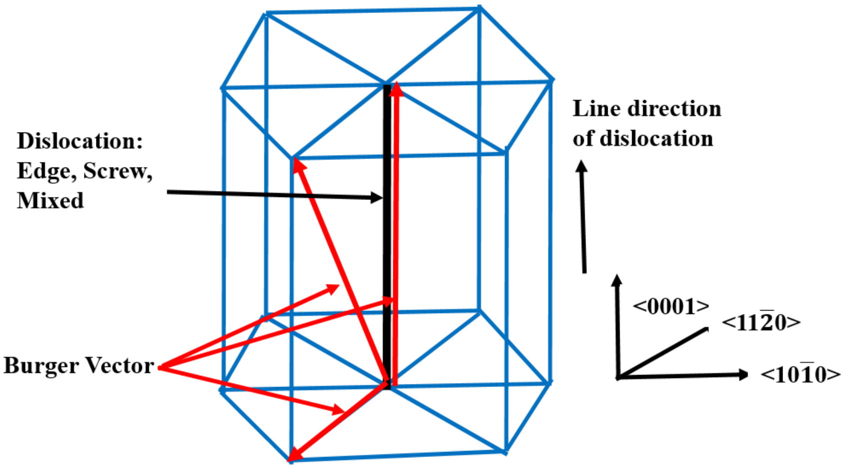

Figure 1.7. Schematic of the perfect dislocations in an hcp unit cell [45].

1.3.4 Doping in ZnO

ZnO is a crucial material for multi-functional properties e.g. semiconducting as well as piezoelectric properties. However, key properties of ZnO for many applications can be enhanced by doping a suitable impurity in specific concentration to manipulating electrical and optical properties. The intrinsic conductivity found to be *n*-type and the ZnO crystals grown in oxygen deficient partial pressure atmosphere significantly enhance the n-type character. ZnO based dilute magnetic semiconductor for the ferromagnetism and large magnetization could be achieved by dopant of transition metals (e.g. Co and Mn). However, dopants from rare earth metals greatly influence the microstructure as well as defects concentrations used as luminescent centers and their emission properties can be manipulated toward selected wavelength. Several applications with multi-color emission are used in light emitting devices.

Among donor impurities, it is pertinent to explore influence of impurities as shallow donors and are frequently seen in as-developed ZnO crystals. For controlling *n*-type conductivity, it is additionally applicable to explore impurities that act as shallow donors and can be utilized to influence *n*-type ZnO in a stable manner. The interstitial and substitutional forms of hydrogen with low formation energies appeared that insertion in significant concentrations. Hydrogen is clearly not only possible donor in ZnO and can be unintentionally incorporated giving rise to *n*-type conductivity [49]. Several elements from Group-III, Al, Ga, In as the substitutional elements for Zn as well as Group-VII, Cl and I elements as the substitutional elements for O can be used for *n*-type conductivity.

Acceptor impurities for Group-I, elements (Li, Na and K) and Group-V, elements (e.g. N, P, and As) are known for ZnO. Using the first principal approach, for interstitial and substitutional Li, Na, and K in ZnO, the ionization energies of 0.09 eV, 0.17 eV and 0.32 eV for substitutional Li, Na and K, respectively are reported in the literature [50]. However, many elements from these Group-I do not contribute considerably to *p*-type conductivity. It has been reported that most potential dopants are the Group-V elements for *p*-type conductivity. These dopants bolstered *p*-type doping efficiency of column-IA elements is limited by the formation of compensating interstitials [51].

1.3.4.1 Rare earth ions doping

Rare earth ions emphasize on the innovation in current optical technology and as an active constituent of ZnO crystal structure after doping. Also new crystal slip activity may be induced after doping [52]. Different rare earth ions provide attractive properties in energy-efficient luminescent materials (e.g. phosphors for fluorescent lamps), electrical varistors, plasma displays and cathode ray tubes (CRT's)[53]. Rare earth elements are difficult to extract in pure form for commercially viable concentrations. The lanthanides, incompletely filled 4*f* shell are generally trivalent state have a stable emission. In the 4*f* elements, characterised by an exceptional structure with partially filled 4*f* shell shielded from 5*s* and 5*p* electrons.

When rare earth (RE = Ce, La, Pr, Er and Yb) is incorporated in crystalline/amorphous ZnO hosts, provide excellent photocatalysis properties [54]. Typically, same rare earths ion can exist in different oxidation states. However, 3^+ or 2^+ is the most common. The 3^+ ions show intense narrow band intra 4*f* luminescence in many hosts and due to shielding by the 5*s* and 5*p* electrons means that rare earth irradiative transitions in solid hosts resembling those of the free ions and electrons phonon as weak coupling. There are several rare earth ions e.g. Gd doped ZnO exhibit magnetic properties useful in the spintronics applications. Also, Ce doped ZnO, Dy doped ZnO and Ho doped ZnO used for their excellent optical properties and photocatalytic activity [53].

The studies found green luminescence and red luminescence emerged from Tb doped ZnO and Eu-doped ZnO respectively, suggesting these materials proven their tunablity useful in optoelectronic applications [53]. The partially occupied 4*f* shell generate band emission throughout the visible and infra-red spectra and can be utilized for various applications e.g. such as lasers, phosphors and solid state optoelectronic devices. Likewise, doping on Rare earth metals in ZnO manipulate the bandgap of semiconductors used for UV display applications, visible, and infrared light emission. Wide band gap exhibits less thermal quenching of emissions than narrow gap semiconductors.

Yttrium doped ZnO contains excellent properties, and proven its ability as sensor coating materials, optical materials and band gap narrowing [55]. Also incorporation of Y in ZnO generates gigantic piezoelectric response can be utilized as piezoelectric nanogenerators [56]. There are several methods of doping Y in ZnO including sol-gel [57], spin coatings etc. [58]. In addition, doping of Yttrium in ZnO thin films (ZnO:Y) can be performed using sputtering deposition resulted in highly preferred *c*-axis oriented (002) diffraction peaks [59]**.** The mechanical properties of Y doped ZnO nanoparticles are studied by instrumented indentation technique and reported the maximum hardness of 0.61 GPa and Young’s Modulus of ~ 15 GPa [60].

A small concentration of Praseodymium in the ZnO improve the photoelectric and luminescent properties [61]. Several deposition techniques and post deposition method were developed to incorporate Prasedymium (Pr) in ZnO (ZnO:Pr) e.g. hot dipping [62], sol-gel [63], and sputtering [61]. Among all, the incorporation of Prasedymium (Pr) in ZnO deposited using the sputtering method results in highly c-axis-oriented thin films**.**

1.3.5 Mechanical properties of ZnO

The mechanical properties include hardness, Young’s modulus, stiffness, and yield strength of the material. When the external forces are applied on solid, distortion is accompanied by the strain. The inherent mechanical strength of materials opposes deformation and tends to restore solid to its un-deformed initial state as depicted by the physical amount stress. Many attempts have been made for better understanding the mechanical behavior and providing actual synthesis conditions as well as microstructure to improve the enhanced strength. Nanoindentation testing emerged as tool to investigate the mechanical properties i.e. indentation hardness and Young’s modulus at micro and nano scale. The consequence of size effect should be considered which is more at shallow indentation depths. Nanoindentation made possible to explore mechanical behavior of coatings without detaching them from substrates in form of load-displacement curve [64].

Hardness estimations are typically done on the (0001) surface of the ZnO crystal utilizing the conventional pyramidal, spherical, or on the other hand, with a sharp triangular indenter. The depth-sensing indentation estimates entire information on the hardness and induced phase transformation of materials. Theoretical approximations performed are in agreement with experimental outcomes for bulk material properties. The crystalline properties of ZnO and elastic constants, both theory and experiments seem efficient of investigations to fit for delivering information that are very reliable for wurtzite phase ZnO. The deformation mechanism of single crystals bulk ZnO was estimated by spherical nanoindentation and atomic force microscopy [65]. ZnO has shown plastic deformation at quite low loads (> 4–13 mN), hardness and Young’s modulus were determined by evaluating loading–unloading data. Hardness of bulk ZnO is found to be 5.0±0.1 GPa at penetration depth of 300 nm and Young’s modulus remained constant over the indenter penetration depth E=111.2±4.7 GPa [35].

Earlier indentation reports on nanostructured polycrystalline ZnO have described a broad range of H ~(1.5-12 GPa) and E ~(40 -120 GPa) [65]. The soft nature with lower hardness for

ZnO is expected due to a low melting point (1975 ^{0}C) and larger ionicity (0.616) compared to GaN (2500 ^{0}C and 0.500, respectively) [65].

1.3.5.1 Mechanical properties of *a*-plane ZnO and *m*-plane ZnO

The indentations were performed on *a*-plane ZnO, *m*-plane ZnO crystals and then illuminated with light to observe the defects response after indentations. It was observed an enormous nonradiative defects created at the indentation site in *a*-plane ZnO. However, preferential slip along the basal planes with the absence of easy-glide mechanisms along ±*c* directions can take place and defects act as non-radiative centers. Also, component of stress normal to basal planes (±*c*-direction) cannot be relieved through slip, subsequently develop a compressive strain in ±*c*-directions along with a tensile strain in ±*m*-directions [48].

Similarly, in the *m*-plane ZnO indentation produces high density of nonradiative defects and spread along the basal planes to the *a*-plane ZnO. Also, compressive strain was observed in the ±*c* directions to the indentation site and tensile strain in the ±*a*-directions. The *m*-plane and *a*-plane ZnO indentation similarly behaves under nanoindentation, with the only difference, that basal plane slip will be along different directions for the *a*- and *m*-plane indentations [48].

1.3.5.2 Mechanical properties of *c*-plane ZnO

Indentation on *c*-plane ZnO behaves in a different manner as *a*-plane and *m*-plane ZnO, containing six-fold instead of two-fold symmetry. The preferential slip along pyramidal plane at the indentation site generating non-radiative defects [66,67]. Moreover, there is no such compressive stress was observed, which is significantly different to *a*-plane and *m*-plane ZnO. The compressive stress compensated by tensile stress developed as a result of dislocations loops introduced by the indenter tip. Tensile-strained lines spreading along the six-fold *a*-directions.

In fact, in *a*-plane ZnO, indenter displacement is relatively eased by slip in three a-directions, so yielding deeper penetration depths in this crystal orientation at specified applied load. However, *m*-plane ZnO revealed lower shear stresses prominent to lower depths in comparison to *a*-plane. In *c*-plane ZnO, indentation usually permits lateral displacement along easy-glide plane and involve secondary slip planes to get same penetration depth as compared to *a*-plane and *m*-plane, thus requiring higher loads [48,52].

For *a*-axis epi-layers and *c*-axis epi-layers on sapphire substrate, yields a hardness of 6.6±1.2 GPa, and 5.75±0.8 GPa, respectively. Threading dislocations, as-grown defects significantly inhibited the slip movement and epilayer found to be harder than bulk ZnO [68]**.** Furthermore, a discontinuity ('pop-in') emerged simultaneously in both bulk as well as epitaxial ZnO thin films, and the most probable indentation displacement to occur 'pop-in' for bulk is 12-20 nm while for thin films between 13-16 nm respectively due to sudden propagation of dislocations [64]**.**

The physical mechanism related with 'pop-in' events in epitaxial films owing to nucleation, propagation and interaction of glissile threading dislocations subjected to mechanical deformation. Also, critical depth during Indentation observed to be 4 nm (i.e. residual impression) at which plastic deformation begins [69]**.** The induced deformation by Berkovich nanoindentation in single-crystal ZnO associated with the clear features of multiple 'pop-ins' in the load–displacement curves, arbitrarily in the loading segment. Also, extended defects/dislocations as a result of deformation appears to be locally distributed at the indentation site [70]**.** Induced multiple 'pop-in' phenomena observed in *c*-plane single-crystal ZnO originated from sudden nucleation, propagation of dislocations through the slip systems along predominately pyramidal plane suggested by cross-sectional transmission electron microscopy [71].

Different thickness of ZnO films deposited on flexible polymer substrates i.e. polyethylene naphthalate (PEN) and polyethylene terephthalate (PET) were subjected to mechanical characterization. During compression, cracking of ZnO thin films observed, depending upon relative thickness and ZnO film at lower thickness on PEN exhibit highest crack onset strains [72]. ZnO thin films deposited on *a*-sapphire, *c*-sapphire and (0001) 6H-SiC substrates and correlated with ratio (*H/E*), indicates elastic to plastic deformation in nanoindentation and observed better mechanical properties at ZnO thin films at *a*- sapphire with high hardness [73].

The elastic modulus, onset of yielding, hardness and shear strength of as-grown ZnO wafer quantified by nanoindentation are 140, 12, 7.1 and 3.6 GPa, respectively along the primary slip with pyramidal plane. Also, thermal annealing effectively reduces the defect concentrations but residual stresses remains unchanged [74]**.** Furthermore, the mechanical properties of polar and non-polar ZnO wafers examined by nanoindentation and analyzed its hardness, elastic modulus and yield strength of *c*-plane, *a*-plane and *m*-plane are; 7.1, 3.9, and 4.0; 140, 159, and 161; 12.0, 6.7, and 4.5 GPa, respectively [75]**.**

1.3.5.3 Effect of different dopants on mechanical properties of ZnO thin films

A variation in mechanical properties observed after doping impurities in to ZnO host matrix as mentioned in the Table 1.2. Different dopants interact with the host matrix and changes the microstructural features depending upon the amount introduced and their oxidation state in the deposition procedures.

Table 1.2. Mechanical properties after doping in ZnO.

S. No.	Thin Film	Hardness (GPa)	Elastic Modulus (GPa)	Ref.
1.	Mn-doped ZnO	14–18	122–167	[76]
2.	B-doped ZnO	9.3-12.1	103.5-114.4	[77]
3	Ga-doped ZnO	8.5-7.4	101.3-138.4	[78]
4	Al-Doped ZnO	4.7-7.0	87.9-92.5	[79]
5	V-doped ZnO	3.3	58.7	[80]
6.	Co-Doped ZnO	3.9-4.5	--------	[81]
7.	C-doped ZnO	8	140	[82]
8	Mo-Doped ZnO	9-14	110-130	[83]

1.3.6 Tribological Properties of ZnO Thin Films

Nano-scratch under ramp up loading in which a progressively increasing normal load is applied at constant loading rate is gaining popularity to find the critical load for the coatings failure [84]. The failure of the thin films is a complex phenomenon; however this technique is an appropriate way by which we can access to find the adhesion of coatings [84]. A ramp up load in scratch testing can provide the adhesive strength of the coatings. The tribological properties of annealed ZnO thin films grown on glass and silicon substrates exhibited better wear resistance, which is further improved by annealing process. Also, the enhanced wear resistance is attributed to the higher hardness and modulus with annealing temperature [85].

Lower surface roughness with higher hardness observed in ZnO thin films on *a*-sapphire provide better lubricating surface properties with reduced friction coefficient as compared to the films with higher surface roughness [73]. The pile-up of ZnO thin-film on silicon substrates using nanoscratch technique were observed indicating as plastic deformation and wear volume decreased with increasing annealing temperature. However, bulging out amongst the groove and film attributed to the adhesion discontinuities and/or cohesion failure of the ZnO films [86]**.** The failure mechanisms was explored using scratch test and to identify critical normal loads of ZnO thin films, which is found to be higher 30 mN for ZnO films on polymer PET substrate [87]. Also, in the scratch testing, major scratch failure mechanisms related with the resistance of ZnO which is influenced by thickness for both PET and PEN substrate. Also, a high scratch loads applied induces secondary failure mechanism related with impregnation of film debris into the polymer substrates [72]**.**

Scratches and constant abrasive wear of ZnO and ZnO: Al have shown better adhesion of films to the substrates. The friction coefficient of pure ZnO film was found to be 0.1 value, higher than ZnO:Al thin films, 0.08 value [88]**.** Al-doped ZnO/glass substrate grown in different microstructures as the sputtering deposition conditions is observed with improved adhesion energy from 0.49 to 0.79 J/m^2 and 0.49 to 0.86 J/m^2, respectively, depending upon substrate temperature variations (room temperature-200^{0}C) and higher sputtering power (50W-200W) respectively [89]. Furthermore, Al-doped ZnO was prepared on quartz substrate and silicon with substrate temperature variations. Films exhibited maximum adhesion of 32 mN at maximum substrate temperature (400 ^{0}C) [90]. Al-doped ZnO/glass substrates films with different thicknesses deposited by sputtering and indented in water to study water effect on adhesion and fracture toughness. Experimental studies have shown that when the films are exposed to the water, the adhesion energy is reduced and limited crack velocity due to water diffuse in to the films [91]**.**

1.4 FINITE ELEMENT MODELING

Finite element (FE) analysis is used to investigate the mechanical properties by solving complex analytical equations. Likewise, FE analysis provide solutions of nanoindentation measurements with sufficient accuracy. The pioneering work of simulations were performed by Bhattacharya and Nix, utilized a conical indentations to generate load-displacement curves [92]. Different measurements using FE analysis were performed to generate load displacement curves and compared with the experimental load-displacement curves. The elastic-plastic deformations in nanoindentation are highly complex, so simulation becomes major tool to study deformation mechanism. Different analytical formulas are developed to simulate different nanoindentation behaviour in metals, composites and polymer. The elastic and plastic deformations can be analyzed using linear power law or Ramberg-Osgood law [93].

The materials properties including different elastic modulus, strain hardening exponents, yield strength and friction coefficients effects can be analyzed on indentation simulations. The crystal plasticity model is developed to see the effect of tip along with materials pile-up and sink-in behaviour around the indenter [94]. In addition, FE analysis is widely accepted for failure analysis of coated solids. FE analysis is performed to analyze elastic deformation and stress field for a few typical combinations of ceramic coatings and metallic substrates [95] as well as mixed-mode fracture mechanics to examine onset of cracks in hard coating/soft substrate as a function of material parameters [96]. Coatings deposited on the base material steel indented by a spherical indenter for a fixed ratio of indenter radius to coating thickness analyzed the influence of friction coefficient, substrate yield strength and strain hardening on the surface plastic strain.

The FE analysis was performed using software ABAQUS^{TM} [97]. FE analysis can be utilized for linear analysis to complex nonlinear simulations. ABAQUS is used in two different analysis modules i.e. Standard, and Explicit, each module can solve range of problems of linear and nonlinear problems with accuracy and reliability. ABAQUS-Explicit is preferable for transient and dynamic finite element formulation. However, nano-indentation is considered as quasi-static problem without considering time effect on procedure. Hence, ABAQUS-Standard module is used for present work.

ABAQUS solved problems in three different steps: pre-processing, simulation and post processing. Non-linearity observed in indentation is predominately because of material nonlinearity and geometric nonlinearity. Stress-strain abide by Hooke’s law at lower values of strain but at high strain, material yields and afterwards stress-strain relationship becomes nonlinear and irreversible described as material non-linearity. In indentation, a large deformation is observed under the indenter. However, geometric nonlinearity depends upon magnitude of displacement, which affects the response of the structure. ABAQUS provides final solution for nonlinear problem using Newton-Raphson method. Indentation loads are applied incrementally until the solution reaches to final. FE analysis of bulk materials such as pure titanium, pure copper, and pure iron are made using ABAQUS. It was observed that the results depend greatly on different mesh size, indenter tip radius and the hardening law used [98]. So, before performing simulations mesh convergence study ensures reliable results.

1.4.1 Power law work hardening

The elastic deformation perceived in all materials when the applied pressure or force is low. Materials having isotropic linear elastic properties, obtained deformation directly proportional to applied load and a uniaxial tension state in terms of stress-strain can be expressed as follows in Eq. (1.2);

$$\sigma = \varepsilon E \tag{1.2}$$

where σ is the uni-axial stress, ε is the uni-axial strain, and E is the elastic modulus, the proportional coefficient also known as Young's modulus. Once the external force is applied on the material, it gets deformed and beyond its elastic limit, material will experience plastic deformation. A power law work hardening model is widely accepted by large number of engineering materials (e.g. metals and alloys), is a material constitutive relation and uniaxial stress-strain (σ-ε) curve of a stress free material can be expressed as follows in Eq. (1.3) [99];

$$\sigma = \begin{cases} E\varepsilon, & \varepsilon \le \dfrac{\sigma_y}{E} \\ K\varepsilon^n & \varepsilon \ge \dfrac{\sigma_y}{E} \end{cases} \tag{1.3}$$

where σ_y is the yield stress, E is the Young's modulus, and n is the work hardening exponent in Eq. (1.3) and Eq. (1.4)

$$K = \sigma_y \left(\frac{E}{\sigma_y} \right)^n \tag{1.4}$$

If, n is zero, Eq. (1.3) is used for elastic-perfectly plastic deformation in material. For completely describing elastic-plastic properties, power-law along with material's independent parameters, such as elastic modulus E, yield stress σ_y, work-hardening exponent n, and Poisson's ratio υ, are required. One of the objectives of this present work, is to correlate above mentioned parameters i.e. $(E, \sigma_y, n, \upsilon)$ with indentation responses. As, the indentation procedure induces very complex stress and strain field beneath the indenter, FE analysis are beneficial in managing upcoming experiments. A true stress-strain curve is obtained using the plastic properties of a material, assuming power law hardening material model in ABAQUS [99]. Using Eq. (1.5), the plastic strain ε_p is estimated as follows;

$$\varepsilon_p = \varepsilon - \frac{\sigma_y}{E} \tag{1.5}$$

1.4.2 Simulation of Indentation Deformation

In the indentation, usually three or two-dimensional model is used (refer Fig. 1.8), and assuming indenter is stiffer than coating-substrate, so the indenter modeled as a perfectly rigid material. FE analysis need not to calculate stiffness or stresses exhibited in rigid body. So it is also beneficial for lower computational work, because variables are only related with rigid surface are rotations and translations on a single node, recognized as rigid body reference node. A reference point is also allocated on the indenter tip to control the indenter movement. The specimen (thin films, substrate) was treated as deformable. The mesh elements are chosen in such a way to provide reliable results. A concentrated force is applied to rigid indenter in incremental steps to converge the solution. Finally, after simulation results will be obtained

Huge works has been performed on the basis of FE analysis including linear plasticity models to the viscoelastic and creep behaviour. Nanomechanical behaviour of orthopedic PMMA-based bone cement were measured. Polymer-like bone cement and its viscoelastic nature identified using conventional indentation combining with FE analysis. A two-layer viscoplasticity model was developed to optimized the behaviour of polymer compared to experimental outcomes [100].

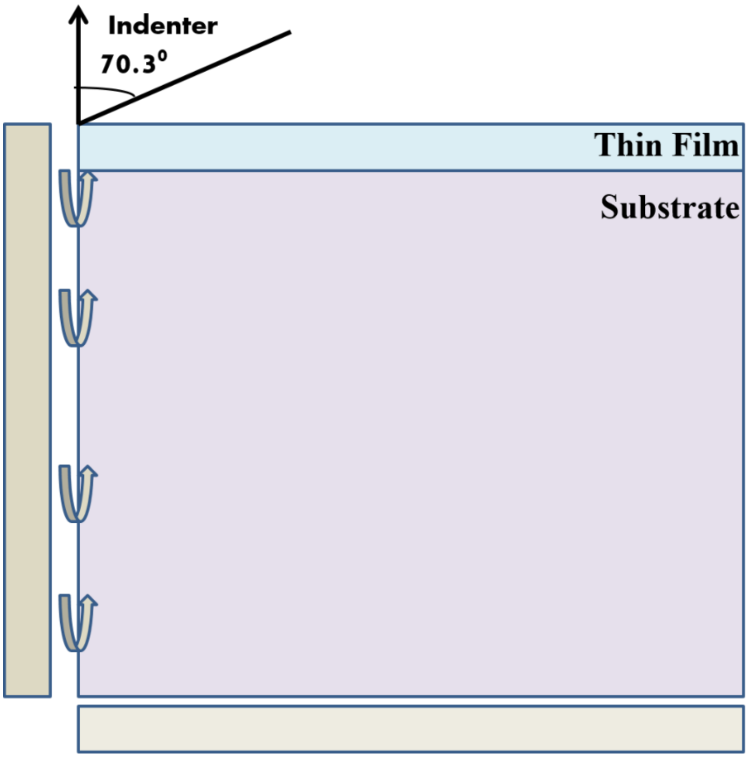

Figure 1.8. Schematic for two dimensional model for indentation.

A two-dimensional axis-symmetric FE model is used to analyze the effect of elastic modulus, yield strength and strain hardening on thin films of variable thickness. This study found greater effect of yield strength and strain hardening of film have on load displacement curve as compare to elastic modulus [101]**.** Thin films of tungsten and aluminum on different substrate e.g. aluminum, silicon, sapphire and glass substrates used to perceive the effects of different substrates. This study probed that mechanical properties were strongly affected when a hard film deposited on relatively soft substrate. In addition, large mismatch in the substrate moduli and film moduli suggested to use King's analysis for estimation of film modulus [102]**.**

Spherical Indenter also used to examine the plastic properties as well as the failure analysis of the coatings and an analytical approach has been developed for determining the critical load and critical displacement. Furthermore, fracture stress is highly depend upon the indenter tip radius as well as film thickness [103]. In an another study, FE analysis of super hard coatings on relatively soft substrates was performed. Substrate effect observed to be more severe and therefore suggested that indentation experiment should be performed within 5% of coating thickness rather than 10% [104]**.**

Nanoindentation of ZnO nano-dimensional films with different thicknesses i.e. 2.1 to 6.3 nm were investigated both molecular mechanics simulations and continuum analyses. A significant size effect on the indentation modulus were observed by molecular mechanics simulations, but such size effect was absents in the continuum studies [105]. The nanoindentation procedure to detect the elastic parameters of isotropic thin films by combining FE analysis and nanoindentation test was performed in the forward analysis. Numerical outcomes provide indentation responses at the adequate ratio of penetration depth to film thickness. As in same study, FE analysis using reverse analysis approach of experimental indentation curves fitted as the power function. The maximum indentation load and the loading curve exponent can be obtained from the experimental indentation curves provide the similar results [106].

FE analysis performed to examine stress distribution in different coating system i.e. single layer and multi-layered while keeping the overall thickness is same. The study observed a comparison with reduced stress distribution and stress intensity in multilayered structure. The quantitive reduction around 50% in tensile stress observed at interface in multi layered structure [107]**.** DLC coating for modulus graded multilayer structure i.e. 1, 3 and 5 layers used for artificial joints was analyzed. For multilayers coatings gradient in modulus is applied using two dimensional axi symmetric model with spherical indenter. Stress distribution was mapped and lowering of stress concentration observed in the multilayer coatings. The quantitive tensile stress in graded multilayer structure reduced by 32% (for 3 layers) and 40% (5 layers). In addition, maximum shear stress reduced 18% (for 3 layers) and 20% (for 5 layers). The overall reduction in the tensile stress or shear stress improve crack resistance and avoid the risk of delamination [108]**.**

1.5 SCOPE AND OBJECTIVES

In the semiconductor industry, there is an ever increasing demand for miniaturization along with multifunctional properties. Furthermore, several synthesis methods have been developed to achieve materials in nano dimension i.e. miniaturized state. Thin films are utmost significant class of the nanomaterials due to its facile synthesis, controlled microstructure as well as high repeatability. In addition, the properties of thin films are influenced by the underlying substrate material. ZnO is a renowned material for its plenty of applications including piezoelectric, solar and sensing applications. Novel properties of ZnO originated from its crystal structure, chemical stability, phase stability, defects and doping. Attempts have been made to miniaturized ZnO thin films also imposes risk of mechanical failure during the synthesis of material or during handling. So, the mechanical stability of ZnO thin films are essential. Nanoindentation and nanoscratch are precise techniques to provide the mechanical as well tribological properties of ZnO thin films and to develop fundamental understanding of thin film mechanics. The extent of induced damage and failure subjected to the surface properties of material, and physical and chemical interaction among its constituents and substrate. The reported literature on the mechanical and tribological properties of pure ZnO and after doping with rare earth is scarce. Also, through Finite element analysis of indentation properties and its validation against the experiments are essential to understand the deformation behaviour of ZnO thin films. The present thesis is focused on investigating mechanical properties as a response of nano-indentation and nano-scratch tests as well as simulation analysis using FE-Models.

1.5.1 Objectives

In the light of above mentioned literature review, the objectives of research work are as follows;

- Synthesis of nanostructured ZnO thin films on fused quartz and glass substrate, with doping of rare earth (RE) elements i.e. praseodymium and yttrium in ZnO and pure ZnO thin films using the sputtering deposition technique.

- The effect of different sputtering deposition conditions i.e. variations in substrate temperature, and sputtering pressure on microstructural, and topological properties of ZnO thin films with and without RE dopants.
- Identification of different crystal phases, crystallite sizes through X-Ray diffraction and different dopant concentration by X-Ray photoelectron spectroscopy and Energy Dispersive X Ray mapping.
- Investigation of nanomechanical properties and deformation mechanism of ZnO thin films with and without RE dopants by Nanoindentation, tribological study of films by Nanoscratch technique.
- Finite element analysis is used to simulate the experimental properties obtained from nanoindentation and generate the load indentation curve.

1.5.2 Organization of the Thesis

- Chapter 1: Introduction and literature review

This chapter established the theoretical backgrounds of ZnO thin films properties as well as summarizes the previous work. The FE analysis is also discussed with its applications.

- Chapter 2: Synthesis and characterization techniques

This chapter emphasizes on the synthesis using the sputtering technique as well as different characterization techniques used to study the behaviour of ZnO thin films.

- Chapter 3: Nanomechanical and nanoscratch properties of ZnO thin films

In this chapter, structural, morphological and mechanical properties of pure ZnO thin films on fused quartz and glass substrate grown at different sputtering conditions are discussed.

- Chapter 4: Nanomechanical and nanoscratch properties of doped ZnO thin films

In this chapter, structural, morphological, mechanical and doping profile were studied for yttrium, and praseodymium doping in ZnO host matrix.

- Chapter 5: Finite element analysis of nanoindentation on ZnO thin films

In this chapter, a finite element model for indentation is developed and simulated based on the experimental results to obtain a simulated load displacement curve and to validate the experimental outcomes.

- Chapter 6: Conclusion

In this chapter, the overall conclusion of the present work and scope for future work has been provided.

Chapter 2

SYNTHESIS AND CHARACTERIZATION TECHNIQUES

In this chapter, fabrication and characterization techniques used for investigating pure ZnO and doped ZnO thin films are discussed. Direct Current (DC) sputtering system has been used for deposition of thin films in the present work. Several characterization techniques such as XRD, XPS, FESEM, AFM, Nanoindentation and Nanoscratch were used to study the micro-structural, nano-mechanical and tribological properties of ZnO thin films, with and without addition of dopants discussed in subsequent sections.

Contents

2.1 DEPOSITION OF THIN FILMS

Generally, thin films comprise of material layers homogeneously spread on a substrate, with crystalline phase, or composite structure. The preparation of suitable substrate on which films are deposited is critical, as it affects the overall properties, crystal structure, adhesion/cohesion, interface, defect and dislocation in thin films. Atomic deposition process of a specific material decides microstructure; property of a thin film and depends on following factors.

- Substrate surface conditions e.g. microstructure, roughness and modification by pre-depositions treatments.
- Deposition process parameters and ambient gas.
- Film growth mechanics on substrate surface and interface development.
- Post-deposition process and treatments.

Thin film deposition emerged as stepwise process of atomistic growth, particulate settlement, coating and surface formation. However, in the atomistic process, atoms collectively form a layer of material by condensing and further diffusion to suitable nucleation and growth sites [109]. Ad-atoms occupy lowest energy configurations although may contain micro-structural imperfections (e.g. dangling bonds, voids formation, defects, lattice mismatch, etc.). The depositing atoms interact with the substrate material to form an interfacial region. Moreover, kinetic energy of incident adatoms decides morphology relying upon deposition technique (Sputtering, Thermal Evaporation, PLD, CVD etc.). Ad-atoms having low kinetic energy make the depositing species relatively immobile and especially mobility of ad-atoms increases with increasing kinetic energy. Surface manipulations/modifications involves ion treatment, thermal, mechanical, or chemical treatments, which can change the surface composition properties [110]. Typically, different deposition processes e.g. physical process and chemical process used for the deposition of nanocrystalline thin films [111]. Different physical vapor deposition (PVD) techniques are thermal evaporation, electron beam evaporation, magnetron sputtering, molecular beam epitaxy (MBE), pulsed laser deposition (PLD), and chemical vapor deposition (CVD) processes like metal-organic chemical vapor deposition (MOCVD), sol-gel and involve following main steps [7].

- First step consists of generations of suitable atomic, molecular or ionic species using the target material.

- In this step, a mechanism is established for transport of these species onto the substrate.
- The final step, involved material layer formation after condensing of incident species on the substrate.

Various CVD and PVD processes have its own unique features. The decision to adopt specific technique depends on the attributes or properties required for application. If the essential prerequisite is to deposit uniform thin films with a moderate size distribution, PVD such as evaporation, magnetron sputtering and laser ablation are extremely proficient. The selection of a deposition process is to obtain homogeneous, defect free thin films based on: lateral uniformity of the films on substrate throughout the exposed area, low stress, high adhesion to the substrates, controlled micro-structure, and roughness distribution to exhibit unique physical and chemical properties. In PVD, generally deposition of thin films carried out from the same material referred as target material, and gas present during deposition influences the purity of thin films. The preferable deposition technique and their comparative analysis are given in Table 2.1.

2.1.1 Sputtering

Sputter deposition is broadly used for coating on tools and cutting surfaces for wear protection, automobile parts, semiconductor coatings and reflective coatings [112]. The deposition process involved irradiation of energetic ions on solid target known as sputtering. Sputter deposition is widely used technique for the erosion of surfaces to deposit the films. Bunsen and groves first observed sputtering in a gas discharge tube [113]. The sputtering process is a momentum transfer process in which momentum is transferred by bombarding energetic ions to the target atoms to eject from the target surface. The bombarding ions are usually gaseous ions (Ar^+) accelerated by an applied electric field. The sputtered species from the target surface compromise of highly energetic atoms and reached at the substrate with energy ranges from 1 to 10 eV which is comparatively higher than chemically grown and thermal evaporation. The disintegration of target during sputtering additionally utilized for several purposes like cleaning surfaces, depth profiling, micromachining, microscopic erosion etc.

Growth of thin films in sputtering relies on magnetron source, positive ions in the plasma, and magnetically improved productivity of the entire process of depositions. The target can be sputtered using either using direct current (DC) or radio frequency (RF) for conductive, non-conductive targets respectively. Among PVD, DC or RF-magnetron sputtering are extensively used in lab or industry as well [113]. Nonetheless, DC-magnetron sputtering may suffer a limitation from arching at the target surface amid deposition in oxygen/nitrogen as surrounding gases.

Table 2.1. Different depositions techniques comparison.

Process	Material	Deposition Rate	Purity	Film density	Uniform	Directional
Sputtering	Metals, Semiconductor Dielectric	Metal: 100Å/s Dielectric 10Å/s	High	Good	Excellent	Some degree
Thermal Evaporation	Materials-low melting point	1-20 Å/s	Low	Poor	Poor	Yes
E-beam Evaporation	Metals and Dielectrics	10-100Å/s	High	Poor	Poor	Yes
PE-CVD	Mainly Dielectric	10-100Å/s	Excellent	Good	Good	Some degree
LP-CVD	Mainly Dielectric	10-100Å/s	Excellent	Good	Excellent	Isotropic

Layer of oxide/nitride at edges of race track (erosion groove) can damage by local heating, melting, which degrade film quality by increasing the density of particulates or pinholes in the deposited films. Likewise, arcing can be effectively prevented in RF sputtering utilizing a capacitivly coupled electrode with alternating positive/negative potentials on the target surface. The negative voltage in the cycle performed the sputtering of target; and ions bombard the cathode while positive voltage in the cycle prevents charge build-up on the target. A standard 13.56 MHz, were used for plasma processing as suggested by Federal Communications Commission. The self-biasing of target and at negative potential, sputtering performed like a DC sputtering shown in Fig 2.1 [114]. The drawback in the RF power supplies for magnetron sputtering is being expensive having lower deposition rates as compared to DC-Sputtering. Sputtering offers several advantages as follows;

- The deposited films have high uniformity throughout the substrate as well as adaptable for large-scale production with phenomenal reproducibility of deposited films. Facile deposition of materials having high melting points with good adhesion is attractive feature of sputtering.
- Large-size targets can be used for sputtered which simplifies deposition of films with uniform thickness over larger substrates.

- The microstructure controlled by adjusting the deposition rate and other sputtering parameters e.g. deposition pressure, sputtering power, target-substrate distance and substrate temperature variations.
- The deposition of nanocomposites coatings and doping can be accomplished well rather than other deposition techniques.

2.1.1.1 Description of sputtering process

In the sputtering process as shown in Fig 2.1, sputtering chamber is evacuated up-to base pressure of ~10^{-6} Torr utilizing pumps such as rotary and turbo molecular pumps in conjugation. An inert gas, usually Argon, at the pressure few to 100 mTorr inserted into sputtering chamber as the ambient gas to initiate plasma process. When a high electric field build up amongst cathode and anode, a glow discharge emerges and maintained between these two electrodes. Initially, very insignificant amount of current flows depending on charge carrier, sooner free electrons present in the sputtering chamber strike Ar atoms to create Ar^+ along with more free electrons.

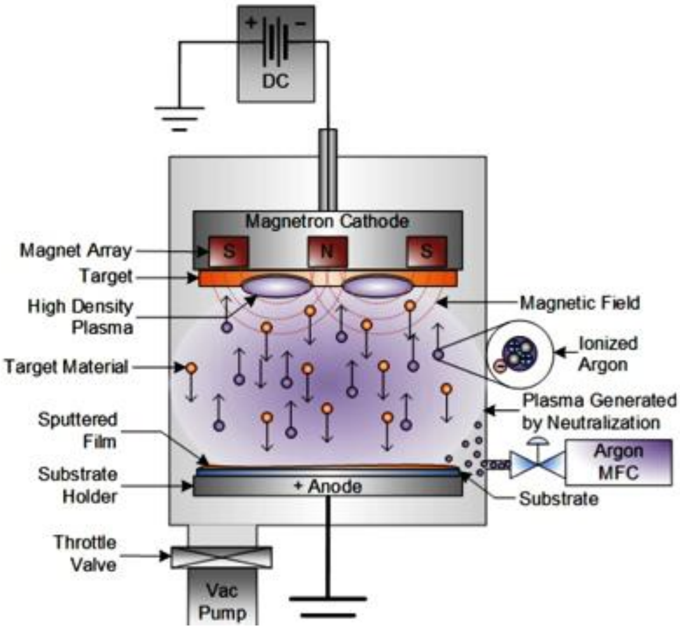

Figure 2.1. Schematic of the Sputtering Process [114].

These free electrons implement plasma process by creating more Ar^+ and accelerated towards direction of the cathode to strike the target. This bombardment on target creates several collisions events to eject neutral target (or sputter) atoms through the momentum transfer and sputtered particles coordinated to get settled on the substrate. Since sputtering was manifested by momentum transfer for breaking bonds in target materials, so Ar^+ should contain enough energy to collide. Generally, sputtered particles are ejected within 1-2 nm of the target surface.

Efficiency in sputtering deposition is estimated by the sputter yield (S) defined as the number of sputtered atoms per incident ions. Sputtering yield vary with different material and depends on the chemical bonding and energy transferred in impact. Sputter yield (S) is defined as

$$s = \frac{\text{ejected atoms}}{\text{incident ion}} \tag{2.1}$$

The sputter yield depends on the energy of the incident ions, masses of the ions and target particles, binding energy of atoms and incident angle of ions. Using Sigmund's theory [115], the sputter yield is given,

For $E < 1$ KeV

$$S = \frac{3\alpha}{4\pi^2}\frac{4M_1M_2}{(M_1+M_2)^2}\frac{E}{E_b} \tag{2.2}$$

where, E_b is the surface binding energy of the target being sputtered, E is the ion bombardment energy, α refers as efficiency in momentum transfer during collision events, and M_1 and M_2 are the masses of the positive ion of the gas and target material, respectively.

For, $E > 1$ KeV

$$S = 3.56\alpha\frac{Z_1Z_2}{Z_1^{2/3}+Z_2^{2/3}}\frac{M_1M_2}{M_1+M_2}\frac{S_n(E)}{E_b} \tag{2.3}$$

where, Z_1 and Z_2 referred as atomic numbers of incident ion and sputtered target particles respectively and $S_n(E)$ is energy loss/length due to collisions events, and it is significantly affected by masses, energy, and atomic numbers of the atoms involved [116]. However, sputtering yields <1 indicates high energy required to eject one sputter particle. When appropriate voltage is applied at electrodes after optimized deposition pressure, a gaseous breakdown leads to formation of plasma containing ions and electrons. The continuous process of energy accelerates electrons to ionizing atoms by electron atom collision [116].

It is mentioned that sputtering yields <1 at bombarding energies of ~100 eV, indicating the large amount of energy input is necessary to eject one atom [113]. Magnetic fields confine the plasma region to improve sputtering performance and achieve higher sputtering yield. Magnetic field trapped secondary electrons to move perpendicular to both electric field and magnetic field, Eq. (2.4). The ions experience like dual field environment under Lorentz forces as follows:

$$\vec{F} = q\left[\vec{E} + \left(\vec{v} \times \vec{B}\right)\right] \tag{2.4}$$

Where ‘*F*’, ‘*E*’, '*B*' is the force, electric field, and magnetic field respectively while '*q*' represents electric charge, and '*v*' instantaneous velocity of particle. This Lorentz force causes drifting of secondary electrons. Moreover, these secondary electrons are trapped nearby the target. These electrons collide with gas atoms or other electrons and lose their kinetic energy. So, dense plasma is generated near the target increases the deposition rate due to enhanced ionization of sputtering gas. The sputtering target is cooled properly to minimize the radiant heat avoiding thermal evaporation.

2.1.1.2 Deposition rates

The sputtering target should be pure during the sputtering process and for that pure Ar is necessary for better deposition rates. During sputtering, deposition rates of metal target drop dramatically when the residual gases react with target and form compound layers on the target surface. In DC sputtering, high gas pressures and applied sputtering power should be optimized to sustain continuous sputtering process. Sometimes at too high deposition pressure, sputtering process could be ceased. The DC/RF reactive-sputtering could be used for high deposition rate with compound thin films. The variation in the composition and microstructure in reactive sputtered films depend on process conditions. Reactive sputtering is generally adopted for depositing compound thin films from pure elements. Flow control of reactive gas and pure argon affects deposition rates and found to be lower than deposition rate from pure elemental target. Optimized partial pressure of the reactive gases to deposit films leads to higher deposition rates with better film properties. Insulating films through reactively to deposit without arcing is possible depends upon pulsed DC-power or mid-frequency AC power.

2.2 CHARACTERIZATION TECHNIQUES

Nanocrystalline ZnO thin films were deposited by DC-sputtering at different sputtering parameters e.g. variations in deposition pressure and substrate temperature are subjected to microstructural and mechanical characterization in the present work. The various characterization techniques are discussed in the following sections.

2.2.1 X-Ray diffraction (XRD)

X-ray diffraction (XRD) is used for analyzing the crystalline properties, phase identification, unit cell characteristic dimensions and micro strain. In fact, XRD identifies unknown crystalline materials related to the crystal structure, including lattice constants, crystallite size, phase analysis, crystal defects, strain, etc. XRD is used for analyzing films thicker than several angstroms on account of the strong penetrating power of the X-rays, however glancing angle XRD can be used for ultra-thin films [117].

2.2.1.1 Fundamental principles of XRD

The underlying principal of XRD is relying on constructive interference in monochromatic X-rays from a crystalline sample. X-rays are generated using cathode ray tube and filtered to get monochromatic radiations. X- ray beam is collimated to concentrate and directed toward the sample. In Fig. 2.2, a parallel beam of X-rays strikes the crystal where the atoms are placed on two parallel planes separated by a distance ‘d’ (inter planar space). The parallel X-ray beams impinge onto the planes at an angle of θ and atoms scatter the X-ray beams in all possible directions. Likewise, detector is placed at an angle of θ on the right, and then only reflected beams having the path difference an integral number of wavelengths could be detected due to constructive interference. This is expressed mathematically by Bragg's Law

$$2d\sin\theta = n\lambda \tag{2.5}$$

In Fig. 2.2, d is the spacing between two adjacent atomic planes, θ refers angle between the crystal plane and the incident X-rays, n is the order of diffraction maximum, and λ is the wavelength of the X-rays [118]. However, diffraction pattern contains positions and intensities of the diffraction effects, which is a fundamental property of the material. Positions of the diffracted peak, intensity and peak shape effect leads to a knowledge of the size, shape and orientation of the unit cell.

2.2.1.2 XRD instrumentation

X-ray diffractometer assembled with three basic components including X-ray tube for X-ray generation, a sample holder for irradiating the sample, and X-ray detector to collect the scattered X-ray [119]. Cathode ray tube has heating filament to generate electrons accelerating toward the target material to strike with sufficient energy so that dislodge inner shell electrons and characteristic X-ray spectra produced.

Crystal mono-chromators are used to filter for monochromatic X-rays. However, $K_{\alpha 1}$ and $K_{\alpha 2}$ are still present in diffracted pattern; because of sufficiently close wavelength and weighted average of these two is used. Copper is most widely used as target material for monochromatic X-ray, with its K_α radiation 1.5418 Å. Further, X-rays are collimated and used to irradiate the sample. Reflected X-rays is recorded in rotated detector. When the incident X-rays satisfies the Bragg's Eq. (2.5), constructive interference occurs affecting the peak intensity. A detector records whole processes and convert X-ray signal into a count rate between 2θ angles.

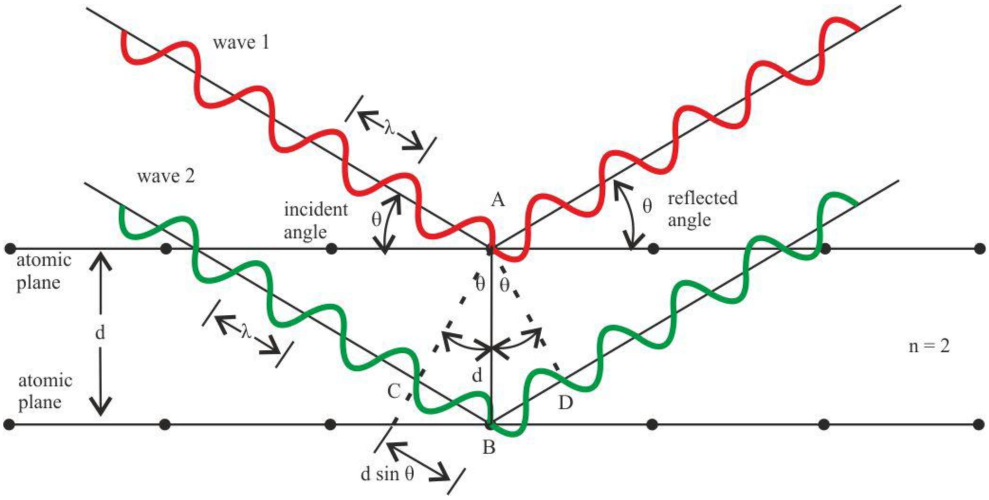

Figure 2.2. Diffraction of X-ray from crystal plane [120]**.**

2.2.1.3 Crystallite Size

The quantitative analysis is accomplished by XRD for measuring crystallite size achieved from coherent scattering by material. Also, crystallite size can be inferred from the width of Bragg reflection. The Scherrers Eq. (2.6) used to get crystallite size (*D*) of the crystalline material from the XRD is given below.

$$D = \frac{k\lambda}{\beta \cos\theta} \tag{2.6}$$

Here, λ is the wavelength of incident radiation, β is the full width half maximum for the peak, k is the shape factor, and θ is angle of peak position.

2.2.1.4 Uniform strain

When a poly-crystalline thin film is deformed in such a manner that strain is uniform over relatively large distances, the lattice plane spacing in crystal planes changes from their stress-free state to corresponding accumulated stress state in the film.

However, new spacing being essentially constant from one grains to another for a particular set of planes [119]. This uniformly distributed strain causes a shift of the diffraction peaks to new *2θ* angular position. The shifting in XRD peaks of deformed sample depends on the nature of residual stress. Compressive residual stress shifts the XRD peaks toward higher angle and tensile residual stress towards lower angular positions. Measuring this peak shift from the standard reported values; provide strain in the thin films. The residual stresses are not only the cause of shifting, change in chemical composition and growth of phases may also shift the XRD peaks. The accumulated micro strain in the thin films can be calculated as follows [118].

$$\text{microstrain} = \frac{a - a_0}{a} \times 100 \tag{2.7}$$

Where, a is the lattice parameter of the strained film calculated from XRD data and a_0 is the unstrained lattice parameter of film.

2.2.1.5 Non-uniform strain

The strain also depending on the defects, dislocation and stacking faults in the material, is more pronounced and lattice planes become locally distorted altering the spacing of any particular (hkl) set from one crystallite to another or may be one part of a crystallite to another. This non-uniform micro-strain broadens the corresponding XRD peaks. Although, micro-strain not solely contribute to broadening in XRD peaks but nano-crystallite size and instrument factor also lead the broadening. In order to calculate micro-strain through peak broadening due to overall micro deformation is given in Eq. (2.8) [121,122].

$$\varepsilon = \frac{\beta}{4\tan\theta} \tag{2.8}$$

ε is the inhomogeneous internal strain, θ is the Bragg reflection angle and β is the measured full width at half maximum (FWHM) of the peak.

2.2.1.6 Applications

There are several new developments in the XRD instruments e.g. Glancing Angle XRD, High Temperature XRD, X-Ray Reflectivity, High Resolution XRD, Texture Measurement XRD provide more versatility. XRD can provide, crystalline properties, phase composition, strain, dislocation density and number of crystallites per unit area [122]. In the present study, XRD has been performed with Cu-K_α radiation using X-ray diffractometer (Bruker AXS, D8 Advance) and

(Rigaku Smartlab, Japan). The XRD could be used obtaining the structural and microstructural features of the materials as given below.

- Characterization of crystalline materials as well as fine-grained materials, nanomaterials, different types of clays, nanoparticles, thin films etc.
- Diffraction pattern provide angular position and used to determine unit cell dimensions also phase purity or impurity within the detection limit of instrument.
- Diffraction pattern of thin films give information about lattice mismatch and strain to predict the type of growth on particular substrate along with dislocation density, quality by rocking curve measurements.
- Determining the epitaxial growth, and super-lattices in multilayered structures, density and thickness by X- ray reflectivity measurements.

2.2.2 Field emission scanning electron microscopy (FESEM)

Scanning Electron Microscopy (SEM) provides plenty of information including phase distribution, morphology, topographical features, crystal structure, crystal orientation, and compositional differences. The mechanism of the process attributed in versatile signals generation, imaging process, high magnification range and depth variations in specimen. In FESEM, the electron beam is a focused of similar energy and trajectory, accelerated towards the sample by electromagnetic fields. The energetic electron beam has a series of complex interactions with the nuclei and electrons of the atoms in the specimen. The interaction occurred with or without energy loss i.e. inelastic interactions or elastic interactions respectively, of the incident electron beam [123].

- Elastic interactions: When the scattering of the incident electron beam by the specimen occurs with negligible energy loss during the collision, it is called elastic interaction. Elastically scattered ‘incident electrons’ through angle of greater than 90°, called back-scattered electrons (BSE) and it provides the sample information including its atomic number.
- Inelastic interactions: When the scattering occurred with a substantial energy loss in collision between incident electron and specimen, exhibiting energy exchanges to that atom, it is called inelastic interaction. Moreover, excitation of specimen could generate secondary electrons (SE) as a result of the ionization, possessing energies $\geq$50 eV and

used as signal to provide topographic features of the samples. Secondary electrons are more influenced by surface properties as compared to the atomic number.

- Auger Electron: These electrons are generated through complex mechanism, in which ionization performed in core shell by incoming electron, then falling an outer shell electron to fill that inner shell vacancy. So, the excitation energy between these two shells is released, which is carried away by Auger electron. This characteristic electron can be used to provide chemical information. Because of their low energies, Auger electrons are emitted only from near the surface.
- Characteristic X-rays: X-rays are produced when an atom’s inner shell electron is dislodged by collision with an incident electron, suddenly an outer shell electron occupy inner shell position to re-establish proper charge/energy balance in its orbital. Thus, an emission of X-ray photon is observed to attain the ground state. The X-ray generated is specific to that level called as characteristic X-ray. These characteristic X-rays provide helpful insight to chemical composition of the specimen.
- Cathodo-luminescence: It occurs when the interaction between specimen and incident electron beam takes place with the emission of light. The mechanism responsible for it include incident electron and atomic electron if semiconductor i.e. in the valence band, which is promoted to the conduction band and accounts for electron hole pair generation. Upon excitation, electron bounce back to its original positions after radiating the energy. This whole process, called as recombination, which leads to emission of a photon carrying the energy [124].

FESEM provides improved spatial resolution up to 1.5 nm compared to conventional SEM, and with minimized sample charging and damage. The underlying mechanism of FESEM, a high voltage is applied between a pointed cathode and a plate anode to flow current. The field emission process depends on work function of the metal, which could be deteriorated by adsorbed gases. So, maintenance of high vacuum is necessary.

The electron beam is energized by the accelerating potential of few hundred eV to 50 keV and the divergent beam is focused by two condenser lenses into a beam with a very fine focal spot size. The first condenser lens is used to working in conjunction with the condenser aperture to narrow the beam and also limit its current. However, a second condenser lens is used to make the electron beam more thin and coherent. Specimen is focused by objective lens, and electron beam is made to deflect over the specimen in the raster form. At each data point, the SE and BSE reaching the detector are counted for determining the relative intensity of the pixel representing that point in the final image.

Limitation associated with the SEM is that the specimen that has to be analyzed should be conducting. In case of non-metals, it is required to make them conducting by covering the sample with a thin layer of conductive material like gold or platinum in order to enhance the imaging. In the present study, field emission scanning electron microscope (Carl Zeiss, Germany, ULTRA plus model) is used as shown in Fig. 2.3. Elemental composition analysis can also be performed by using the energy dispersive X-ray spectrometry (EDS) attached with the FE-SEM system.

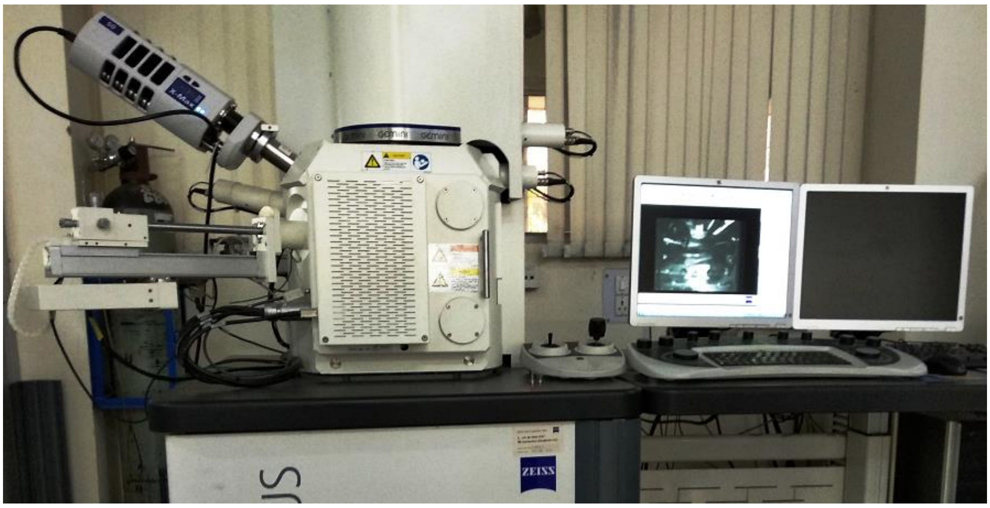

Figure 2.3. FESEM instrument in the laboratory.

2.2.3 Energy dispersive X-ray spectrometry (EDS)

EDS study relies on emitted X-ray spectrum by the specimen which is the result of inelastic scattering beam of electrons and specimen core electrons. These X ray produced are characteristic to the elements and provide localized chemical analysis. EDS is reliable for the analysis of atomic number greater than 4 (Be) to 92 (U), though some instruments has limitations for 'light' elements (atomic number < 10). EDS instrument is assembled with three working components designed together for collecting optimum results, X-ray detector, pulse processor, and analyzer. The ED spectrometer unit converts energy of individual X-ray into a voltage signal of proportional size. Light elements (below carbon) are more prone to Auger electron emission so, observed K-lines are weaker. In the present study, EDS attached to FE-SEM was used.

2.2.4 Atomic force microscopy (AFM)

AFM is a versatile tool which provides advantage comparatively to other microscopy techniques [125]. AFM mechanism is based on the force, between an AFM tip and the specimen, force used as input to produce the topographic image. AFM is associated a control system is attached to provide feedback to piezoelectric actuators and display images. A vibration isolation unit is attached with the AFM to dampen ambient vibrations. The laboratory set up of AFM instrument manufactured by NTEGRA Russia model from NT-MDT used in the present studies is shown in Fig. 2.4. AFM cantilevers coated with silicon nitride (Si_3N_4), typically having 10 to 40 µm in width, 100 to 200 µm in length, and 0.3 to 2 µm in thickness. Cantilever deflects in the upward direction when it senses a net repulsive force and deflects downward direction under net attractive force from the specimen. These deflections of tip are associated with topographic information and are further converted to image formation.

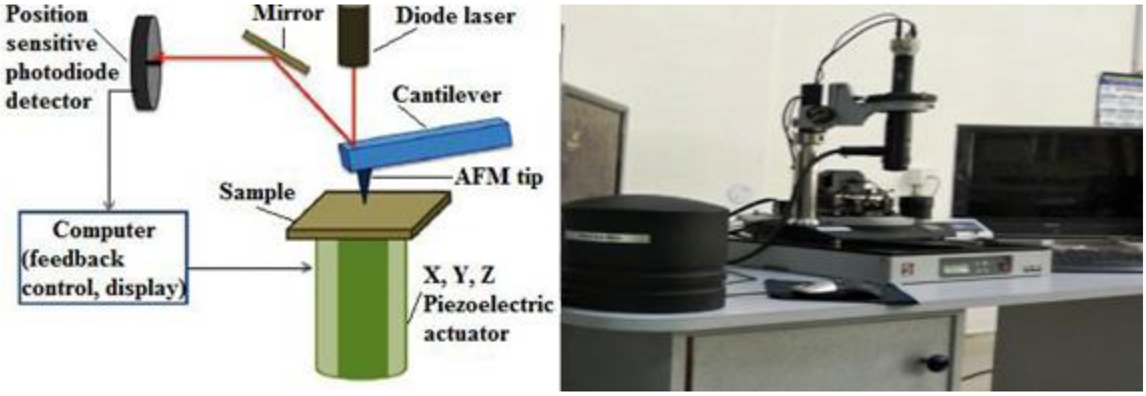

Figure 2.4: AFM instrument in the laboratory.

However, deflection measured through optical lever containing laser diode, is focused at end of the cantilever. Also, a reflective coating at the back of cantilever allows to reflection of laser light to position-sensitive photo-diode detector. Net forces from specimen act on AFM tip produce bending or twisting and so the reflection is occurred at different angles. The difference in the output generated in photodiodes used as output signal depends on the deflection in cantilever. Different modes of operation e.g. force control or height control is possible in AFM. During operation, user defines set points and adjusting the height of the tip on specimen, so that set a feedback signal to attain better quality images. Also, AFM may be operated different environments e.g. ambient, vacuum conditions, condensed phase or liquid phase at high or cryogenic temperatures and variable pressures. Different modes of operations i.e. Non-contact and Contact depend upon distances between AFM tip and specimen. When the gap is reduced between AFM tip and the specimen, the net force changes its nature from attractive to repulsive. So, AFM can be used under three different imaging modes as follows;

- Contact mode, AFM Tip and specimen remain in close proximity during image acquisition. In this mode, AFM tip scan the specimen either constant height above the surface or at applied constant force. In constant height operation height of the tip is fixed during scanning and in force constant mode, deflection of the cantilever operating at constant force, z-direction motion of the scanner is recorded. A softer cantilever is used to probe the specimen in contact mode to avoid damages. Deflection is sensed as observed in cantilever and compared in feedback amplifier to some pre-defined values. Any changes force feedback amplifier to apply a voltage to piezo-actuator to change the position of cantilever which determines the height of features on the specimen surface.
- Non-contact mode, more separation between AFM tip and specimen surface gives rise to attractive force by the inter-molecular force. In non-contact, AFM tip is oscillated at some resonant frequency with 0.1-10 nm separation distance between tip and specimen. The voltage signal applied to piezoelectric actuator to maintain the resonant frequency is used to generate a topographic image and attractive Vander Waals forces between AFM tip and specimen are detected. The attractive forces are substantially weaker than repulsive force as in contact mode; therefore, the tip is given a small oscillation and AC detection methods can be used to detect the small forces between the tips.
- Tapping mode or Intermitted Mode, AFM tip making an intermittent type of contact with a tip-specimen separation distance 0.5-2 nm. The cantilever is oscillated at its natural frequency using piezo-actuator assembly. The oscillating tip brings in close proximity until it just taps with the specimen and lifted off. The contact time with specimen fairly small of its oscillation period. The specimen used to scan continuously beneath the tip. The oscillation amplitude in the tapping period changes accordingly to feedback in such a way that tip can maintain at constant height or force. This feedback signal is a measure of the surface features.

2.2.5 X-Ray Photoelectron Spectroscopy (XPS)

X-Ray Photoelectron Spectroscopy (XPS) is based on photoelectric effect in which electrons are produced through electromagnetic radiation. In XPS, X-rays are utilized in the emanation of photoelectrons (PE). The X-rays interact to energize electrons of outer and inner core shells within the molecule.

XPS is a surface sensitive, non-destructive technique to probe the first few layers ̴10 nm of the surface [126]. Auger lines, a three electron involved process are likewise recorded amid XPS measurements. Initially, a core shell vacancy created after ejection of an electron from the core shell (e.g. in the K-shell) and then an electron from outer shell (e.g. L_1) filled this vacancy. Amid the relaxation process, an amount of energy is released, which is further used to expel another electron (e.g. $L_{2,3}$) having a lower binding energy. Also, XPS provides a better quantification of the peak areas [127]. XPS also known as electron spectroscopy for chemical analysis (ESCA) and adaptable to be utilized on extensive assortment of samples [128].

2.2.5.1 Principles of the technique

Every atom/molecule on the surface of a material (aside from hydrogen) comprises of valence electrons that are associated with chemical bonding alongside core electrons. These core electrons have an exceptional binding energy which is characteristic to the sort of atoms to which it is bound. However, binding energies of the electrons along with the peak areas make possible to quantitative elemental surface analysis [129]. In the furthest 10 nm of a surface, XPS can give; distinguishing proof of all components (with the exception of H and He) and more noteworthy when the concentration is more than 0.1 atomic percent. Likewise, information about the sub-atomic condition (oxidation state, bonding atoms, etc.), recognition of organic groups can be possible. Nondestructive depth profiles up to 10 nm in the sample and its surface heterogeneity assessment to measure lateral variations in the surface composition is possible with this instrument.

Since the electrons can just travel a short separation through the sample without experiencing inelastic impacts, bringing about an intense loss of energy, XPS is considered to be very surface delicate [128]. So, the surface investigation by XPS starts by setting the sample in ultra-high vacuum environment (~ 10^{-10} Torr) and after irradiating the material with a wellspring of low-energy X-rays. If the excitation energy of X-rays is more as compared to the binding energies for elements, photoemission would occur [128]. The resulting photoelectrons are emitted from the surface having a kinetic energy (E_k) measured. Using the known X-ray energy ($h\nu$), the binding energy (E_b) is ascertained utilizing the Einstein relation seen in Eq. (2.9), where φ is the work function of the spectrometer [126].

$$E_b = h\nu - E_k - \varphi \tag{2.9}$$

The photoelectrons are isolated according to energy, counts, and related to the atomic and sub-atomic condition from which they were catapulted. A range of the quantity of ejected electrons versus binding energy is obtained. Albeit, particular electrons of an atom have specific binding energies, and the chemical condition of the atoms can make varieties in the qualities. These variations in the binding energy values, or shifts, represent covalent or ionic bonds amongst atoms help to conclude the compound structure of the material surface. Binding energy peak assignments was performed using carbon 1s peak as reference. The core region of XPS spectrum is the easiest region to interpret since each type of atom has core electrons in a characteristic region, resulting in instantaneous atomic identification.

Additional information about the chemical conditions and subsequent chemical bonds of the atoms is then provided by core chemical shifts. The resolved carbon 1s and oxygen 1s regions peak fitted to show overlapping features corresponding to different chemical functionalities. Each region is fitted to a number of component peaks, each peak corresponding to a different surface functionality. All the energy levels involved in chemical interaction, specific to the species can be seen. Because core chemical shifts are sometimes not unpretentious between certain subtle chemical differences, the valence band can assume essential part in surface characterization. In the present study, Omicron ESCA instrument is used for XPS analysis.

2.2.6 Nanoindentation

The indentation peak load P_{max} and the contact area A_c, made during nanoindentation is used to obtain hardness using the equation given below.

$$H = \frac{P_{\max}}{A_c} \tag{2.10}$$

Nanoindentation has a shorter length scale in nanometers of tip radius as compared to other conventional indentation having scale of mili- or micro-meters. This scaled down length scale provides higher resolution for estimating nanomechanical properties. The indentation depth is precisely measured using nano indenter and therefore it is called depth-sensing indentation [130]. Nanoindentation can be used for measuring hardness as well as plasticity, fracture toughness, adhesion [84]. The relationship between the parameters derived directly from indentation test e.g. load and indentation depth, and contact area is established as discussed as follows.

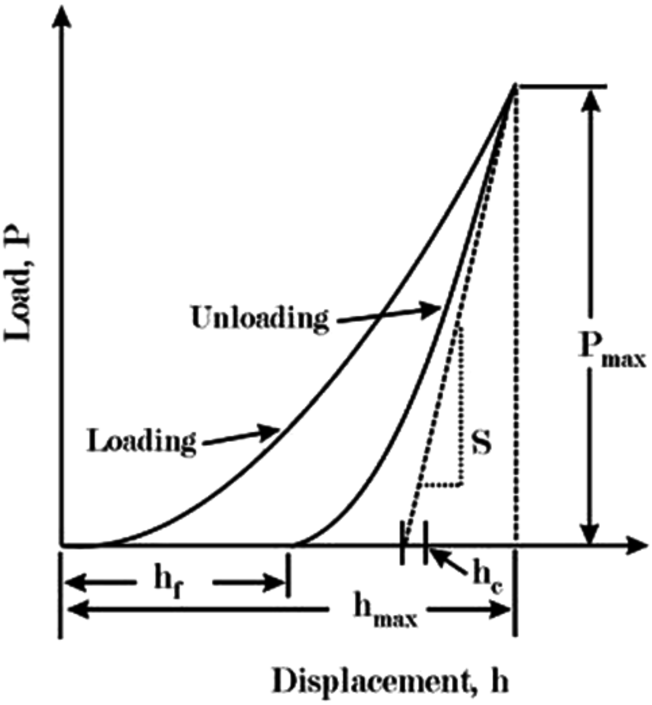

Figure 2.5. Load-Indentation depth curve.

A load-displacement curve is obtained from the indentation test as shown in the Fig. 2.5. P_{max}, $h_{\max}$ is the peak indentation load, maximum indentation depth as provided in Fig. 2.5, while h_f, S is final displacement and stiffness of the test material, respectively. Elastic response could occur amid unloading. Subsequently, stiffness of the test materials can be found by

$$S = \frac{dp}{dh} \tag{2.11}$$

$$\frac{1}{E_r} = \frac{1-\upsilon^2}{E} + \frac{1-\upsilon'^2}{E'} \tag{2.12}$$

The reduced modulus E_r is measured using Eq. (2.12), where E, E' are elastic modulus of test material and indenter tip. The Poisson’s ratio of tested material is referred as υ and indenter tip, it is referred as υ' respectively. Standard diamond probe is used as the indenter tip, thus E' is high. Oliver and Pharr has proposed a relationship to evaluate the contact area based on elastic-plastic response during unloading [131].

$$P = B(h - h_f)^m \tag{2.13}$$

Where, m and B are found by power-law fitting of unloading curve. Using Eq. (2.11) and (2.13)

$$S = \frac{dp}{dh}\left(P = P_{max}\right) = mB\left(h_{max} - h_f\right)^{m-1} \tag{2.14}$$

The contact depth h_c, maximum indentation depth h_{max} are given by;

$$h_c = h_{\max} - \epsilon \frac{P_{max}}{S} \tag{2.15}$$

Where, ϵ is referred as geometry constant relying upon the shape of indenter tip. The radius of tip is only reliant on geometry of tip. In general, it is inconceivable that only elastic response exists and plasticity observed along with process of indentation. In indentation, the most well-known indenters are sharp indenters, among which two broadly utilized are the four-sided Vickers indenter and the three-sided Berkovich indenter. Pyramidal indenters and other conical indenters depend on cone angle that provides area to depth relationship as mentioned in Table 2.2 and Fig. 2.6. [132].

Table 2.2: Contact Area for different indenter geometries [130]

Different Indenter Type	Indenter Projected Area	Indenter Semi-angle	Intercept Factor	Geometry Correction factor
Berkovich	$3\sqrt{3}\, h_p^2 tan^2\theta$	65.3°	0.75	1.034
Vickers	$4h_p^2 tan^2\theta$	68°	0.75	1.012
Knoop	$2\mathrm{h}_\mathrm{p}^2 \tan\theta 1 \tan\theta 2$	θ_1 = 86.25°, θ_2 = 65°	0.75	1.012
Cube corner	$3\sqrt{3}\, h_p^2 tan^2\theta$	35.26°	0.75	1.034
Sphere	$\pi 2Rh_p$	N/A	0.75	1
Cone	$\pi h_p^2 tan^2\alpha$	A	0.72	1

For any punch geometry that can be portrayed as a solid of revolution of a smooth function, Sneddon demonstrated general connections among load and displacement as [29-30];

$$P = \alpha h^m \tag{2.16}$$

Where 'P' is applied load, h, elastic displacement of the indenter, α and m are constants in Eq. (2.16).

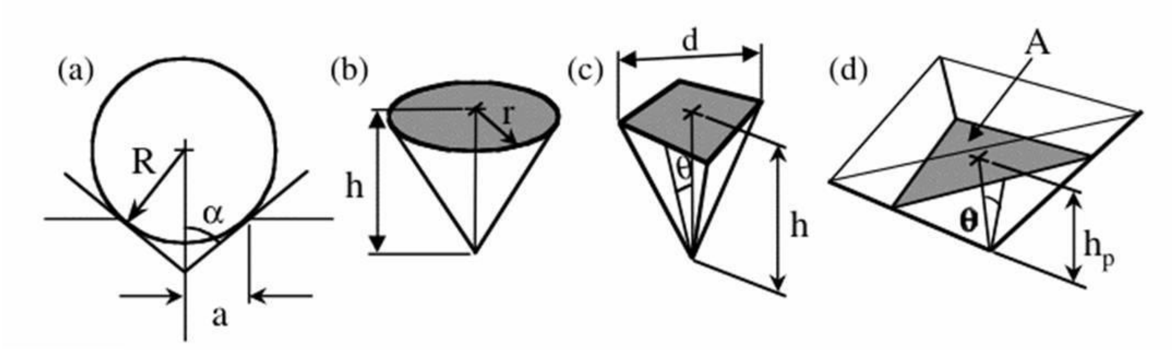

Figure 2.6. Indentation Parameters for (a) Spherical, (b) Conical, (c) Vickers and (d) Berkovich Indenter.

In the mid-1970s, Buylchev, Alekhin, Shorshorov performed micro-hardness testing to obtain a load-displacement plot and develop an equation known as Buylchev-Alekhin-Shorshorov (BASh) equation [133].

$$S = \frac{dp}{dh} = \frac{2\beta E_r \sqrt{A}}{\sqrt{\pi}} \tag{2.17}$$

In Eq. (2.17), *S* is the experimentally estimated stiffness from the upper portion of unloading data and *A* is the projected area of the elastic contact which is equivalent to the optically estimated zone of the hardness impression. Though Eq. (2.17) was initially determined for a cone shaped indenter, it was demonstrated that this holds similarly well for circular and tube shaped indenters and theorized that it should apply to different geometries [134]. In this manner, Pharr, and Oliver demonstrated that Eq. 2.17 applies to any indenter geometries.

2.2.6.1 Oliver and Pharr Method

In 1992, Oliver and Pharr proposed a strategy based on analytical solutions and curvature in the unloading data [131,135]. They reported that the direct estimation of the contact zone is not generally precise and advantageous, and proposed a system to decide contact area based on the indentation depth and indenter shape function. Such a solution is called “depth-sensing indentation testing". During loading, the total displacement h is expressed in Fig. 2.7.

$$h = h_c + h_s \tag{2.18}$$

Where contact depth, h_c is the distance along which contact is actually made. h_s is known as displacement of the surface at the edge of the contact as shown in Fig. 2.7.

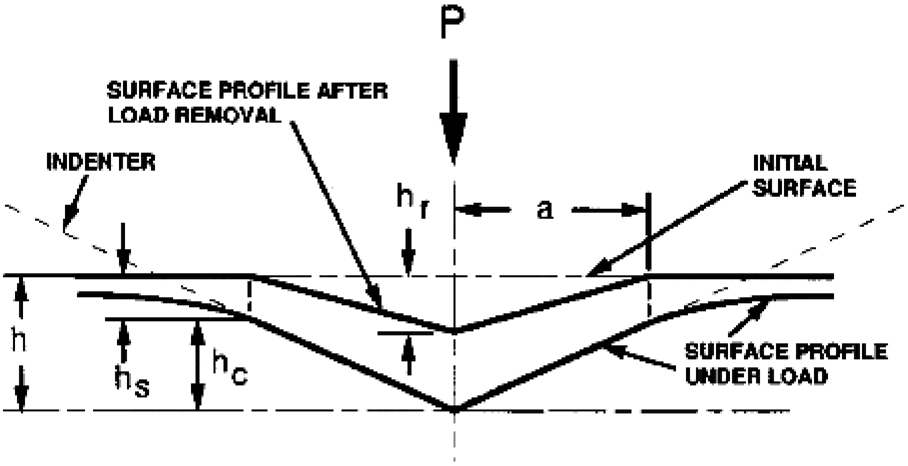

Figure 2.7: Schematic Representation of a Section through an Indenter.

Elastic displacement is recovered and depth h_f, indenter completely pulled back is remaining. The projected contact area, *A* is measured as a function *F* of the contact depth;

$$A = F(h_c) \tag{2.19}$$

$$h_c = h - h_s \tag{2.20}$$

For the conical indenter

$$h_s = \frac{(\pi - 2)}{\pi}(h - h_f) \tag{2.21}$$

$$(\mathrm{h} - \mathrm{h}_f) = 2\frac{\mathrm{P}}{\mathrm{S}} \tag{2.22}$$

From these equations at peak load

$$h_s = h_{\max} - \epsilon\frac{P_{max}}{S} \tag{2.23}$$

$$\epsilon = \frac{2}{\pi}(\pi - 2) = 0.72 \tag{2.24}$$

S and the contact depth h_c, obtained by intercept of initial unloading slope, which is same as proposed by Doerner and Nix [134].

2.2.6.2 Area Function and Load Frame Compliance

It is essential to evaluate both load frame compliance and area function precisely to figure out elastic properties. Oliver and Pharr demonstrated load frame and the specimen as two springs in series.

$$C = C_s + C_f \tag{2.25}$$

Where, C, C_s, and C_f is total measured compliance, specimen and compliance of the load frame, respectively. Specimen compliance is inverse of the stiffness S,

$$C = C_f + \frac{\sqrt{\pi}}{2E_r\sqrt{A}} \tag{2.26}$$

For a material with consistent modulus, a plot C versus $1/\sqrt{A}$ is straight and intercept is load frame compliance. Estimation of C_f from information of large indents can be made. The perfect area function for a Berkovich indenter is

$$A\left(h_c\right) = 3\sqrt{3}h_c^2 tan^2\theta = 24.5h_c^2 \tag{2.27}$$

To represent flawed indenter geometry, huge indents are made in quartz and corrected area function is measured using the equation given below

$$A(h_c) = 24.5h_c^2 + C_1h_c^1 + C_2h_c^{(1/2)} + C_3h_c^{(1/4)} + ... + C_8h_c^{(1/128)} \tag{2.28}$$

2.2.6.3 Nanoindentation using Hysitron Triboindenter

The Hysitron© Tribo-Indenter TI-950 Nanoindentor was utilized for the experiments with software interface Triboscan in the present work. The nano-indenter provides capabilities to measure indentation and load-displacement curve plotting and automatic calculation of modulus and hardness. These capacities are altogether used all through experimental procedures. The transducer and piezo assembly are the strength of this instrument. A standard Berkovich tip with radius of 100 nm was used in present indentation. The trapezoidal load function was used to apply indentation during a single load cycle indentation. Maximum loading was performed in 8 seconds and maximum load was held constant for 2 seconds (holding period). Finally, the load was completely released in 8 seconds. The Load versus displacement response during tip inside sample was recorded during whole indentation process[136].

Elastic properties were assessed from the final unloading curve using the Oliver and Pharr method. Before performing indentation on ZnO thin films, the area function was calibrated on a standard fused silica of known modulus as 69.6 GPa.

2.2.7 Nanoscratch

Adhesion between coating and the substrate could be used for evaluating the tribological performance of a layered framework. The huge number of various test strategies, such as the four-point bending, peeling, nanoindentation and nanoscratch tests portraying adhesion effects, yet none of these systems is "immaculate" [133,137]. The durability of devices coated with hard films since an inadequately adhered films to the substrate brings about delamination of the coating and the devices will then wear rapidly [138].

As one of the delegate techniques estimating attachment, four-point bending, blister test is generally acknowledged. Crack propagation can be observed by four-point flexure loaded as sandwiched structure. However, this strategy has a few constraints on the grounds that the achievement is firmly subject to the planning procedure and testing system [139]. Another technique for estimating bond quality at the interface is nanoindentation [84,140]. The nanoindentation permits to quantify load and displacement precisely with an initiation of a crack. Likewise, pile up and sink in mechanism affected elastic modulus measurement [141]. By estimating the critical bucking length and interfacial fracture energy can provide the adhesion. To measure the delamination of the coating, the nano-indentation method depends on the arrangements of an expansion of plastic zone in the substrate. When a ductile film or a brittle film deposited to hard substrate, the crack initiation or failure events are different.

The nanoscratch is one of the established methods for adhesion measurements. A diamond tip is used to initiate the failure mechanism including delamination, peeling etc. as tip moving in downward and translational motion along the surface. The nanoscratch testing strategy is thought to be the most ideal way in estimating adhesion, and the indenter tip generates excessive stresses to get the interfacial strength of a well adhering film [142]. Albeit, relationship among the critical load and adhesion is complex due to stress distribution at the end of the tip [143].

Several analytical models developed to measure adhesion and shear strength also with the energy release rate from a scratch test. The pertinence of these models relies on the failure mode observed. Benjamin and Weaver proposed a model to evaluate the surface energy of an interfacial crack which can be resolved utilizing the Griffith approach [18]. A nanoscratch test was performed utilizing Hysitron TI-950 Tribo-scan equipped 100 nm radius Berkovich tip in the present work. A high load transducer performed experiments to induce excessive stress to delaminate ZnO coating on a glass and fused substrate. The scratch is performed in normal load in ramped up mode. So, variations of different normal load applied to cause delamination of ZnO thin films [144]. Load controlled measurements were made to capture the discontinuity at the event of delamination/failures in lateral force. The scratch length was 10 μm -15 μm.

Chapter 3

NANOMECHANICAL AND NANOSCRATCH PROPERTIES OF ZnO THIN FILMS

This chapter divided into two sections. First section, **section 3.1** describes the effect of substrate temperatures variations on the ZnO thin films deposited on glass substrate. Second section, **section 3.2** describes the effect of deposition pressure on the mechanical properties of crystalline ZnO thin films deposited on fused quartz substrate.

Contents

3.1 ZnO THIN FILMS DEPOSITED ON GLASS SUBSTRATE: SUBSTRATE TEMPERATURE VARIATIONS

3.1.1 Introduction

ZnO is inherently *n*-type semiconductor with wurtzite hexagonal structure, extensively used in wide range of applications due to its unique properties such as direct band gap, high exciton energy and high piezoelectric coefficients [29]. Also, it is used in solar cell, gas sensor, and light emitting diodes, etc. [145,146]. ZnO has a low lattice mismatch with GaN and therefore it could serve as an ideal substrate for the epilayer growth of GaN, desirable for fabrication of optoelectronic devices [66]. ZnO is found in abundance and therefore cheap, nontoxic, and promising for the replacement of expensive materials in several functional applications. ZnO nanowires, nanotubes, and thin films are thermodynamically stable and their properties can be easily tailored by altering its surface to volume ratio, dimensions and synthesis route [147].

A huge interest in ZnO is also governed by the fact that there are several synthesis routes available for producing it by physical evaporation methods as well as chemical methods [37]. Also, deposition processes in higher vacuum provide thin films free from unwanted impurities. The diversity in synthesis route allows manipulating the existing properties of ZnO nanostructures. Among physical routes, sputtering is a unique class of depositing technique for large area synthesis, higher adhesion to the substrate and also compatible with the manufacturing at the industrial scale. The sputtered thin films are generally polycrystalline in nature [148,149]. The sputtered species with high energy yields dense and compact microstructure in thin films. The grain size, morphology and preferred orientation of the thin films are influenced by sputtering parameters such as substrate temperature, argon/oxygen partial pressure, and sputtering power, etc. The stresses induced during the deposition process in thin films affect its functional properties [150].

The mechanical properties of wide band gap semiconductor ZnO at nanoscale are important for its structural integrity as MEMS, sensors and solar cell applications [151]. Nanoindentation and nano-scratch have been developed as a key technique to measure the mechanical properties such as elastic-plastic properties, hardness, Young’s modulus and friction properties of low dimensional nanostructures. Nanoindentation is performed with high sensitivity along with continuous measurement of applied load and displacement. Scratch with ramping up load technique is used to measure failure events and adhesion strength of the thin films [136].

Mechanical properties of thin films are influenced by the microstructures of films as well as substrate mechanical properties. The hardness of ZnO thin films has been reported on different substrates such as Sapphire (5.75-6.6 GPa) [68], Silicon (4-6GPa) [152,153], and Langasite (9.2-10.4 GPa) [152]. When relatively soft films are deposited on hard substrate, substrate effect comes in to play after 0.2*t* (*t*=thickness of films) indentation depth, beyond that hardness gradually increases with penetration depth. However, when the hard films are deposited on soft substrate, the hardness is influenced even at smaller indentation depths below 0.05*t* [153]. In the present study, corning glass is used as substrate which exhibits high hardness of ~8 GPa [154]. In previous studies, discontinuity was observed in load-displacement curve during indentation, referred as the slip band movement during indentation [64]. The literature on adhesive strength of sputter deposited ZnO thin films using nanoscratch test is limited. Therefore, the present work has been focused to investigate the mechanical properties such as hardness, Young’s modulus, and scratch resistance of ZnO thin films and further to correlate with the micro structural characteristics of films deposited under varying substrate temperature conditions in DC-sputtering.

3.1.2 Experimental details

The ZnO thin films were deposited on the glass substrate using DC sputtering. The deposition was performed in a chamber of 12´´ diameter by using pure ZnO target. The substrates were cleaned using deionized water and acetone under ultrasonic vibrations for 15 minutes. After drying substrates in hot air, the target and substrate were fixed in target holder and substrate holder, respectively. The sputtering chamber was evacuated to 2×10^{-5} Torr pressure to remove residual gases present in the chamber. Thereafter, high purity Ar/O_2 gas at the flow rate (20:5 sccm) was introduced in to the chamber. The other sputtering parameters such as working pressure and sputtering power were 10mTorr and 50W, respectively, and maintained constant during the deposition process. The pre-sputtering was carried out for 10 minutes to eliminate surface contamination of the target. The substrate temperature varied from RT (25^0C) to 100^0C, 200^0C and 300^0C. Structural properties were characterized by the XRD performed with Cu-K_α radiation using X-ray diffractometer with (θ–2θ) geometry. Diffractograms recorded data in the angular range of 25-70^0 with a scan speed of 1^0/min. The grain size ‘*D*’ of the ZnO thin films was calculated by Scherrers formula using Eq. (2.6) [122]. However, the line broadening of XRD peaks is not only related with crystallite size but also the function of internal strain that is developed in the thin films during the film deposition process.

The deviation from perfect lattice arrangement is calculated using Stokes Wilson equation in Eq. (2.8) [121]. Real crystal is not perfectly arranged as they have some lattice imperfection, such as dislocation, grain boundaries, stacking faults, etc [155,156]. The length of dislocation lines/volume called as the dislocation density (δ) can be obtained by using Williamson & Smallman relation in Eq. (3.1) [157,158]. The higher grain size '*D*' indicate a lower dislocation lines/volume with better crystallinity.

$$\delta = \frac{1}{D^2} \tag{3.1}$$

In Eq. (3.1), '*D*' is the grain size calculated by Scherrers formula. In this Eq. (3.1), dislocations are assumed to be isotropically distributed and it lie along the grain boundaries. The number of crystallites '*N*' per unit area can be calculated using the following relation Eq. (3.2) [159], where, *t* & *D* stands for the thickness and grain size, respectively.

$$N = \frac{t}{D^3} \tag{3.2}$$

3.1.3 Nanoindentation

Nanoindentation test is performed by using three sided pyramidal Berkovich indenter. The sharp Berkovich indenter can apply more localized pressure in the region with same load as compared to spherical indenter. Hardness, Young's modulus, and coefficient of friction of ZnO thin films were obtained by Hysitron TI-950 Tribo-Nanoindentor using Berkovich diamond tip of 100 nm radius. The loading rate is maintained at constant 50 µN/s and holding time of 2 seconds at maximum load. There are several factors like thermal drift, instrument compliance, indenter geometry, pile up or sinking in effect, indentation size effect, surface roughness, which can affect the measurement during indentation [130]. Before performing indentation, tip area function of indenter tip was calibrated on standard fused silica sample. The hardness *'H'* refers to the resistance provided by material to the plastic deformation. The indentation hardness and elastic modulus of the material were determined by Oliver and Pharr method [131] discussed in Chapter 2, section 2.3.6.

The area under the loading-displacement curve shows the total energy dissipated in whole indentation process. However, area under unloading curve corresponds to elastic deformation energy. The scratch test is performed by applying a normal load 0-4000 µN with the loading rate of 133.34 µN/s for 30s (8s-38s). The total scratch length was 15 µm in each test. The morphology of thin films was determined by using FE-SEM.

The elemental compositional analysis was carried out by EDS. The RMS roughness and surface topography of ZnO thin films was characterized by using the AFM with integrated optical view system.

3.1.4 Result and Discussion

The growth characteristics of thin films deposited by DC sputtering are affected primarily by two factors, kinetic energy of sputtered species and substrate temperature [160]. Self-heating of substrate is a special feature in sputtering, which enables the formation of highly crystalline ZnO thin films even at low temperature. The ZnO thin films were deposited on glass substrate, which were held at room temperature (25^0C) to 100^0C, 200^0C, 300^0C. XRD pattern revealed that growth of ZnO thin films along peak at $2\theta = 34.028^0$, 62.22^0 corresponds to (002) plane and (103) plane, respectively, which has hexagonal crystal structure (JCPDS card 89-1397) as shown in Fig. 3.1. XRD pattern confirms that ZnO thin films reveal prominent plane (002), *c*-axis orientation of thin films perpendicular to the substrate surface.

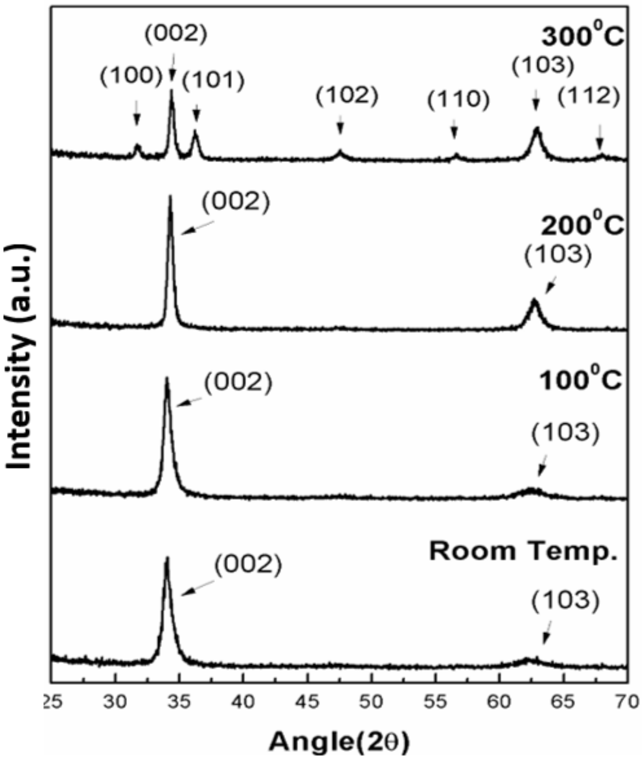

Figure 3.1. The XRD pattern of ZnO thin films at different substrate temperatures.

It may be mentioned that ZnO nuclei have tendency to grow in (002) (polar plane) in a columnar fashion even at room temperature to minimize the surface free energy of ZnO films [161]. The ad-atoms accumulate in such a way that they occupy the minimum energy position by surface diffusion. The dislocation and defects affect the growth of crystal [155,156]. Other than that, the density of defects such as stacking faults and threading dislocations are found to be higher in non-polar ZnO films [162].

Although anisotropy in growth is an inherent property of material, deposition rate and surface of top most layers also influence the growth rate of ZnO thin film in particular plane [163]. Drift model of growth, states that crystal reflection with fastest rate of growth is more predominant [164]. The position and intensity of XRD peaks of the thin films have changed and shifted towards higher 2θ angle at higher substrate temperature. Concomitantly, (103) diffraction plane emerged with higher intensity with increasing substrate temperature. At substrate temperature of 300^0C, several non-polar crystal planes emerged, forming polycrystalline thin films.

Table 3.1. X-ray diffraction parameters of ZnO thin films on glass substrate.

films @ (^0C)	(2θ)	*d*-spacing(Å)/(*hkl*)	'*D*' (*nm*)	Lattice strain (10^{-4})	Dislocation Density (nm^{-2})	*N* (nm^{-2})	Zn/O At. %	'*t*' (*nm*)
25	34.028	2.632/ (002)	11.6	8.48	0.0074	0.139	31.06/ 68.94	218
100	34.043	2.631/ (002)	12.9	7.37	0.0060	0.107	53.74/ 46.26	230
200	34.283	2.613/ (002)	19.4	2.58	0.0026	0.032	51.46/ 48.54	240
300	34.386	2.605/ (002)	20.5	1.55	0.0023	0.069	52.51/ 47.49	600

The increment in substrate temperature leads to grain growth as it increased grain size from 11.6 nm to 20.5 nm. The lattice strain, grain size, dislocation density, and number of crystallites per unit area calculated from the most predominant crystallographic (002) plane given in Table 3.1. The lattice spacing (d_{002}) has decreased with the higher substrate temperature close to reference set (JCPDS card 89-1397) of crystal structure of ZnO, which suggested reduced internal strain as well as formation of uniform grains at higher substrate temperature. The XRD peak profile is closely related with micro-strain as well as grain size.

The internal strain has also decreased at elevated substrate temperature, which is attributed to decrease in lattice imperfection. One of the reasons of lattice imperfection is due to thermal gradients on substrate. The dislocation density has reduced at higher substrate temperature [165]. Higher crystallinity of the thin films is due to higher mobility of ad-atom, influenced by substrate temperature.

3.1.1.1 Hardness and Young's modulus of ZnO thin films

Nanoindentation measurement is performed in load controlled mode to optimized penetration depth; load is increased continuously at a constant loading rate in the segment 'QL' and held for 2s in 'LC' segment, followed by unloading started in 'CP' segment with the same rate as shown in Fig 3.2(a). However, in the scratch test, normal load is increased from zero, with loading rate during the segment 'SF' as shown in Fig. 3.2(b). The load-displacement curves of ZnO thin films deposited at different substrate temperature are shown in Fig. 3.3. Nanoindentation testing involves an elastic, reversible transition as well as plastic, irreversible transition of material under applied load with a desired loading rate. The mechanical properties of ZnO thin films dependent on cohesive strength i.e. bond strength and the fraction of ionic bonding. The substrate also affects the mechanical properties of thin films. To minimize the substrate effect, the penetration depth of indenter in to the films is kept below 10% to total thickness, but this rule holds when the total thickness of films is more than 1 µm [79].

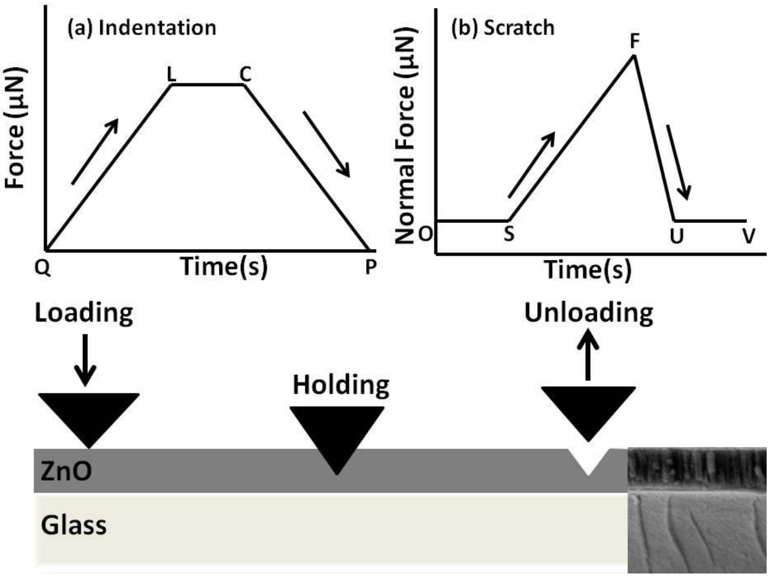

Figure 3.2. Schematic of Loading and unloading using sharp indenter (a) Nanoindentation segment of loading and unloading (b) Scratch segment for ramp loading.

In the present work, thickness of the films is less than 1 µm (refer-Table. 3.1.), and at the same time, ZnO thin films are considered relatively soft as compared to glass substrate [154]. So, indentation depth maintained less than 20 percent to total thickness, minimizing the substrate and tip rounding effect [79,153]. The load displacement curves provide the elastic-plastic deformation under the applied load at a certain penetration depth, which give the hardness and Young's modulus [166]. The non-linear behavior of load-displacement curve depends upon strain rate/loading rate of indentation and elastic plastic nature of material.

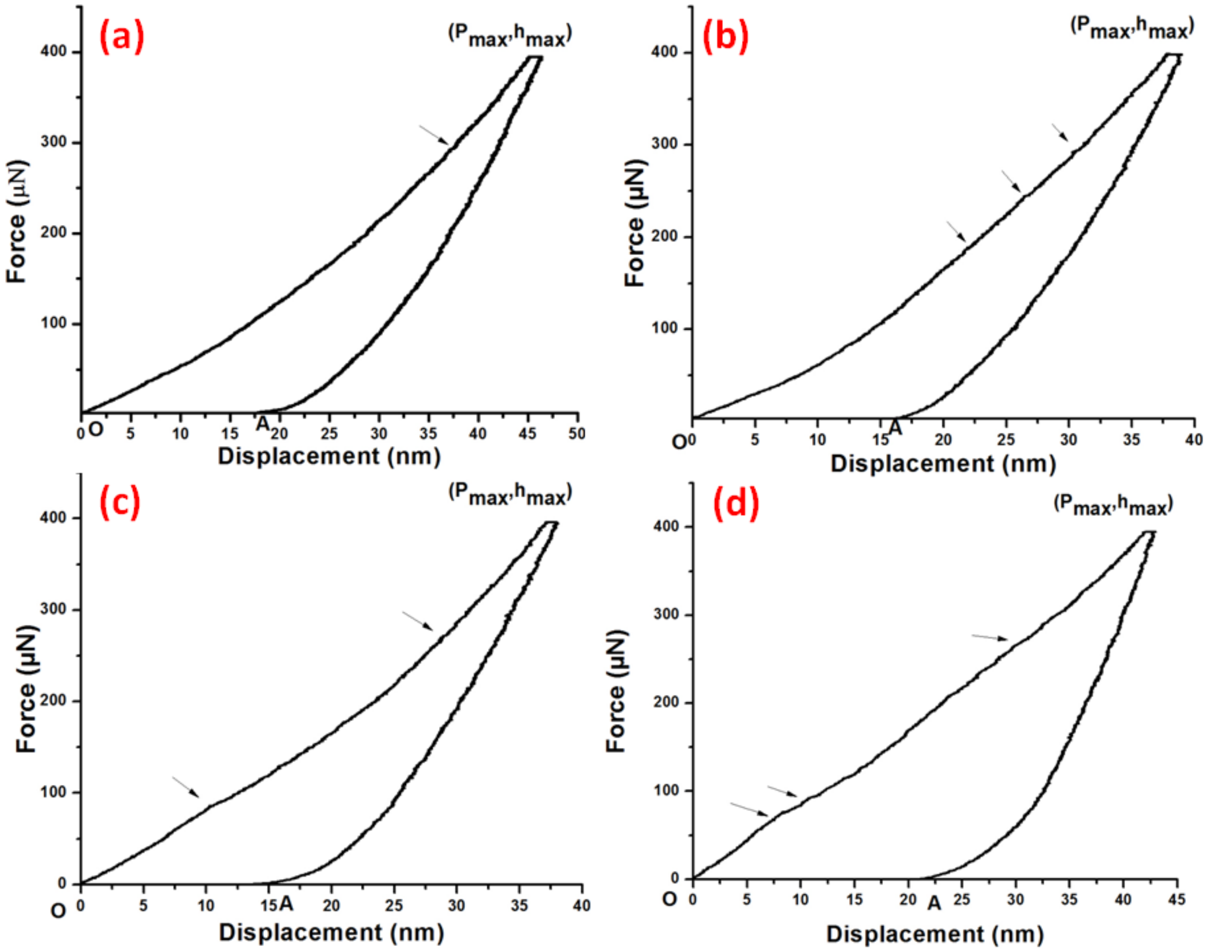

Figure 3.3: Load displacement curve of ZnO thin films at substrate temperature (a) RT (25^{0}C) (b) 100^{0}C (c) 200^{0}C (d) 300^{0}C.

There is no major discontinuity in displacement during indentation. The discontinuity in displacement is considered to be minor if it is spanning (jump) of less than 2 nm at continuous applied load [167,168]. This kind of displacement discontinuity showing singular events of slip or dislocation movement in the thin films, ruled out the possibility of major cracking, delamination or inclusion. It reveals that thin films are defects free, well adhered and dense. The saw type bands in the load–displacement curve are due to the propagation of discrete slip events.

For reliable results at least 10 indents were performed on each sample. The value of hardness and Young's modulus is analysed after multi curve analysis, which is given in Table 3.2 with standard deviations.

The substrate temperature affects the quality and crystalline nature of thin films, which in turn affects hardness and Young's modulus of thin films. The *a*-plane oriented bulk ZnO shows hardness '*H*' and Young's modulus '*E*' of 2.2 ± 0.2 GPa, 163 ± 6 GPa value, respectively, as compared to *c*-plane oriented bulk ZnO exhibiting *H* and *E* value of 4.8 ± 0.2 GPa and 143 ± 6 GPa, respectively [68]. Generally the hardness of the ZnO thin films is varied between 6-10 GPa on different substrates and microstructure [64,152]. In the present study, variation in hardness of films (6.2-7.72 GPa) is observed by varying the substrate temperature with preferred texture in (002) diffraction plane coexisted with other diffraction plane. However, hardness did not vary a much at RT (25^0C) to 200^0 C. The maximum hardness (7.72±0.44 GPa) of thin films is observed at 100^0C, attributed to highest peak intensity ratio $I_{(002)}/I_{(103)}$ (counts) and highly textured *c*-diffraction (texture coefficient (002) = 1.735) plane obtained by Harris texture relation [14].

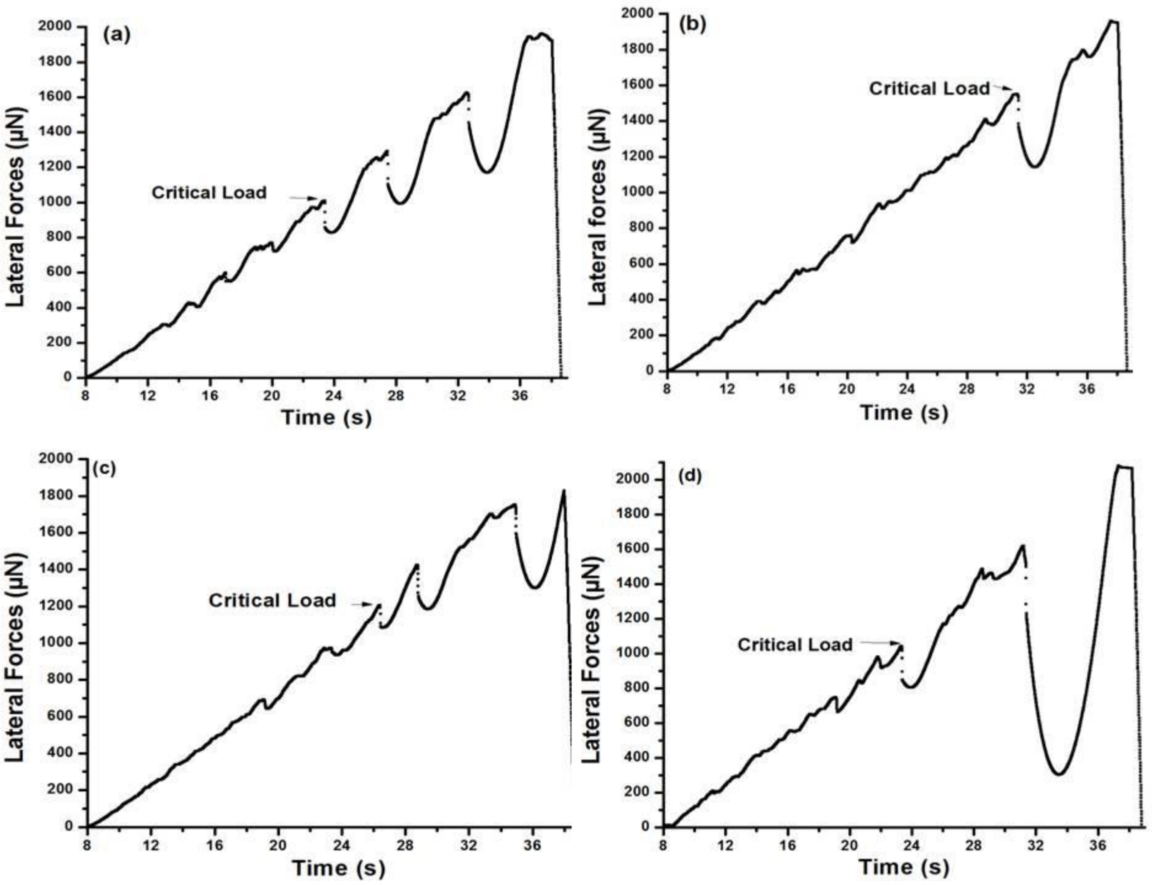

Figure 3.4: Lateral force curve of ZnO thin films at substrate temperature (a) RT (25^0C) (b) 100^0C (c) 200^0C (d) 300^0C.

The variation in hardness except film at 300 ^{0}C depends on the film quality and grain size, whereas hardness of the films gets reduced at 300 ^{0}C due to the presence of new non polar crystal planes. It is well established that ZnO has hexagonal crystal structure with different mechanical behavior depending upon the crystallographic planes [68,169]. The non-polar crystal planes are emerged at 300^{0}C substrate temperature; which is not close packed plane of ZnO as compared to *c*-plane facilitating slip events with ease. So, the hardness of thin films at 300^{0}C reduced showing in line agreement with bulk *a*-plane ZnO.

At the same time, Young’s modulus of thin film increases and having highest value at 300^{0}C. The *H/E* i.e. hardness to Young’s modulus ratio of thin films is an important parameter for determining the indentation scratch, as well as wear properties. High value of *H/E* ratio of thin films is good for the wear resistance properties in materials[170]. The ratio of elastic work done to the total work is directly proportional to *H/E* ratio. For the lower value of the *H/E* ratio, a large amount of work is consumed in plastic deformation within same deformation. So, the larger amount of plasticity is assumed in lower *H/E* ratio [171]. The values of *H/E* ratio are given in Table 3.2. The number of serrations in load displacement curve in Fig. 3.3 depends on substrate temperature, which moves towards lower penetration depth at 300^{0}C. These serrations refer to shear band nucleation and propagation and it is loading rate dependent [172]. Also, serrations and load-displacement curve shape altered by varying the substrate temperature in order to get a different microstructure of films.

Table 3.2. Mechanical properties & roughness of ZnO thin films on glass substrate.

ZnO thin films (substrate temperature)	Hardness (*GPa*)	Young’s Modulus (GPa)	*H/E* Ratio	Critical Load (μN)	RMS Roughness (*nm*)
RT (25^0C)	7.1±0.74	98.4±5.4	0.072	2013.4	3.9
100^0C	7.72±0.44	127.3±13.9	0.060	3126.7	6.5
200^0C	7.6±0.29	132.9±17.4	0.057	2446.9	7.9
300^0C	6.2±0.74	169.5±6.9	0.036	2059.6	13.5

This step wise plastic deformation is likely to start at lower penetration depth in ZnO thin films at 300^{0}C substrate temperature. Indentation provides information about indentation plasticity in the thin films. Plastic deformation refers to stress relaxation with permanent deformation in shape within the materials. Easy stress relaxation corresponds to larger the amount of plasticity present in the material. In the ZnO films deposited at RT to 200^0 C, indentation plasticity is suppressed to maximize the hardness, while in thin film at 300 ^{0}C, indentation plasticity has increased [173].

During Nano-scratch, two different forces act on ZnO thin film. Normal force is employed by the indenter in perpendicular and downward direction on thin film and lateral force, which acts in tangential direction due to the indenter dynamics. Indenter slides on the material's surface with increasing normal load. However, initially, the interaction between the indenter tip and material surface is elastic in nature but at higher normal load, it acts as plowing force and induces plastic deformation in the materials. The sudden drop down in the lateral force indicates an initiation and propagation of crack related with delamination, fracture or fragmentation. Normal load at which this sudden discontinuity appeared in lateral forces is called as critical load of the coatings as shown in Fig. 3.4. Also, critical normal load required for the delamination of thin film and is considered as the adhesive strength of the thin films. [8].

However, it is also reported, that the initial discontinuity in loading curve or lower critical load is resistance for the crack initiation but not completely the failure of films. There must be some upper critical load where the film completely peels off. The toughness of the film is also dependent on the critical load and directly proportional to value of lower critical load, as well as the difference between higher to lower critical load [174]. High hardness is primary property for exhibiting good scratch resistance; likewise, high *H/E* ratio can represent better wear resistance properties. The critical load has shown a tendency to follow *H/E* ratio except films at RT (25^0C). It depends not only on hardness or *H/E* ratio but other parameters like interfacial stress, microstructure of films and substrate contribute their effect.

The internal stresses are prone to develop during synthesis of films. The phase transition, unit cell parameters in films can also affect internal stress, and if thin films tend to changes its volume ($\varepsilon_T = \theta/3$), it induces stress in the films, where θ is the volume shrinkage [175]. The delamination of thin films depends on microstructure, density and defects, which in turn affect the interfacial strength. It is clear that the adhesion strength is the composite effect of thin film and substrate with the contact mechanics of indenter. ZnO thin films at room temperature exhibits highest amount of internal strain and thermal mismatch in the films, due to which its interfacial strength gets reduced.

However, the adhesion strength of thin films is maximum (3126.7 µN) at 100^0C given in Table 3.2, which is attributed to highly textured (002) plane, high hardness, and high *H/E* ratio [176]. The emerging (103) plane alters the internal stress because atomic density changes with diffraction plane and slip activity which further influences the mechanical properties.

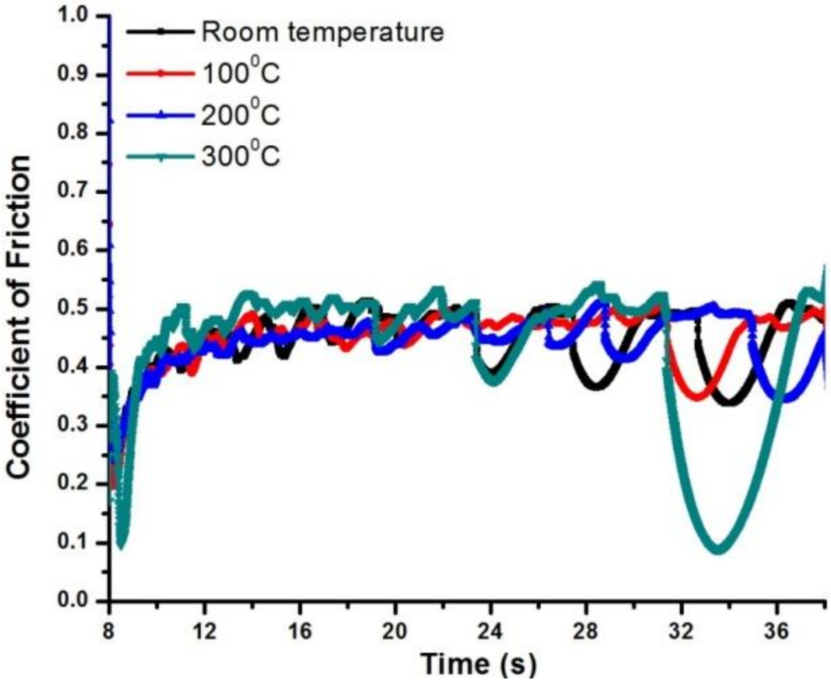

Figure 3.5. Coefficient of friction of ZnO thin films on glass substrate.

The coefficient of friction (COF) is ratio between lateral forces and normal forces during scratch. Frictional forces are dependent on the nature of outermost surface layer of thin film i.e. adsorbed species, roughness, surface structure and topography. Sliding under high normal load involved a plastic deformation followed by several events like micro crack formation, fragmentation of material. The oscillation in friction coefficient provides the information about pile up, nano scale fracture, wear properties and adhesion. When the hard materials (indenter) slide on relatively softer material, the friction force arises due to shear component. Initially, COF of the films is found to be increasing with roughness of the films [177]. The roughness has a pronounced effect on mechanical properties of films at shallow penetration depth. The COF is higher for rough surface and its increasing value leads to increasing shear stress at the interface, resulting in a reduced critical load for adhesion [178]. The coefficient of friction of the ZnO thin films has varied between 0.1 and 0.5 as shown in Fig. 3.5. During initial phase of scratch segment, the ZnO thin films at 300^0C has highest coefficient of friction (~0.5)

3.1.4.1 Surface and Compositional analysis

The high resolution FE-SEM images shows the as grown ZnO thin films are smooth, uniform and fully covered. The grains are showing columnar type growth and very densely packed for the films deposited at room temperature. There is no observation of inclusion or voids in thin film. The initial grain growth and shape of grains depend on the substrate temperature as well as thickness of films. As compared to X-ray diffraction, the grains are larger in FE-SEM study, as in the former, grains are those domains in crystal that scatter the X-rays coherently, while in the latter, the grains are agglomerated to larger grains in size [179].

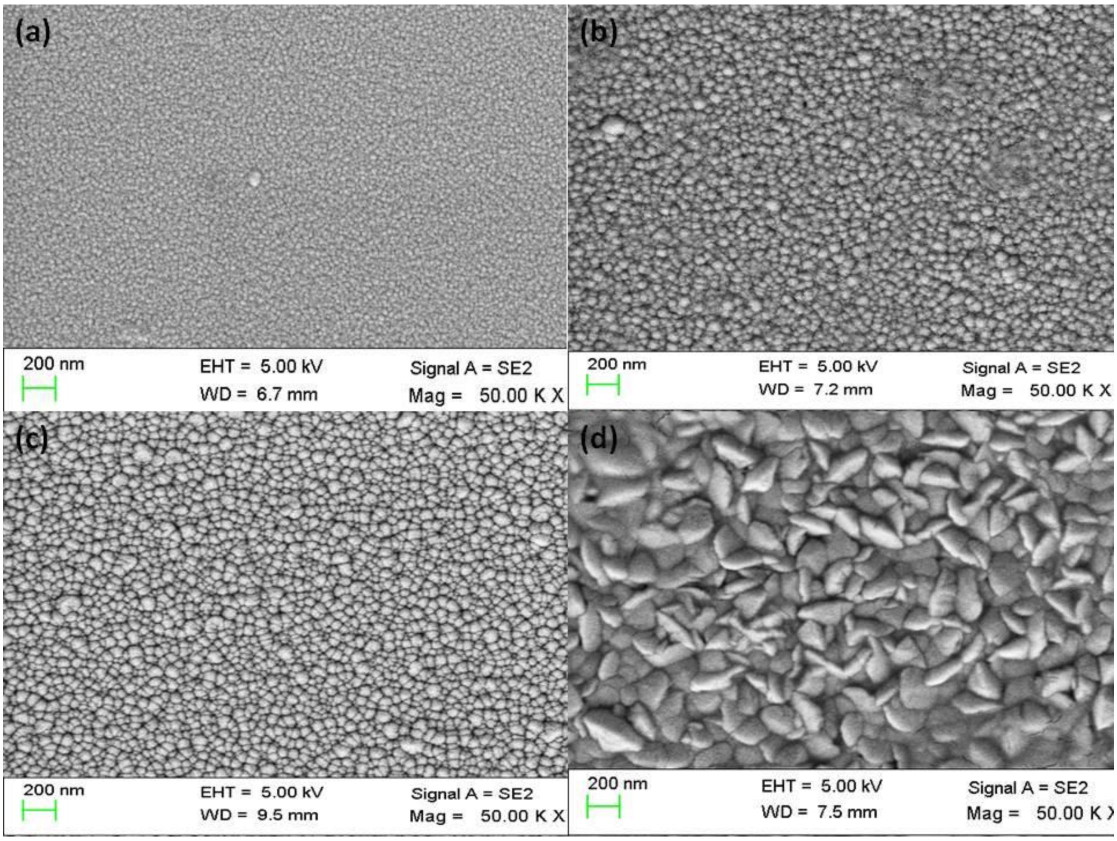

Figure 3.6. FE-SEM analysis of ZnO thin films at substrate temperature (a) RT (25^0C), (b)100^0C, (c) 200^0C, (d) 300^0C.

The ZnO thin films deposited at lower substrate temperature have low adatoms mobility and shadowing effect and therefore the films prefer to grow for minimizing free surface energy, i.e. *c*-axis orientation normal to substrate with columnar microstructure [180,181]. At higher substrate temperature, thin film has the sufficient amount of kinetic energy and mobility to overcome self-shadowing effect. The observation is in tandem with XRD results, with the change in crystal orientation, the microstructure features also get altered. The crystallographic orientation also affects the grain morphology and the grain becomes faceted, elongated and wedge like structure at 300 ^{0}C substrate temperature [182]. It is evident from Fig. 3.6, and Fig. 3.7 that the ZnO thin films is uniform, smooth, and dense having columnar structure.

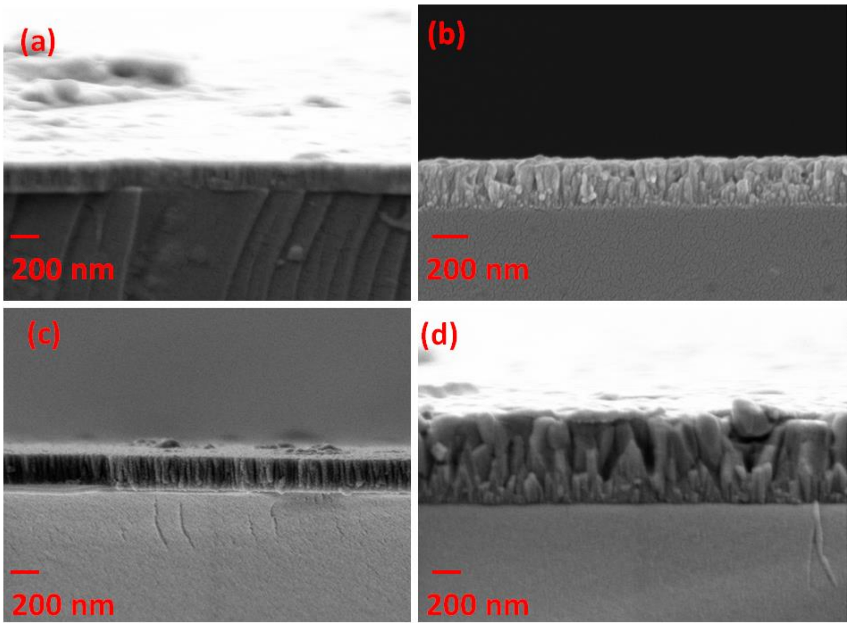

Figure 3.7. ZnO films thickness at substrate temperature (a) RT (25^{0}C) (b) 100^{0}C (c) 200^{0}C (d) 300^{0}C.

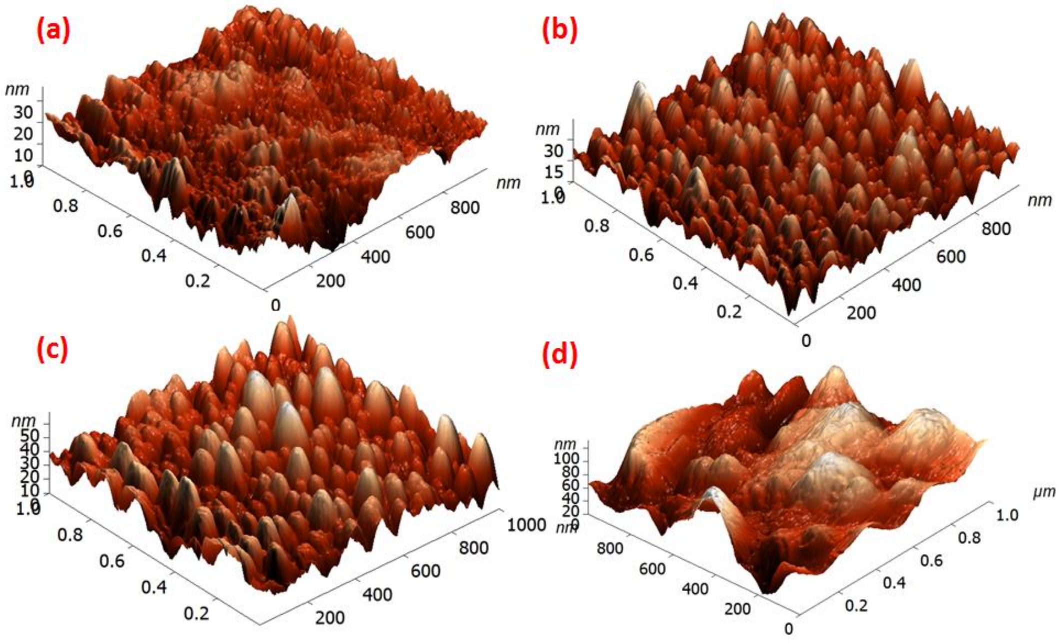

Figure 3.8. AFM images of ZnO thin films at substrate temperature (a) RT (25 ^{0}C) (b) 100^{0}C, (c) 200^{0}C, (d) 300 ^{0}C.

The elemental composition of O & Zn pattern of thin film is obtained by EDX analysis, provided in Table 3.1. The presence of Zn and O is verified in thin films. The surface topography is investigated by atomic force microscopy in tapping mode, scanning the area 1 µm × 1 µm shown in Fig. 3.8. It is observed that substrate temperature strongly influence shape, size and distribution of grains of ZnO thin films.

The topography of ZnO thin films are uniform and well-shaped except films deposited at 300^0C, where grains start coalescence with each other. The RMS value of the roughness of films increases with the substrate temperature shown in Table 3.2. Higher substrate temperature provides higher kinetic energy for mobility to incident sputtered species on substrate, resulting higher probability to agglomeration that leads to bigger grains in size. When the indenter and film surface come in contact, the distribution, height and geometry of surface asperities affect the contact mechanics and deformation behavior as compared to flat surface of films. Due to un-evenness of surface, indenter cannot sense real hardness value at shallow depth. For the planar contact and fully developed plastic zone beneath indenter, the film should have minimum surface asperities. The critical load is found to be decreasing with increasing surface roughness [183]. This result is consistent with X-ray and FE-SEM results confirming the better crystallinity and bigger grain size with increasing substrate temperature.

3.1.5 Conclusion

The ZnO thin films were deposited on glass substrate at different substrate temperatures RT (25^0C) to 100^0C, 200^0C, 300^0C by DC sputtering. The different texture and micro-structural features of films observed were used to substantiate the deformation behavior of the films.

- The increment in grain size of ZnO films and reduction of lattice strain were observed at elevated substrate temperature. The (002) diffraction plane is prominent crystal plane, concomitantly (103) crystal plane grew with higher substrate temperature. The anisotropic growth of film in particular crystal plane depends on the thermal mismatch (substrate-film), surface energy minimization and strain energy. The emergence of non-polar planes leads to variation in atomic density and tends to change interfacial shear stress which further deteriorates the mechanical performance of films.
- No major discontinuity in displacement during indentation is observed, ruling out the possibility of cracking, delaminating, or mechanical failure at the normal applied load. The hardness (7.72±0.44 GPa) and Young's modulus (127.38±13.96 GPa) of ZnO is

observed to be higher for the films deposited at 100^0C substrate temperature with better adhesive strength (3126.7 µN).

- The morphology of the films is observed to be columnar to wedge shaped at 300^0C substrate temperature. Higher surface undulation leads to higher friction coefficient and lower *H/E* ratio.

3.2 ZnO THIN FILMS DEPOSITED ON FUSED QUARTZ SUBSTRATE: DEPOSITION PRESSURE VARIATIONS

3.2.1 Introduction

In modern era, multi-functionality in nanostructured thin films paves a way to design and develop nanotechnologies for promising applications such as in optoelectronics, MEMS devices, corrosion and heat resistant devices etc. [184,185]. Huge usage of thin films devices generate a reliability issue and a risk of mechanical failure including fracture, fatigue, damage and possibility of cracking and delamination during handling of devices [16]. The mechanical characteristics of thin films significantly affect device fabrication and reliability during service conditions. Several factors like crystallinity, internal stress, grain size, defects and dislocation etc. can affect mechanical responses of thin films. However, generation of internal stresses affects microstructure, which is highly sensitive to the synthesis conditions as well as the underlying substrate properties. High internal stress itself may cause failure of thin films [186]. The process conditions in synthesis techniques namely physical vapor deposition as well as chemical deposition techniques can be tailored to engineer the microstructure so as to deposit thin films with desirable functional properties [187]. However, deposition of high quality thin films depends on growth mechanisms, uniformity in thickness and better adhesion of films to the substrate depends on the deposition techniques [188].

The conventional instruments based on visually imprint of the Vickers indenter are not useful for the precise measurement of mechanical properties of thin films and nanostructures. Hardness, Young’s modulus as well as adhesion are considered as fundamental mechanical properties of the thin films and therefore it should be measured precisely for the prediction of mechanical stability [189]. Adhesion of the film to substrate referred as mechanical interlocking depending upon interface morphology, thermodynamic state, bond energy and stress etc. [7]. Assessment of adhesion failure using nano-scratch method has recently gained popularity to evaluate critical load of thin films; however, several methods such as tape peeling. abrasive test are reported in the literature much earlier [190]. Nano-indentation and scratch under ramp up loading are now well established technique to obtain hardness, Young's modulus and adhesive strength of thin films [131,136]. The nature of thin films from ductile to brittle character exhibits different failure mechanisms, which can affect the adhesion of films on substrate. Delamination of thin films can be observed during indentation, delamination are more prone to occur during loading segment when the film/substrate interface is relatively weaker as compared to film and substrate material, however if the film/substrate interface is strongly bonded delamination is most probable to occur in unloading segment [191].

ZnO nanostructured films exhibits wide direct band gap, high exciton binding energy, high piezoelectric coefficient, sensing properties, non-toxicity [29,192]. These properties of ZnO can be exploited for fabrication of piezoelectronics devices, UV-photo detectors, gas sensors, and dye sensitized solar cells etc. [193]. Dopants such as Ga, Al, In and N could be used to tailor the optical and piezoelectric properties of ZnO thin films [194]. The commercialization of ZnO based nanostructured devices is heavily dependent on its structural integrity apart from its functional properties. Mechanical properties of ZnO thin films are size dependent and superior as compared to bulk part. The thermal treatment of films could increase its hardness by reducing its defects [195]. The mechanical deformation of bulk ZnO during indentation has shown a discontinuity in load versus displacement curves termed as pop-in event as reported [71]. The pop-in event is also observed in ZnO thin films. The pop-in event is related to the plastic flow in the material, burst out as collection of dislocation in active slip systems [196]. However, discontinuity in unloading displacement is called as pop-out.

The present study was focused to investigate mechanical failure, pop-in/pop-out and peel-off in crystalline ZnO thin films deposited on fused quartz. The influence of sputtering deposition pressure on ZnO thin films underlying mechanical properties was measured. Fused quartz is a substrate of commercial interests and it exhibits a hardness ~9.7 GPa [197]. The soft ZnO films on hard substrate could lead to the effect of pile-up nearby indenter at larger displacements. The plastic flow of material during indentation is inhibiting by hard substrate, which may ultimately lead to incorrect estimation of hardness. However, the effect of hard substrate on soft ZnO thin films is more pronounced when the displacement of indenter is beyond 20 percent of film thickness. Hence, displacement depth should be less than $.2t$ (t=thickness of films) during indention [153]. The micro structural features of the ZnO thin films characterized through FE-SEM and AFM are correlated with the measured mechanical properties.

3.2.2 Experimental detail

ZnO as thin films were deposited on the fused quartz substrate by using DC sputtering. The deposition was performed by using pure ZnO target. Prior to depositions, fused quartz substrates were cleaned using acetone, deionized water in ultrasonic vibrations for 10 min. Further, the substrates dried in the hot air; the ZnO target and fused quartz substrate were mounted in target holder and substrate holder, respectively. The sputtering chamber was evacuated to 2.0×10^{-5} Torr to remove gases present in the chamber. Thereafter, high purity Ar/O_2 gas was introduced in to the chamber. The pre-sputtering was carried out for 10 minutes to eliminate surface contamination of the target. The Argon/Oxygen is introduced at flow rate of 20:5 sccm respectively. The sputtering parameters such as substrate temperature and sputtering power were 100^0 C and 50W, respectively, maintained constant during the deposition. The sputtering deposition pressure is varied from 5mTorr to 10mTorr, 15mTorr and 20 mTorr.

3.2.2.1 Structural study and Roughness measurement

The crystal structure of thin films was analysed by the X-ray diffraction (XRD) carried out with Cu-K_α radiation using X-ray diffractometer. The diffraction data are recorded in the angular range of $25\text{-}70^0$. Thin films consist of nano-grains and its size is calculated by Scherrers formula in Eq. (2.6) [198]. However, in Eq. (2.6), the contribution of non-uniform strain in XRD peak profile is insignificant; the micro strain is developed during synthesis process. It essential to note that micro strain i.e. deviation from perfect lattice arrangement present in thin films estimated by X-ray diffraction peak profile using Stokes Wilson equation using Eq. (2.8) [121]. The ideal crystal is considered to be perfectly arranged while crystal structure deviates in thin film from its perfectly arrangement due to presence of lattice imperfection, vacancies, dislocation, grain stacking faults, boundaries, etc.

The dislocation density (δ) termed as length of dislocation lines/volume and obtained by using G. K. Williamson & R. E. Smallman relation using Eq. (3.1) [157]. The theory suggested that grain boundaries are reduced with higher grain size which could lead to a lower dislocation density at the grain boundaries were calculated. At the same time, the dislocations per unit volume supposed to be isotropically distributed in crystal and lie only along the grain boundary.

The volume fraction of the grain boundaries 'f' is quantified by assuming the crystallites as spherical form with diameter 'D' and surrounded by the shell of thickness 't' regarding it as the grain boundary [199].

$$f = 1 - \left[\frac{D}{D+t} \right]^3 \tag{3.3}$$

Where '*f'* is calculated by assuming t=1 nm (grain boundary width) and '*D*' is crystallite size calculated using XRD peaks. The surface roughness of the samples is analyzed by using AFM operated in semi-contact mode with pyramidal-type geometry of tip having silicon nitride (Si_3N_4) coating. The data is analyzed using software Nova 1.0.26. The surface roughness of the ZnO thin films is presented as root mean square average (RMS) values. The elemental analysis, thickness and morphology of thin films are determined by using FE-SEM/EDS.

3.2.2.2 Nanomechanical measurements

Hardness is the primary mechanical property of the materials, which can be correlated with wear and friction. The Archard's equation calculates volume loss per sliding distance (*Q*) as given below

$$Q \propto \frac{L}{H} \tag{3.4}$$

Where '*L*' is applied normal load and '*H*' is hardness, high hardness will contribute in lower volume loss i.e. good wear resistant properties [171], Although some exceptions to Eq. (3.4) also exists, nanostructured thin films is influenced by number of other factors such as grain size, strain, substrate effect, etc. which affect significantly to mechanical strength [200]. The hardness, effective Young's modulus, and coefficient of friction of these ZnO thin films are measured by Nanoindentor using standard Berkovich diamond tip of ~100 nm radius. Load-displacement profile is a 'finger print' of depth sensing mechanical responses of thin films, which provide hardness and Young's modulus. Nanoindentation measurements were performed continuously in a load controlled mode (50 µN/s; loading rate) in which indenter is moved downward up to maximum load (400 µN). Before performing indentation, parameters like instrument compliance, thermal drift, indenter geometry and indentation size effect should be of taken care [130]. So, it is necessary to calibrate the tip area function and machine compliance which is performed on standard fused quartz (homogenous and isotropic). Before testing of samples, air calibration is performed on indentation and scratch mode. The indentation hardness *H* and Young's modulus *E* of materials is calculated by Oliver and Pharr method [131] discussed in Chapter 2, section 2.3.6.

The indentation hardness is measured using load-displacement curve. The area under the loading-displacement curve is related with the total energy consumed during the whole process. The area under unloading-curve is referred as elastic deformation energy. The scratch test of the ZnO films is performed to get frictional forces arising due to the sliding of Berkovich indenter tip on the sample surface. To get the critical load, normal load is applied continuously in a ramp up mode, until the films gets peeled-off/fractured from the substrate [136]. The normal applied load corresponding to the critical load is referred as adhesive strength of the thin films. The scratch test is performed by applying a normal load of 0-4000 µN with the normal loading rate of 133.34 µN/s for 30 seconds. The scratch length was 10 µm (time; 8-38s) in each test. Several scratch tests are performed to get adhesive strength of the films.

3.2.3 Result and Discussion

The ZnO thin films were deposited on fused quartz substrate at different sputtering deposition pressure from 5 mTorr to 10 mTorr, 15 mTorr and 20 mTorr and shown in Fig 3.9. It is evident from the Fig 3.9. that the films are well crystallized in hexagonal crystal structure (JCPDS Card-891397) with angle $2\theta \sim 33.88^0$ range that corresponds to (002) diffraction plane. The XRD patterns reveal that ZnO thin films grown in (002) diffraction plane and maintained (002) peak of thin films throughout all deposition condition used in this work.

The evolution of (002) diffraction plane during deposition are reported in the earlier literature as outcome of surface energy minimization [201,202]. However, film growth mechanics is governed by the kinetic energy of incident sputter species to the substrate, adsorption and ad-atoms surface diffusion. Surface to volume ratio invokes a driving force for the growing grains in particular diffraction plane to achieve thermodynamical stability. The same was suggested by Drift model, a plane with higher growth rate is more predominant [203]. Assuming the tetrahedral configuration, Fujimura calculated the surface energies of ZnO planes and found that the minimum surface energy in (002) plane leads to growth in columnar fashion [204]. However, evolution of different crystal planes that may be feasible during growth depends upon deposition conditions, also minimum presence of Zn to ZnO ions in sputter plasma favored the formation of (002) plane [205]. So, any change in the ratio of Zn to ZnO ions in plasma leads to further growth of films in different crystallographic orientations. The variation in sputtering pressure substantially changes kinetic energy of striking of ad-atoms, which influence the growth mechanics as indicated by Eq. 3.5.

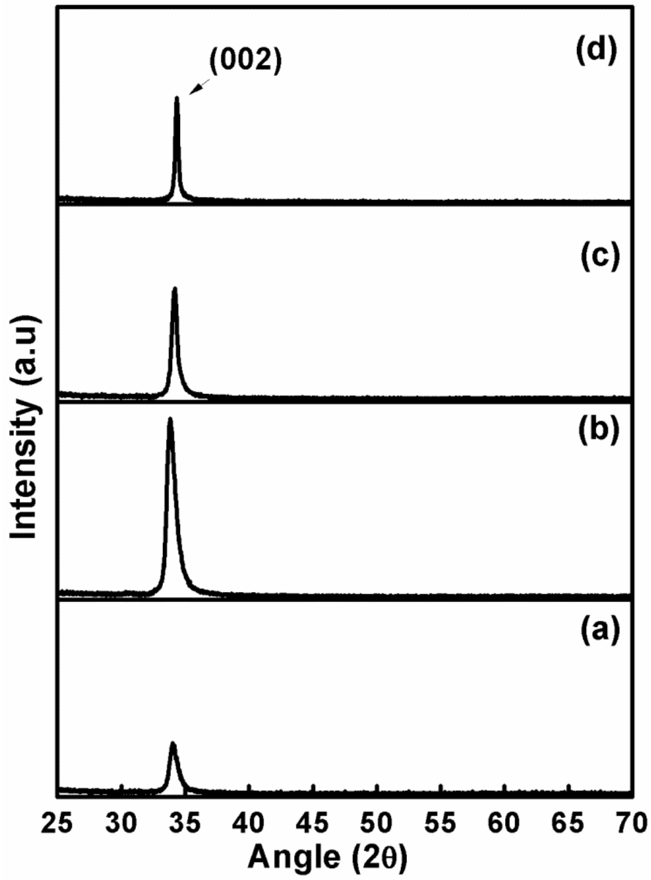

Figure 3.9. XRD pattern of ZnO thin films deposited at (a) 5mTorr (b) 10mTorr (c) 15 mTorr (d) 20mTorr.

$$d_m = 2.33 \times 10^{-20} \frac{T}{(P\,\gamma^2)} \tag{3.5}$$

Where, d_m, T, P, γ are notations used for mean free path, temperature, sputtering pressure and molecular diameter of the sputtering gas, respectively [206]. According to Eq. (3.5), higher sputtering pressure lowers the mean free path facilitating large number of collisions that leads to thermalization effect, which affects the deposition rate [207]. Materials (films and substrate) with different thermal properties could contribute to total strain in the films by deforming the lattice under thermal effect. Thermal expansion coefficient for ZnO is α_a=4× 10^{-6}/K, α_c= 2.49 ×10^{-6}/K, while the fused quartz has thermal expansion coefficient of 0.55×10^{-6}/K [35]. Overall, the growth of films is a complex mechanism and emerged crystallinity is a conjugate function of strain, interface, and surface energy minimization, substrate effect and deposition parameters.

As in Fig. 3.9, the angular position of (002) peaks shift towards higher 2θ side with higher deposition pressure. Concomitantly, peak (002) intensity in XRD pattern rises initially and then falls with higher deposition pressure leads to variation in crystallinity. From the full width half maximum, grain size is calculated by using Scherrers formula and it varied from 12 nm to 28.9 nm. The peak position, crystal *d*-spacing, grain size, lattice strain, dislocation density and grain boundary volume fraction are extracted from (002) diffraction plane and given in Table 3.3. The grain growth is observed with reducing grain boundary volume fraction at higher sputtering pressure. The lattice spacing *d* has varied in the range of 2.64 to 2.60 Å (d_{ref}=2.606 Å, JCPDS Card-891397). The lattice spacing in thin films has decreased with the higher deposition pressure, which led to formation of uniform grains. The lattice strain and dislocation density have also varied with higher sputtering pressure.

Table 3.3. XRD diffraction parameters of ZnO thin films on fused quartz substrate.

ZnO thin films at deposition pressure	Positions of Peak (2θ)	*d*-spacing (Å)	(hkl)	Crystallite size (*nm*)	Grain boundary volume fraction	Dislocation Density (nm^{-2})	Lattice strain (10^{-4})
5mTorr	34.085	2.628	(002)	12.0	0.213	.0069	7.17
10mTorr	33.882	2.643	(002)	12.1	0.211	.0068	10.6
15mTorr	34.166	2.622	(002)	17.0	0.157	.0034	4.24
20mTorr	34.342	2.609	(002)	28.9	0.097	.0011	1.35

3.2.3.1 Hardness and Young's Modulus of ZnO Thin Films

ZnO thin films show anisotropic mechanical properties, vary from polar (*c*-plane) to non-polar planes (i.e. *a*-planes & *m*-planes) [75]. ZnO thin films in polar diffraction plane (002) enables to investigate the mechanical behavior of films deposited on fused quartz. The loading-unloading curves of ZnO thin films deposited at different sputtering deposition pressure are shown in Fig. 3.10. The load-displacement curve directly provides a view of maximum load, displacement and pop-in events. The load is increasing at constant loading rate; the non-linearity observed in load-displacement curve depends on Berkovich indenter (shape of tip, material of tip), response of thin film to applied stress (elastic as well as plastic) and substrate effect.

To achieve the intrinsic properties of thin film material without substrate influence, displacement of indenter should remain $\leq t/10$, where '*t*' is film thickness but this is only effective when film thickness ≥ 1 µm [79]. In the present work, thickness variation is below 1 µm and to preclude the substrate effect, tip rounding effect and the shallow depth of indentation, indentation was performed below 20 % to total thickness.

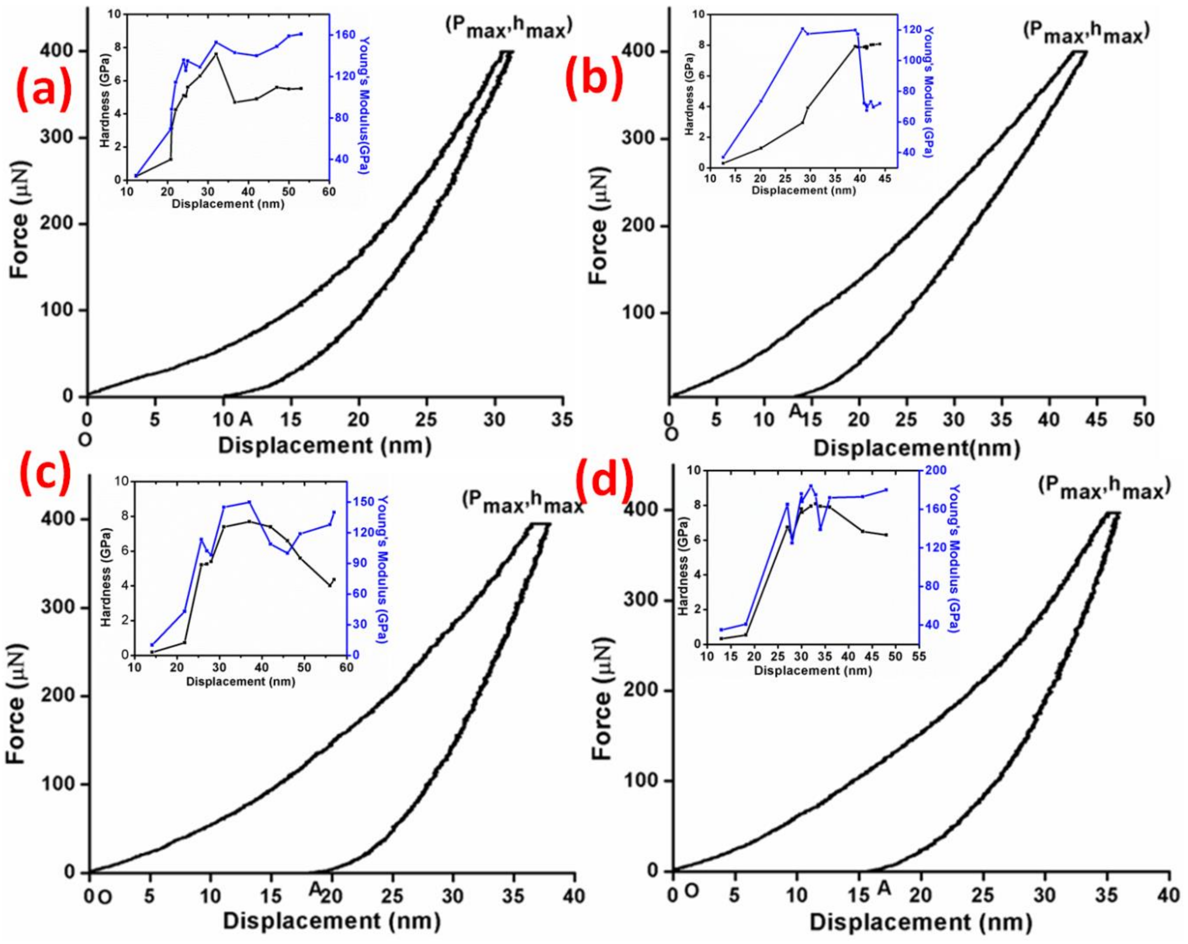

Figure 3.10. Loading-Unloading Curves of ZnO thin films deposited at (a) 5mTorr (b) 10mTorr (c) 15mTorr (d) 20mTorr.

Also, it is visualized from the Fig. 3.10. inset that the load dependent effect on hardness value i.e., indentation size effect is more pronounced at low load indentation and shallow indentation depths [208]. The indentation size effect depends upon several factors such as effect of larger strain gradients, work hardening, geometry necessary dislocations and statistically stored dislocations etc. [209]. In the present work, the indentation was performed at same loading rate on different indentation depths. The hardness of the ZnO thin films is increasing up to indentation depth of~25 nm; it is attributed as transition phase between elastic to plastic contact and after that developed plastic zone is formed for actual hardness.

It is evident from Fig. 3.10. that ZnO thin films are adhering to the substrate without any major discontinuity, and there are no major pop-in event, crack formation, and dislocation burst [84]. However, previous studies found pop-in event in bulk single crystal ZnO as well as ZnO thin films due to pre-existing defects and strain energy of films [64]. A localized stress is developed beneath the indenter after elastic deformation and the presence of serrations in load displacement curve depicts shear band nucleation and propagation, which could lead to plastic deformation. The nature of serration in load-displacement curve is loading rate dependent as it is pronounced more at low loading rate [172].

If the loading rate is slow, discrete shear bands have enough time to accommodate its effect at applied strain leading to distinct strain burst. When the loading rate is increased, the multiple shear bands activated simultaneously might have different deformation with lesser or no serrations [210]. Even in previous studies on ZnO thin films, the multiple pop-in event occurs depending upon the loading rate, and threshold value for multiple discontinuity is increased at higher loading rate in ZnO [65]. Also, the enhanced hardness is reported at higher loading rate for ZnO thin films [211].

Discontinuity persists in displacement curve is minor if it has a magnitude less than 2 nm at the same loading environment [167]. This minor discontinuity correlated the existence of a single event of slip or dislocation movement in the thin films. For the reliability of results, at least 10 indents on each sample were performed. The indents are performed in 20 µm× 20 µm matrix to configure contour map and provide a view of mechanical response of each indent. The map can correlate in a comprehensive way to hardness and Young's modulus analysis at different microstructure regions in an area of 400 μm^2 as shown in Fig 3.11 and Fig 3.12.

As observed from atomic force microscopy that each grain is oriented uniquely at surface, which can be visualized by the interacting force; similarly, each region exhibits a different mechanical response during indentation as shown by color fill contour map [212]. The hardness of thin films along with Young's modulus is given after multi curve analysis in Table 3.4. The deposition pressure affects microstructure and crystallinity of thin films that can be correlated with underlying mechanical properties. In this connection, single crystalline *a*-plane bulk ZnO and *c*-plane oriented bulk ZnO having different hardness value and Young's modulus of 2.2 ± 0.2 GPa, 163 ± 6 GPa, and 4.8 ± 0.2 GPa and 143 ± 6 GPa, respectively [213]. ZnO is soft material in bulk but thin films have high hardness of 6-10 GPa [75]. The plastic deformation in crystalline material primarily depends on the slip events and dislocation movements. Bulk oxides are usually prone to brittle failure but the ductility can be induced by refining grain size to nanometers in thin films. The increment in hardness is contributed by the morphology, dislocation mechanisms, strain, and grain size of thin films [213].

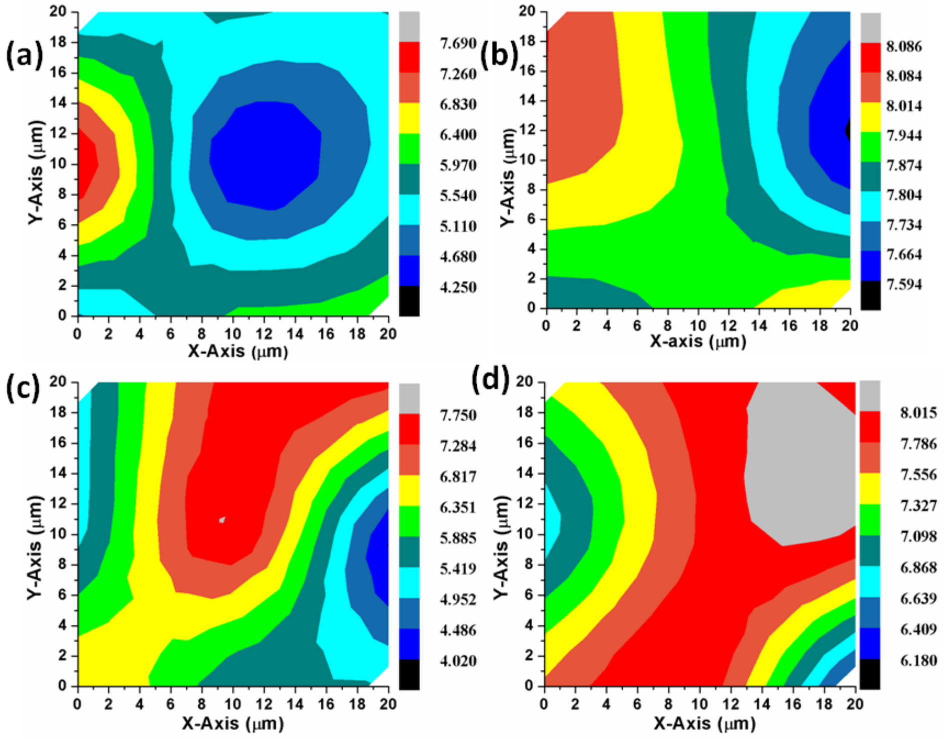

Figure 3.11. Hardness Map of ZnO thin films deposited at (a) 5mTorr (b) 10mTorr (c) 15mTorr (d) 20mTorr.

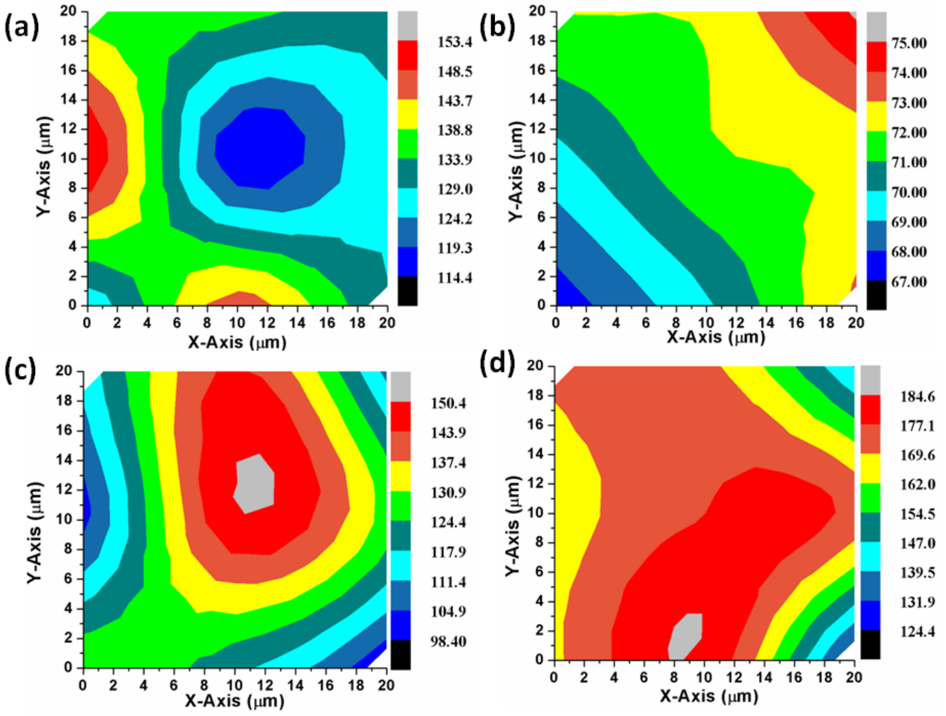

Figure 3.12. Young's Modulus Map of ZnO thin films deposited at (a) 5mTorr (b) 10mTorr (c) 15mTorr (d) 20mTorr.

Even the strain compensation sites, threading dislocations can impede the slip movement, which increases hardness of thin films [64]. The maximum hardness achieved for the films deposited at 10mTorr is attributed to highest crystallinity in polar plane, considered as hard plane in wurtzite ZnO [75]. With the decrease in crystallinity, the hardness also drops to a lower value. Young’s modulus (164.03±18.33 GPa) and high hardness value (7.51±0.60 GPa) are observed for the films deposited at 20mTorr deposition conditions. Frictional forces are governed by adhesive and plowing forces during scratch. The adhesive force is experienced during initial interaction during scratch, while the force needed to deform the material is plowing force. The adhesion is pronounced when indenter applies interfacial shear stress to a critical value to detach films from substrate, primarily depending upon bonding between film-substrate, thickness of the film, tip radius, coefficient of friction, interfacial stress and contact mechanics of indenter to films [214].

The increment in hardness of substrate increases the critical shear stress required for delamination of the films [215]. According to the energy balance theory by Laugier, the energy required to create a new surface must be lower than the released stored elastic energy assuming that films is relaxed after detaching [214]. During the scratch testing, a prescribed normal force is applied in perpendicular direction on thin films with transverse motion using Berkovich indenter; the lateral forces are stored as frictional energy. During ramp scratch mode, plowing force induce plastic deformation in materials affected by grains, grain boundaries and surface topography. A sudden discontinuity in the lateral forces indicates that the films are fractured/peeled-off as shown in Fig. 3.13. Normal load is termed as critical load of the coatings at which this sudden dropdown in lateral forces occurs. So, normal load needed for delamination of films is termed as adhesive strength of the thin films. However, it is also reported that crack initiation starts at lower critical load but it does not indicate complete failure of films. At some higher value of normal load, the film is completely peeled off, referred as upper critical load. Fracture toughness exhibited a dependence on the critical load and proportional to lower critical load, as well as the difference between upper and lower critical load [174]. During the scratch, buckling and peeling observed. The horizontal force needed for delamination depends on several factors such as hardness of film/substrate, shear force per unit area and shear stress at interface microstructure and crystal structure [18]. The smooth lateral force curve indicates high scratch resistance before delamination and high adhesive strength (3043.9 µN) in the films deposited at 20mTorr, caused by low internal stress, higher grain size and high hardness of ZnO thin films.

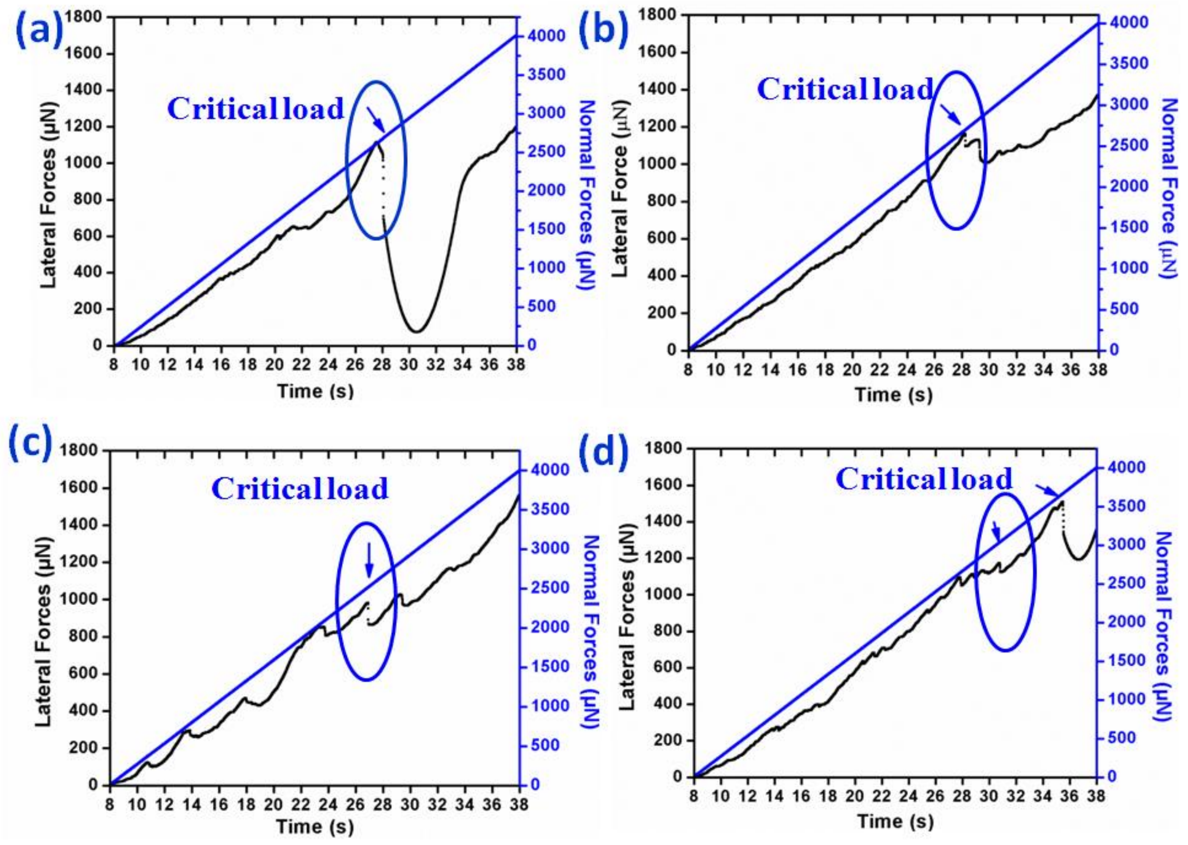

Figure 3.13. Frictional forces of ZnO thin films deposited at (a) 5mTorr (b) 10mTorr (c) 15mTorr (d) 20mTorr.

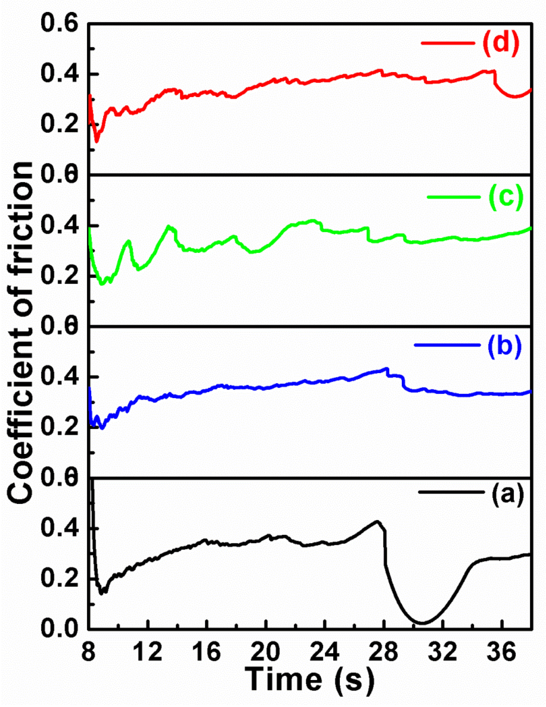

Figure 3.14. Coefficient of Friction of ZnO thin films deposited at (a) 5mTorr (b) 10mTorr (c) 15mTorr (d) 20mTorr.

Table 3.4. Mechanical Properties of ZnO thin films on fused quartz substrate.

Working Pressure (*mTorr*)	Hardness (*GPa*)	Elastic Modulus (*GPa*)	Critical Load (*μN*)	Zn At. *%*	O At. *%*	Roughness (*nm*)
5	5.67±0.90	133±10.8	2685.8	45.78	54.22	8.37
10	7.90±0.14	75±13.37	2680.9	48.83	51.17	6.96
15	6.10±1.20	121±17.1	2515.2	44.33	55.67	5.22
20	7.51±0.60	164±18.3	3043.9	44.66	55.34	4.83

The variations in adhesive strength in terms of critical load depend upon the surface topography as well as microstructure. The critical load is given in Table 3.4. The coefficient of friction is analysed at increasing normal load shown in the Fig. 3.14. It is ratio of lateral forces and normal forces during scratch [73]. The frictional forces arise by the contact mechanics between two solid bodies, indenter and thin films. The stress distribution beneath indenter caused to plastic flow and events like initiation of crack, propagation of cracks and fragmentation of material could occur and appear as oscillation in Fig. 3.14. The friction coefficient gently increases at the beginning of scratch under the influence of plowing force and attain a steady value before any discontinuity.

All the films having low coefficient of friction in the beginning due to lower plowing force contribute less significantly during scratch. However, discontinuity or bursts can be observed in coefficient of friction at the critical load of the thin films. The minor discontinuity can be seen in coefficient of friction, during initial stage of scratch, due the difference in scratch resistance at grain boundaries [216]. The coefficient of friction lies between 0.2 to 0.4 having similar result with previous reports [180].

3.2.3.2 Surface and Thickness analysis

The surface topography of thin films was investigated by using atomic force microscopy in tapping mode, under the scanning area of 2 µm × 2 µm shown in Fig. 3.15. Surface asperities of the films affect the contact mechanics between indenter and films. The nano-indentation process is depth and surface sensitive process and for the precise measurement, plastic zone should be fully developed. The sputtering deposition pressure strongly influences microstructure as well as the topography. At lower sputtering pressure, the grains agglomerated show high RMS roughness.

With the increasing deposition pressure, surface topography has become smooth and uniformly distributed with the columnar type topography. The maximum height of surface particles is also reduced with higher deposition pressure shown in Fig. 3.15. The RMS roughness of films is given in Table 3.4. The grain size of ZnO thin films observed by AFM and XRD may vary; actually the grain size in XRD depends on coherency of grains that give a diffracted signal for measurement. While in AFM, the tip is in direct contact with surface of the sample. .

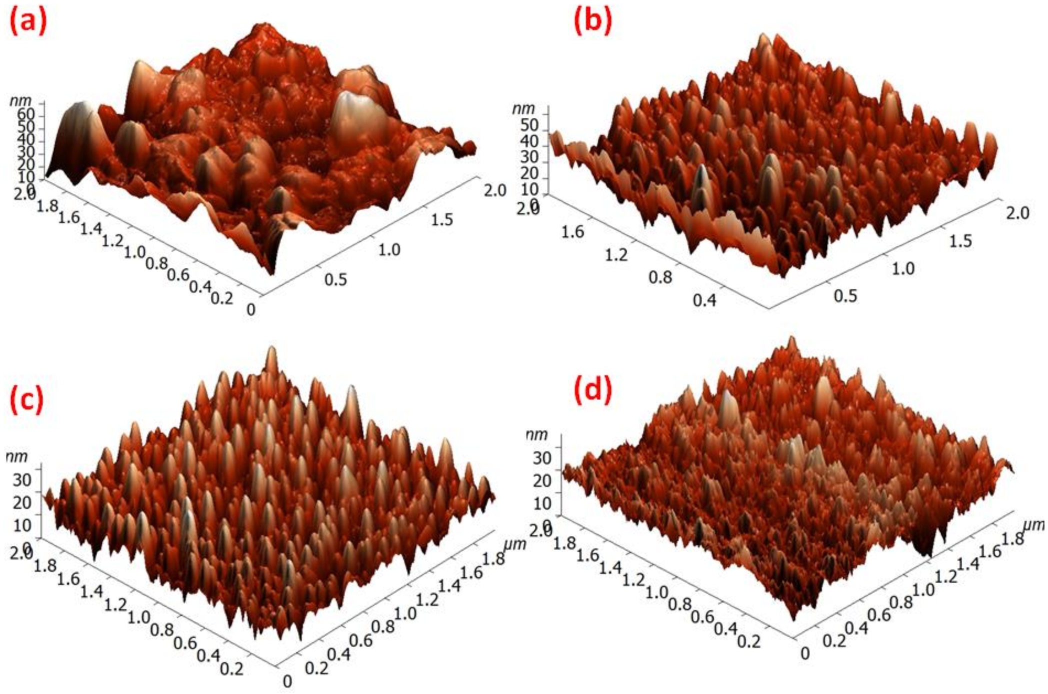

Figure 3.15. AFM images of ZnO thin films deposited at (a) 5mTorr (b) 10mTorr (c) 15mTorr (d) 20mTorr.

The thickness for ZnO thin films is varied between 260 nm to 300 nm as evident from Fig. 3.16.

The grown films are uniformly distributed throughout the interface and oriented normal to substrate in columnar fashion. It can be visualized that film grown at 20mTorr sputtering pressure is densely packed and there is no evidence of voids and crack. As the sputtering pressure is increased, the lateral grain becomes more elongated and aligns to the normal of substrate. The surface morphology of ZnO thin films at different deposition pressure is shown in Fig. 3.16.

The sputtering pressure affects morphology of the films in terms of grains growth as well as the shape of grains. At low sputtering pressure, bigger grains are observed with a heterogeneous nature of interfacial properties as shown in Fig. 3.16 (a). However, the distribution of grains is uniform and homogeneous at higher working pressure. which depends upon adatoms mobility and surface diffusion [180]. The ZnO thin films have dense morphology at 20 mTorr resulting in high adhesive strength. The EDS mapping and EDS spectra is performed to ensure film purity and chemical composition as shown in Fig. 3.17.

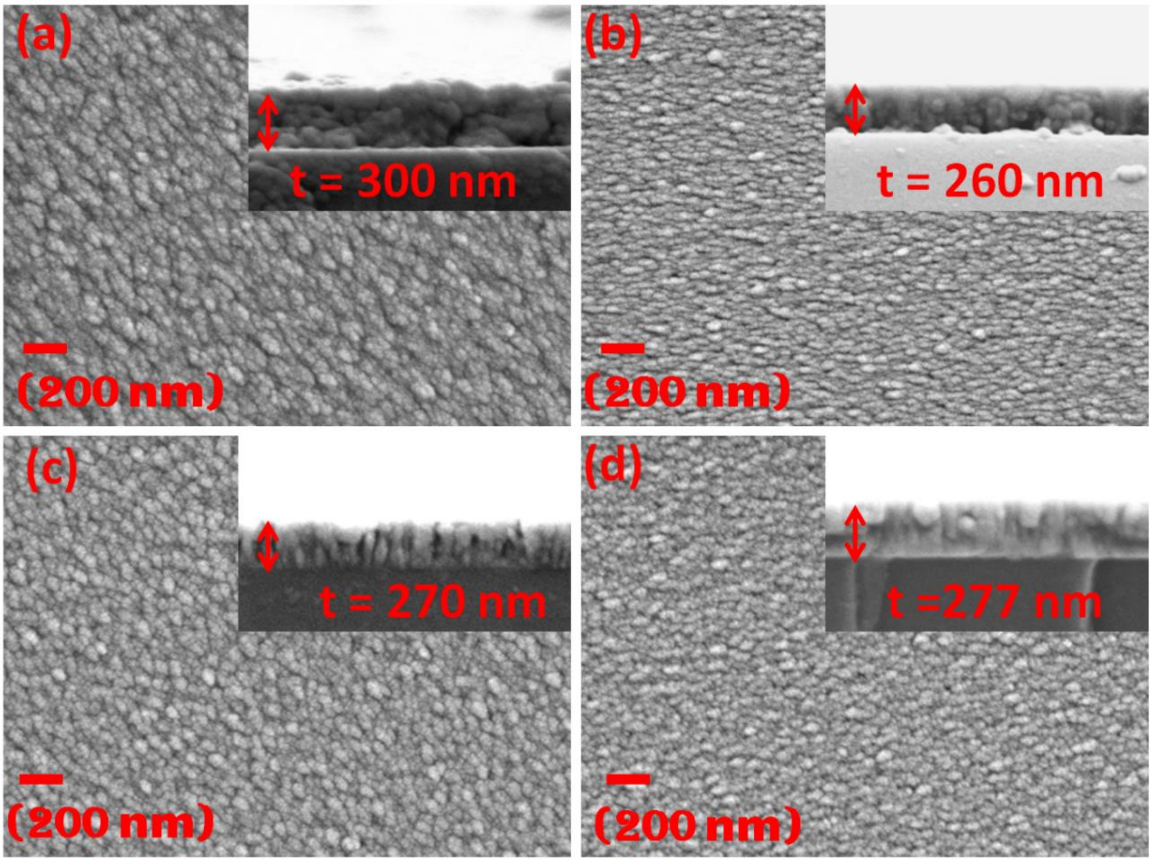

Figure 3.16. FESEM images of ZnO thin films deposited at (a) 5mTorr (b) 10mTorr (c) 15mTorr (d) 20mTorr.

The EDS mapping suggests the uniform distribution of Zn and O element in ZnO thin film area. The presence of peak ~1.0 Kev and ~0.57 Kev in the EDS spectrum is related Zn and O elements, respectively. The Zn and O atomic percentage is given in Table 3.4. The ZnO thin films are oxygen rich; however, the fused quartz substrate can contribute to quantification of O weight percentage as given in Fig. 3.17. The SEM and XRD results of thin films are in accordance with each other and found to be crystalline and columnar growth at higher sputtering pressure.

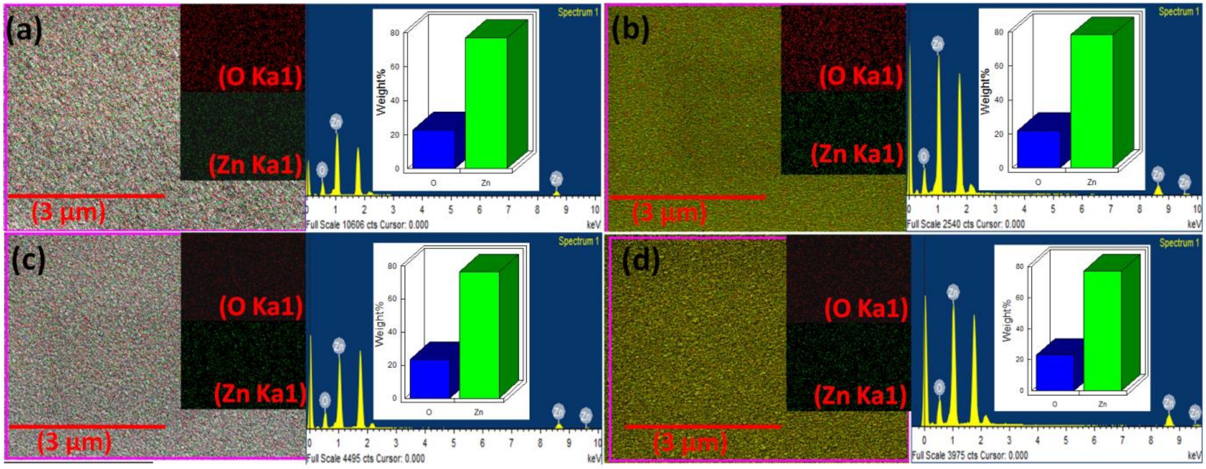

Figure 3.17. EDS Mapping of ZnO thin films deposited at (a) 5mTorr (b) 10mTorr (c) 15mTorr (d) 20mTorr.

3.2.4 Conclusion

DC sputtering was used to deposit highly crystalline growth ZnO thin films on fused quartz substrate. The mechanical properties of films are investigated by nanoindentation technique. The following conclusions are made based on the present work.

- The ZnO thin films were successfully grown on fused quartz substrate at deposition pressure 5mTorr to 10mTorr, 15mTorr, 20mTorr using DC sputtering. The grain size and crystallinity affects the deformation behavior of ZnO thin films.
- The increment in grain size and reduction of lattice strain were observed for the ZnO films deposited at higher deposition pressure. Also, crystalline quality of films rises initially and after that, it deteriorates with deposition pressure.
- The surface morphology of the films was observed as densely packed, crack free and the grains elongated towards the normal of substrate with the increasing deposition pressure. The RMS roughness of ZnO thin films has reduced to achieve smoother surface with denser and uniform grains at high deposition pressure.
- There is no evidence for major discontinuity (pop-in/pop-out) persists in the load–displacement curve, revealed better adherence to substrate and ruled out the possibility of cracking and rupture of film during indentation.
- ZnO thin films deposited at 20 mTorr exhibited minimum lattice strain (1.35×10^{-4}) and higher grain size (28.9 nm) leads to better mechanical properties i.e. high value of hardness (7.51± 0.60 GPa) with better adhesive strength (3043.9 µN) and maximum Young's modulus (164.03±18.33 GPa).

Chapter 4

NANOMECHANICAL AND NANOSCRATCH PROPERTIES OF DOPED ZnO THIN FILMS

The mechanical and tribological properties of doped ZnO thin films have been discussed in detail. This chapter is divided into two sections. First section, **section 4.1** describes the effect of Yttrium doping and substrate temperatures variations on the ZnO thin films. Second section, **section 4.2** describes the effect of deposition pressure on the mechanical properties of Praseodymium doped ZnO thin films deposited on fused quartz substrate.

Contents

4.1 YTTRIUM (Y) DOPED ZnO THIN FILMS

4.1.1 Introduction

Among oxide semiconducting materials, ZnO has been extensively studied due to its great technological impact with unique properties such as high chemical stability, gas sensing, excellent optical, piezoelectric properties and environment friendly with outstanding applications. Wide direct band gap (~3.4 eV), native *n*-type doping, high excitonic energy (60 meV) of ZnO makes it promising material for optoelectronics, UV detection, piezoelectric and chemical sensors based devices [29,217]. ZnO nanostructure offers great flexibility in fabrication route and allows different morphologies with controlled dimensions. Variations in sizes, shapes and dimensions at nanostructured level provides different physical and chemical properties driven by the quantum confinement effect, enhanced surface free energy, higher surface to volume ratio and growth conditions as compared to bulk ZnO.

Apart from the pure ZnO nanostructure, elements of doping/co-doping in host ZnO are of immense research interests to tailor the properties of ZnO nanostructures. Both cation doping Ga^{+3} [218], Al^{+3} [219], and anion doping F^- [220] in ZnO is feasible. Different dopants in certain amounts can be induced in ZnO, which can tailor the specific properties of interest such as optical properties, ferroelectric properties, magnetic properties and piezoelectric properties [29,221]. Moreover, rare earth ions as dopants in host ZnO, provides remarkable properties like reduction of band gap after Ce doping (red shift) [222], Er doping increases the band gap [223], and La doping improves photocatalytic performance [224,225] etc. The Y^{3+} doped ZnO has proven its ability as sensor coating materials, optical materials and band gap narrowing [55,226]. Doping of cations or anions can affect the microstructure by acquiring substitutional or interstitial positions in the lattice [227,228]. Also, new defect states generated depending upon growth mechanism as well as amount of dopants introduced in the matrix compared to pure ZnO thin films.

Doping in thin films is possible via physical or chemical synthesis methods at different deposition conditions [7,229]. However, each deposition method has its own merits and demerits, physical synthesis methods have emerged to develop well adhered with high packing density, repeatability and better crystallinity and lower defects in thin films. Sputtering is recognized as the promising technique to develop high quality thin films, also favored by industry with the advantage of large area synthesis and high yield. The mechanism underlying sputtering is kinetic movements of high energetic ions under electric and magnetic fields and different substrate conditions (substrate temperature, substrate angle, substrate surface patterning) provide control over nucleation rate, adatoms mobility, and diffusion on the substrates [7]. Doping in ZnO thin films can be performed using sputtering [230]. Mechanical performance of thin films is foremost and crucial for design and development of devices. Nanoindentation with scratch testing is emerged as a tool with wide acceptance for ensuring precise measurement of the mechanical and tribological properties of nano-sized thin films at low load conditions. The estimation of hardness and Young's modulus is possible by Oliver-Pharr calculation method using load-displacement curve [131]. Moreover, the scratch resistance in terms of lateral force curve of films failure can be achieved in scratch mode under ramp up loading. It is responsible for good adhesion/cohesion, determined by stress state, thermodynamics and bond energy [231]. The mechanical properties of doped ZnO such as Al-doped ZnO thin films [232], Ga-doped ZnO thin films [233], and ZnO-Ag thin films [234] etc. were reported.

The mechanical behavior of Y doped ZnO thin film is scarce in the literature. Therefore, the mechanical properties of YZO thin films deposited at different substrate temperature were investigated in the present work using nano-indentation technique and scratch testing. The difference in coefficient of friction, hardness and Young's modulus of YZO thin films on different substrates were studied. The doping profile of Y^{+3} incorporated in host compound ZnO, micro-structural characteristics such as size, shape, roughness and distribution of grains of the films were analyzed by using XPS, FESEM/EDAX mapping and AFM.

4.1.2 Experimental detail

Y (yttrium) doped ZnO thin films (YZO) were deposited using DC-sputtering simultaneously on glass substrate and fused quartz substrates at different substrate temperature (RT˜25^0C and 100^0 C) using ZnO: Y_2O_3 (98:2 at. %) target. Glass and Fused quartz substrates were cleaned, placed in sputtering chamber. A base pressure of 4×10^{-6} Torr was set up to eliminate the residual gases in the chamber. Thereafter, total gas flow regulated at Ar:O_2 (20:5 sccm) was introduced in to the chamber. Deposition of YZO thin films was performed at room temperature (~25^0C) and 100^0C substrate temperature, while keeping other sputtering parameters fixed. Other sputtering parameters; working pressure, sputtering power were kept at 10mTorr, 55W, respectively, maintained at same level throughout the process.

4.1.3 Coating characterization

The crystallinity of YZO thin films was determined by X-ray diffraction with Cu-K_α radiation. The crystallite size '*D*' using FWHM of YZO thin films was measured by Scherrers formula using Eq. (2.6) [235]. The micro strain developed during growth of YZO thin films by XRD peak profile can be quantified using Stokes Wilson Eq. (2.8) [235]. The surface roughness analysis was performed using AFM in semi-contact mode by pyramidal shaped tip coated with silicon nitride (Si_3N_4). The RMS roughness is calculated using standard deviation in peak to valley difference in height within image area.

$$R_{rms} = \left[\frac{1}{N} \sum_{i=1}^{N} \left(h_i - \langle h \rangle \right)^2 \right]^{1/2} \tag{4.1}$$

Where, $\langle h \rangle$ *is* mean height distance, h_i is the height of i^{th} pixel and N is the number of pixels in the image, Nova 1.0.26 software is used to get AFM Images and roughness. The XPS provides information about stoichiometry and interaction between Y (yttrium) and ZnO. The FE-SEM/EDS is used for characterizing morphology, cross-sectional thickness and elemental scanning of films.

It is well known that high hardness of coatings improves wear properties and friction effect in the films. The mechanical strength of nanostructured YZO thin films is affected by strain, doping, grain size, substrate effect, etc. Nanoindentor with Berkovich tip of radius 100 nm radius was used in the present work. The load (μN)-displacement (nm) provides the deformation behavior in continuous applying of normal load, 0 to maximum load 400 μN (loading rate: 50μN/s). Maximum load is achieved by optimizing the maximum penetration of indenter. The indenter was calibrated for tip area function and air calibration before indentation. The ramp-up mode scratch testing i.e. progressively increasing normal load was applied from 0 μN to maximum-4000 μN for 30 seconds over sliding of scratch distance 10 μm (time; 8-38s) at normal loading rate of 133.34 μN/s [231]. A critical normal load in scratch corresponds to fracture events during sliding of indenter. However, different modes of failure/fracture events are possible depending upon brittle-ductile nature of films.

4.1.4 Result and Discussion

XRD results of nanostructured yttrium doped ZnO (YZO) thin films on glass substrate /fused quartz substrate at substrate temperature i.e. RT to 100^0C is presented in Fig. 4.1. YZO films show preferential *c*-axis orientation, indicating dominantly (002) diffraction plane, confirming wurtzite hexagonal structure (Ref-JCPDS Card, 891397). There is no other XRD peak corresponding to yttrium oxide (Y_2O_3) or yttrium (Y) observed within the detection limit of XRD instrument. Y is incorporated in ZnO and expected on lattice sites rather than forming

Y_2O_3 phase, which implies the substitution of Y^{3+} on Zn^{2+} ion sites. However, films on fused quartz substrate exhibited a diffused XRD peak, corresponding to noncrystalline phase as compared to glass substrate as shown in Fig. 4.1. The distortion of crystalline lattice is more significant on fused quartz, correlated with thermal expansion coefficients of different materials provides a different interfacial stress as well as the thermal energy to facilitate surface diffusion. Also, shifting of XRD peaks may be related to the different ionic radii of Zn^{2+} (0.74 Å) and Y^{3+} ions (0.89 Å) [236]. However, improved crystallinity at higher temperature is attributed to higher adatoms mobility with high diffusion on the substrate.

Several crystal planes emerged on fused quartz depending upon different stress state at interface with incident elements from sputter plasma. Although, preferred orientation in (002) diffraction plane is the effect of surface energy minimization during growth which has favored columnar type growth. Growth and crystalline nature of YZO thin films is manifested through complex mechanism, depending upon the contribution of surface energy minimization, strain, interface, deposition parameters and substrate effect. The FWHM and peak positions extracted from preferential (002) diffraction plane is used to obtain grain size, which is varied from 7.4 nm to 10.2 nm. The lattice strain, grain size, peak position is provided in Table 4.1. There are slight variations in the grain size.

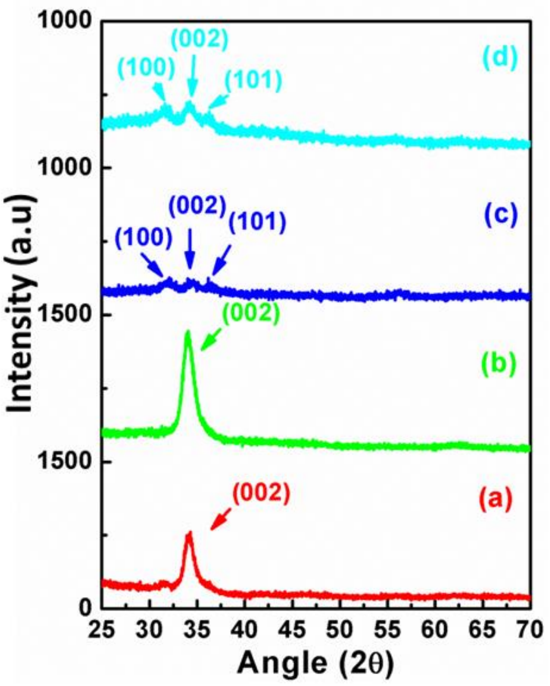

Figure 4.1. XRD pattern of YZO thin films deposited on (a) Glass substrate at room temperature, (b) Glass substrate at 100^0C, (c) Fused quartz substrate at room temperature, (d) Fused quartz substrate at 100^0C.

Table 4.1. Properties of Y doped ZnO thin films.

YZO thin films/substrate	(2θ)	d-spacing (Å)	(hkl)	Crystallite size (nm)	Lattice strain (10^{-4})
Glass at RT	34.111	2.626	(002)	10.2	8.06
Glass at 100^0C	34.008	2.634	(002)	8.7	11.8
Fused quartz at RT	34.422	2.603	(002)	7.4	3.32
Fused quartz at 100^0C	34.212	2.618	(002)	9.4	6.86

4.1.4.1 Nanomechanical and Scratch resistance of YZO thin films

A variation in mechanical properties observed in ZnO depends on crystalline growth and orientations [75]. ZnO in bulk possess lower hardness as compared to nanostructured ZnO thin films, which can sustain higher hardness depending upon the underlying substrate and thickness [68,75,237]. Considering the bonding effect, bulk oxides usually undergo brittle failure, but grain size refinement can introduce ductility in nanomaterial [238]. The Y introduced in ZnO lattice affects mechanical properties because of lattice distortion and new defect state generation. The applied load-penetration depth of YZO thin films is shown in Fig. 4.2.

Indentation load is applied on the indenter penetrated in material surface up to a characteristic depth depending upon elastic-plastic nature of materials and substrate effect. It is established that thin film intrinsic mechanical response can preferably be achieved when indenter movement in sample is ≤ t/10 (t is film thickness) excluding substrate influence, however, effective on thin films with thickness ≥ 1 μm [79]. YZO thickness variation is less than 1 μm, and indentation was performed accordingly below 20% to total thickness to preclude the substrate effect. However, displacement is optimized more than 40 nm in each indentation to overcome the effect of shallow indentation and indentation size effect.

The interface with different substrate material manifests different growth mechanism in different crystal planes driven by surface, mis-orientation of grains and grain boundary related to differently oriented ZnO, which affect overall strength of the films. Hardness of the ZnO thin films found to be increasing at higher substrate temperature (5.06±0.70 GPa). YZO thin films were well adhering without fracturing or delamination to the substrate during indentation, no major discontinuities/pop-in (≥ 2 nm) in displacement is observed due to defects sites of strain consequences. Minor discontinuities predominately related with singular event of slip and propagation inhibited at grain boundaries or substrate [167].

The mechanism responsible is localized stress accumulation beneath indenter, causing shear band nucleation and propagation. Further, It leads to a discontinuity, release stored energy and subsequently particular slip system is activated [167], sometimes as consecutive multiple pop-in event i.e. more probable at higher loading rate in ZnO [65]. Mechanical properties of sample are provided in Table 4.2. The enhanced hardness at higher substrate temperature is due to better crystallinity and crystallite size of thin films.

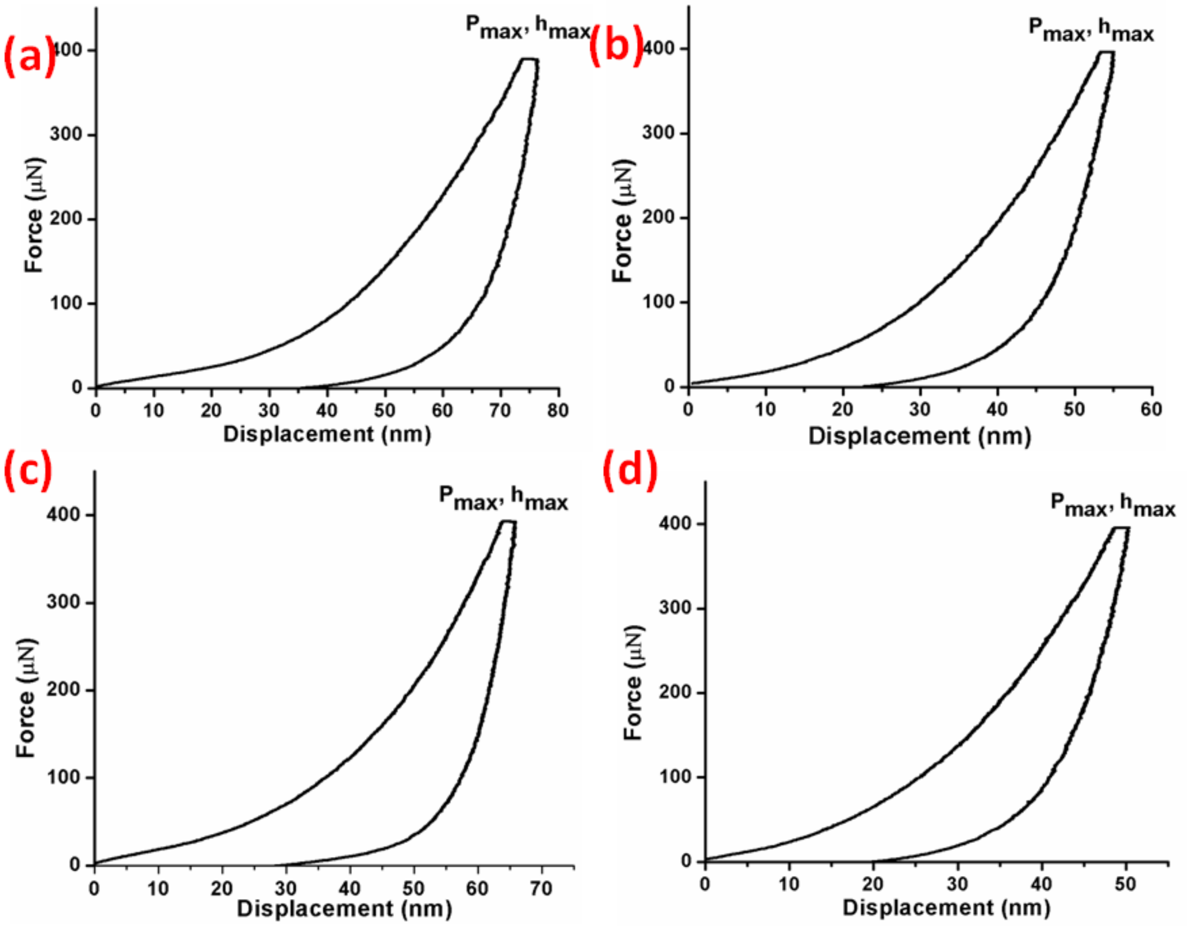

Figure 4.2. Loading-Unloading Curves of YZO thin films deposited on (a) Glass substrate at room temperature, (b) Glass substrate at 100^0C, (c) Fused quartz substrate at room temperature, (d) Fused quartz substrate at 100^0C.

Maximum hardness (5.06±0.70 GPa) was attained for the YZO films at 100^0C substrate depositions, associated with better polar plane (002) crystallinity [68,75]. Also, the films showed high Young's modulus (166.81±16.39) GPa deposited at 100^0C substrate temperature. The ZnO films deposited at room temperature showed poor strength. Frictional forces arise from adhesive and plowing interactions observed during scratch scan.

Initial phase of scratch involved the elastic interaction, while the plastic deformation/fracture occurs at increasing applied forces. However, after doping of Y in ZnO, scratch behavior has changed as a consequence of incorporation of Y^{3+} on Zn lattice sites, which can be seen from previous work [237]. The film strength is affected by bonding between film-substrate as well as constituents of film itself, thickness of the film, stress accumulations and distributions during contact of indenter to films [214]. The higher hardness of substrate is more susceptible to higher shear stress accumulation at interface for delamination of the films [215].

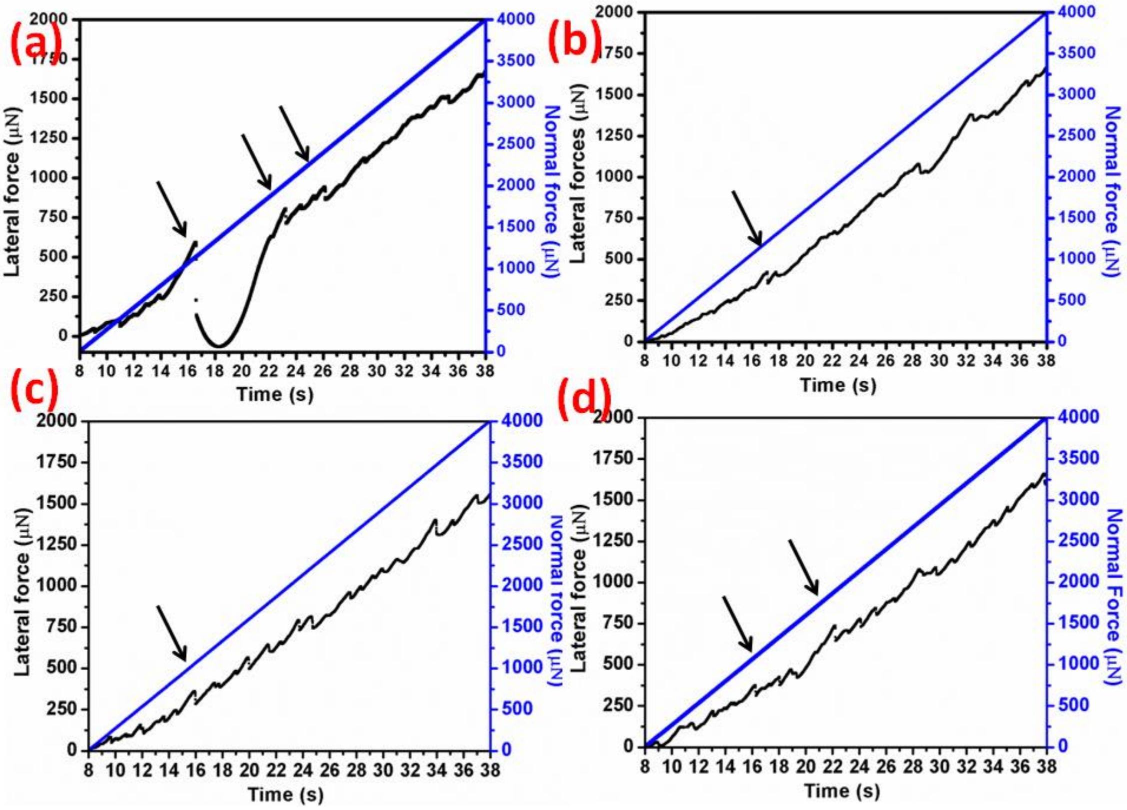

Figure 4.3: Frictional forces of YZO thin films deposited on (a) Glass substrate at room temperature, (b) Glass substrate at 100^{0}C, (c) Fused quartz substrate at room temperature, (d) Fused quartz substrate at 100^{0}C.

Progressively increasing normal load induces a sudden breakout in lateral forces causing damages, is considered as critical load for film failure and usually coating undergoes cracking in brittle coatings. Several consecutive discontinuities in the lateral force curve could appear and first discontinuity is assumed as first critical load of coating as given in Fig. 4.3. Films exhibit sharper and periodic transitions in lateral force causing oscillations under normal ramped load.

Thin films have fractured without bearing significant plastic deformation and several discontinuities in lateral force curve is accounted for lower cohesive nature among its constituents as well as increase in brittle character of coating.

Table 4.2. Mechanical parameter and roughness of Y doped ZnO films.

YZO thin films /substrate	Hardness (*GPa*)	Elastic Modulus (*GPa*)	Critical load L_{c1} (μN)	RMS Roughness (*nm*)	Zn /O At. %	Y At. %
Glass at RT	2.37±0.3	128.86±19.7	1164.4	14.90	46.51/52.3	1.10
Glass at 100^0C	4.22±0.4	156.54±10.2	1210.6	8.10	48.04/50.7	1.18
Fused quartz at RT	2.74±0.1	141.52±6.58	1038.9	15.09	47.72/50.9	1.33
Fused quartz at 100^0C	5.06±0.7	166.81±16.3	1095.2	10.11	47.47/51.2	1.30

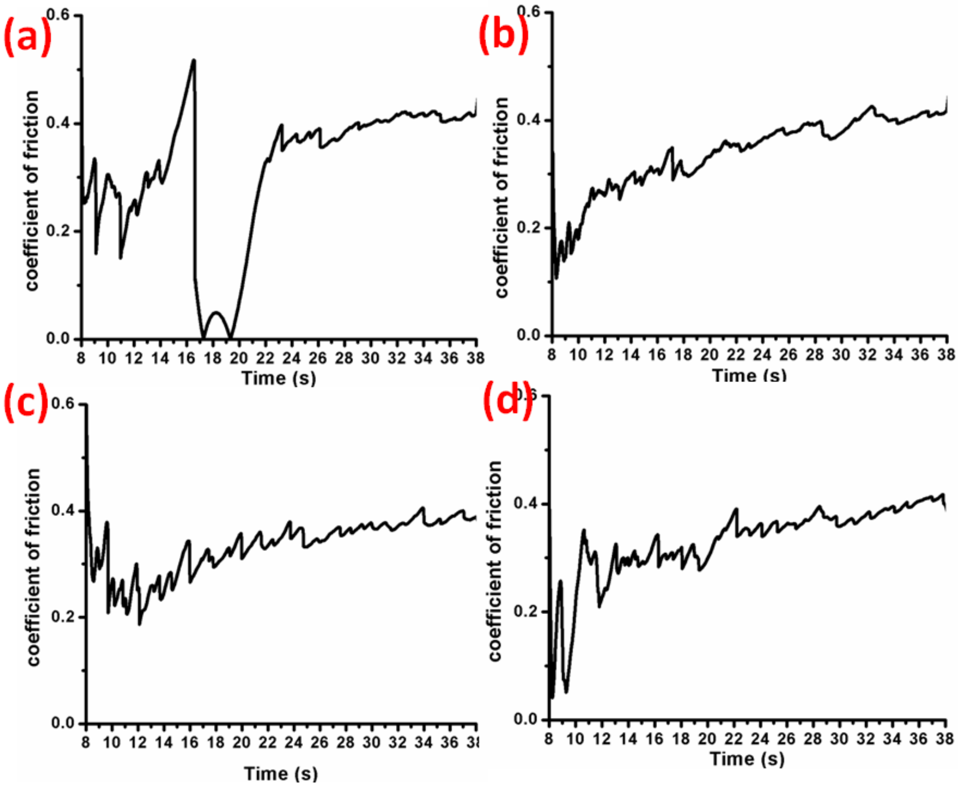

Figure 4.4. Coefficient of Friction of YZO thin films deposited on (a) Glass substrate at room temperature, (b) Glass substrate at 100^0C, (c) Fused quartz substrate at room temperature, (d) Fused quartz substrate at 100^0C.

During the scratch, observed oscillation is related to buckling and chipping in films. The smoothness and oscillation in lateral force curve indicate scratch resistance behavior before fracture. However, film failure is a complex phenomenon involving crack initiation at initial or first critical load and the complete failure is pronounced at upper critical load. The difference in upper and lower critical load significantly affects fracture toughness [174]. Lower cohesive strength among films constituents itself causes lower scratch resistance, which also deteriorates overall adhesive strength of thin films. In general, doping of metallic ions in host ZnO could induce several crystalline defects, which can deteriorate the mechanical performance.

Coefficient of friction (COF) during scratch evaluates the performance of coatings in tribological applications [239]. The curve of COF provides nature of contact between indenter and thin films, particularly forces acting on them. The stress distribution has led to plastic flow and observed as oscillation related with cohesive/adhesive strength of materials as well as crack mechanism after fragmentation of material., Any discontinuity or bursts is related to the fracturing/fragmentation in the thin film. The minor discontinuities in initial segment of scratch are a result of different scratch resistance at grain boundaries. In Fig. 4.4, Oscillations events consist of the initial part of scratch apparent of plowing force, grain boundaries resistance to scratch, roughness attains a steady value [216].

4.1.4.2 XPS and Morphological analysis of YZO thin films

XPS provides compositional analysis of upper surface layer (~10 nm) of YZO thin films. The elemental as well as chemical state of Y and ZnO were analysed as given in Fig. 4.5 and labeled as Zn, Y and O. Fig. 4.5-(b), (c) and (d) show the spectra of Zn (2p), Y (3d) and O (1s). The spectra reveal no undesirable impurities nearby surface regions as shown in Fig. 4.5(a). The selective XPS survey represented here has confirmed better mechanical properties of films deposited over corning glass and fused quartz substrate at 100^0C.

The binding energies of elements are marked using C (1s) photoelectron peak (BE= 284 eV) as reference signal. As shown in Fig. 4.5 (b), the peak emerged at (BE=1020.02 eV) and (BE=1043.09 eV) is associated with Zn $2p_{3/2}$, and Zn $2p_{1/2}$, respectively. These peaks are referred as regular lattice Zn in ZnO [240]. The spin orbital splitting energy between two lines, 23.07 eV lies in the nearby range of standard reference value of ZnO [236].The O (1s) peak, is deconvoluted to peaks having binding energies as 529.2 eV, 530.02 eV and 530.81 eV shown in Fig. 4.5 (d). Lower peak 529.2 eV is attributed as the O^{2-} ion presence in the local sites of wurtzite structure of Zn-O bonds [240].

The intermediate binding energy of 530.02 eV is the oxygen deficient regions within the YZO matrix and intensity of this peak may be attributed to the oxygen vacancies [241]. The peak at binding energy of 530.81 eV indicates the traces of loosely bound oxygen such as adsorbed H_2O or O_2 on the surface of YZO films [241]. Fig. 4.5(c) shows the XPS spectra Y (3d) regions, and two deconvoluted peaks observed as 157.5 eV and 159.6 eV, which are referred as Y $3d_{5/2}$ and Y $3d_{3/2}$, respectively, indicating the oxidation state as trivalent in nature [236]. However, slight variation is noticed as compared to standard values of Y $3d_{5/2}$ and Y $3d_{3/2}$ as a consequence of variation in Y-O distance in ZnO lattice as compared to pure Y_2O_3 [236,242].

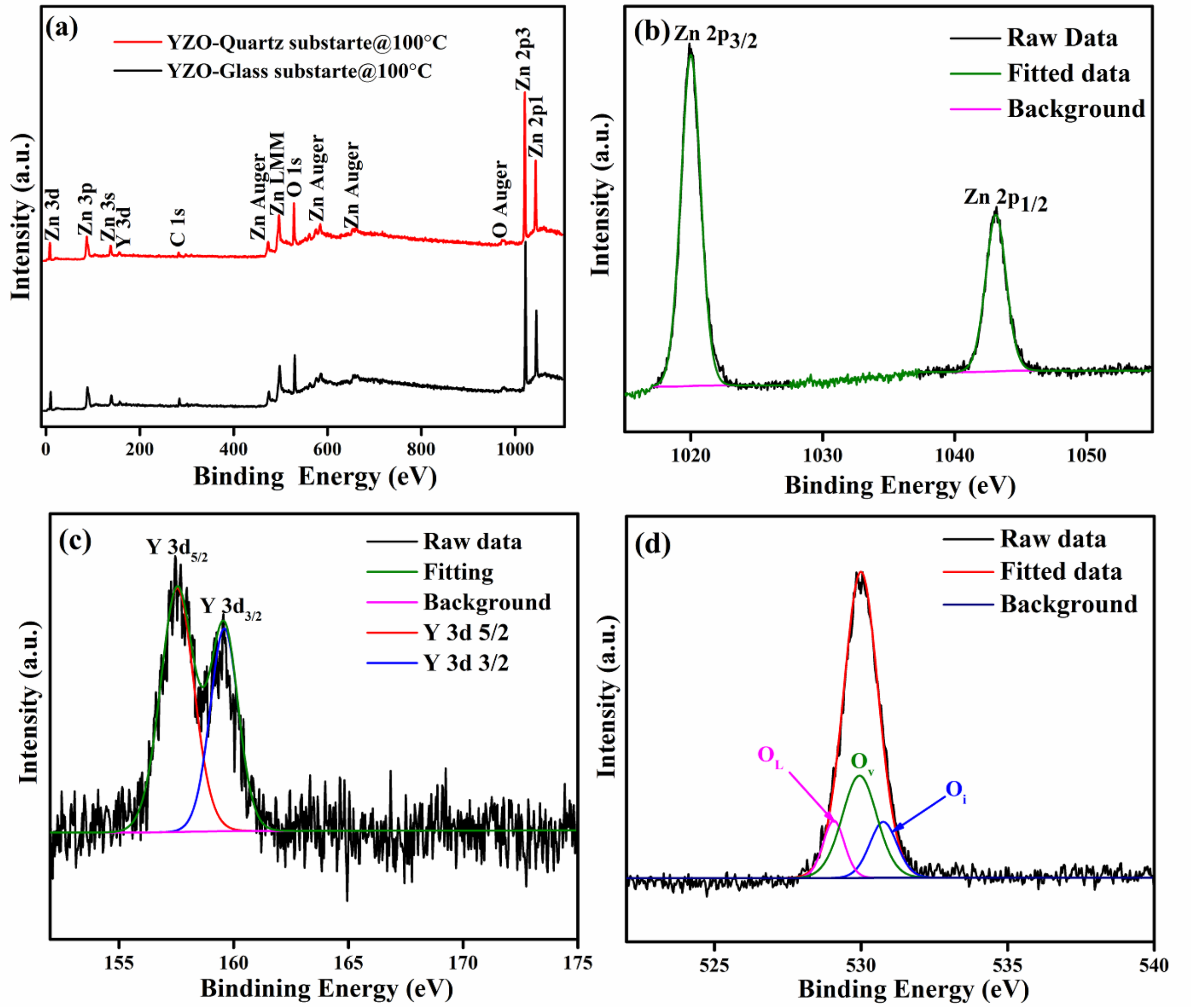

Figure 4.5. XPS spectra of YZO thin films (a) Full survey (b) Zn (2p) spectra (c) Y (3d) spectra (d) O (1s) spectra.

The RMS roughness of the YZO thin films was measured using the AFM operated in tapping mode in region of 2 µm × 2 µm as shown in Fig. 4.6. The grain distributions in the films deposited on corning glass substrate show elongated grains, distinct and length of grains is reduced at higher substrate temperature, while grains in the films on fused quartz are agglomerated. Thin films with lower roughness provides flat surface for indentation and mechanical properties can be evaluated precisely at even low penetration depth. The films deposited at room temperature show high RMS roughness as compared to films deposited at 100^0C substrate temperature as shown in Table 4.2.

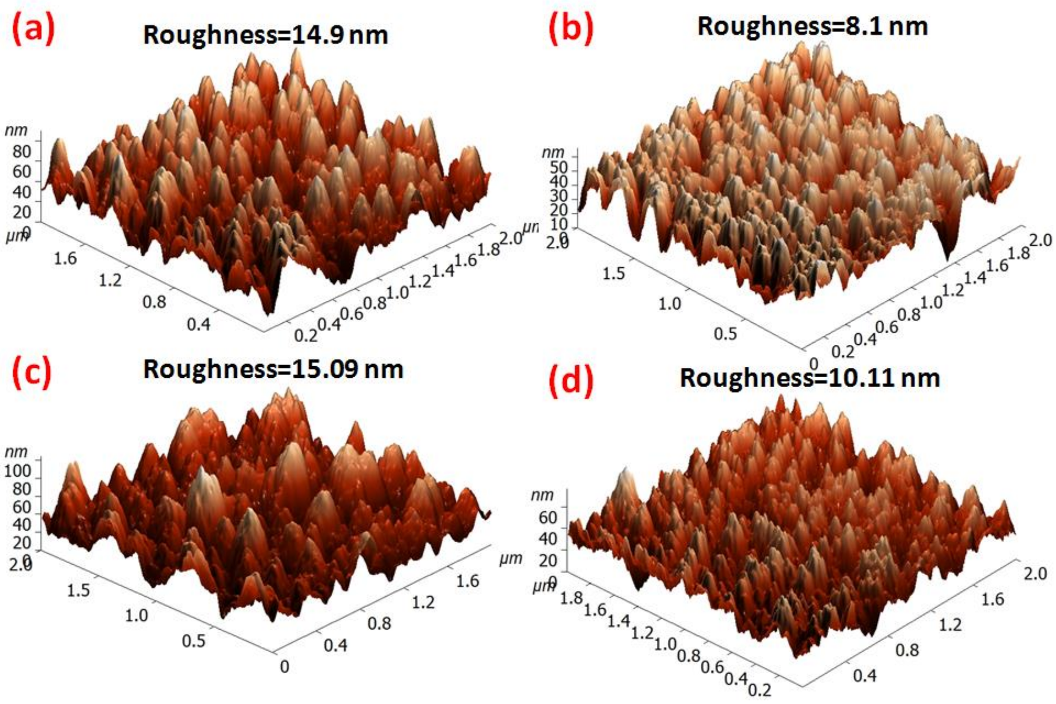

Figure 4.6. AFM images of YZO thin films deposited on (a) Glass substrate at room temperature, (b) Glass substrate at 100^0C, (c) Fused quartz substrate at room temperature, (d) Fused quartz substrate at 100^0C.

Moreover, the roughness of films is found to be higher on quartz substrate. The substrate temperature strongly influences grain growth as well as microstructure and decreased roughness is attributed to the effect of fine grain size as well as high thermal energy provided to adatoms for settlement. The high temperature imparts the sufficient energy for structural rearrangements. The surface topography becomes smooth and uniform with the columnar shape at higher substrate temperature. Grain size of YZO thin films observed by AFM and XRD vary and grain size is reduced at high temperature [180].

The same observation is established by FESEM micrographs showing agglomerated grains without sharp and clear boundaries on quartz substrate. Thickness of YZO thin films is found to be between 520 nm to 640 nm for different deposition conditions, measured by cross sectional FESEM analysis of films. However, it can be visualized from Fig. 4.7 inset, YZO films growth is uniformly and evenly spread throughout composed of small grains and films grown at

100^0C substrate temperature is more densely packed faceted kind of grain boundaries as seen in Fig. 4.7.

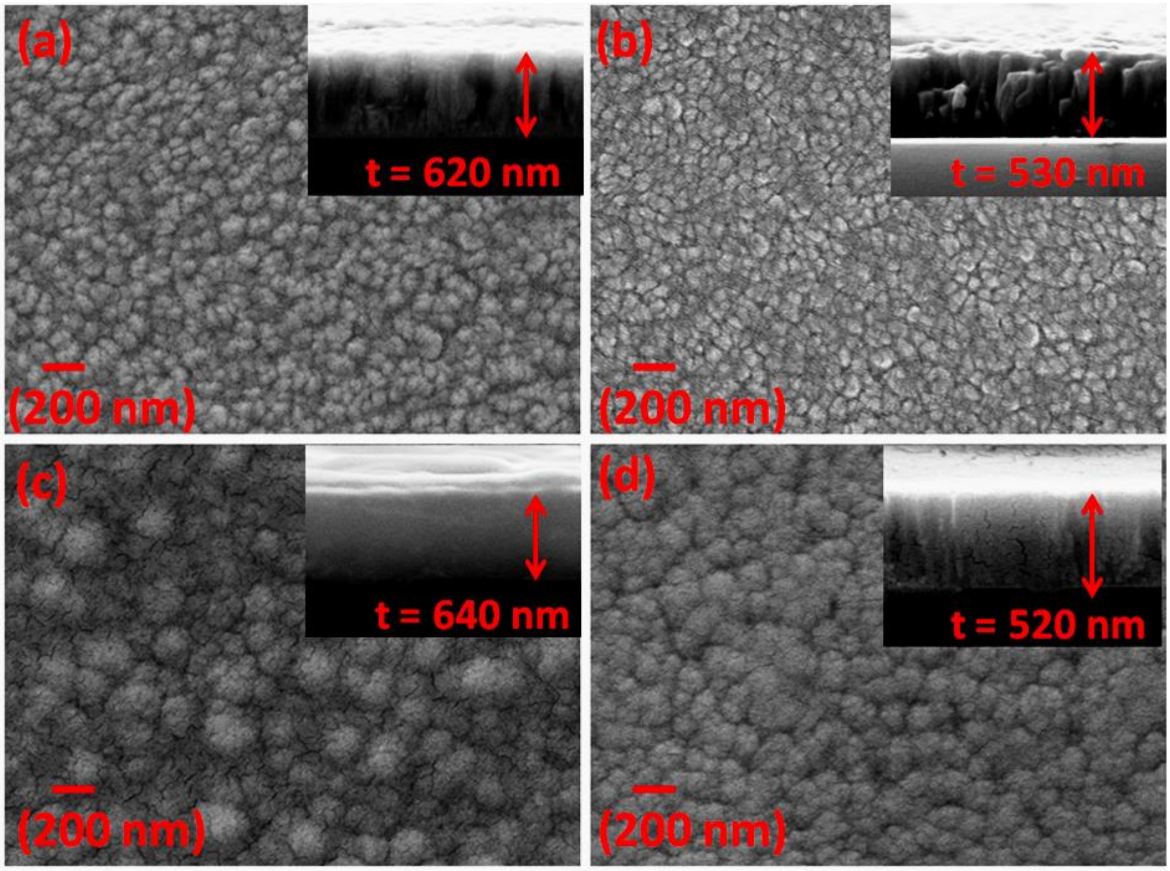

Figure 4.7. FESEM images of YZO thin films deposited on (a) Glass substrate at room temperature, (b) Glass substrate at 100^0C, (c) Fused quartz substrate at room temperature, (d) Fused quartz substrate at 100^0C.

However, the films on fused quartz films morphology show granular shape. The morphology of sputter deposited YZO films varies with temperature in terms of grains growth as well as the shape of grains. At room temperature, large grains observed are agglomerated due the fact that low substrate temperature does not provide enough energy to movement of adatoms for surface diffusion as compared to adatoms at higher substrate temperature. The transition from agglomerated morphology to faceted type structures is attributed to higher thermal energy provided by the substrate. It is observed that films on quartz exhibits more inter-grain connections on RT depositions due to coarsening of grains. The scratch resistance of thin films depends on morphology and nanocrystalline grains with more distinguishable and clear boundaries on glass as compared to fused quartz [243]. The composition of films was measured by EDS mapping along with EDS spectra to ensure film purity and distribution of elements throughout the scanning area (Fig. 4.8).

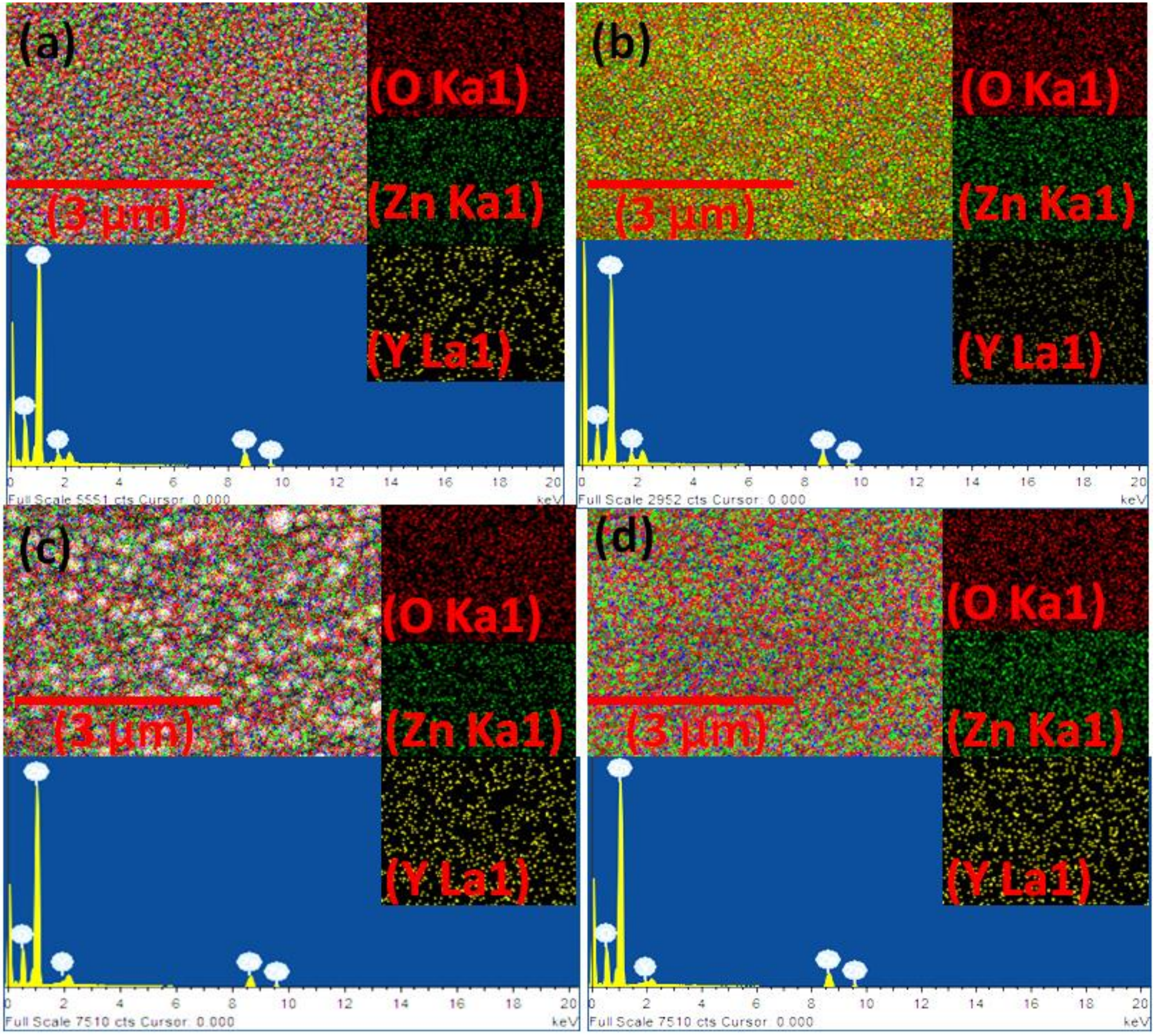

Figure 4.8. EDS Mapping of YZO thin films deposited on (a) Glass substrate at room temperature, (b) Glass substrate at 100^{0}C, (c) Fused quartz substrate at room temperature, (d) Fused quartz substrate at 100^{0}C.

EDS mapping shows a uniform distribution of elements Y, Zn and O in YZO thin film exposed area. The atomic percentage of Y, Zn, and O of ZnO films is given in Table 4.2 and it is found to be oxygen rich. The XRD as well as SEM, AFM results of YZO thin films correlates with each other, observed crystalline growth at higher substrate temperature with columnar morphology.

4.1.5 Conclusion

Highly crystalline YZO thin films were successfully deposited using DC sputtering in the present work. The mechanical properties and tribological behavior of films were investigated and the following conclusions are drawn.

- There is no evidence of XRD peaks related to Yttrium or Y_2O_3 in YZO films and therefore, it is expected that Y acquires substitutional positions in ZnO lattice. Doping profile Y in ZnO thin films were studied by XPS and it has shown the presence of tri-valent oxidation state of Yttrium (Y^{3+}).
- The FESEM and AFM confirm the formation of nanostructured morphology of grains in YZO films, which depend on synthesis condition as well as the substrate material. The inter-grain connections are more pronounced for the films deposited on fused quartz substrate. The RMS roughness is more prominent for the films deposited at room temperature.
- Nanoindentation study of YZO films has shown the high hardness (5.06±0.70) GPa, Young's modulus (166.81±16.39) GPa and critical load (1210.6) µN, for the films deposited at (100^0C) substrate temperature, indicating better adherence of films. However, there is a slight difference between hardness, Young's modulus of the films on both the substrates but the critical load for coating fracture suggested a good scratch resistance on corning glass attributed to better crystallinity.
- During the initial phase of oscillation in scratch at lower normal load are more related to the different scratch resistance behavior at grain boundaries as well as roughness, which affect the contact mechanics of two surfaces.
- The XPS result provided the surface analysis and confirms the incorporation of Yttrium in ZnO host. The same is suggested by EDS mapping with uniform presence of Yttrium throughout the scanning area. Also, presence of oxygen deficient peak at (530.02 eV) XPS analysis could act as defect center which could lead to fracturing of YZO thin films

4.2 PRASEODYMIUM (Pr) DOPED ZnO THIN FILMS

4.2.1 Introduction

Rare earth ions incorporated in ZnO have shown the enhancement of several properties including photocatalytic activity, luminescence properties, gas sensing, magnetic properties and optical properties etc. [53,244]. Moreover, ZnO-Bi_2O_3 or addition of MnO_2, Bi_2O_3, and Co_3O_4 based ceramics are used in electronic devices as varistors due to their nonlinear current-voltage characteristics as well as energy handling capabilities and pyroelectric sensors [245]. Pr_6O_{11}-based ZnO varistors provide substitution for Bi_2O_3-based ZnO varistors [246], and thin films of Pr_6O_{11} doped ZnO can also be used as varistors applications [62,247]. The nonlinear electrical behavior is due to the grain boundary effect, leading to non-linear current–voltage behavior [248].

Even a small amount of Pr content could improve opto-electrical performance [63,244], photocatalytic activity [249–251], photoelectric and luminescent properties of ZnO thin films [61]. In addition, Pr doped ZnO thin films were studied for optical, electrical properties. Nanoindentation technique can provide local information of mechanical behavior of coated system in small region without detaching it from substrate. During nanoindentation, load-indentation depth curve is generated from which hardness and Young' modulus properties can be evaluated.

Nanoscratch on the coated system in the load ramp up mode provides the critical load for coating failure or delamination [84]. In addition, progressively increasing load provides the films damage mechanics throughout whole range of normal and lateral forces as well as viscoelastic properties, phase transformation, friction and wear properties [252]. The nanoscratch test can also probe the cracking, chipping and buckling events observed during the onset of failure in thin films [253]. The bulk ZnO with hardness value of 5.0±0.1 GPa, at penetration depth ~300 nm has been reported [65], which is prone to damage. However, there is considerable difference in hardness depending upon morphologies of ZnO nanostructure [254].

Mechanical properties of ZnO thin films are influenced by crystalline orientation [48], deposition parameters [255], grain size effect [256], different indentation load [211], creep behavior [211] as well as doping element [77,78]. The evaluation of mechanical properties of thin films depends upon the type of indenter such as Berkovich, spherical or Knoop [257,258]. The deformation mechanism by indentation loading is primarily depends on slip events through basal and pyramidal planes in ZnO [66,259]. The literature on mechanical properties of rare earth doped ZnO thin films is limited. Hence, the present work is focused to study the hardness, Young's modulus and scratch behavior of Pr doped ZnO thin films using Nanoindentation technique.

4.2.2 Experimental details

Pr (Praseodymium) doped ZnO thin films (ZnO: Pr) were deposited using DC sputtering simultaneously on corning glass and fused quartz substrate at different deposition pressure e.g. 5mTorr and 10mTorr using ZnO:Pr$_6$O$_{11}$ (97:3 at.%) target. Corning glass and fused quartz substrates were ultrasonically cleaned acetone and dried before putting in sputtering chamber. Afterwards, sputtering chamber is prepared to evacuate residual gases present in the chamber and a vacuum is established up to base pressure of 4.3×10^{-6} Torr. The deposition is carried out at Ar:O$_2$ gas inserted to the chamber and flow regulated at 20:5 sccm.

Sputtering deposition pressure during deposition of thin films was at 5mTorr and 10mTorr, maintaining other sputtering parameters e.g. substrate temperature at 200^0C, sputtering power 50W, target-substrate distance, 4.5 cm constant. In addition, the pre-sputtering was performed to get clean target free from surface contamination.

4.2.2.1 Structural and Roughness Analysis

The crystalline structure of ZnO: Pr thin films were examined using characteristic Cu-K_α with wavelength λ in X-ray diffractometer. The angular spectrum '2θ' varies as $25\text{-}70^0$, crystallite size 'D' were calculated by using Debye Scherrers equation as given in Eq. (2.6) [118]. However, the presence of lattice strain during growth of ZnO:Pr thin films in XRD peak can be quantified using Stokes Wilson equation using Eq. (2.8) [121,260]. The AFM was operated in semi-contact mode using pyramidal tip coated with silicon nitride (Si_3N_4) to measure surface roughness parameters. AFM images were analysed using software Nova 1.0.26. The XPS on the films was performed to get stoichiometry and chemical state of Pr (Praseodymium) and host matrix ZnO was analysed. The FE-SEM/EDS is used for morphology, cross-sectional thickness and elemental scanning.

4.2.3 Nano-mechanical Analysis

Mechanical properties of thin films depend on growth, crystal structure and affected by doping, strain, grain size, substrate effect etc. [200]. Nanoindentor with Berkovich tip of radius ~100 nm radius was used in the present work. The Berkovich tip considered as sharp tip having a three sided geometry, which terminates at the end. However, a transition depth for Berkovich tip beyond that tip act as sharp indenter is 0.09 R, where R is the tip radius i.e. 100 nm [261]. Hence, beyond 9 nm, indenter could be treated as sharp to get elastic-plastic properties. For small depth, area function calibrations were performed on fused quartz same as in present work, which can be applied over the range of 20 nm-7000 nm to ensure reliable results [262].

The load (µN)-displacement (nm) curve provides in depth sensing mechanical responses of spatial location on thin films during loading/unloading segments [131]. However, the consumed total energy pertained to whole process is correlated with the bound area by curve load (P_{max})- displacement (h_{max}), while elastic deformation energy is indicated by area under unloading-curve [263]. Nanoindentation is performed in continuous operating normal load up to maximum load (500µN) in a load controlled mode at loading rate 62.5 µN/s. The maximum load is chosen by optimizing the average penetration of indenter.

Several other factors influence accurate measurement in nanoindentation such as machine compliance, thermal drift, and indentation size effect [130]. The relative mechanical performance is presented here as a function of different sputtering pressure. The scratch testing of the ZnO:Pr thin films is performed using the Berkovich tip to get frictional forces and coefficient of friction. The critical load of film failure i.e. normal load at which a discontinuity in lateral force is observed indicating film material peel-off, could be observed by scratch ramp up mode [136]. However, failure events could be related to several mechanisms related to film cohesive strength, film-substrate adhesive strength and also influenced by material brittle-ductile nature, which overall affect the critical load [264]. The scratch was performed using ramp up normal load of 0-3000 µN with the normal loading rate applied 100 µN/s for 30 seconds. The scratch length was 10 µm (time; 8-38s) in each test. Several scratch tests were performed to access critical load and film failure of the films.

4.2.4 Result and discussion

Nanostructured Pr doped ZnO thin films were deposited on fused quartz/corning glass substrate at sputtering deposition pressure of 5mTorr and 10mTorr as shown in XRD scan (θ-2θ), Fig 4.9. It is observed at 10mTorr pressure; optimized deposition rate is invoked to grow ZnO: Pr thin films preferentially in *c*-axis crystalline orientation with better crystallinity. Films grown at 5mTorr pressure appeared with several crystal planes e.g. (100), (002), (101) and (110), observed as polycrystalline accompanied amorphous in nature. However, crystal structure of thin films deposited on both substrates is found to be standard wurtzite hexagonal crystal structure ZnO (Ref-JCPDS Card-891397) [265].

No separate XRD peak corresponding to Pr element or any impurities/residue is appeared within the detection limit of XRD, as shown in Fig. 4.9. This could be related with low atomic percentage of Pr in ZnO thin films as mentioned in Table 4.3, as well as Pr ions are dispersed in ZnO lattice. Since rare earth dopants having a quite dissimilar ionic radii compared to the Zn^{2+}, so incorporation of Pr ions (Pr^{3+}/Pr^{4+}) radius within the host may cause the replacement of Zn cations or Pr making a separate phase with oxygen change the bonding characteristics within the lattice [62,265]. The crystallinity and microstructure heavily depend on the Pr content in film, even a small amount of Pr ions in ZnO affects crystallites and formation of polycrystalline aggregates as well as the dislocation mechanism along with defect state, which can generate as tailing effect in overall band gap reported in the literature [249].

The different sputtering pressure influencing mean free path could lead to variation in collision frequency, deposition rate and the striking energy of ad-atoms, which affects the nucleation and growth conditions [206]. The similar response observed and marked a difference in crystallinity and crystal orientation in XRD spectra as shown in Fig. 4.9. Self-heating feature in sputtering offers the crystalline films even at low temperature and the crystal orientations could follow surface energy minimization [201].

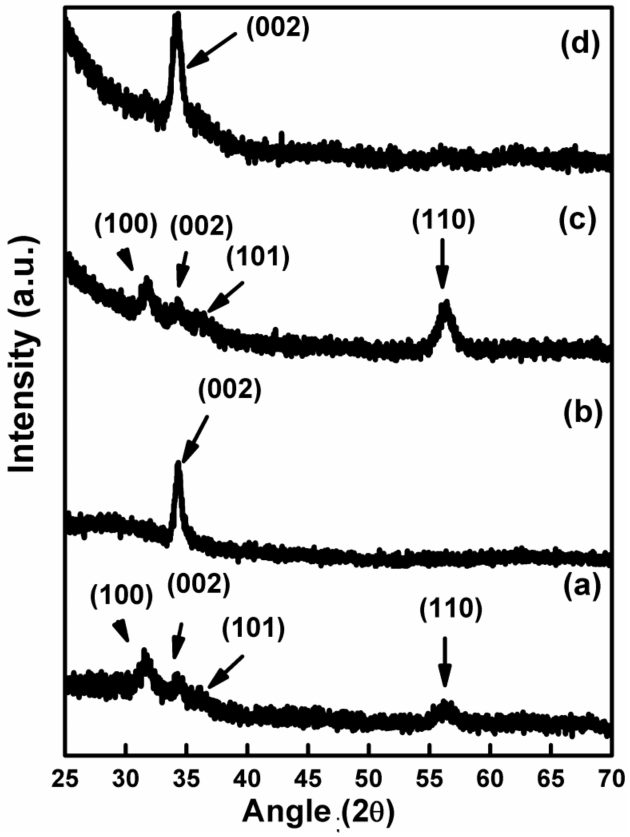

Figure 4.9. XRD pattern of ZnO: Pr thin films deposited on (a) Glass substrate at 5mTorr, (b) Glass substrate at 10mTorr, (c) Fused quartz substrate at 5mTorr, (d) Fused quartz substrate at 10mTorr.

The growth of films observed with single XRD diffraction peak on amorphous substrate, which is without long range crystalline order has special significance for the films deposited at 10mTorr pressure. The full width half maximum extracted from the XRD pattern in Fig. 4.9, as the (002) is common peak at all deposition parameters and calculated crystallite size using Scherrers formula, which is varied from 11.1 nm to 15.0 nm. The peak position in *2θ*, crystallite size, lattice strain, crystal *d*-spacing were provided in Table 4.3. There are slight variations in the crystallite size depending upon the sputtering deposition pressure variation and substrate effect.

Table 4.3. Properties of ZnO: Pr thin films.

ZnO:Pr thin films/substrate	Positions of Peak (*2θ)*	d-spacing (*Å*)	(hkl)	Crystallite size (*nm*)	Lattice strain (10^{-4})	Zn /O At. *%*	Pr At. *%*
Glass at 5mTorr	34.353	2.608	(002)	11.1	3.37	24.12/75.71	0.16
Glass at 10mTorr	34.307	2.611	(002)	14.2	3.26	23.66/75.90	0.44
Fused quartz at 5mTorr	34.300	2.612	(002)	15.0	3.18	20.43/79.20	0.38
Fused quartz at 10mTorr	34.200	2.619	(002)	12.3	5.38	33.97/65.79	0.24

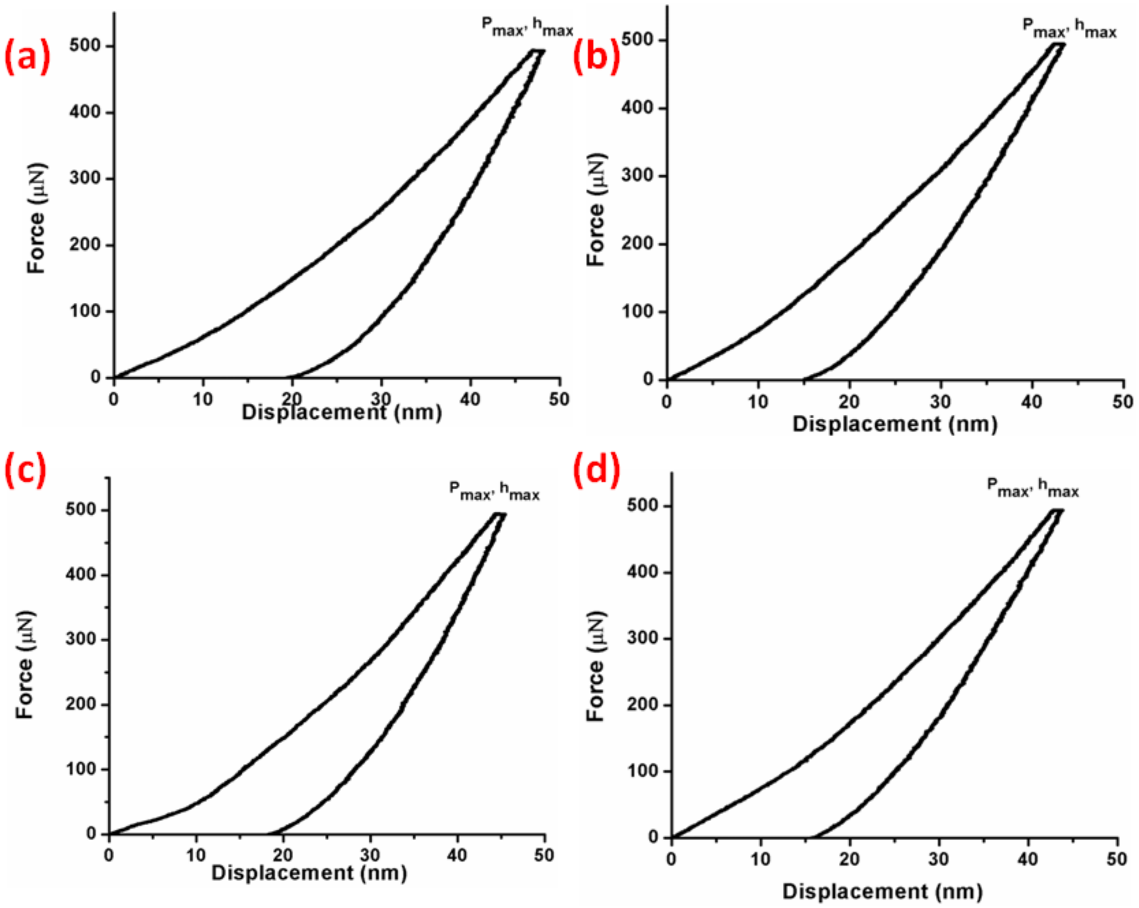

Figure 4.10. Loading-Unloading Curves of ZnO: Pr thin films deposited on (a) Glass substrate at 5mTorr, (b) Glass substrate at 10mTorr, (c) Fused quartz substrate at 5mTorr, (d) Fused quartz substrate at 10mTorr.

4.2.4.1 Nanomechanical and Scratch Crack Propagation Resistance of ZnO: Pr Films

ZnO thin films show variations in mechanical properties depending upon the size scale as well as crystalline growth and orientations of films [68]. Defect free ZnO thin films usually follow higher hardness than bulk depending upon the microstructure [64]. In addition, the ionic and covalent bonding in lattice affects the mechanical properties as well as failure in the films is altered by introducing a foreign element/impurity in the lattice, which leads to the formation of new defect states [65]. The Pr ion introduced in ZnO lattice could result in similar change and influence its mechanical properties. The experimental observation during loading-displacement-unloading segments of ZnO: Pr thin films at different deposition pressures are shown in Fig. 4.10. Indenter loading is increased from 0- 500 µN and it penetrates in material surface up to optimized depth depending upon elastic-plastic nature of materials. The penetration depth of indenter should not exceed in sample beyond ≤ t/10 (t is film thickness) to avoid substrate influence. However, it is valid to the samples where thickness of the coatings is ≥ 1 µm [79].

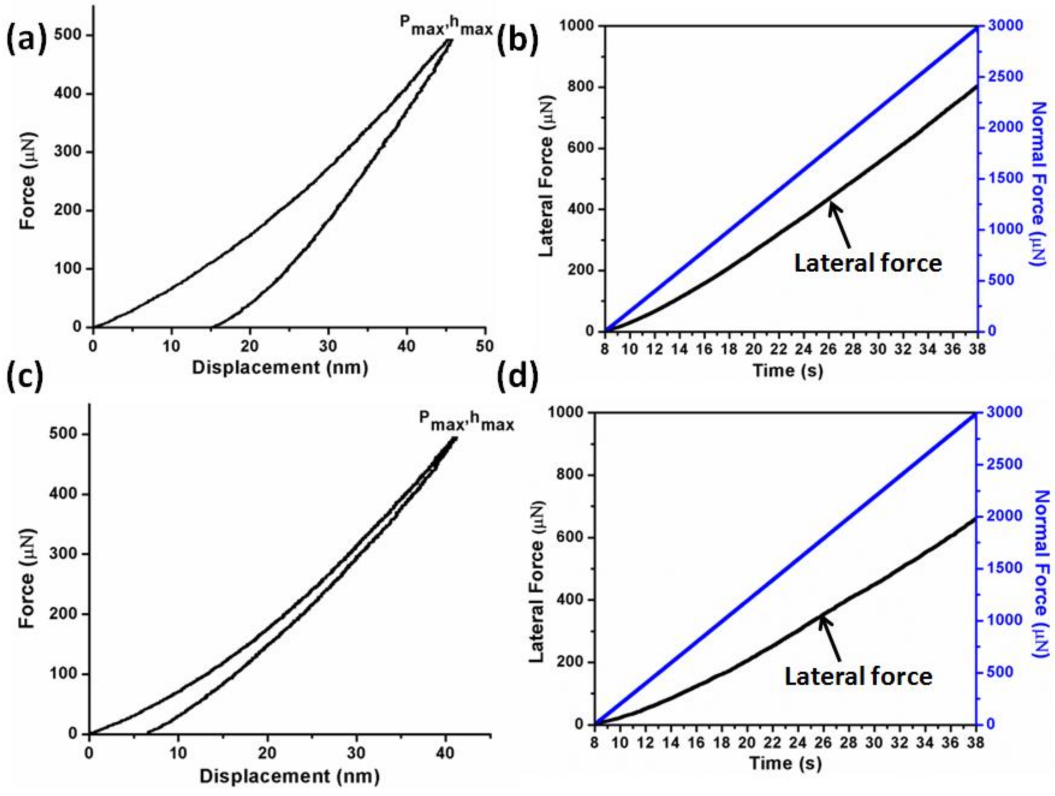

Figure 4.11. (a) Uncoated glass substrate loading-unloading curves, (b) Uncoated glass substrate scratch curves, (c) Uncoated fused quartz substrate loading-unloading curves, (d) Uncoated fused quartz substrate scratch curves.

The thickness of the films lies between 220 nm to 310 nm samples and therefore the indentation displacement is kept below 20% ($t/5$) to total thickness 't' to minimize the substrate effect. However, displacement is optimized around 40 nm in each indentation to overcome the effect of shallow indentation and indentation size effect, which is more pronounced at shallow indentation depths [208]. The coating and substrate is a composite system and substrate has a huge effect on the film mechanical properties, however with the increase of penetration depth, substrate effect becomes more pronounced due to its closer proximity with the indenter. It is observed, hard film on soft substrate is more prone to be affected by substrate at lower penetration depth. In the present work, the indentation was performed at several locations with same maximum load and same loading rate. Finally, averages were taken with standard deviations to ensure accuracy.

Uncoated substrates i.e. glass substrate and fused quartz mechanical properties are measured as shown in Fig. 4.11. The hardness of uncoated glass substrate is 8.1±1.19 GPa and Young's modulus, 89.5±10.1 GPa, respectively. The fused quartz exhibited the hardness and Young's Modulus, 9.31±0.35 GPa and 73.6±1.42 GPa, respectively. The scratch curve of normal forces and lateral forces were found to be free from any discontinuity, and average coefficient of friction for fused quartz and glass substrate found to be 0.15-0.2 and 0.2-0.24, respectively.

It is clear from Fig. 4.10 that ZnO:Pr thin films having loading/unloading curve without discontinuities/pop-in (≥ 2 nm) during the penetration of indenter, indicate better adherence to the substrate and rules out fracturing or delamination during indentation [84]. Major discontinuities or sudden jump during penetration of indenter could arise due to incorporated defects sites but minor discontinuity as collective event of slip and propagation can be inhibited by grain boundaries or at substrate [64,167]. The plastic deformation and fracture events are influenced by the dislocation dynamics through active slip system depending upon the stored energy and localized stress induced by indenter tip in the material [167]. Multiple events of pop-in were reported in ZnO as a consequence of initiation of slip and dislocation burst [65] depending upon the loading rate [211].

Average mechanical properties of ZnO: Pr films are given in Table 4.4 after multi curve analysis. The underlying substrates (glass/fused quartz) were amorphous which affects interface and growth of films thereby influencing mechanical properties of ZnO: Pr thin films. However, there is slight variations in the hardness but enhanced hardness at 10mTorr sputtering deposition pressure is due to better crystallinity and grain size of thin films [213]. The hardness of the ZnO thin films is slightly higher at 10mTorr sputtering deposition pressure (9.89±0.14 GPa) at glass substrate. The highest crystallinity in polar plane accounts for higher hardness observed in ZnO as compared to *a*-plane or *m*-plane depending upon the ease of slip events [48]. Also, the films showed high Young's modulus (112.12±3.45) GPa deposited at 5mTorr sputtering deposition pressure.

Scratch scan is recorded as frictional forces indicating elastic-plastic interaction of the loading and sliding indenter as well as the event of failure. The elastic interaction is observed during the beginning of the scratch test at lower normal load; however, the increased applied forces deform materials plastically.

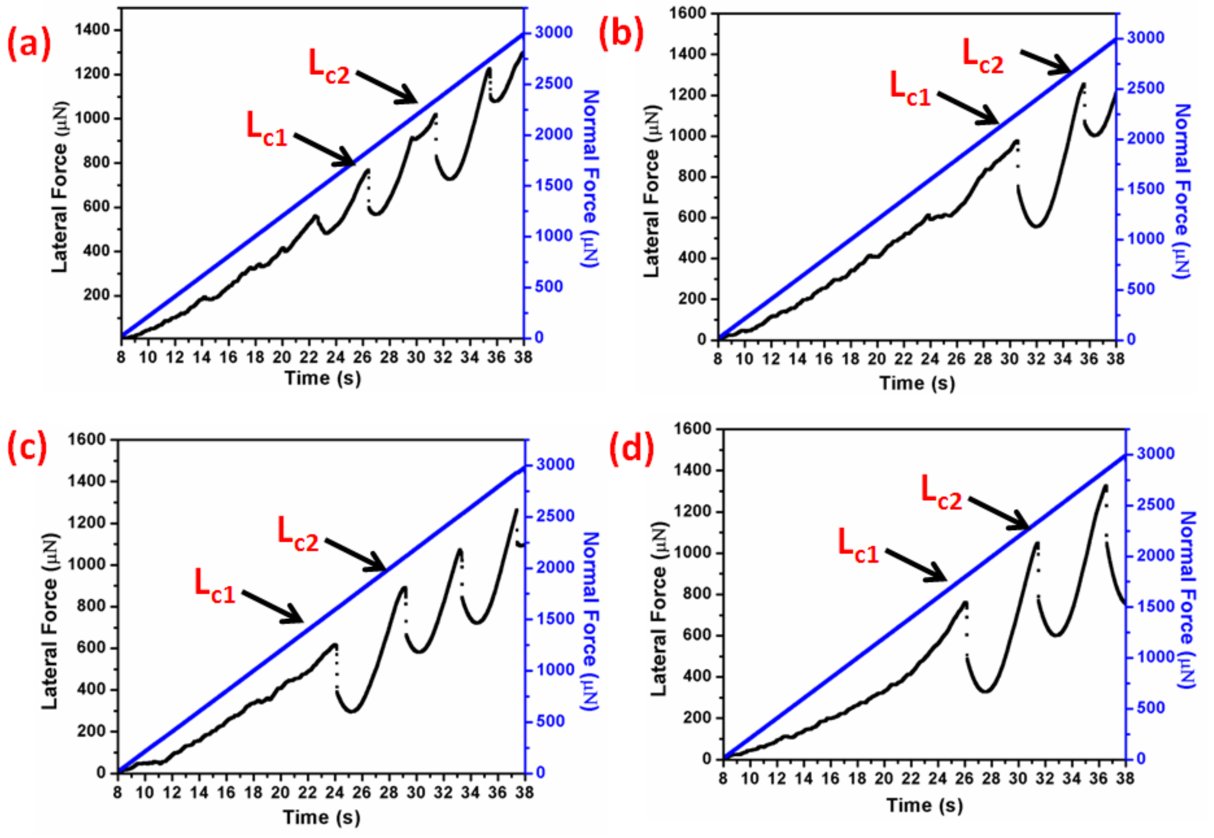

Figure 4.12. Frictional forces of ZnO: Pr thin films deposited on (a) Glass substrate at 5mTorr, (b) Glass substrate at 10mTorr, (c) Fused quartz substrate at 5mTorr, (d) Fused quartz substrate at 10mTorr.

The failure events are correlated with adhesive/cohesive interaction which primarily depends on the applied shear force per unit area and interfacial shear stress between film and substrate [18]. However, scratch behavior has changed as a consequence of incorporation of Pr ions on Zn lattice sites as compared to pure ZnO [237]. Progressively increasing normal force applied from 0 μN to 3000 μN load exhibiting failure event is responsible for sudden discontinuity in the lateral force curve at lower L_{c1} and upper critical force at L_{c2} as given in Table 4.4, and Fig. 4.12. The Pr doped ZnO thin films has fractured after bearing significant plastic deformation but the scratch curve is smooth before fracture as shown in Fig. 4.12. The smooth and oscillation free curve observed in lateral force indicate good scratch resistance.

The initial or lower critical load is a complex phenomenon, which is not considered as complete failure of films as it depends on the upper critical load. Difference in upper and lower critical load significantly affects the fracture toughness of the films [174]. Lower cohesive strength of films causes lower scratch resistance and therefore deteriorates overall strength of thin films. The scratch crack propagation resistance indicates durability and toughness of ZnO: Pr films. The initial critical load L_{c1} is believed to be initiation for crack event and propagation and upper critical load L_{c2} as complete failure. The parameter as $(L_{c2}\text{-}L_{c1})$ represents the scratch toughness of the ZnO: Pr thin films. The scratch crack propagation resistance parameter (CPR_S) in Eq. (4.2) represents resistance to crack initiation and propagation and qualitative response of coatings [143] is expressed as,

$$CPR_s = L_{c1}\left(L_{c2} - L_{c1}\right) \tag{4.2}$$

The CPRs ratio of ZnO: Pr films are given in Table 4.4 and observed higher CPRs for the films with higher crystallinity at 10mTorr pressure The films strength can be predicted by using *H/E* ratio (hardness/Young's modulus) termed as plasticity index given in Table 4.4, Higher *H/E* materials are expected to have better wear resistant properties due to small accumulated strain energy [171,266]. The higher *H/E* ratio observed in the present work indicates better wear resistance properties at 10mTorr pressure depositions in accordance with CPRs parameters. Lateral forces ratio to normal forces gives friction coefficient during scratch which provides insight on performance of coatings in tribological applications [64,267].

It can be observed from Fig. 4.13 that friction coefficient has varied from 0.2 to 0.4 and with film friction coefficient increasing beyond 0.4, a sudden fall or breakdown is observed. The friction curve provides nature of contact between sliding indenter on thin films and stress distribution. Initially, scratch section experiences lower contribution of plowing force and more elastic interaction will occur but as the normal load increases, grain boundaries resistance to scratch, roughness and several other factors come into play before fracturing the films. Minor discontinuities or oscillations initially were considered as the effect of different scratch resistance at grain boundaries which is correlated with different crystalline orientations to grain growth

[216]. The coefficient of friction lies between 0.2 to 0.4, in accordance with the reported values in the literature [73].

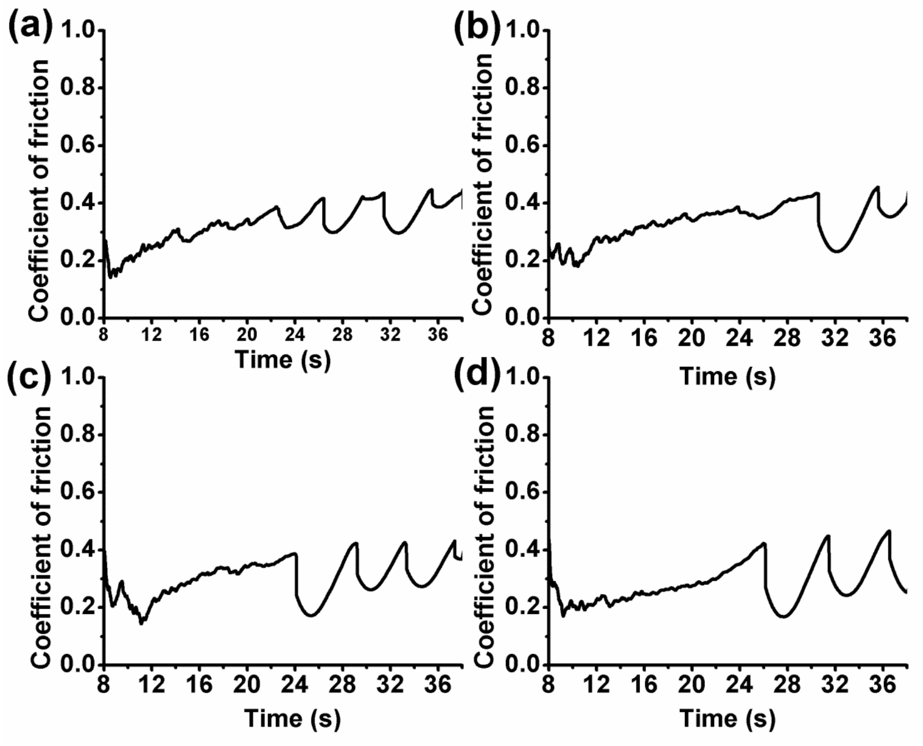

Figure 4.13. Coefficient of Friction of ZnO: Pr thin films deposited on (a) Glass substrate at 5mTorr, (b) Glass substrate at 10mTorr, (c) Fused quartz substrate at 5mTorr, (d) Fused quartz substrate at 10mTorr.

Table 4.4. Mechanical Properties and Roughness of ZnO: Pr thin films.

ZnO:Pr thin films /substrate	Hardness (*GPa*)	Elastic Modulus (*GPa*)	*H/E* ratio	Critical load L_{c1}/L_{c2} (μN)	CPRs Ratio (10^5)	Roughness (*nm*)
Glass at 5mTorr	9.72±0.4	112.12±3.4	0.086	1848.4/ 2343.8	9.15	5.17
Glass at 10mTorr	9.89±0.1	103.52±4.6	0.095	2250.5/ 2754.5	11.34	8.66
Fused quartz at 5mTorr	9.57±0.3	110.9±3.7	0.086	1587.4/ 2117.1	8.40	3.54
Fused quartz at 10mTorr	9.83±0.2	101.08±6.0	0.097	1809.3/ 2340.2	9.60	3.76

4.2.4.2 XPS and morphological analysis of ZnO:Pr thin films

XPS spectroscopy technique is widely accepted for surface characterization and ensuring chemical composition or impurity. However, XPS only provides information about the elements in the top layer of material, below 10 nm in the samples surface. XPS analysis indicated Zn 2p, Pr 3d and O 1s peaks in ZnO: Pr thin films as shown in Fig. 4.14, and labeled as Zn, Pr and O. Fig. 4.14 (b-d) shows the spectra of Zn (2p), Pr (3d) and O (1s).

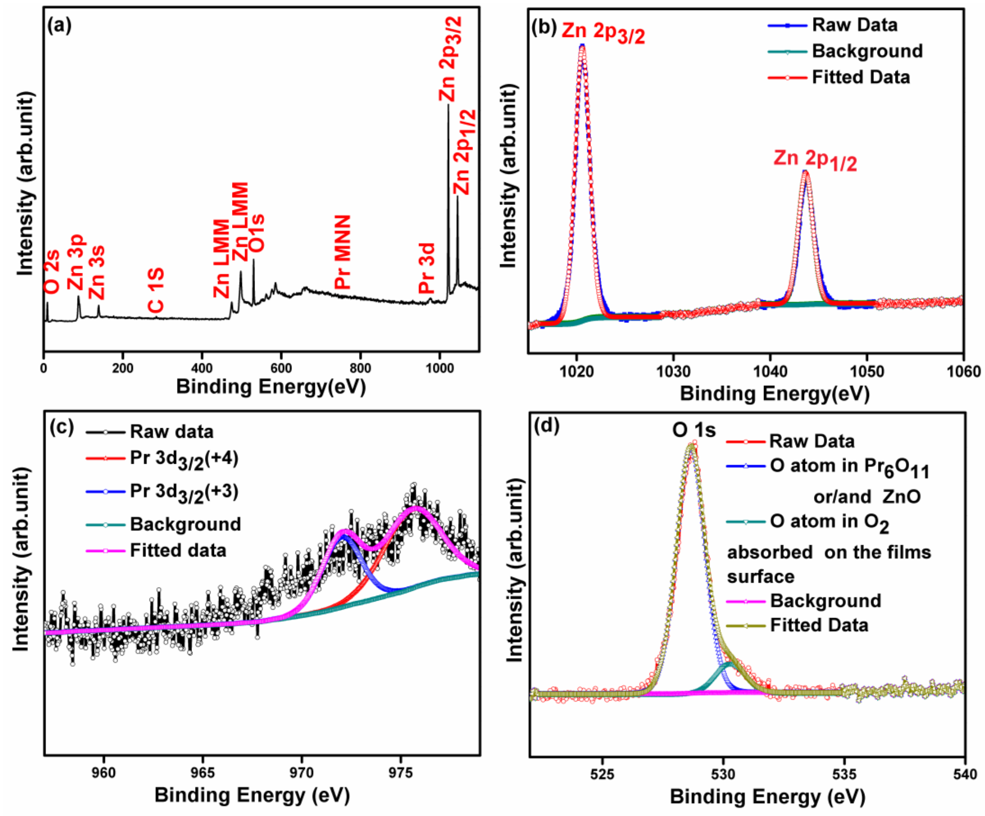

Figure 4.14: XPS spectra of ZnO:Pr thin films (a) Full survey (b) Zn (2p) spectra (c) Pr (3d) spectra (d) O (1s) spectra.

The full spectrum as shown in Fig. 4.14 (a) indicates that Pr is composite with the zinc oxide films. The energy scale is calibrated using C 1s peak as reference signal of the carbon contamination (BE= 284 eV). As shown in Fig. 4.14 (b), two peaks of Zn 2p are detected. The peak located at 1020.6 eV and 1043.57 eV can be attributed to the binding energy of Zn–O bond associated with Zn $2p_{3/2}$, and Zn $2p_{1/2}$, respectively. These peaks are referred as regular lattice of Zn in ZnO [240]. The spin orbit splitting energy between two lines, 22.97 eV lying in the nearby range of standard reference value of ZnO [268]. The ‘O’ deconvoluted first peak has a binding energy of 528.6 eV, which can be attributed to the oxygen atoms in ZnO or Pr_6O_{11} [62].

The peak with higher binding energy of 530.3 eV indicates the traces of loosely bound oxygen such as adsorbed O_2 on the surface ZnO:Pr [241]. The asymmetric Pr $3d_{3/2}$ narrow spectrum can be deconvoluted in to two peaks. The strong peak located at 975.8 eV corresponds to Pr^{4+} oxidation state, while the weak peak at 972.04 eV can be assigned to Pr^{3+} oxidation state [62]. Pr^{3+} and Pr^{4+} can coexist in the Pr_6O_{11} crystal structure; however, the difference of spin orbit splitting of energy could lead to Pr ions also incorporated in to ZnO lattice.

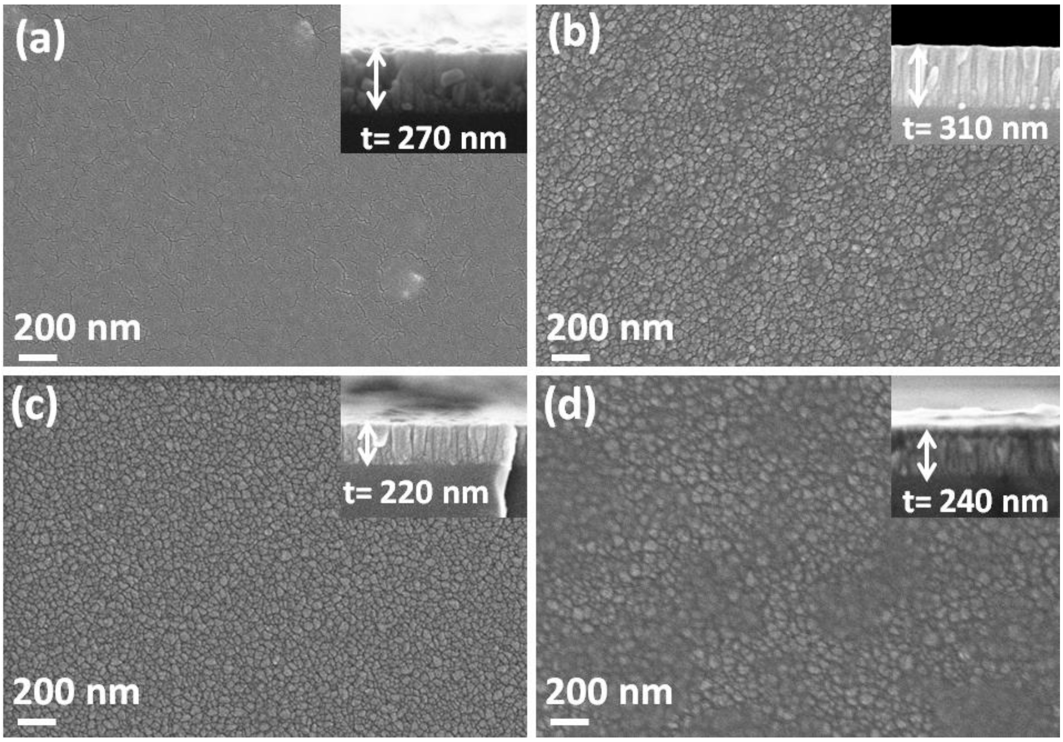

Figure 4.15. FESEM images of ZnO: Pr thin films deposited on (a) Glass substrate at 5mTorr, (b) Glass substrate at 10mTorr, (c) Fused quartz substrate at 5mTorr, (d) Fused quartz substrate at 10mTorr.

Thickness of ZnO: Pr thin films is found to be between 220 nm to 310 nm at different deposition conditions, measured by cross sectional FESEM analysis of films shown in Fig. 4.15 inset. ZnO: Pr thin films uniformly spread throughout the substrate, composed of small elongated grains and films are densely packed faceted kind of grain boundaries as seen in Fig. 4.15. However, the films morphology has shown granular shapes with clear boundaries except for Fig 4.15 (a). The morphology of sputter deposited ZnO: Pr films vary with sputtering deposition pressure and underlying substrate in terms of grains growth as well as the shape of grains. Large grains size is observed due to the fact that the kinetic energy is changed at high sputtering pressure and deposition rate could lead to more agglomeration of particles. The coarsening of grains, inter-grain connections are more significant in Fig 4.15 (d).

The composition of films was measured by EDS. EDS mapping along with EDS spectra is shown to ensure film purity and distribution of elements throughout the scanning area (Fig. 4.16). EDS mapping shows a uniform distribution of elements Pr, Zn and O in the scanned area of films. The atomic percentage of Pr, Zn and O of ZnO films is given in Table 4.3 and thin films are found to be oxygen rich. The SEM and XRD results of thin films are in accordance with each other and found to be crystalline and columnar growth at high sputtering pressure.

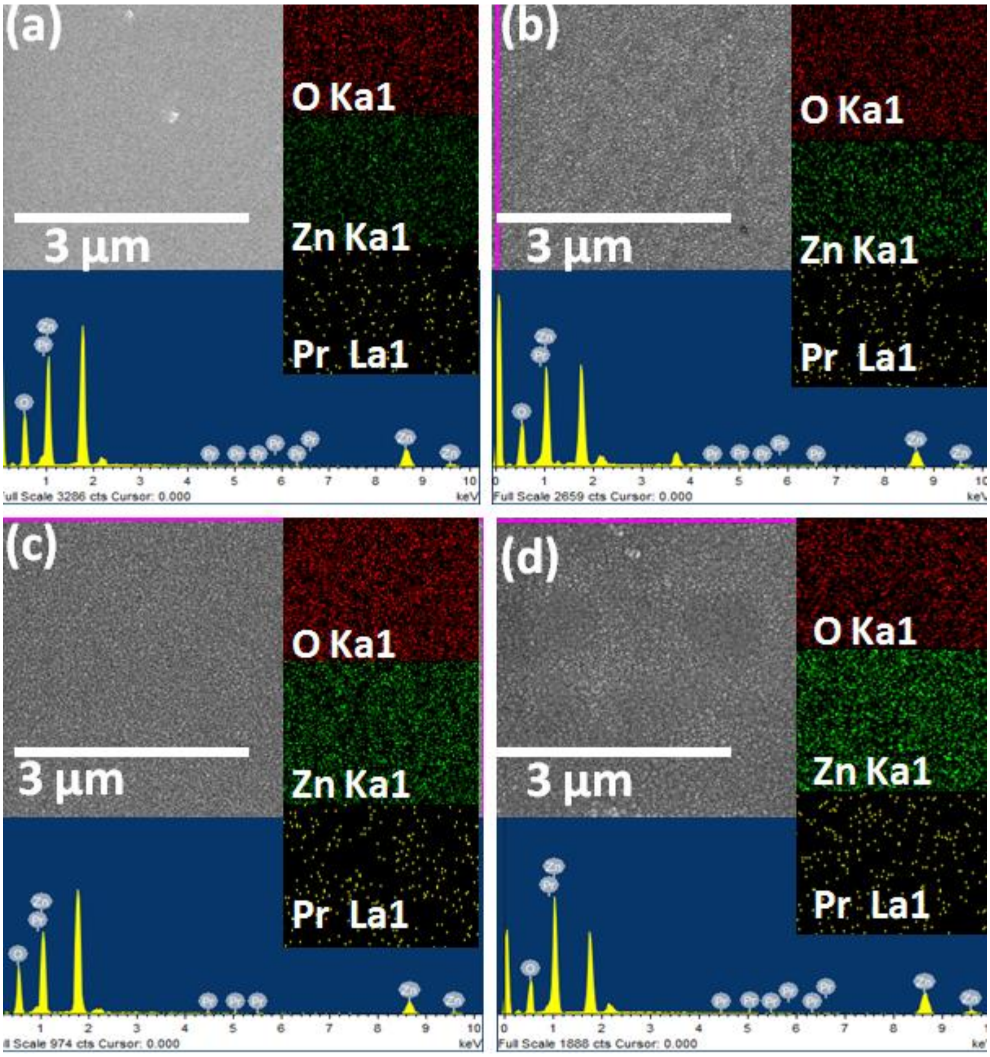

Figure 4.16: EDS Mapping of ZnO: Pr thin films deposited on (a) Glass substrate at 5mTorr, (b) Glass substrate at 10mTorr, (c) Fused quartz substrate at 5mTorr, (d) Fused quartz substrate at 10mTorr

The root mean square roughness of the ZnO: Pr thin films was measured AFM in semi contact mode of region 2 µm × 2 µm as shown in Fig. 4.17.

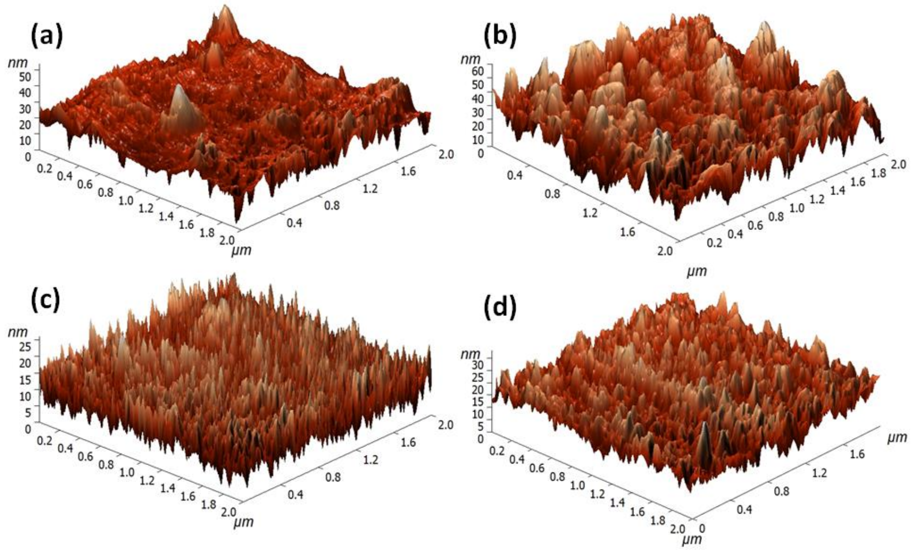

Figure 4.17. AFM images of ZnO:Pr thin films deposited on (a) Glass substrate at 5mTorr, (b) Glass substrate at 10mTorr, (c) Fused quartz substrate at 5mTorr, (d) Fused quartz substrate at 10mTorr.

The distributions of grains are distinct, elongated particles and length of grains increased at 10mTorr on glass substrate and fused quartz substrate. The grains are elongated and thicker in size at 10mTorr sputtering deposition pressure and showed higher RMS roughness as seen from Table 4.4. The same kind of observation is established by FESEM micrographs where grains size increases at 10mTorr sputtering depositions. Sputtering deposition conditions strongly influence in terms of kinetic energy of ad-atoms and the deposition rate, showing higher roughness of films at high sputtering pressure.

4.2.5 Conclusion

Highly crystalline Pr doped ZnO thin films were successfully deposited using DC sputtering in the present work. The mechanical properties and tribological behavior of films were investigated and the following conclusions are drawn.

- There is no evidence of XRD peaks related to Pr or Pr_6O_{11} in thin films and therefore, it is expected that Pr acquires substitutional positions in ZnO lattice.
- The FESEM and AFM confirm the formation of nanostructured morphology of grains in ZnO: Pr films, which depend on synthesis condition as well as the substrate material. The RMS roughness and inter-grain connections are more pronounced for the films deposited on at 10mTorr sputtering pressure.

- Nanoindentation study of ZnO: Pr films has shown the high hardness (9.89±0.14) GPa, Young's modulus (112.12±3.45) GPa, highest initial critical load 2250.5 µN and CPRs ratio 11.34×10^5, for the films deposited indicating good adherence of films. However, there is a slight difference between hardness, Young's modulus of the films on both the substrates but the critical load for coating fracture suggested a good scratch resistance on glass substrate attributed to better crystallinity.
- The XPS result provided the surface analysis and confirms the presence of Pr ions and it is in accordance with EDS mapping with uniform presence of Pr ions throughout the scanning area. Also, Pr 3d in thin films with XPS peak were deconvoluted located at 975.8 eV corresponding to Pr^{4+} oxidation state, while the weak peak at 972.04 eV can be assigned to Pr^{3+} oxidation state, which is also relevant to Pr ions being composite with the zinc oxide films.

Chapter 5

FINITE ELEMENT ANALYSIS OF NANOINDENTATION ON ZNO THIN FILMS

Contents

5.1 INTRODUCTION

The innovation of semiconductor devices has been progressed extremely fast alongside the assembling and manufacturing techniques prompting miniaturization of electronics micro-electro-mechanical system (MEMS) and nano-electro-mechanical system (NEMS) devices. The diversity in the functional properties of thin films at nanoscale allowed to manipulate the existing properties can be treated due to the size effect as a result of nano-size confinement [16]. These fairly small sized components for electronics have their unique mechanics of strength [269]. ZnO thin films is renowned semiconductor pursuing attractive properties like wide band gap, large exciton (electron-hole pair) binding energy, high thermal and chemical stability that make ZnO thin films a phenomenal candidate in sensing, solar cell, MEMS device and transparent conducting oxide etc. [34,270]. Likewise, ZnO can also be used as optoelectronics application, but the soft nature (compare to GaN) of bulk ZnO, including indentation, pop-in events, wear properties, and cracking event during contact is of superior interests [65]. Nanoscale ZnO thin films can alter their bulk properties by variations in grain size, crystalline properties and existing residual strain.

The sputtering has been outstanding synthesis technique for depositing thin films with high crystallinity, dense microstructure and better adhesion even at low temperature. Other than this, sputtering is commercially viable for large area synthesis and unique microstructure depending on the deposition conditions e.g. sputtering pressure, substrate temperature, sputtering power and Ar/O_2 ratio etc. which can substantially affect mechanical response of thin films [37,271]. Amid processing or utilization of thin films are subjected to sustain elastic-plastic deformation, additionally miniaturization of materials e.g., thin film, nanostructures etc. as a device application is also imposed a risk of mechanical failure and complexity. To accomplish these issues, it is better to insight the mechanical reliability along with miniaturization of material [272].

The elastic-plastic properties and crystallinity of thin films provide overall mechanical strength and deformation mechanism in uniaxial tension/compression significantly depends upon the microstructure of thin films. The mechanical properties of thin films at nanoscale cannot precisely accessed by utilizing a conventional hardness tester with visual imprint method. With the advent of Nanoindentation technique to characterize the mechanical properties over a smaller probe area, gains popularity for precise and continuous measurement the mechanical response from extracting the information about, hardness, Young’s modulus [131,197] .

Nanoindentation is straightforward to execute with a fast response without delaminating thin film from substrate. Nanoindentor measure force and displacement simultaneously; and the load-displacement curve observed with non-linearity, or discontinuity and serrations depends upon thin films as well as substrate effect. It is accounted to maintain a separation from substrate to avoid its influence; indenter displacement ought to be under 10 % of aggregate film thickness for substantially thick films (≥ 1 μm). In present case, thickness of films is less than 1 μm, so varied displacement upto 20% of the film thickness to minimize the substrate influence [79].

Finite element (FE) analysis provides a way to anticipate the mechanical properties along with failures during service or processing. Several FE models developed to extract the load-indentation curve from nanoindentation experiments [273,274]. The actual problem of indentation using Berkovich tip can be analyzed by three dimensional FE-model [275]. Likewise, the two dimensional model developed for indentation process preferred because it does not require large computing efficiency and obtained approximately equivalent outcomes [273,276]. The FE analysis provides an in-depth overview of mechanical properties and extend their correlation with substrate effect (elastic-plastic properties) [277].

It is noteworthy to study the intrinsic mechanical behavior of ZnO thin films as well as substrate effect by independently configuring different yield stresses as plastic properties. The nanoindentation combined with finite element analysis on ZnO thin films are scarce in literature. The present study was involved to get the film mechanical properties by nanoindentation and generalized by FE method to insight the contact interaction by extremely sharp Berkovich indenter to load-indentation response as a function of tip shape from cubic geometry to spherical geometry.

5.2 EXPERIMENTAL DETAILS

ZnO thin films were deposited on the fused quartz substrate by pure ZnO target using Direct Current Sputtering. The fused quartz substrate was ultrasonically cleaned to get homogeneous and uniform depositions. The dried substrates and target fitted in their respective position in sputtering chamber. The deposition chamber was evacuated to 4×10^{-6} Torr to remove residual gases from the chamber. Thereafter, high purity Ar/O_2 gas (20:5 sccm) inserted in to the chamber. The sputtering parameters such as working pressure, substrate temperature and sputtering power were 10mTorr, 200^0C and 50W, respectively are maintained constant during the deposition process. The pre-sputtering was carried out for 10 minutes to eliminate surface contamination of the target. Crystalline properties were analyzed using X-ray diffraction (XRD) performed with Cu-K$_\alpha$ radiation recorded in the angular range of 25-70^0.

5.2.1 Nanoindentation

Nanoindentation was performed applying load as a function of displacement by pyramidal shaped Berkovich indenter at room temperature, in the one complete course of loading and unloading. Hardness and Young's modulus of ZnO thin films were obtained by auto-evaluation using Hysitron TI-950 nano-indenter with standard Berkovich of 100 nm tip radius and analytical approach developed by Oliver and Pharr [131]. However, it is assumed that tip has finite roughness, and after some cycle of operations tip radius may vary up to 100-200 nm. For the precise measurement of mechanical properties, factors like thermal drift, instrument compliance, and tip area calibrations should be performed before indentation [130].

Nanoindentation directly provides non-linear load-displacement curve; and several approaches have been developed to extract the hardness and Young's modulus. Among all, Oliver and Pharr is widely accepted [131,278] as a development of Doerner and Nix approach [279]. After initiation of plastic deformation in material, loading curve contain both elastic and plastic deformation and their relative contribution is complex. However, unloading part regarded as purely elastic and main source of data analysis. The hardness and elastic modulus is measured at maximum load and upper portion of unloading curve respectively. The hardness ' H ' refers to the resistance provided by material to the plastic deformation. The indentation hardness and elastic modulus calculated by Oliver and Pharr method discussed in Chapter 2, section 2.3.6 [131]; Poisson's ratio of a thin film is complicated to measure because the standard tension test for Poisson's ratio is not appropriate for thin films. Furthermore, the absolute value of Poisson's ratio of thin films is generally far less than one and has an insignificant effect on the nanoindentation outcomes [280].

5.2.2 Finite Element Analysis

It is acknowledged that in continuum mechanics, two dimensional FE models has the capability to provide mechanical properties of thin film by sufficient accuracy, depend upon mesh width and computational efficiency [277]. The continuum mechanics effective even at smaller indentation depth ~10 nm however below this depth atomistic approach would be more appropriate [281]. A two dimensional (2D) axi-symmetric model with Berkovich indenter containing deformable thin film and substrate was created using standard FE software [97]. The sharp indenter modeled as an undeformable rigid surface pertaining cone angle of 70.3^0 and a radius 150 nm.

The Tip shape is considered extreme sharp at the contact area, however complexities exist in the real case of a non-ideal indenter shape (tip rounding) [282]. The non-ideal shape of an indenter attributes in difficult contact area calculations. Specifically, the contact area did not actually increase in a consistent manner with increasing penetration depth like it would with an ideally sharp indenter shape. This arise with non-ideal indenter geometries which overall affect hardness and Young's modulus [282,283]. The rigid cone i.e. Berkovich and cubic corner tip is easy to fabricate as well as simulation by changing the half angle of rigid cone FE simulations can be performed [284].

The FE analysis is performed in load controlled mode by applying load and optimizing the penetration depth of Indenter as in experimental study; with similar loading rate is maintained. The best fit calculations of load displacement curve depend upon the input properties of thin films as well as mesh element size. The coating and substrate were modeled with thickness of 250 nm and 4.5 μm respectively. The interface between the coating and substrate is perfectly bonded. So there is no slippage or debonding on the interface. The interaction between the free surface of coating and indenter was defined as sliding which stand for frictionless or friction (depending upon the coefficient of friction) contact. The coating was modeled as isotropic, elastic-plastic solids using the classical plasticity model [97].

The plasticity model uses the Mises Yield surface model with plasticity flow rule. The contact region of indenter and coatings were meshed finer as compare to other region to record deformation beneath the indenter. So denser mesh is applied in the vicinity of contact where high stress is expected [285]. The mesh element is CAX4R (4-node bi-linear axi-symmetric quadrilateral with reduced integration) used same as previous work performed on nanoindentation simulations [281,286] and reduced integration used to lower computational time as well as avoiding for stiffness locking [287]. The selection of element's size is to save computational time with sufficient accuracy. For that, the mesh convergence analysis is finds out for different mesh width. The higher mesh density in the region 'I' (refer Fig. 5.1) is used just beneath the indenter to capture deformation effects as shown in Fig 5.1 (a), therefore the width and height of each mesh element is 2.5 nm while the other region of mesh size varies between 2.5-25 nm.

The total number of mesh elements used in the simulation in this conditions were ~39000. However, reducing mesh size below 2.5 nm would not generate significant affect.

The mesh convergence study with respect to the von Mises stress generated provided in the Fig. 5.1 (b). In the schematic diagram of two dimensional assembly shown in the Fig. 5.1 (a), the bottom of the substrate was fixed and constraint all the motions and rotations; however, nodes lying on the symmetry axis of the mesh were only free to move in the indentation direction i.e. *y*-direction, subsequently indenter can move in this direction.

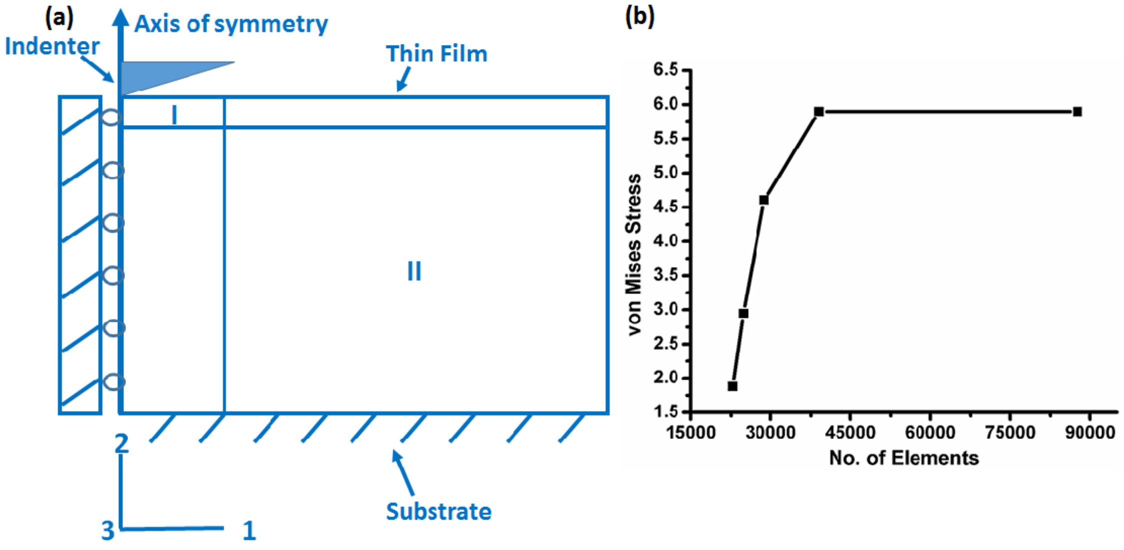

Figure 5.1. (a) Schematic diagram of two-dimensional model (b) Mesh Convergence Analysis.

Additionally, indenter is modeled as master surface moved to normal downward to slave surface i.e. thin film, only master surface penetrate into slave surface and generate deformations. Furthermore, boundary conditions applied to the tip that placed close to the indentation interaction volume also influence the load–displacement curve [288]. During the loading, indented material experiences elastic and plastic deformation after yielding, while the unloading procedure pertaining purely elastic behavior. The rigid indenter was statically displaced downward in steps up to a maximum applied load 300 µN as the same in experimental set-up. The contact behavior at the coating–substrate interface was modeled utilizing frictionless condition and perfectly bonded interface. So during loading or unloading there is no slippage or delamination occurred at the interface. The two homogeneous region i.e. substrate and coating assumed to be free from defects were containing isotropic properties maintaining same elastic–plastic behavior throughout, and power law of hardening used to substantiate plasticity behavior.

The yield stress used for the simulation was determined by fitting the simulated nanoindentation curve to the experimental data (refer Fig 5.2) with least possible dissimilarity. It was assuming that the substrate was fully homogeneous and elastic and the plastic deformation occurred only in the thin films. However, much interest exists in the possibility that further characterization of the elastic-plastic properties of coatings explored from different yields stress, contact friction effect and substrate elastic-perfectly plastic properties would generate load–displacement curves by means of simulations. Further characterization, in theory, would allow the properties extracted from a small volume of material to be assumed representative of the material in bulk. Ultimately, one's goal is to be able to develop a full characterization of the true. However several methods has been developed microscopic and macroscopic stress/strain character [285]. Amid nanoindentation, plasticity properties can be inserted decided by hardening law, uniaxial stress–strain relationship of a material was experience deformation by way of its load-displacement indentation curve and modeled as power law of hardening as discussed in the chapter 1, section 1.4.1 [277].

The work-hardening exponent n, lies between 0.1 and 0.5 for most of the metals [289,290]. However, for completely characterize a material needs four independent parameters, Elastic modulus E, yield stress σ_y work-hardening exponent n and Poisson's ratio v. For 'n' is zero is the applied for an elastic–perfectly plastic solid used for substrate [289]. According to Eq. 5.1, the relationship between indentation hardness and yield stress of metal material can be expressed as the following equation [291].

$$H = C\sigma \tag{5.1}$$

Where, σ is the uniaxial yield stress and H is the indentation hardness. The factor C is termed as elastic constraint factor and approximately 3 for metals. The yield stress value in Eq. (1.3) corresponds to the plastic strain also depends on the geometry of the indenter tip from Berkovich, Cube-corner indenters to Vickers [291]. Also, for most metals $(E/\sigma_y)>100$ constraint factor is approximately equal to 3 (C ~3) and For polymers, the ratio of $(E/\sigma_y)<10$, and the constraint factor is less than 3 [292]. Three-dimensional model yields nearly identical results as the two-dimensional simulation thereby making the latter a more practical approach [293]. In simulation, the standard fused quartz substrate is modeled as an elastic solid with Young's modulus 73 GPa and poisson's ratio 0.17 [294]. However, variations in the coating and substrate properties were discussed in the present work.

A variation in yield stress of ZnO coatings was tested for best fit approximations for the experimental load–displacement curve and the yield stress found in compression which is in the range of 2.0-3.0 GPa based on the slip system and crystal orientation with respect to the loading direction. However, the Young's modulus of ZnO coatings is always kept constant as received by experimental analysis. The fact that the simulated curve is not perfectly similar can be attributed to the small discrepancy in geometry between simulated and indentation tips and, specifically at the beginning of load the tip radius for shallow nanoindentation in experimental analysis as shown in Fig. 5.2. The top side of the coating surface was exposed as the free surface in order to enable direct contact between the tip of the indenter during penetration. The coating has the crystalline phase had a preferential texture (002) plane and cross sectional area (~250 nm).

The shape of the coatings was chosen to enable the two-dimensional model, which greatly reduced the computational requirements. Local variations in friction and yield stress caused by the mechanical anisotropy of the coating were separately considered. During FE analysis, nanoindentation of ZnO thin films was simulated in applying maximum load and load is applied continuously up to maximum load (0-300 μN) in a fixed time (8s) and followed by unloading segment (8s) indenter come out to its prefix position. For each segment, FE analysis was performed several iterations to achieve convergence. In Fig 5.2, ZnO thin film simulated curve from, the Berkovich tip radius 150 nm, tip half angle 70.3^0, hardness (4.72±1.22 GPa), elastic modulus (86.6±6.36 GPa), Yield stress 2.5 GPa, *n*= 0.25 were used respectively and keeping Poisson's ratio 0.3 compared with its experimental counterpart.

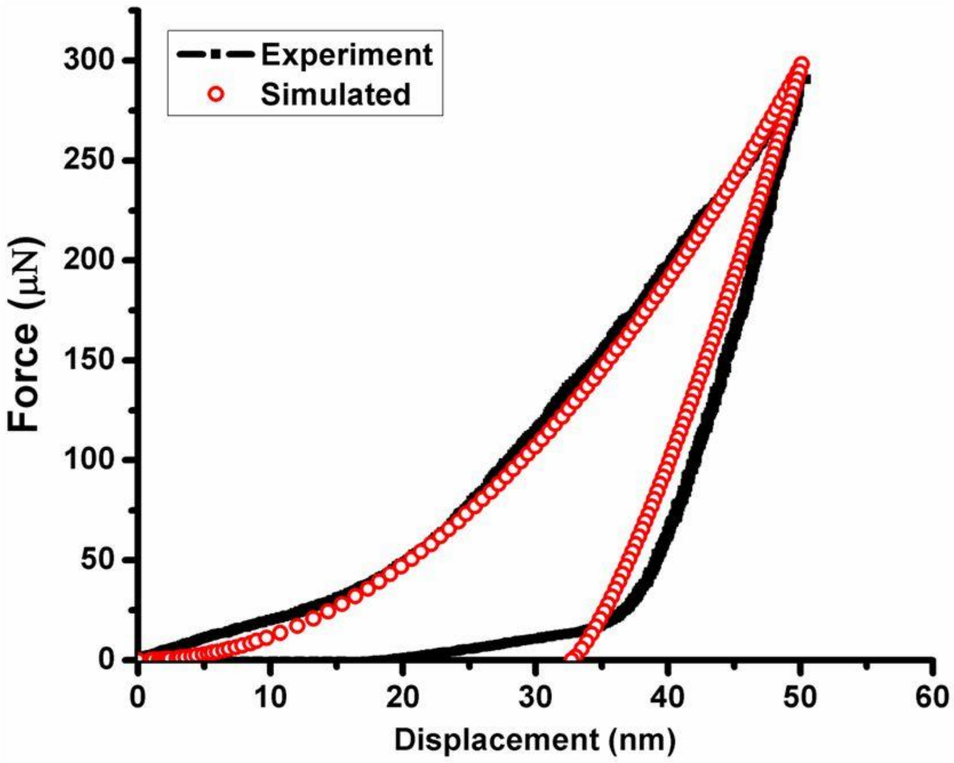

Figure 5.2. Experimental and simulated Load-displacement curve of ZnO thin films.

The indentation testing involves the depth dependent mechanical behaviors up to a certain depth called as shallow indentation depth. So at a shallow indentation depth the mechanical behavior is bit different as compare to the actual properties. For higher accuracy it is believed that real mechanical behavior can be analyzed after 10-15 nm [295]. So indentation is performed at a depth around 50 nm. However, the mismatch between experimental load-displacement curves with simulation curve even at best fit depends upon several parameters e.g., surface roughness effect, indentation size effect, the bonding between film and substrate may not be perfect etc.

5.3 RESULT AND DISCUSSION

ZnO thin films were deposited on fused quartz substrate shown in XRD pattern ensures ZnO films are well crystallized as shown in Fig. 5.3. ZnO film exhibit hexagonal crystal structure (JCPDS Card-891397) angle 2θ =34.27^0 corresponds to (002) diffraction plane. Evolution of different crystal planes that may be feasible during growth depends upon the variations in the deposition condition [296]. From the full width half maximum, crystallite size is calculated by using Scherrers formula (Eq. 2.6) was 19 nm [118]. ZnO have anisotropic mechanical properties; vary from polar (*c*-plane) to non-polar (*a*-planes & *m*-planes) planes [68,75,297]. A highly crystalline ZnO thin film grown in polar diffraction plane (002) enables to investigate the mechanical response. The experimental loading-unloading curves of ZnO thin films are shown in Fig. 5.2. The load-displacement curve provides materials behavior at increasing load, displacement and pop-in events. The non-linearity observed at constant loading rate in load-displacement curve depends on indenter shape, material of tip along elastic-plastic response of thin film and substrate effect [130].

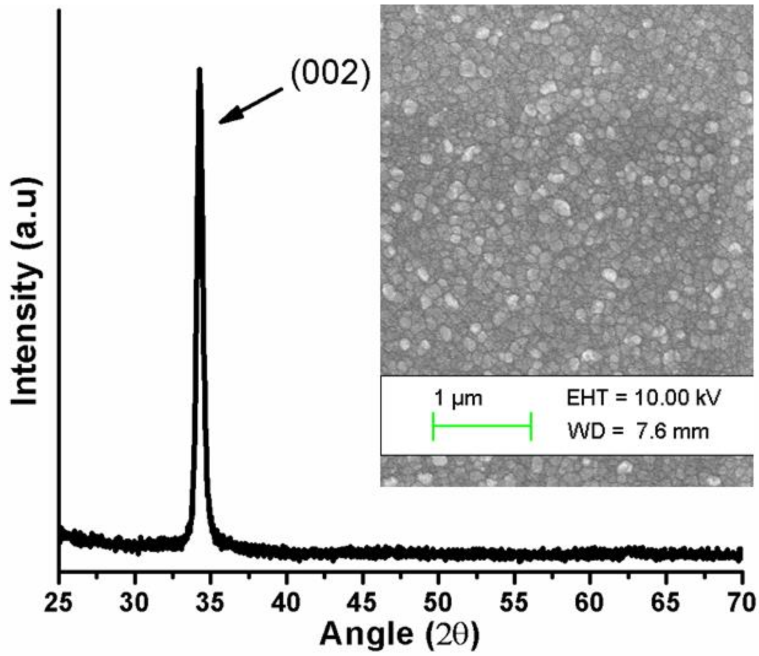

Figure 5.3: XRD pattern of ZnO thin films.

ZnO coatings stick to the substrate so when the indenter comes in the contact of thin film and record mechanical response, a significant substrate effect also comes into play. A deformation zone is developed under the indenter tip which is fully reversible for perfectly elastic materials however as plasticity induced in materials after initial yield point and material permanently changes its shape. And shape of plastic zone contains information about the plastic flow in material [298].

It is evident from Fig. 5.2 that ZnO thin films are adhering to the substrate without any major discontinuity to induce crack formation [84,299]. Discontinuity in loading cycle is considered as existence of an event of slip or dislocation movement in the thin films [167]. The distribution of localized stress beneath the indenter after elastic deformation observed in load displacement curve depicting shear band nucleation and propagation as consequence of plastic deformation. Synthesis condition affects microstructure correlated with underlying mechanical properties as shown in Fig. 5.3 inset. Single crystalline *a*-plane bulk ZnO and *c*-plane oriented bulk ZnO having different hardness value and Young’s modulus of 2.2 ± 0.2 GPa, 163 ± 6 GPa, and 4.8 ± 0.2 GPa and 143 ± 6 GPa, respectively [68]. Bulk oxides are usually prone to brittle failure but the ductility can be induced by refining grain size to nanometers in thin film. The increment in hardness is contributed by the dislocation mechanism, micro strain, and the grain size of thin films and threading dislocations is created to impede the slip movement increases hardness of thin films [64].

5.3.1 Effect of different yield stress

In this section, examined the situation where the nanoindentation tip would encounter coating oriented along the direction that yields to the largest slip resistance. The simulated load–displacement curves on ZnO coatings with uniform elastic and friction properties, but a difference of yield stress between the indenter and the coating free surface is shown in Fig. 5.4. During the variations in the coating yield stress the other properties including substrate properties were fixed same as in Fig. 5.2. It is worth noting that the plastic yield phenomenon was considered at coating homogeneous scale using an isotropic yielding. The penetration depth of indenter in the nanoindentation curves decreased gradually as the yield stress of the coatings was varied from the yield stress (Y1 = 2.0 GPa) to (Y2 = 2.5 GPa, Y3=3.0 GPa) as shown in Fig. 5.4. The change was observed when the first portion of the tip was brought into contact and slope of the curves varies with different yield stress. It is expected that difference in pile-up morphology around the indent between a coating and indenter would affect at lower yield stress.

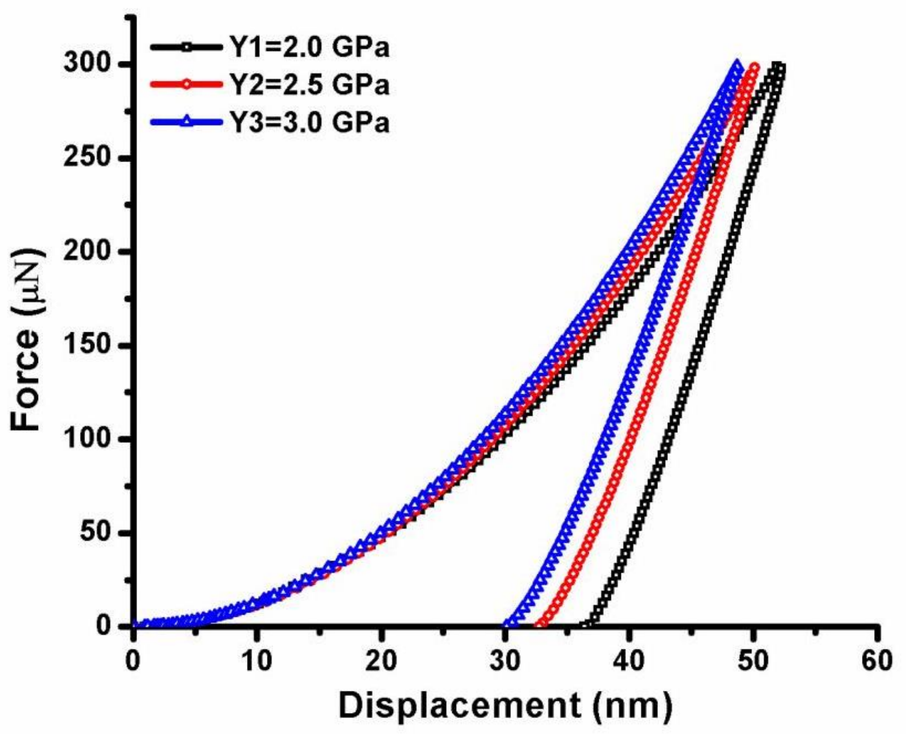

Figure 5.4. Simulated load–displacement curves of ZnO coatings with uniform elastic Properties and local variations in yield stress.

5.3.2 Effect of interface friction

Furthermore, friction effects at the indenter tip–coating interface become significant when the tip geometry is sharp. Therefore, we used our FE model to vary only the coefficient of friction along the free surface of the coating while keeping all other properties (substrate) constant as in the Fig. 5.2. The coefficient of friction of ZnO thin films could significantly increase to a value of 0.6 [300]. So the effect of local variations in friction force at the tip–coating interface was simulated as shown Fig. 5.5. In the simulated curve ruled out any significant change in the nanoindentation curve with friction coefficient variations. This may be expected due the small sliding on free surface during indentation. It is suggested that friction effect between tip and thin film not much effective and can be ignored due to the small scale [277,301]. Additionally the curvature of loading curve is usually unaffected by friction [302].

5.3.3 Effect of substrate deformation

In this section, we input different substrate properties while the other properties were same as in Fig. 5.2. The simulation of substrate effect was modeled with elastic properties as Young’s modulus 73 GPa and Poisson’s ratio equal to 0.17 of standard fused quartz substrate [294]. However, the substrate was modeled for different conditions assuming elastic-perfectly plastic properties. The influence of substrate mechanical properties on film performance can be correlated with load-displacement curve seen in Fig. 5.6.

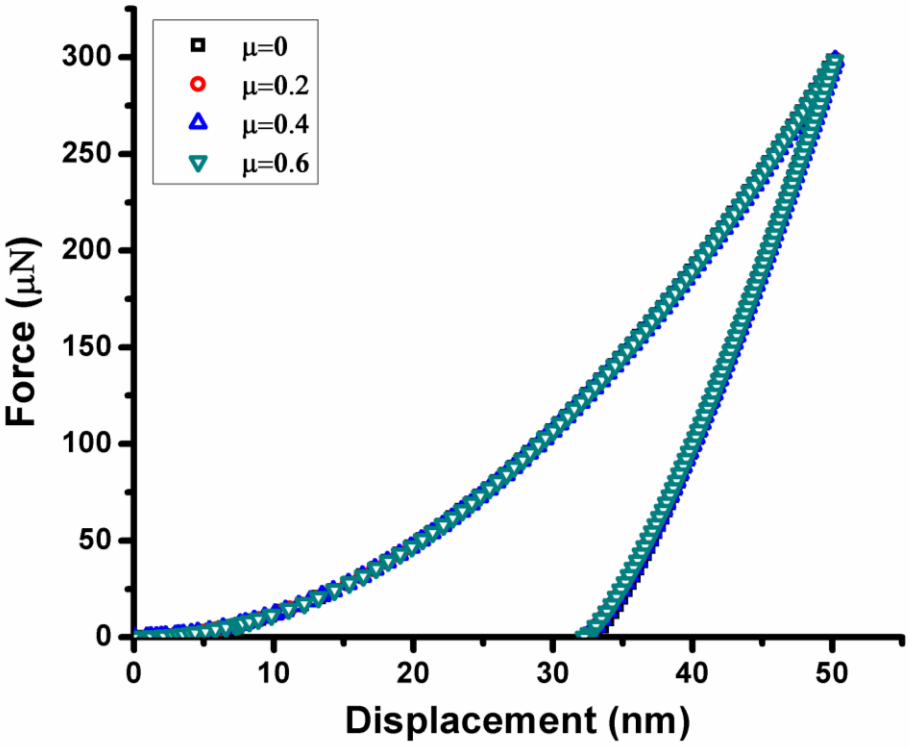

Figure 5.5. Simulated load–displacement curves on ZnO coatings with different coefficient of friction.

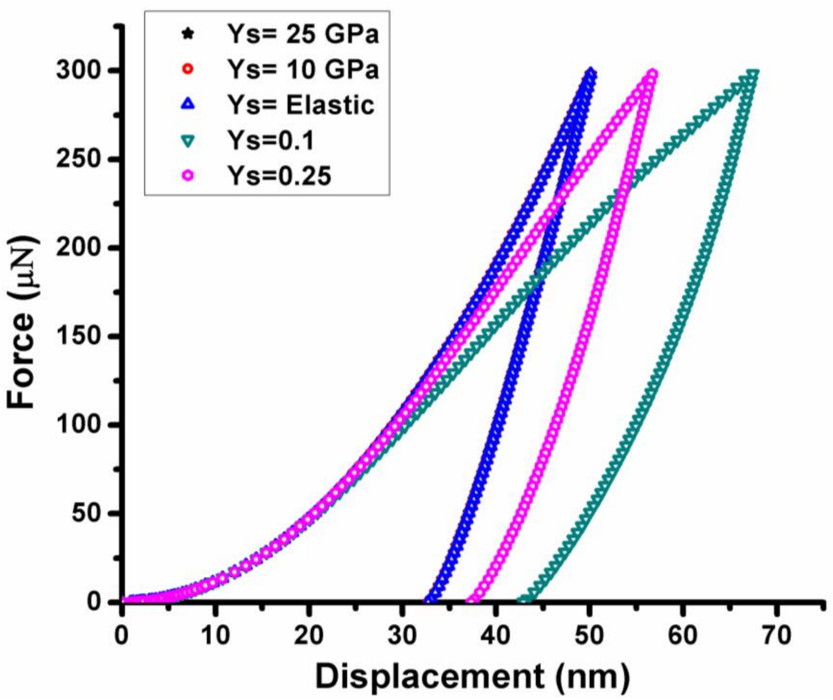

Figure 5.6. Simulated load–displacement curves on ZnO coatings with different substrate plastic properties and yield stress.

It is based on an understanding that subsurface deformation by sharp indenter is heavily depending upon substrate plastic properties. The curve has same penetration depth when the substrate was elastic or yielding at stress Y_s, 10 GPa, 25 GPa which is considerable higher as compare to coatings yielding stress 2.5 GPa. However, when the substrate yield stress Y_s lower as compare to the coatings as a result penetration depth of indenter suddenly increases as an indication of sink-in effect showing major plastic deformation occurred in substrate. This outcomes suggest that hard film on soft substrate were usually affected significantly at the same loading conditions as compare to soft films on hard substrates [274]. In this study, the analogy remains valid so long as the plastic zone remains confined to the region underneath the tip within a deforming solid.

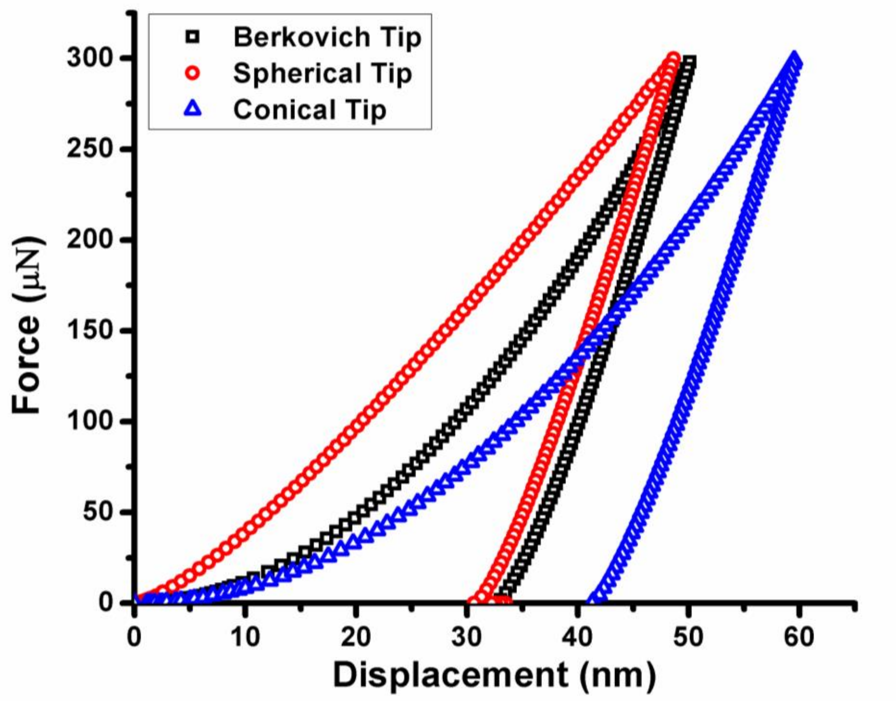

Figure 5.7. Berkovich and Spherical tip interaction with free surface of coating at the same input properties.

5.3.4 Effect of tip shape

It is worth noting that stress distribution under different indenter is different as the tip geometry is changed due to the contact mechanics as well as interacting depth to area of the tip is changed. Which can be seen by Fig. 5.7, a pointed indenter tip with conical tip with lower half angle 65.3^0 can penetrate larger depth at same load and yield stress with more sharp impact. Although most of studies have been performed using sharp indenter but spherical indenter has also its importance. Shape of load-displacement curve is different for spherical indenter and follows a different trend as compare to pointed conical tip which is observed less curvature in loading curve as shown in Fig. 5.7. In case of pointed indenter, by change the tip angle penetration displacement is changed due to higher stress generated in the sharp indenter, however the shape of load-displacement curve is similar. The indentation depth is more at same load when the indenter tip half angle is changed 70.3 to 65.3. The former tip has more flat in nature while the indenter tip with 65.3 half angle is more sharp can go to higher displacement with the same set of film properties at 300 µN load.

5.4 CONCLUSION

The simulations were intended to produce load–displacement curves directly comparable to obtained experimental outcomes. The experimentally findings of ZnO thin films have hardness and the Young's modulus is 4.72±1.22 GPa and 86.6±6.36 GPa. The materials properties from experiments and requires a few additional considerations including elastic and plastic properties of coating and substrate to get simulated curve.

- The best-fit simulation to load-displacement curve generated from mechanical properties of the ZnO thin film with Young's modulus, 86.6 GPa, Yield stress, 2.5 GPa; Poisson's ratio, 0.3 and work hardening exponent n=0.25.
- The simulated curve similar to the experimental curve however still some discrepancies exists depends upon several parameters, e.g. tip approximated as a perfectly sharp and rigid body. Furthermore, boundary conditions applied to the tip that are placed too close to the indentation interaction volume also influence the load–displacement curve.
- The indenter shape i.e. tip rounding effect, tip angle has a huge impact over stress distribution under the indenter which in turn reflects different mechanical behaviors indicating in load-displacement curve at the same load and yield stress.
- The substrate-coating plastic properties would affect the pile-up or sink-in morphology around the indenter depend upon the nature of materials and major plastic deformation is likely to be occurring in substrate if the substrate yields before coatings during nanoindentation. So the hard film on soft substrate significantly affected as compare soft film on hard substrate during indentation process.

Chapter 6

CONCLUSION

The primary focus of the thesis presented is to explore micro-structural and mechanical properties of pure ZnO thin films and study its deformation mechanism after incorporation of dopants in ZnO thin films. The microstructural characterization of ZnO thin films are carried out by XRD, FESEM and AFM. Similarly, dopant distribution i.e. Yttrium and Praseodymium ions and their concentrations in the ZnO thin films was measured by XPS and EDS Mapping along with the mechanical properties using Nanoindentation and Nanoscratch. The mechanical properties of thin films in each study has been provided in the Table 6.1. In addition to the experimental results, FE analysis is performed for ZnO thin films to obtain simulated load-indentation curve, which is best fit to the experimental curve. The following conclusions are made based on the results obtained on the ZnO thin films. The suggestions for the future work are proposed at the end.

Table 6.1. Mechanical properties of ZnO thin films with and without dopants.

S.No	Hardness (GPa)	Young's Modulus (GPa)	First Critical Load (μN)
ZnO/Glass Substrate	7.72±0.44	169.5±6.9	3126.7
ZnO/Fused Quartz	7.90±0.14	164.0±18.3	3043.9
ZnO: Y/ Glass Substrate	4.22±0.40	156.5±10.2	1210.6
ZnO: Y/ Fused Quartz	5.06±0.70	166.8±16.3	1095.2
ZnO: Pr/ Glass Substrate	9.89±0.14	103.5±4.6	2250.5
ZnO: Pr/ Fused Quartz	9.83±0.24	101.0±6.0	1809.3

1. Undoped ZnO thin films were deposited on glass substrate at different substrate temperatures variations using DC sputtering. Higher thermal energy provided to substrate used for the increment in grain size of ZnO films and reduction of lattice strain. The

anisotropic growth of film in crystal (002) diffraction plane is prominent, while (103) crystal plane also grew with higher substrate temperature. ZnO thin films mechanical properties greatly influenced with the emergence of non-polar planes leads to variations in active slip system and interfacial shear stress. The mechanical properties achieved for these sputtering conditions are given in Table 6.1 There is no major discontinuity in displacement during indentation is observed, ruling out the possibility of cracking, delaminating, or mechanical failure at the normal applied load. The morphology of the films is observed to be columnar to wedge shaped at 300^0C substrate temperature.

2. Crystalline ZnO thin films were successfully grown on fused quartz substrate at different deposition pressure variations using DC-sputtering. The grain size and crystallinity affects the deformation behavior of ZnO thin films. The increment in grain size and reduction of lattice strain were observed for the ZnO films deposited at higher deposition pressure. Also, crystalline quality of films rises initially and after that, it deteriorates with deposition pressure. The surface morphology of the films was observed as densely packed, crack free and the grains elongated towards the normal of substrate with the increasing deposition pressure. There is no evidence for major discontinuity (pop-in/pop-out) persists in the load–displacement curve, revealed better adherence to substrate and ruled out the possibility of cracking and rupture of film during indentation. The mechanical properties obtained from this study, are given in Table 6.1.
3. Crystalline Y doped ZnO thin films were successfully deposited using DC-sputtering. The mechanical properties and tribological behavior of films were investigated. There is no evidence of XRD peaks related to Yttrium or Y_2O_3 in YZO films; however, XPS confirm the presence of tri-valent oxidation state of Yttrium (Y^{3+}). The FESEM and AFM confirm the formation of nanostructured morphology of grains in YZO films, which depend on synthesis condition as well as the substrate material. The inter-grain connections are more pronounced for the films deposited on fused quartz substrate. However, there is a slight difference between hardness, Young’s modulus of the films on both the substrates but the critical load for coating fracture suggested a good scratch resistance on glass substrate attributed to better crystallinity given in Table 6.1.
4. Highly crystalline Pr doped ZnO thin films were successfully deposited using DC-sputtering and its mechanical and tribological properties are given in Table 6.1. There is no evidence of XRD peaks related to Pr or Pr_6O_{11} in thin films and therefore, it is expected that Pr acquires substitutional positions in ZnO lattice. The FESEM and AFM confirm the formation of nanostructured morphology of grains in ZnO: Pr films, which depend on

synthesis condition as well as the substrate material. A difference in the critical load for coating fracture suggested a good scratch resistance on glass substrate attributed to better crystallinity. The XPS result provided the surface analysis and confirms the presence of Pr ions and it is in accordance with EDS mapping with uniform presence of Pr ions throughout the scanning area.

5. The FE analysis were intended to produce simulated load–displacement curves directly comparable to obtained experimental outcomes with few additional considerations including elastic and plastic properties of coating and substrate. The indenter shape i.e. tip rounding effect, tip angle has a huge impact over stress distribution under the indenter, which in turn reflects different deformation behaviors indicating in load-displacement curve at the same load and yield stress. The relative substrate-coating plastic properties would affect the pile-up or sink-in morphology around the indenter depend upon the nature of materials. The major plastic deformation is likely to be occurring in substrate if the substrate yields before coatings during nanoindentation. So, a hard film on soft substrate is significantly affected as compared to soft film on hard substrate during indentation process.

Suggestions for Future Work

Based on the present work carried out on the investigation of ZnO and rare earth element doped ZnO thin films, the following studies could form a scope for the future work

1. ZnO thin films with and without rare earth dopants can also be prepared using the chemical techniques, which could affect grown microstructure and mechanical performance as compared to sputter grown films.
2. The variation in rare earth dopant concentration can induce different nucleation and growth kinetics of nanostructured ZnO thin films. Therefore, different concentration of dopants as the active constituents of ZnO deposited ought to be investigated for understanding the various growth morphologies of ZnO thin films.
3. FE analysis can be performed for scratch simulations to determine the critical load of pure and doped ZnO thin films for assessing its damage and failure mechanisms.

REFERENCES

---

[1] Y. Lv, W. Xiao, W. Li, J. Xue, J. Ding, Controllable synthesis of ZnO nanoparticles with high intensity visible photoemission and investigation of its mechanism, Nanotechnology. 24 (2013) 175702. doi:10.1088/0957-4484/24/17/175702.

[2] P. Mahesh, D. Pamu, Effect of deposition temperature on structural, mechanical, optical and dielectric properties of radio frequency sputtered nanocrystalline (KxNa1 − x)NbO3 thin films, Thin Solid Films. 562 (2014) 471–477. doi:10.1016/J.TSF.2014.04.007.

[3] A. Vadiraj, M. Kamaraj, Characterization of fretting fatigue damage of PVD TiN coated biomedical titanium alloys, Surf Coatings Technol. 200 (2006) 4538–4542. doi:10.1016/J.SURFCOAT.2005.03.036.

[4] M. Okazaki, S. Yamagishi, Y. Yamazaki, K. Ogawa, H. Waki, M. Arai, Adhesion strength of ceramic top coat in thermal barrier coatings subjected to thermal cycles: Effects of thermal cycle testing method and environment, Int J Fatigue. 53 (2013) 33–39. doi:10.1016/J.IJFATIGUE.2012.02.014.

[5] J. Sheng, K.-L. Han, T. Hong, W.-H. Choi, J.-S. Park, Review of recent progresses on flexible oxide semiconductor thin film transistors based on atomic layer deposition processes, J Semicond. 39 (2018) 011008. doi:10.1088/1674-4926/39/1/011008.

[6] L.B. Freund, S. Suresh., Thin Film Materials, Cambridge University Press, 2004.

[7] M. Ohring, Materials science of thin films, Academic press, 2001.

[8] J. Ayers, T. Kujofsa, P. Rago, J. Raphael, Heteroepitaxy of semiconductors: theory, growth, and characterization, CRC press, 2016.

[9] J.A. Venables, G.D.T. Spiller, M. Hanbucken, Nucleation and growth of thin films, Reports Prog Phys. 47 (1984) 399.

[10] Z.Y. Hang, C. V Thompson, Grain growth and complex stress evolution during Volmer–Weber growth of polycrystalline thin films, Acta Mater. 67 (2014) 189–198.

[11] D. Dojima, K. Ashida, T. Kaneko, In-situ growth mode control of AlN on SiC substrate by sublimation closed space technique, J Cryst Growth. 483 (2018) 206–210.

[12] V. Tonchev, Classification of step bunching phenomena, ArXiv Prepr ArXiv. (2012) 1203.2061.

[13] H. Scheel, T. Fukuda, Crystal growth technology, John Wiley & Sons, 2005.

[14] T.F. Zhang, Z.X. Wan, J.C. Ding, S. Zhang, Q.M. Wang, K.H. Kim, Microstructure and high-temperature tribological properties of Si-doped hydrogenated diamond-like carbon films, Appl Surf Sci. 435 (2018) 963–973. doi:10.1016/J.APSUSC.2017.11.194.

[15] G.W. Stachowiak, Wear: materials, mechanisms and practice, John Wiley & Sons, 2006.

[16] L. Ben Freund, S. Suresh, Thin film materials: stress, defect formation and surface evolution, Cambridge University Press, 2004.

[17] V.N. Koinkar, B. Bhushan, Effect of scan size and surface roughness on microscale friction measurements, J Appl Phys. 81 (1997) 2472–2479. doi:10.1063/1.363954.

[18] P. Benjamin, C. Weaver, Measurement of adhesion of thin films, in: Proc R Soc London A, The Royal Society, 1960: pp. 163–176.

[19] J. He, Q. Wang, H. Zhang, L. Dai, T. Mukai, Y. Wu, et al., Dynamic deformation behavior of a face-centered cubic FeCoNiCrMn high-entropy alloy, Sci Bull. 63 (2018) 362–368. doi:10.1016/J.SCIB.2018.01.022.

[20] J. Musil, Hard and superhard nanocomposite coatings, Surf Coatings Technol. 125 (2000) 322–330. doi:10.1016/S0257-8972(99)00586-1.

[21] C.S. Rao, C.E. Reddy, Finite element modeling of nanoindentation to extract load-displacement characteristics of bulk materials and thin films, in: CSIR, 2009.

[22] J. Musil, Hard Nanocomposite Coatings: Thermal Stability, Protection of Substrate against Oxidation, Toughness and Resistance to Cracking, in: Adv Ceram Coatings Mater Extrem Environ III, 2014: pp. 55–65. doi:10.1002/9781118807651.ch6.

[23] F. Ge, C. Jia, K. Li, P. Li, P. Zhu, T. Shao, et al., High Wear Resistance of Magnetron Sputtered Cr80Si20N Nanocomposite Coatings: Almost Independent of Hardness, Tribol Lett. 66 (2018) 70. doi:10.1007/s11249-018-1022-1.

[24] T. Hoornaert, Z.K. Hua, J.H. Zhang, Hard Wear-Resistant Coatings: A Review, Adv Tribol. (2010) 774–779. doi:10.1007/978-3-642-03653-8_257.

[25] T. Burakowski, T. Wierzchon, Surface engineering of metals: principles, equipment, technologies, CRC press, 1998.

[26] J. Song, Z. Wang, Y. Huang, A. Srinivasan, F. Beckmann, K.U. Kainer, et al., Effect of Zn addition on hot tearing behaviour of Mg–0.5Ca–xZn alloys, Mater Des. 87 (2015) 157–170. doi:10.1016/J.MATDES.2015.08.026.

[27] A. Srinivasan, Y. Huang, C. Mendis, H. Dieringa, C. Blawert, K. Kainer, et al., Microstructure, Mechanical and Corrosion Properties of Mg-Gd-Zn Alloys, Trans Tech Publ. 765 (2013) 28--32.

[28] K. Chopra, Thin film device applications, Springer Science & Business Media, 2012.

[29] Ü. Özgür, Y.I. Alivov, C. Liu, A. Teke, Ma.A. Reshchikov, S. Doğan, et al., A comprehensive review of ZnO materials and devices, J Appl Phys. 98 (2005) 041301. doi:10.1063/1.1992666.

[30] S. Fairose, S. Ernest, S. Daniel, Effect of Oxygen Sputter Pressure on the Structural, Morphological and Optical Properties of ZnO Thin Films for Gas Sensing Application, Sens Imaging. 19 (2018) 1. doi:10.1007/s11220-017-0184-5.

[31] X. Tang, E.S.G. Choo, L. Li, J. Ding, J. Xue, Synthesis of ZnO Nanoparticles with Tunable Emission Colors and Their Cell Labeling Applications, Chem Mater. 22 (2010) 3383–3388. doi:10.1021/cm903869r.

[32] R. Kouser, A. Vashist, M. Zafaryab, M.A. Rizvi, S. Ahmad, Biocompatible and mechanically robust nanocomposite hydrogels for potential applications in tissue engineering, Mater Sci Eng C. 84 (2018) 168–179. doi:10.1016/J.MSEC.2017.11.018.

[33] S. Chen, G. Ma, H. Wang, P. He, H. Wang, M. Liu, Evaluation of adhesion strength between amorphous splat and substrate by micro scratch method, Surf Coatings Technol. 344 (2018) 43–51. doi:10.1016/j.surfcoat.2018.02.073.

[34] U. Ozgur, D. Hofstetter, H. Morkoc, ZnO devices and applications: a review of current status and future prospects, Proc IEEE. 98 (2010) 1255–1268.

[35] V.A. Coleman, C. Jagadish, Chapter 1 - Basic Properties and Applications of ZnO, in: Zinc Oxide Bulk, Thin Film Nanostructures, Elsevier Science Ltd, Oxford, 2006. doi:http://dx.doi.org/10.1016/B978-008044722-3/50001-4.

[36] J. Leitner, V. Bartůněk, D. Sedmidubský, O. Jankovský, Thermodynamic properties of nanostructured ZnO, Appl Mater Today. 10 (2018) 1–11. doi:10.1016/j.apmt.2017.11.006.

[37] R. Kumar, G. Kumar, O. Al-Dossary, A. Umar, ZnO nanostructured thin films: depositions, properties and applications—a review, Mater Express. 5 (2015) 3–23.

[38] D. Pamu, G.L.N. Rao, K.C.J. Raju, Effect of particle size and ZnO addition on microwave dielectric properties of nanocrystalline ($Zr_{0.8}Sn_{0.2}$) TiO_4 ceramics, Adv Appl Ceram. 106 (2007) 202–208. doi:10.1179/174367607X178157.

[39] X.-L. Nan, H.-Y. Wang, Z.-Q. Wu, E.-S. Xue, L. Zhang, Q.-C. Jiang, Effect of c/a axial ratio on Schmid factors in hexagonal close-packed metals, Scr Mater. 68 (2013) 530–533. doi:10.1016/J.SCRIPTAMAT.2012.12.006.

[40] C. Bates, W. White, R. Roy, New high-pressure polymorph of zinc oxide, Science.Sciencemag.Org. 137 (1962) 993.

[41] A.S. Kamble, B.B. Sinha, K. Chung, M.G. Gil, V. Burungale, C.-J. Park, et al., Effect of hydroxide anion generating agents on growth and properties of ZnO nanorod arrays, Electrochim Acta. 149 (2014) 386–393. doi:https://doi.org/10.1016/j.electacta.2014.10.049.

[42] Y. Sun, D. Cherns, R.P. Doherty, J.L. Warren, P.J. Heard, Reduction of threading dislocations in ZnO/(0001) sapphire film heterostructure by epitaxial lateral overgrowth of nanorods, J Appl Phys. 104 (2008) 23533. doi:10.1063/1.2957082.

[43] R.S. Fertig III, S.P. Baker, Capture cross-section of threading dislocations in thin films, Mater Sci Eng A. 551 (2012) 67–72.

[44] H. Zhou, M.F. Chisholm, P. Pant, H.J. Chang, J. Gazquez, S.J. Pennycook, et al., Atomic structure of misfit dislocations in nonpolar ZnO/Al2O3 heterostructures, Appl Phys Lett. 97 (2010) 121914. doi:10.1063/1.3489687.

[45] S.-K. Hong, H.K. Cho, Structural Defects in GaN and ZnO, in: Oxide Nitride Semicond, Springer, 2009: pp. 261–310. doi:10.1007/978-3-540-88847-5_6.

[46] Y. Ohno, H. Koizumi, Y. Tokumoto, K. Kutsukake, H. Taneichi, I. Yonenaga, Slip systems in wurtzite ZnO activated by Vickers indentation on and surfaces at elevated

temperatures, J Cryst Growth. 393 (2014) 119–122. doi:http://dx.doi.org/10.1016/j.jcrysgro.2013.11.033.

[47] H. Iwanaga, K. Suzuki, S. Takeuchi, Direct observation of dislocation motion in ZnO, Phys Status Solidi. 38 (1976) K119–K122. doi:10.1002/pssa.2210380246.

[48] R. Juday, E.M. Silva, J.Y. Huang, P.G. Caldas, R. Prioli, F.A. Ponce, et al., Strain-related optical properties of ZnO crystals due to nanoindentation on various surface orientations, J Appl Phys. 113 (2013) 183511. doi:10.1063/1.4804309.

[49] A. Janotti, C.G. Van De Walle, Fundamentals of zinc oxide as a semiconductor, Reports Prog Phys. 72 (2009) 126501. doi:10.1088/0034-4885/72/12/126501.

[50] H. Morkoç, Ü. Özgür, Zinc oxide: fundamentals, materials and device technology, John Wiley & Sons, 2008.

[51] A. Ievtushenko, V. Karpyna, J. Eriksson, I. Tsiaoussis, I. Shtepliuk, G. Lashkarev, et al., Effect of Ag doping on the structural, electrical and optical properties of ZnO grown by MOCVD at different substrate temperatures, Superlattices Microstruct. 117 (2018) 121–131. doi:10.1016/J.SPMI.2018.03.029.

[52] F. Kang, Z. Li, J.T. Wang, P. Cheng, H.Y. Wu, The activation of <c + a> non-basal slip in Magnesium alloys, J Mater Sci. 47 (2012) 7854–7859. doi:10.1007/s10853-012-6344-z.

[53] D. Daksh, Y.K. Agrawal, Rare earth-doped zinc oxide nanostructures: a review, Rev Nanosci Nanotechnol. 5 (2016) 1–27.

[54] E. Cerrato, C. Gionco, I. Berruti, F. Sordello, P. Calza, M.C. Paganini, Rare earth ions doped ZnO: Synthesis, characterization and preliminary photoactivity assessment, J Solid State Chem. 264 (2018) 42–47. doi:10.1016/J.JSSC.2018.05.001.

[55] H. Parangusan, D. Ponnamma, M.A.A. Al-Maadeed, A. Marimuthu, Nanoflower-like Yttrium-doped ZnO Photocatalyst for the Degradation of Methylene Blue Dye, Photochem Photobiol. 94 (2018) 237–246.

[56] N. Sinha, S. Goel, A.J. Joseph, H. Yadav, K. Batra, M.K. Gupta, et al., Y-doped ZnO nanosheets: Gigantic piezoelectric response for an ultra-sensitive flexible piezoelectric nanogenerator, Ceram Int. 44 (2018). doi:10.1016/J.CERAMINT.2018.02.066.

[57] S.K. Sharma, S.P. Singh, D.Y. Kim, Fabrication of the heterojunction diode from Y-doped ZnO thin films on p-Si substrates by sol-gel method, Solid State Commun. 270 (2018) 124–129. doi:10.1016/J.SSC.2017.12.010.

[58] N. Kaur, Y. Lee, D.Y. Kim, S. Lee, Optical bandgap tuning in nanocrystalline ZnO:Y films via forming defect-induced localized bands, Mater Des. 148 (2018) 30–38. doi:10.1016/J.MATDES.2018.03.042.

[59] M. Kumar, H. Jeong, A. Kumar, B.P. Singh, D. Lee, Magnetron-sputtered high performance Y-doped ZnO thin film transistors fabricated at room temperature, Mater Sci Semicond Process. 71 (2017) 204–208.

[60] S. Kaya, D. Akcan, O. Ozturk, L. Arda, Enhanced mechanical properties of yttrium doped ZnO nanoparticles as determined by instrumented indentation technique, Ceram Int. 44 (2018) 10306–10314. doi:10.1016/J.CERAMINT.2018.03.038.

[61] M. Balestrieri, M. Gallart, M. Ziegler, P. Bazylewski, G. Ferblantier, G. Schmerber, et al., Luminescent Properties and Energy Transfer in Pr3+ Doped and Pr3+-Yb3+ Co-doped ZnO Thin Films, J Phys Chem C. 118 (2014) 13775–13780.

[62] Y. Wang, Z. Peng, Q. Wang, C. Wang, X. Fu, High-performance varistors simply by hot-dipping zinc oxide thin films in Pr6O11: Influence of temperature, Sci Rep. 7 (2017) 41994.

[63] H.Y.J. Li, J. Meng, Y. Liu, B. Zhang, G. Cheng, Effect of Pr DopY ing on the photoelectric properties of ZnO transparent conducting thin films, Mater Rev. 29 (2015).

[64] R. Navamathavan, K.-K. Kim, D.-K. Hwang, S.-J. Park, J.-H. Hahn, T.G. Lee, et al., A nanoindentation study of the mechanical properties of ZnO thin films on (0001) sapphire, Appl Surf Sci. 253 (2006) 464–467.

[65] S.O. Kucheyev, J.E. Bradby, J.S. Williams, C. Jagadish, M. V Swain, Mechanical deformation of single-crystal ZnO, Appl Phys Lett. 80 (2002) 956–958.

[66] J.E. Bradby, S.O. Kucheyev, J.S. Williams, C. Jagadish, M. V Swain, P. Munroe, et al., Contact-induced defect propagation in ZnO, Appl Phys Lett. 80 (2002) 4537–4539.

[67] Y. Zhang, C. Liu, J. Liu, J. Xiong, J. Liu, K. Zhang, et al., Lattice strain induced remarkable enhancement in piezoelectric performance of ZnO-based flexible

nanogenerators, ACS Appl Mater Interfaces. 8 (2016) 1381–1387.

[68] V.A. Coleman, J.E. Bradby, C. Jagadish, P. Munroe, Y.W. Heo, S.J. Pearton, et al., Mechanical properties of ZnO epitaxial layers grown on a-and c-axis sapphire, Appl Phys Lett. 86 (2005) 203105. doi:10.1063/1.1929874.

[69] R. Navamathavan, K.-K. Kim, D.-K. Hwang, S.-J. Park, T.G. Lee, G.-S. Kim, et al., Deformation behavior during nanoindentation of epitaxial ZnO thin films on sapphire substrate, Mater Lett. 61 (2007) 2443–2445.

[70] S.-R. Jian, Mechanical responses of single-crystal ZnO, J Alloys Compd. 494 (2010) 214–218.

[71] S.-R. Jian, Pop-in effects and dislocation nucleation of c-plane single-crystal ZnO by Berkovich nanoindentation, J Alloys Compd. 644 (2015) 54–58.

[72] K.A. Sierros, D.A. Banerjee, N.J. Morris, D.R. Cairns, I. Kortidis, G. Kiriakidis, Mechanical properties of ZnO thin films deposited on polyester substrates used in flexible device applications, Thin Solid Films. 519 (2010) 325–330.

[73] S.-R. Jian, I.-J. Teng, P.-F. Yang, Y.-S. Lai, J.-M. Lu, J.-G. Chang, et al., Surface morphological and nanomechanical properties of PLD-derived ZnO thin films, Nanoscale Res Lett. 3 (2008) 186.

[74] T.H. Sung, J.C. Huang, J.H. Hsu, S.R. Jian, T.G. Nieh, Yielding and plastic slip in ZnO, Appl Phys Lett. 100 (2012) 211903. doi:10.1063/1.4720169.

[75] T.H. Sung, J.C. Huang, H.C. Chen, Mechanical response of polar/non-polar ZnO under low dimensional stress, Appl Phys Lett. 102 (2013) 241901.

[76] M. Venkaiah, R. Singh, Effect of thickness on structural, optical and mechanical properties of Mn doped ZnO nanocrystalline thin films RF sputtered in nitrogen gas environment, Superlattices Microstruct. 72 (2014) 164–171.

[77] S. Zhao, Y. Zhou, Y. Liu, K. Zhao, S. Wang, W. Xiang, et al., Enhanced hardness in B-doped ZnO thin films on fused quartz substrates by pulsed-laser deposition, Appl Surf Sci. 253 (2006) 726–729.

[78] S.-K. Wang, T.-C. Lin, S.-R. Jian, J.-Y. Juang, J.S.-C. Jang, J.-Y. Tseng, Effects of post-annealing on the structural and nanomechanical properties of Ga-doped ZnO thin films

deposited on glass substrate by rf-magnetron sputtering, Appl Surf Sci. 258 (2011) 1261–1266.

[79] L.-Y. Lin, M.-C. Jeong, D.-E. Kim, J.-M. Myoung, Micro/nanomechanical properties of aluminum-doped zinc oxide films prepared by radio frequency magnetron sputtering, Surf Coatings Technol. 201 (2006) 2547–2552.

[80] Y.Q. Chen, X.J. Zheng, S.X. Mao, W. Li, Nanoscale mechanical behavior of vanadium doped ZnO piezoelectric nanofiber by nanoindentation technique, J Appl Phys. 107 (2010) 94302.

[81] N. Bahadur, A.K. Srivastava, S. Kumar, M. Deepa, B. Nag, Influence of cobalt doping on the crystalline structure, optical and mechanical properties of ZnO thin films, Thin Solid Films. 518 (2010) 5257–5264.

[82] R. Mohammadigharehbagh, S. Özen, H.H. Yudar, V. Şenay, S. Pat, Ş. Korkmaz, Investigation on the physical properties of C-doped ZnO thin films deposited by the thermionic vacuum arc, Eur Phys J Plus. 132 (2017) 28.

[83] Y.C. Lin, C.C. Chen, W.Y. Lai, Mechanical Properti es of ZnO: Mo Transparent Conducting Oxide Thin Film Prepared by Sputtering, Chinese J Phys. 51 (2013) 619–627.

[84] S.J. Bull, Nanoindentation of coatings, J Phys D Appl Phys. 38 (2005) R393. doi:10.1088/0022-3727/38/24/R01.

[85] L.-Y. Lin, D.-E. Kim, Effect of annealing temperature on the tribological behavior of ZnO films prepared by sol–gel method, Thin Solid Films. 517 (2009) 1690–1700.

[86] W.-K. Wang, H.-C. Wen, C.-H. Cheng, W.-C. Chou, W.-H. Yau, C.-H. Hung, et al., Nanotribological behavior of ZnO films prepared by atomic layer deposition, J Phys Chem Solids. 75 (2014) 334–338.

[87] C.-W. Huang, M.-H. Weng, C.-T. Pan, R.-Y. Yang, Nanoindentation evaluation of cathodic vacuum arc deposited ZnO film on PET substrate, Mater Lett. 175 (2016) 60–62.

[88] R. Pietruszka, B.S. Witkowski, S. Zimowski, T. Stapinski, M. Godlewski, Abrasion resistance of ZnO and ZnO: Al films on glass substrates by atomic layer deposition, Surf Coatings Technol. 319 (2017) 164–169.

[89] S.-Y. Chang, Y.-C. Hsiao, Y.-C. Huang, Preparation and mechanical properties of

aluminum-doped zinc oxide transparent conducting films, Surf Coatings Technol. 202 (2008) 5416–5420. doi:10.1016/j.surfcoat.2008.06.024.

[90] R. Wen, L. Wang, X. Wang, G.-H. Yue, Y. Chen, D.-L. Peng, Influence of substrate temperature on mechanical, optical and electrical properties of ZnO:Al films, J Alloys Compd. 508 (2010) 370–374. doi:https://doi.org/10.1016/j.jallcom.2010.08.034.

[91] X. Pang, H. Ma, K. Gao, H. Yang, X. Wu, A.A. Volinsky, Fracture toughness and adhesion of transparent Al: ZnO films deposited on glass substrates, J Mater Eng Perform. 22 (2013) 3161–3167.

[92] A.K. Bhattacharya, W.D. Nix, Finite element simulation of indentation experiments, Int J Solids Struct. 24 (1988) 881–891. doi:10.1016/0020-7683(88)90039-X.

[93] T. Xu, Y. Du, H. Luo, Z. Hu, X. Wang, L. Guo, et al., Characterization of the Mechanical Behavior of Colorado Mason Sand at Grain-Level by Nanoindentation, Exp Mech. 58 (2018) 449–463. doi:10.1007/s11340-017-0358-z.

[94] W.Z. Yao, J.H. You, Berkovich nanoindentation study of monocrystalline tungsten: a crystal plasticity study of surface pile-up deformation, Philos Mag. 97 (2017) 1418–1435.

[95] K. Komvopoulos, Elastic-plastic finite element analysis of indented layered media, ASME J Tribol. 111 (1989) 430–439.

[96] E. Weppelmann, M. V Swain, Investigation of the stresses and stress intensity factors responsible for fracture of thin protective films during ultra-micro indentation tests with spherical indenters, Thin Solid Films. 286 (1996) 111–121.

[97] D.S. Simulia, Abaqus 6.12 documentation, Provid Rhode Island, US. (2012).

[98] J.D. Bressan, A. Tramontin, C. Rosa, Modeling of nanoindentation of bulk and thin film by finite element method, Wear. 258 (2005) 115–122.

[99] S.N.V.R.K. Kurapati, Elastic-plastic Indentation Deformation in Homogeneous and Layered Materials: Finite Element Analysis, University of Kentucky, 2008.

[100] H.A. Shirazi, S.A. Mirmohammadi, M. Shaali, A. Asnafi, M.R. Ayatollahi, A constitutive material model for a commercial PMMA bone cement using a combination of nano-indentation test and finite element analysis, Polym Test. 59 (2017) 328–335.

[101] L. Gan, B. Ben-Nissan, The effects of mechanical properties of thin films on nano-indentation data: Finite element analysis, Comput Mater Sci. 8 (1997) 273–281.

[102] R. Saha, W.D. Nix, Effects of the substrate on the determination of thin film mechanical properties by nanoindentation, Acta Mater. 50 (2002) 23–38.

[103] D. Mercier, V. Mandrillon, G. Parry, M. Verdier, R. Estevez, Y. Bréchet, et al., Investigation of the fracture of very thin amorphous alumina film during spherical nanoindentation, Thin Solid Films. 638 (2017) 34–47. doi:https://doi.org/10.1016/j.tsf.2017.07.040.

[104] J.L. He, S. Veprek, Finite element modeling of indentation into superhard coatings, Surf Coatings Technol. 163 (2003) 374–379.

[105] G. Cao, X. Chen, The size effect of nanoindentation on ZnO nanofilms, J Appl Phys. 102 (2007) 123513. doi:10.1063/1.2826722.

[106] J.S. Wang, X.J. Zheng, H. Zheng, S.T. Song, Z. Zhu, Identification of elastic parameters of transversely isotropic thin films by combining nanoindentation and FEM analysis, Comput Mater Sci. 49 (2010) 378–385. doi:10.1016/j.commatsci.2010.05.025.

[107] X. Zhao, Z. Xie, P. Munroe, Nanoindentation of hard multilayer coatings: Finite element modelling, Mater Sci Eng A. 528 (2011) 1111–1116.

[108] Y. Liu, X. Zhao, L.-C. Zhang, D. Habibi, Z. Xie, Architectural design of diamond-like carbon coatings for long-lasting joint replacements, Mater Sci Eng C. 33 (2013) 2788–2794.

[109] D.M. Mattox, Handbook of physical vapor deposition (PVD) processing, William Andrew, 2010.

[110] E. Maawad, H.-G. Brokmeier, L. Wagner, Y. Sano, C. Genzel, Investigation on the surface and near-surface characteristics of Ti–2.5Cu after various mechanical surface treatments, Surf Coatings Technol. 205 (2011) 3644–3650. doi:10.1016/J.SURFCOAT.2011.01.001.

[111] T.R. Gopalarao, S. Ravi, D. Pamu, Effect of Film Thickness in Electrical Resistivity and Magnetic Properties of Nd0.7Sr0.3MnO3 Thin Films, J Supercond Nov Magn. 29 (2016) 2567–2572. doi:10.1007/s10948-016-3563-6.

[112] R.C. Shivamurthy, M. Kamaraj, R. Nagarajan, S.M. Shariff, G. Padmanabham, Slurry

Erosion Characteristics and Erosive Wear Mechanisms of Co-Based and Ni-Based Coatings Formed by Laser Surface Alloying, Metall Mater Trans A. 41 (2010) 470–486. doi:10.1007/s11661-009-0092-y.

[113] K. Wasa, S. Hayakawa, Handbook of sputter deposition technology, (1992).

[114] Matt Hughes, What is DC Sputtering?, (n.d.). http://www.semicore.com/news/94-what-is-dc-sputtering (accessed May 15, 2018).

[115] P. Sigmund, Theory of sputtering. I. Sputtering yield of amorphous and polycrystalline targets, Phys Rev. 184 (1969) 383.

[116] N. Laegreid, G.K. Wehner, Sputtering yields of metals for Ar+ and Ne+ ions with energies from 50 to 600 eV, J Appl Phys. 32 (1961) 365–369.

[117] H.-G. Brokmeier, Hard X-Rays for In Situ Strain and Texture Measurements, Part Part Syst Charact. 26 (2009) 117–124. doi:10.1002/ppsc.200800050.

[118] B.D. Cullity, S.R.B.D. Cullity, S.R. Stock, Elements of X-ray Diffraction, 2001.

[119] J. Rebelo-Kornmeier, M. Hofmann, W. Gan, C. Randau, K. Braun, K. Zeitelhack, et al., New Developments of the Materials Science Diffractometer STRESS-SPEC, Trans Tech Publ. 905 (2017) 151--156.

[120] N. Waeselmann, Structural transformations in complex perovskite-type relaxor and relaxor-based ferroelectrics at high pressures and temperatures, Fachbereich Geowissenschaften der Universität Hamburg, 2012.

[121] A.R. Stokes, A.J.C. Wilson, The diffraction of X rays by distorted crystal aggregates-I, Proc Phys Soc London, Sec A. 56 (1944) 174.

[122] A. Purohit, S. Chander, A. Sharma, S.P. Nehra, M.S. Dhaka, Impact of low temperature annealing on structural, optical, electrical and morphological properties of ZnO thin films grown by RF sputtering for photovoltaic applications, Opt Mater . 49 (2015) 51–58.

[123] R. Reichelt, Scanning electron microscopy, in: Sci Microsc, Springer, 2007: pp. 133–272.

[124] B.G. Yacobi, D.B. Holt, Cathodoluminescence scanning electron microscopy of semiconductors, J Appl Phys. 59 (1986) R1–R24.

[125] P. Eaton, P. West, Atomic force microscopy, Oxford University Press, 2010.

[126] D. Briggs, M.P. Seah, Practical surface analysis: by auger and x-ray photoelectron spectroscopy, Wiley, 2003.

[127] M.P. Seah, I.S. Gilmore, S.J. Spencer, Quantitative XPS: I. Analysis of X-ray photoelectron intensities from elemental data in a digital photoelectron database, J Electron Spectros Relat Phenomena. 120 (2001) 93–111.

[128] B.D. Ratner, D.G. Castner, Electron spectroscopy for chemical analysis, Surf Anal Princ Tech 2nd Ed. (2009) 47–112.

[129] J.M. Walls, Methods of surface analysis: techniques and applications, CUP Archive, 1990.

[130] A.C. Fischer-Cripps, Nanoindentation, Springer-Verlag , New York, USA, 2011. doi:10.1007/978-1-4419-9872-9.

[131] W.C. Oliver, G.M. Pharr, An improved technique for determining hardness and elastic modulus using load and displacement sensing indentation experiments, J Mater Res. 7 (1992) 1564–1583.

[132] C. Jin, D.M. Ebenstein, Nanoindentation of compliant materials using Berkovich tips and flat tips, J Mater Res. 32 (2017) 435–450.

[133] A.C. Fischer-Cripps, Contact mechanics, in: Nanoindentation, Springer, 2011: pp. 1–19.

[134] K.L. Johnson, Contact mechanics, Cambridge university press, 1987.

[135] I.N. Sneddon, Application of integral transforms in the theory of elasticity, Springer-Verlag New York, 1975.

[136] Q. Tian, H. Liu, Electrophoretic deposition and characterization of nanocomposites and nanoparticles on magnesium substrates, Nanotechnology. 26 (2015) 175102.

[137] K.L. Mittal, Adhesion measurement of thin films, Act Passiv Electron Components. 3 (1976) 21–42.

[138] D. Kesavan, M. Kamaraj, The microstructure and high temperature wear performance of a nickel base hardfaced coating, Surf Coatings Technol. 204 (2010) 4034–4043. doi:10.1016/J.SURFCOAT.2010.05.022.

[139] P. Tran, S.S. Kandula, P.H. Geubelle, N.R. Sottos, Comparison of dynamic and quasi-static measurements of thin film adhesion, J Phys D Appl Phys. 44 (2010) 34006.

[140] S. Du, K. Zhang, M. Wen, P. Ren, Q. Meng, C. Hu, et al., Tribochemistry dependent tribological behavior of superhard TaC/SiC multilayer films, Surf Coatings Technol. 337 (2018) 492–500. doi:10.1016/J.SURFCOAT.2018.01.064.

[141] M. Okazaki, T. Ozaki, Some Problems on Evaluating Elastic Modulus of APSed Ceramic Top Coat for TBCs by Indentation Method, Trans Tech Publ. 353 (2007) 1802–1805.

[142] S.J. Bull, Failure mode maps in the thin film scratch adhesion test, Tribol Int. 30 (1997) 491–498.

[143] M.S. Kabir, P. Munroe, Z. Zhou, Z. Xie, Scratch adhesion and tribological behaviour of graded Cr/CrN/CrTiN coatings synthesized by closed-field unbalanced magnetron sputtering, Wear. 380–381 (2017) 163–175. doi:https://doi.org/10.1016/j.wear.2017.03.020.

[144] S.J. Bull, E.G. Berasetegui, An overview of the potential of quantitative coating adhesion measurement by scratch testing, Tribol Interface Eng Ser. 51 (2006) 136–165.

[145] L. Schmidt-Mende, J.L. MacManus-Driscoll, ZnO–nanostructures, defects, and devices, Mater Today. 10 (2007) 40–48.

[146] M.C. Carotta, A. d Cervi, V. Di Natale, S. Gherardi, A. Giberti, V. Guidi, et al., ZnO gas sensors: a comparison between nanoparticles and nanotetrapods-based thick films, Sensors Actuators B Chem. 137 (2009) 164–169. doi:10.1016/j.snb.2008.11.007.

[147] A. Wei, L. Pan, W. Huang, Recent progress in the ZnO nanostructure-based sensors, Mater Sci Eng B. 176 (2011) 1409–1421.

[148] K. Haga, M. Kamidaira, Y. Kashiwaba, T. Sekiguchi, H. Watanabe, ZnO thin films prepared by remote plasma-enhanced CVD method, J Cryst Growth. 214 (2000) 77–80. doi:10.1016/S0022-0248(00)00068-3.

[149] G. Bräuer, B. Szyszka, M. Vergöhl, R. Bandorf, Magnetron sputtering–Milestones of 30 years, Vacuum. 84 (2010) 1354–1359.

[150] A. Fluri, C.W. Schneider, D. Pergolesi, In situ stress measurements of metal oxide thin films, in: Met Oxide-Based Thin Film Struct, Elsevier, 2018: pp. 109–132.

[151] P. Joshi, J. Singh, R. Sharma, V.K. Jain, J. Akhtar, A facile approach to fabricate ZnO thin film based micro-cantilevers, Microelectron Eng. 187 (2018) 50–57.

[152] P.-F. Yang, H.-C. Wen, S.-R. Jian, Y.-S. Lai, S. Wu, R.-S. Chen, Characteristics of ZnO thin films prepared by radio frequency magnetron sputtering, Microelectron Reliab. 48 (2008) 389–394.

[153] Y.-C. Huang, S.-Y. Chang, Substrate effect on mechanical characterizations of aluminum-doped zinc oxide transparent conducting films, Surf Coatings Technol. 204 (2010) 3147–3153.

[154] K.-Y. Tsai, T.-S. Chin, H.-P.D. Shieh, Effect of grain curvature on nano-indentation measurements of thin films, Jpn J Appl Phys. 43 (2004) 6268.

[155] Y. Zhang, X. Hu, K. Wu, M. Zheng, Application of GL dislocation model in low frequency damping capacities of AZ91D and SiCw/AZ91D composites, Trans Tech Publ. 546 (2007) 495--498.

[156] F. Liu, H. Yuan, J. Yin, J.T. Wang, Influence of stacking fault energy and temperature on microstructures and mechanical properties of fcc pure metals processed by equal-channel angular pressing, Mater Sci Eng A. 662 (2016) 578–587. doi:10.1016/J.MSEA.2016.03.022.

[157] G.K. Williamson, R.E. Smallman, III. Dislocation densities in some annealed and cold-worked metals from measurements on the X-ray debye-scherrer spectrum, Philos. Mag. . 1 (1956) 34–46.

[158] C. Manoharan, G. Pavithra, M. Bououdina, S. Dhanapandian, P. Dhamodharan, G. Pavithra, et al., Characterization and study of antibacterial activity of spray pyrolysed ZnO: Al thin films, Appl Nanosci. 6 (2016) 815–825. doi:10.1007/s13204-015-0493-8.

[159] A. Purohit, S. Chander, S.P. Nehra, M.S. Dhaka, Effect of air annealing on structural, optical, morphological and electrical properties of thermally evaporated CdSe thin films, Phys E Low-Dimensional Syst Nanostructures. 69 (2015) 342–348.

[160] V. Tvarozek, I. Novotny, P. Sutta, S. Flickyngerova, K. Schtereva, E. Vavrinsky, Influence of sputtering parameters on crystalline structure of ZnO thin films, Thin Solid Films. 515 (2007) 8756–8760.

[161] S. Tricot, M. Nistor, E. Millon, C. Boulmer-Leborgne, N.B. Mandache, J. Perriere, et al., Epitaxial ZnO thin films grown by pulsed electron beam deposition, Surf Sci. 604 (2010) 2024–2030.

[162] J.W. Lee, J.-H. Kim, S.K. Han, S.-K. Hong, J.Y. Lee, S.I. Hong, et al., Interface and defect structures in ZnO films on m-plane sapphire substrates, J Cryst Growth. 312 (2010) 238–244.

[163] F. Fenske, B. Selle, M. Birkholz, Preferred orientation and anisotropic growth in polycrystalline ZnO: Al films prepared by magnetron sputtering, Jpn J Appl Phys. 44 (2005) L662.

[164] G.A. Kumar, M.V.R. Reddy, K.N.N. Reddy, Structural, optical and electrical characteristics of nanostructured ZnO thin films with various thicknesses deposited by RF magnetron sputtering, J Phys Sci. 1 (2013) 17–23.

[165] S. Lalitha, R. Sathyamoorthy, S. Senthilarasu, A. Subbarayan, K. Natarajan, Characterization of CdTe thin film—dependence of structural and optical properties on temperature and thickness, Sol Energy Mater Sol Cells. 82 (2004) 187–199.

[166] M. Salah, S. Azizi, C. Khaldi, J. Lamloumi, Nanoindentation and AFM characterization of lithium-doped ZnO sprayed thin films, in: Renew Energy Congr (IREC), 2018 9th Int, IEEE, 2018: pp. 1–5.

[167] J. Li, K.J. Van Vliet, T. Zhu, S. Yip, S. Suresh, Atomistic mechanisms governing elastic limit and incipient plasticity in crystals, Nature. 418 (2002) 307–310.

[168] N. Mukhopadhyay, A. Belger, P. Paufler, D. Kim, Nanoindentation studies on Cu–Ti–Zr–Ni–Si–Sn bulk metallic glasses, Mater Sci Eng A. 449 (2007) 954--957.

[169] C.-H. Chao, P.-W. Chi, D.-H. Wei, Investigations on the crystallographic orientation induced surface morphology evolution of ZnO thin films and their wettability and conductivity, J Phys Chem C. 120 (2016) 8210–8219.

[170] K. Johansson, E. Lewin, Influence of oxygen content on structure and material properties of reactively sputtered Al-Ge-ON thin films, J Alloys Compd. 738 (2018) 515–527.

[171] W. Ni, Y.-T. Cheng, M. Lukitsch, A.M. Weiner, L.C. Lev, D.S. Grummon, Novel layered tribological coatings using a superelastic NiTi interlayer, Wear. 259 (2005) 842–848.

[172] C.A. Schuh, T.G. Nieh, Y. Kawamura, Rate dependence of serrated flow during nanoindentation of a bulk metallic glass, J Mater Res. 17 (2002) 1651–1654.

[173] Y. V. Milman, B.A. Galanov, S.I. Chugunova, Plasticity characteristic obtained through

hardness measurement, Acta Metall Mater. 41 (1993) 2523–2532. doi:10.1016/0956-7151(93)90122-9.

[174] S. Zhang, D. Sun, Y. Fu, H. Du, Effect of sputtering target power on microstructure and mechanical properties of nanocomposite nc-TiN/a-SiN x thin films, Thin Solid Films. 447 (2004) 462–467. doi:10.1016/S0040-6090Ž03.01125-8.

[175] Z. Suo, Cracking and debonding of microlaminates, J Vac Sci Technol A Vacuum, Surfaces, Film. 11 (1993) 1367–1372.

[176] P. Dubey, V. Arya, S.K. Srivastava, D. Singh, R. Chandra, Study of thermal stability and mechanical properties of fcc phase Zr 22 W 19 N 58 thin films deposited by reactive magnetron sputtering, Surf Coatings Technol. 245 (2014) 34–39.

[177] I.P. d Hayward, I.L. Singer, L.E. Seitzman, Effect of roughness on the friction of diamond on CVD diamond coatings, Wear. 157 (1992) 215–227.

[178] P.S. Alexopoulos, T.C. O'sullivan, Mechanical properties of thin films, Annu Rev Mater Sci. 20 (1990) 391–420.

[179] T. Ungár, G. Tichy, J. Gubicza, R.J. Hellmig, Correlation between subgrains and coherently scattering domains, Powder Diffr. 20 (2005) 366–375.

[180] J.A. Thornton, The microstructure of sputter deposited coatings, J Vac Sci Technol A Vacuum, Surfaces, Film. 4 (1986) 3059–3065.

[181] J. Ghatak, J.-H. Huang, C.-P. Liu, Derivation of the surface free energy of ZnO and GaN using in situ electron beam hole drilling, Nanoscale. 8 (2016) 634–640. doi:10.1039/C5NR06198A.

[182] J.L. Sun, P.W. Trimby, F.K. Yan, X.Z. Liao, N.R. Tao, J.T. Wang, Grain size effect on deformation twinning propensity in ultrafine-grained hexagonal close-packed titanium, Scr Mater. 69 (2013) 428–431. doi:10.1016/J.SCRIPTAMAT.2013.06.001.

[183] J. Takadoum, H.H. Bennani, Influence of substrate roughness and coating thickness on adhesion, friction and wear of TiN films, Surf Coatings Technol. 96 (1997) 272–282.

[184] D. Wang, G.P. Bierwagen, Sol–gel coatings on metals for corrosion protection, Prog Org Coatings. 64 (2009) 327–338. doi:10.1016/J.PORGCOAT.2008.08.010.

[185] A.A.M. Ralib, A.N. Nordin, N.A. Malik, R. Othman, A.H.M.Z. Alam, S. Khan, et al., A study on controllable aluminium doped zinc oxide patterning by chemical etching for MEMS application, Microsys. Technol. 23 (2017) 3851--3862.

[186] R. Daniel, A. Zeilinger, T. Schöberl, B. Sartory, C. Mitterer, J. Keckes, Microstructure-controlled depth gradients of mechanical properties in thin nanocrystalline films: Towards structure-property gradient functionalization, J Appl Phys. 117 (2015) 235301. doi:10.1063/1.4922666.

[187] X. Tang, W.B.A. Ho, J.M. Xue, Synthesis of Zn-Doped AgInS $_2$ Nanocrystals and Their Fluorescence Properties, J Phys Chem C. 116 (2012) 9769–9773. doi:10.1021/jp207711p.

[188] P.J. Kelly, R.D. Arnell, Magnetron sputtering: a review of recent developments and applications, Vacuum. 56 (2000) 159–172.

[189] N.K. Mukhopadhyay, A. Belger, P. Paufler, E. Uhrig, S. Brühne, W. Assmus, Nanoindentation studies on single crystals of Zn–Mg–Er and Zn–Mg–Ho icosahedral phases, J Alloys Compd. 466 (2008) 160–164. doi:10.1016/J.JALLCOM.2007.11.084.

[190] J.-E. Lee, H.-J. Kim, D.-E. Kim, Assessment of adhesion between thin film and silicon based on a scratch test, J Mech Sc Tech. 24 (2010) 97–101.

[191] J. Chen, S.J. Bull, Approaches to investigate delamination and interfacial toughness in coated systems: an overview, J Phys D Appl Phys. 44 (2011) 034001. doi:10.1088/0022-3727/44/3/034001.

[192] L. Znaidi, Sol–gel-deposited ZnO thin films: a review, Mater Sci Eng B. 174 (2010) 18–30.

[193] C.F. Klingshirn, A. Waag, A. Hoffmann, J. Geurts, Zinc oxide: from fundamental properties towards novel applications, Springer Science & Business Media, 2010.

[194] S. Lu, Q. Liao, J. Qi, S. Liu, Y. Liu, Q. Liang, et al., The enhanced performance of piezoelectric nanogenerator via suppressing screening effect with Au particles/ZnO nanoarrays Schottky junction, Nano Res. 9 (2016) 372–379.

[195] C. Lai, K. Lin, S. Rosmaidah, Effect of annealing temperature on the quality of Al-doped ZnO thin films prepared by sol–gel method, J Sol-Gel Sci Technol. 61 (2012) 249–257. doi:10.1007/s10971-011-2621-6.

[196] W.-H. Yau, P.-C. Tseng, H.-C. Wen, C.-H. Tsai, W.-C. Chou, Luminescence properties of mechanically nanoindented ZnSe, Microelectron Reliab. 51 (2011) 931–935.

[197] N. Tayebi, A. Polycarpou, T. Conry, Effects of substrate on determination of hardness of thin films by nanoscratch and nanoindentation techniques, J Mater Res. 19 (2004) 1791--1802.

[198] L. Sagalowicz, G. Fox, Planar defects in ZnO thin films deposited on optical fibers and flat substrates, J Mater Res. 14 (1999) 1876–1885.

[199] F. Sun, F.H.S. Froes, Synthesis and characterization of mechanical-alloyed Ti–xMg alloys, J Alloys Compd. 340 (2002) 220–225. doi:10.1016/S0925-8388(01)02027-8.

[200] L. Kolodziejczyk, W. Szymanski, D. Batory, A. Jedrzejczak, Nanotribology of silver and silicon doped carbon coatings, Diam Relat Mater. 67 (2016) 8–15. doi:http://dx.doi.org/10.1016/j.diamond.2015.12.010.

[201] D. Bao, H. Gu, A. Kuang, Sol-gel-derived c-axis oriented ZnO thin films, Thin Solid Films. 312 (1998) 37–39.

[202] M.S. Kim, K.G. Yim, M.Y. Cho, J.Y. Leem, D.Y. Lee, J.S. Kim, et al., Post-annealing effects on the structural and the optical properties of ZnO thin films grown by using the hydrothermal method, J Korean Phys Soc . 58 (2011) 515–519.

[203] A. Van der Drift, Evolutionary selection, a principle governing growth orientation in vapour-deposited layers, Philips Res Rep. 22 (1967) 267–288.

[204] N. Fujimura, T. Nishihara, S. Goto, J. Xu, T. Ito, Control of preferred orientation for ZnOx films: control of self-texture, J Cryst Growth. 130 (1993) 269–279. doi:http://dx.doi.org/10.1016/0022-0248(93)90861-P.

[205] C.R. Aita, A.J. Purdes, K.L. Lad, P.D. Funkenbusch, The effect of O2 on reactively sputtered zinc oxide, J Appl Phys. 51 (1980) 5533–5536. doi:doi:http://dx.doi.org/10.1063/1.327472.

[206] V. Dave, P. Dubey, H.O. Gupta, R. Chandra, Influence of sputtering pressure on the structural, optical and hydrophobic properties of sputtered deposited HfO 2 coatings, Thin Solid Films. 549 (2013) 2–7.

[207] L.-P. Peng, A.-L. He, L. Fang, X.-F. Yang, Structure and properties of indium-doped ZnO

films prepared by RF magnetron sputtering under different pressures, Rare Met. (2015) 1.

[208] T.K. Roy, Assessing hardness and fracture toughness in sintered zinc oxide ceramics through indentation technique, Mater Sci Eng A. 640 (2015) 267–274. doi:10.1016/j.msea.2015.05.107.

[209] D. Maharaj, B. Bhushan, Scale effects of nanomechanical properties and deformation behavior of Au nanoparticle and thin film using depth sensing nanoindentation, Beilstein J Nanotechnol. 5 (2014) 822–836. doi:10.3762/bjnano.5.94.

[210] D. Misra, S. Sohn, W. Kim, D. Kim, Rate-dependent serrated flow and plastic deformation in Ti45Zr16Be20Cu10Ni9 bulk amorphous alloy during nanoindentation, Sci Technol Adv Mater. 9 (2008) 045004.

[211] T.-H. Fang, W.-J. Chang, C.-M. Lin, Nanoindentation characterization of ZnO thin films, Mater Sci Eng A. 452–453 (2007) 715–720. doi:https://doi.org/10.1016/j.msea.2006.11.008.

[212] A. Gayle, R. Cook, Mapping viscoelastic and plastic properties of polymers and polymer-nanotube composites using instrumented indentation, J Mater Res. 31 (2016) 2347–2360.

[213] J. Musil, Hard nanocomposite coatings: thermal stability, oxidation resistance and toughness, Surf. Coat. Technol. 207 (2012) 50–65.

[214] N. Deyneka-Dupriez, U. Herr, H. Fecht, A. Pfrang, T. Schimmel, B. Reznik, et al., Interfacial adhesion and friction of pyrolytic carbon thin films on silicon substrates, J Mater Res. 23 (2008) 2749–2756.

[215] M. Blees, G. Winkelman, A. Balkenende, J. Den Toonder, The effect of friction on scratch adhesion testing: application to a sol–gel coating on polypropylene, Thin Solid Films. 359 (2000) 1–13.

[216] B. Bhushan, L. Xiaodong, Micromechanical and tribological characterization of doped single-crystal silicon and polysilicon films for microelectromechanical systems devices, J Mater Res. 12 (1997) 54–63.

[217] A. Manivasaham, K. Ravichandran, K. Subha, Light intensity effects on the sensitivity of ZnO: Cr gas sensor, Surf Eng. 33 (2017) 866–876.

[218] H. Mahdhi, J.L. Gauffier, K. Djessas, Z. Ben Ayadi, Thickness dependence of properties

Ga-doped ZnO thin films deposited by magnetron sputtering, J Mater Sci Mater Electron. 28 (2017) 5021–5028.

[219] N. Sharma, S. Kumar, J. Kumar, Synthesis and structural properties of ZnO doped nanoparticles prepared by hydrothermal method, Integr Ferroelectr. 186 (2018) 115–119.

[220] K.-M. Kang, H.-H. Park, Effect of Atomic Layer Deposition Temperature on the Growth Orientation, Morphology, and Electrical, Optical, and Band-Structural Properties of ZnO and Fluorine-Doped ZnO Thin Films, J Phys Chem C. 122 (2018) 377–385. doi:10.1021/acs.jpcc.7b08943.

[221] Y. Wang, Z.J. Peng, Q. Wang, X.L. Fu, Tunable electrical resistivity of oxygen-deficient zinc oxide thin films, Surf Eng. 33 (2017) 217–225.

[222] M. Sowjanya, D. Pamu, R. Chowdhury, R. Jayaganthan, Effects of CeO2 Dopant on Structural and Optical Properties of ZnO Thin Films Prepared by RF Sputtering, Adv Sci Lett. 22 (2016) 896--900.

[223] L. Agarwal, B.N. Naik, S. Tripathi, Highly reflective Er-doped ZnO thin-film coating for application in a UV optical ring resonator, Nanotechnology. 28 (2017) 465707.

[224] R. Bomila, S. Srinivasan, S. Gunasekaran, A. Manikandan, Enhanced Photocatalytic Degradation of Methylene Blue Dye, Opto-magnetic and Antibacterial Behaviour of Pure and La-doped ZnO Nanoparticles, J Supercond Nov Magn. 31 (2017) 855–864.

[225] U. Alam, A. Khan, D. Ali, D. Bahnemann, M. Muneer, Comparative photocatalytic activity of sol–gel derived rare earth metal (La, Nd, Sm and Dy)-doped ZnO photocatalysts for degradation of dyes, RSC Adv. 8 (2018) 17582–17594.

[226] R. Yogamalar, P. Venkateswaran, M. Benzigar, K. Ariga, A. Vinu, A. Bose, Dopant induced bandgap narrowing in Y-doped zinc oxide nanostructures, J Nanosci Nanotechnol. 12 (2012) 75–83.

[227] L.K. Singh, A. Srinivasan, U.T.S. Pillai, M.A. Joseph, B.C. Pai, The Effect of Yttrium Addition on the Microstructure and Mechanical Properties of Mg Alloys, Trans Indian Inst Met. 68 (2015) 331–339. doi:10.1007/s12666-014-0464-x.

[228] H.S. Jiang, X.G. Qiao, M.Y. Zheng, K. Wu, C. Xu, S. Kamado, The partial substitution of Y with Gd on microstructures and mechanical properties of as-cast and as-extruded Mg-

10Zn-6Y-0.5Zr alloy, Mater Charact. 135 (2018) 96–103. doi:10.1016/J.MATCHAR.2017.11.025.

[229] Z. Zhang, Y. Xu, Y. Li, W. Zheng, Z. Zhao, R. Wang, Color tuning of up-conversion emission in ytterbium, erbium, aluminum tri-doped zinc oxide crystal by adjusting aluminum concentration, Spectrosc Lett. 51 (2018) 31–36.

[230] E. Vinoth, S. Gowrishankar, N. Gopalakrishnan, RF magnetron sputtered Cd doped ZnO thin films for gas-sensing applications, Mater Manuf Process. 32 (2017) 377–382.

[231] D. Bravo-Bárcenas, I. Campos-Silva, H. Cimenoglu, J. Martínez-Trinidad, M. Flores-Jiménez, H. Martinez-Gutiérrez, Characterisation of CoB–Co2B coatings by the scratch test, Surf Eng. 32 (2016) 570–577.

[232] Z. Yun, W. Yue, W. Peng-Fei, L. Hong-Yu, W. Shou-Yu, Optical and mechanical properties of transparent conductive Al-doped ZnO films deposited by the sputtering method, Chinese Phys Lett. 29 (2012) 38103.

[233] H. Akazawa, Mechanical and transparent conductive properties of ZnO and Ga-doped ZnO films sputtered using electron-cyclotron-resonance plasma on polyethylene naphtalate substrates, J Vac Sci Technol A Vacuum, Surfaces, Film. 32 (2014) 021503. doi:10.1116/1.4831979.

[234] F. Lekoui, S. Hassani, M. Ouchabane, M. Hamici, Optical and mechanical properties of ZnO-Ag films deposited by thermal evaporation, in: Dielectr Mater Photovolt Syst, 2014: pp. 1–3.

[235] Z. Wang, H. Zhou, D. Han, F. Gu, Electron compensation in p-type 3DOM NiO by Sn doping for enhanced formaldehyde sensing performance, J Mater Chem C. 5 (2017) 3254–3263.

[236] J.H. Zheng, J.L. Song, Q. Jiang, J.S. Lian, Enhanced UV emission of Y-doped ZnO nanoparticles, Appl Surf Sci. 258 (2012) 6735–6738. doi:http://doi.org/10.1016/j.apsusc.2012.03.010.

[237] V. Bhardwaj, R. Chowdhury, R. Jayaganthan, Adhesion strength and nanomechanical characterization of ZnO thin films, J Mater Res. 32 (2017) 1432–1443. doi:10.1557/jmr.2017.85.

[238] G.D. Fan, M.Y. Zheng, C.H. Ju, X.S. Hu, K. Wu, W.M. Gan, et al., Effect of grain size on cyclic microplasticity of ECAP processed commercial pure magnesium, J Mater Sci. 48 (2013) 1239–1248. doi:10.1007/s10853-012-6865-5.

[239] K. Rajkumar, S. Aravindan, Tribological studies on microwave sintered copper–carbon nanotube composites, Wear. 270 (2011) 613–621. doi:10.1016/J.WEAR.2011.01.017.

[240] L. Armelao, G. Bottaro, M. Pascolini, M. Sessolo, E. Tondello, M. Bettinelli, et al., Structure−Luminescence Correlations in Europium-Doped Sol−Gel ZnO Nanopowders, J Phys Chem C. 112 (2008) 4049–4054. doi:10.1021/jp710207r.

[241] T. Basu, M. Kumar, S. Nandy, B. Satpati, C.P. Saini, A. Kanjilal, et al., Thickness-dependent blue shift in the excitonic peak of conformally grown ZnO:Al on ion-beam fabricated self-organized Si ripples, J Appl Phys. 118 (2015) 104903. doi:10.1063/1.4930223.

[242] D. Barreca, G.A. Battiston, D. Berto, R. Gerbasi, E. Tondello, Y2O3 Thin Films Characterized by XPS, Surf Sci Spectra. 8 (2001) 234–239. doi:10.1116/11.20020404.

[243] S. Xiang, X. Wang, M. Gupta, K. Wu, X. Hu, M. Zheng, Graphene nanoplatelets induced heterogeneous bimodal structural magnesium matrix composites with enhanced mechanical properties, Sci Rep. 6 (2016) 38824.

[244] A.A. Dakhel, Nanocrystalline Pr-doped ZnO insulator for metal–insulator–Si Schottky diodes, J Cryst Growth. 311 (2009) 4183–4187.

[245] D. Xu, K. He, R.H. Yu, Y. Tong, J.P. Qi, X.J. Sun, et al., Microstructure and electrical properties of praseodymium oxide doped Bi2O3 based ZnO varistor films, Mater Technol. 30 (2015) A24–A28.

[246] T. Senda, R.C. Bradt, Grain Growth in Sintered ZnO and ZnO-Bi2O3 Ceramics, J Am Ceram Soc. 73 (1990) 106–114.

[247] X. Tang, E.S.G. Choo, L. Li, J. Ding, J. Xue, One-Pot Synthesis of Water-Stable ZnO Nanoparticles via a Polyol Hydrolysis Route and Their Cell Labeling Applications, Langmuir. 25 (2009) 5271–5275. doi:10.1021/la900374b.

[248] T.K. Gupta, Application of zinc oxide varistors, J Am Ceram Soc. 73 (1990) 1817–1840.

[249] N.K. Divya, P.P. Pradyumnan, Photoluminescence quenching and photocatalytic

enhancement of Pr doped ZnO nanocrystals, Bull Mater Sci. 40 (2017) 1405–1413.

[250] Y. Sato, T. Mizoguchi, F. Oba, M. Yodogawa, T. Yamamoto, Y. Ikuhara, Identification of native defects around grain boundary in Pr-doped ZnO bicrystal using electron energy loss spectroscopy and first-principles calculations, Appl Phys Lett. 84 (2004) 5311–5313.

[251] C. Wang, S. Ma, A. Sun, R. Qin, F. Yang, X. Li, et al., Characterization of electrospun Pr-doped ZnO nanostructure for acetic acid sensor, Sensors Actuators B Chem. 193 (2014) 326–333.

[252] C. Shi, H. Zhao, H. Huang, S. Wan, Z. Ma, C. Geng, et al., Effects of probe tilt on nanoscratch results: An investigation by finite element analysis, Tribol Int. 60 (2013) 64–69.

[253] K. Fu, L. Chang, C. Yang, L. Sheppard, H. Wang, M. Maandal, et al., Plastic behaviour of high-strength lightweight Al/Ti multilayered films, J Mater Sci. 52 (2017) 13956–13965.

[254] N.-R. Kang, Y.-C. Kim, H. Jeon, S.K. Kim, J. Jang, H.N. Han, et al., Wall-thickness-dependent strength of nanotubular ZnO, Sci Rep. 7 (2017) 4327.

[255] N.Y. Yuan, S.Y. Wang, C.B. Tan, X.Q. Wang, G.G. Chen, J.N. Ding, The influence of deposition temperature on growth mode, optical and mechanical properties of ZnO films prepared by the ALD method, J Cryst Growth. 366 (2013) 43–46.

[256] C.-Y. Yen, S.-R. Jian, G.-J. Chen, C.-M. Lin, H.-Y. Lee, W.-C. Ke, et al., Influence of annealing temperature on the structural, optical and mechanical properties of ALD-derived ZnO thin films, Appl Surf Sci. 257 (2011) 7900–7905.

[257] G. Peng, Z. Lu, Y. Ma, Y. Feng, Y. Huan, T. Zhang, Spherical indentation method for estimating equibiaxial residual stress and elastic–plastic properties of metals simultaneously, J Mater Res. 33 (2018) 884–897.

[258] D.B. Marshall, Controlled flaws in ceramics: a comparison of Knoop and Vickers indentation, J Am Ceram Soc. 66 (1983) 127–131.

[259] I.A. Alhafez, C.J. Ruestes, Y. Gao, H.M. Urbassek, Nanoindentation of hcp metals: a comparative simulation study of the evolution of dislocation networks, Nanotechnology. 27 (2015) 45706.

[260] G.S. Thool, A.K. Singh, R.S. Singh, A. Gupta, M.A.B.H. Susan, Facile synthesis of flat crystal ZnO thin films by solution growth method: a micro-structural investigation, J Saudi Chem Soc. 18 (2014) 712–721.

[261] A. Gouldstone, H.-J. Koh, K.-Y. Zeng, A.E. Giannakopoulos, S. Suresh, Discrete and continuous deformation during nanoindentation of thin films, Acta Mater. 48 (2000) 2277–2295. doi:10.1016/S1359-6454(00)00009-4.

[262] T. Tsui, W. Oliver, G. Pharr, Indenter geometry effects on the measurement of mechanical properties by nanoindentation with sharp indenters, in: MRS Online Proc Libr Arch, 1996.

[263] S. Zhang, Nanostructured thin films and coatings: mechanical properties, CRC Press, 2010.

[264] M.M. Quazi, M. Ishak, A. Arslan, M. Nasir Bashir, I. Ali, Scratch adhesion and wear failure characteristics of PVD multilayer CrTi/CrTiN thin film ceramic coating deposited on AA7075-T6 aerospace alloy, J Adhes Sci Technol. 32 (2018) 625–641.

[265] H.-Y. He, Microstructural, Optical and Electrical Properties of ZnO: Pr Thin Films: Pr-Doping Level Effect, Micro Nanosyst. 8 (2016) 19–25.

[266] M. Uthayakumar, S. Aravindan, K. Rajkumar, Wear performance of Al–SiC–B4C hybrid composites under dry sliding conditions, Mater Des. 47 (2013) 456–464. doi:10.1016/J.MATDES.2012.11.059.

[267] K. Rajkumar, S. Aravindan, Tribological performance of microwave sintered copper–TiC–graphite hybrid composites, Tribol Int. 44 (2011) 347–358. doi:10.1016/J.TRIBOINT.2010.11.008.

[268] C. Wang, X. Tan, S. Chen, R. Yuan, F. Hu, D. Yuan, et al., Highly-sensitive cholesterol biosensor based on platinum–gold hybrid functionalized ZnO nanorods, Talanta. 94 (2012) 263–270. doi:http://doi.org/10.1016/j.talanta.2012.03.037.

[269] N.K. Mukhopadhyay, P. Paufler, Micro- and nanoindentation techniques for mechanical characterisation of materials, Int Mater Rev. 51 (2006) 209–245. doi:10.1179/174328006X102475.

[270] A. Kulandaisamy, J. Reddy, P. Srinivasan, K. Babu, G. Mani, P. Shankar, et al., Room temperature ammonia sensing properties of ZnO thin films grown by spray pyrolysis:

Effect of Mg doping, J Alloys Compd. 688 (2016) 422–429.

[271] K.-J. Ahn, J.-H. Park, B.-K. Shin, W. Lee, G.Y. Yeom, J.-M. Myoung, Effect of sputtering power on the properties of ZnO:Ga transparent conductive oxide films deposited by pulsed DC magnetron sputtering with a rotating cylindrical target, Appl Surf Sci. 271 (2013) 216–222. doi:10.1016/J.APSUSC.2013.01.163.

[272] Y. Gao, T. Cao, F. Cellini, C. Berger, W.A. De Heer, E. Tosatti, et al., Ultrahard carbon film from epitaxial two-layer graphene, Nat Nanotechnol. 13 (2018) 133–138. doi:10.1038/s41565-017-0023-9.

[273] M. Lichinchi, C. Lenardi, J. Haupt, R. Vitali, Simulation of Berkovich nanoindentation experiments on thin films using finite element method, Thin Solid Films. 312 (1998) 240--248.

[274] A. Pelegri, X. Huang, Nanoindentation on soft film/hard substrate and hard film/soft substrate material systems with finite element analysis, Compos Sci Technol. 68 (2008) 147–155.

[275] G. Li, R. Shi, Q. Fan, Y. Xia, H. Zhang, Three-dimensional microstructure-based micromechanical modeling for TC6 titanium alloy, Mater Sci Eng A. 685 (2017) 327–331. doi:https://doi.org/10.1016/j.msea.2017.01.025.

[276] T. Rousseau, C. Nouguier-Lehon, P. Gilles, T. Hoc, Finite element multi-impact simulations using a crystal plasticity law based on dislocation dynamics, Int J Plast. 101 (2018) 42–57. doi:https://doi.org/10.1016/j.ijplas.2017.10.008.

[277] X. Huang, A.A. Pelegri, Mechanical characterization of thin film materials with nanoindentation measurements and FE analysis, J Compos Mater. 40 (2006) 1393–1407. doi:10.1177/0021998305059728.

[278] M. Reibold, A. Belger, N.K. Mukhopadhyay, P. Gille, P. Paufler, The impact of nanoindentation at room temperature upon the real structure of decagonal AlCoNi quasicrystals, Phys Status Solidi. 202 (2005) 2267–2276. doi:10.1002/pssa.200521040.

[279] M.F. Doerner, D.S. Gardner, W.D. Nix, Plastic properties of thin films on substrates as measured by submicron indentation hardness and substrate curvature techniques, J Mater Res. 1 (1986) 845–851. doi:10.1557/JMR.1986.0845.

[280] S.D. Mesarovic, N.A. Fleck, Spherical indentation of elastic–plastic solids, Proc R Soc London A Math Phys Eng Sci. 455 (1999) 2707–2728.

[281] X. Huang, A.A. Pelegri, Finite element analysis on nanoindentation with friction contact at the film/substrate interface, Compos Sci Technol. 67 (2007) 1311–1319. doi:10.1016/j.compscitech.2006.10.005.

[282] F.M. Borodich, L.M. Keer, C.S. Korach, Analytical study of fundamental nanoindentation test relations for indenters of non-ideal shapes, Nanotechnology. 14 (2003) 803.

[283] J.H. Choi, C.S. Korach, Tip bluntness transition measured with atomic force microscopy and the effect on hardness variation with depth in silicon dioxide nanoindentation, Int J Precis Eng Manuf. 12 (2011) 345–354.

[284] S. Swaddiwudhipong, J. Hua, K.K. Tho, Z.S. Liu, Equivalency of Berkovich and conical load-indentation curves, Model Simul Mater Sci Eng. 14 (2006) 71–82. doi:10.1088/0965-0393/14/1/006.

[285] Y. Mukai, H. Kagawa, M. Okazaki, Finite Element Analysis on Crack Tip Deformation Behavior under Mode-II Loading in Single Crystal Superalloy., Key Eng Mater. 665 (2015) 281–284.

[286] Y. Zhang, H. Wang, X. Li, H. Tang, A.A. Polycarpou, A finite element correction method for sub-20 nm nanoindentation considering tip bluntness, Int J Solids Struct. 129 (2017) 49–60. doi:10.1016/J.IJSOLSTR.2017.09.015.

[287] A. Bower, Applied mechanics of solids, CRC press, 2009.

[288] F. Bedoui, F. Sansoz, N.S. Murthy, Incidence of nanoscale heterogeneity on the nanoindentation of a semicrystalline polymer: Experiments and modeling, Acta Mater. 56 (2008) 2296–2306.

[289] F. Campbell, Elements of metallurgy and engineering alloys, 2008.

[290] Y.C. Lu, S.N. Kurapati, F. Yang, Finite element analysis of deep indentation by a spherical indenter, J Mater Sci. 43 (2008) 6331.

[291] M. Liu, C. Lu, K.A. Tieu, C.-T. Peng, C. Kong, A combined experimental-numerical approach for determining mechanical properties of aluminum subjects to nanoindentation, Sci Rep. 5 (2015) 15072.

[292] Y.E. Lee, J. Bin Lee, Y.J. Kim, H.K. Yang, J.C. Park, H.J. Kim, Microstructural evolution and preferred orientation change of radio frequency magnetron sputtered ZnO thin films, J Vac Sci Technol A Vacuum, Surfaces, Film. 14 (1996) 1943–1948.

[293] M. Dao, N. v Chollacoop, K.J. Van Vliet, T.A. Venkatesh, S. Suresh, Computational modeling of the forward and reverse problems in instrumented sharp indentation, Acta Mater. 49 (2001) 3899–3918.

[294] F. Sansoz, T. Gang, A force-matching method for quantitative hardness measurements by atomic force microscopy with diamond-tipped sapphire cantilevers, Ultramicroscopy. 111 (2010) 11–19. doi:10.1016/J.ULTRAMIC.2010.09.012.

[295] W. Gerberich, N. Tymiak, J. Grunlan, M. Horstemeyer, M. Baskes, Interpretations of indentation size effects, J Appl Mech. 69 (2004) 433--442.

[296] B. Wen, C.Q. Liu, N. Wang, H.L. Wang, S.M. Liu, W.W. Jiang, et al., Properties of boron-doped ZnO thin films deposited by pulsed DC magnetron sputtering at different substrate temperatures, Appl Phys A. 121 (2015) 1147–1153. doi:10.1007/s00339-015-9479-3.

[297] X. Yan, M. Dickinson, J.P. Schirer, C. Zou, W. Gao, Face dependence of mechanical properties of a single ZnO nano/microrod, J Appl Phys. 108 (2010) 056101. doi:10.1063/1.3462381.

[298] M. Mata, O. Casals, J. Alcala, The plastic zone size in indentation experiments: The analogy with the expansion of a spherical cavity, Int J Solids Struct. 43 (2006) 5994--6013.

[299] G. Patriarche, F. Glas, G. Le Roux, L. Largeau, A. Mereuta, A. Ougazzaden, et al., TEM study of the morphological and compositional instabilities of InGaAsP epitaxial structures, J Cryst Growth. 221 (2000) 12–19.

[300] J.S. Zabinski, J. Corneille, S. V Prasad, N.T. Mc Devitt, J.B. Bultman, Lubricious zinc oxide films: synthesis, characterization and tribological behaviour, J Mater Sci. 32 (1997) 5313–5319. doi:10.1023/a:1018614811131.

[301] J. Bucaille, S. Stauss, E. Felder, J. Michler, Determination of plastic properties of metals by instrumented indentation using different sharp indenters, Acta Mater. 51 (2003) 1663--1678.

[302] X.H. Tan, Y.-L. Shen, Modeling analysis of the indentation-derived yield properties of metallic multilayered composites, Compos Sci Technol. 65 (2005) 1639–1646. doi:10.1016/J.COMPSCITECH.2004.12.051.